

Copyright
by
Jonathan D. Luisi
2019

**The Dissertation Committee for Jonathan David Luisi Certifies that this is the
approved version of the following dissertation:**

**Longitudinal Visualization of Neurodegeneration:
Digital Biopsy of the Retina**

Committee:

Massoud Motamedi, PHD

Gracie Vargas, PHD

Wenbo Zhang, PHD

Bill Ameredes, PHD

Erik van Kuijk, M.D., PHD

Dean, Graduate School

**Longitudinal Visualization of Neurodegeneration:
Digital Biopsy of the Retina**

by

Jonathan David Luisi

B.S. in Biomedical Engineering

Dissertation

Presented to the Faculty of the Graduate School of

The University of Texas Medical Branch

in Partial Fulfillment

of the Requirements

for the Degree of

Pharmacology & Toxicology Graduate Program

The University of Texas Medical Branch

March 2019

Dedication

To my parents and Danielle for all their support.

Acknowledgements

I would thank my friends and family for their support all their support. Thanks for the loving support from my parents William and Cathy, Sara and Jason, Jack, Haddie, Kenzie, and Danielle. Thanks to my best friends Nick and Kim for their drive. My classmates Brent, Feidi, Javier, Lisa, Liza, Norah, Sanaalarab, Shariq, Syed, and Talia for helping me through everything.

I would also like to thank my committee Dr. Massoud Motamedi, Dr. Gracie Vargas, Dr. Wenbo Zhang, Dr. Bill Ameredes, and Dr. Erik van Kujik for all their efforts and support. For the support in the multitude of projects the members of the Center for Biomedical Engineering and Ophthalmology Department. Of the past and current members thanks to the following for all the support in experiments: Adam Boretsky, David Briley, Edward Kraft, Ethan Hinds, Fan Xu, Jamal Saada, Jinping Yang, Jonathan Lin, Lorenzo Ochoa, Mauro Montalbano, Olivia Solomon, Paula Villarreal, Praveena Gupta, Rahul Pal, Shuang Zhu, Steven Giannos, Wen Huang, Wei Liu, Yong Zhu, Yongquan Jiang. From Dr. Allan Brasier's collaborative lung and exosome group, special thanks to Dr. Jamaluddin Mohammad, Dr. Maria del Rosario Maroto, and Dr. John E. Wiktorowicz for their aid and support in the exosome protocol development. From the Pharmacology and Toxicology Department to Dr. Fernanda Laezza for bringing me to the graduate program.

And lastly, thanks to the administrative staff Lanette Harris, Nicole Bilotta, Patricia Grazzoli, and Penny Welsh for all the aid in keeping me funded and enrolled. Additionally, acknowledgments for the funding from the NIEHS T32 Environmental Toxicology Pre-doctoral Fellowship T32ES007254, The UT Brain Initiative, and the Center for Biomedical Engineering.

**Longitudinal Visualization of Neurodegeneration:
Digital Biopsy of the Retina**

Publication No. _____

Jonathan David Luisi, PhD Biomedical Sciences
The University of Texas Medical Branch, 2018

Supervisor: Massoud Motamedi, PhD

As treatment for most retinal diseases only begins after vision impairing degeneration is detectable, a better understanding of what changes lead to neurodegeneration is required. Due to the isolated physiology of the eye, the classical markers of inflammation are not detectable in-vivo without an invasive biopsy. The major aims of this dissertation are to explore optical methods for a digital biopsy and demonstrate their utility in animal models of disease. In this dissertation, traditional ophthalmology methods were augmented with emerging optical techniques and biological markers to track inflammatory progression in different disease models.

TABLE OF CONTENTS

List of Tables	xi
List of Figures	xii
List of Illustrations	xvi
List of Abbreviations	xvi
i	
1. BACKGROUND.....	1
1.1. Anatomy and Pathology of the Eye	1
1.1.1. Cell Types of the Retina and Central Nervous System	2
1.1.2. Anatomical and Pharmacological Isolation of the Retina	3
1.1.3. Age Related Macular Degeneration (AMD).....	4
1.1.3.1. Choroidal Neovascularization	5
1.1.4. Microglia Activation and Neuroinflammation	7
1.1.4.1. Microglia in Chronic Inflammation.....	7
1.1.4.2. Microglia in CNV	8
1.1.4.3. Microglia Activation.....	8
1.1.4.4. Known Pathways and Markers of Neuroinflammation	10
1.1.5. Exosomes as a novel form of Cellular Communication	11
1.1.5.1. Exosome Origin.....	11
1.1.5.2. Standardization of Exosome Isolation Procedures	12
1.2. Imaging of the Eye.....	13
1.2.1. Fundus Imaging	13
1.2.2. Fluorescent Imaging and Angiography	15
1.2.3. Optical Coherence Tomography (OCT).....	17
1.2.4. Optical Coherence Tomography Angiography (OCTA)	20

2.	OPTICAL COHERENCE TOMOGRAPHY (OCT) AND IMAGE BIOMARKERS	22
2.1.	Abstract.....	22
2.2.	Introduction.....	22
2.3.	Method Development	23
2.3.1.	Image Acquisition.....	24
2.3.2.	A Method for Digital Biopsy.....	25
2.3.3.	A New Algorithm For En-Face OCTA	27
2.3.3.1.	The Basis of a En-Face Spatial-Temporal Contrast OCTA Algorithm.....	28
2.3.3.2.	OCTA Volume.....	29
2.3.4.	Improving Specificity With Projections.....	29
2.3.4.1.	Standard Deviation (STDEV) Projection	30
2.3.4.2.	Mean Intensity Projection (MIP).....	30
2.3.4.3.	Color-Encoded Depth Projection.....	30
2.4.	Results.....	31
2.4.1.	Single Frame Volume: A Digital Biopsy.....	31
2.4.2.	OCTA: Flow Dependent signal	32
2.4.3.	Frame Average by Mean	33
2.4.4.	OCTA: STDEV	35
2.4.5.	Comparisons of Projection Methods	36
2.4.6.	OCTA: MIP	38
2.5.	Conclusions.....	39
3.	OCT LONGITUDINAL STUDIES OF INFLAMMATION.....	41
3.1.	Abstract:.....	41
3.2.	Introduction.....	41
3.3.	Methods	44
3.3.1.	Lesion Verification.....	45
3.3.2.	En-face OCTA Procedure.....	46

3.3.3.Lesion Dynamic Descriptors:	47
3.3.4.Lesion Dynamics: B-Scan Measurements:.....	47
3.3.5.Retinal and Choroid Flatmounts:.....	48
3.3.6.Statistics:.....	48
3.4. Results.....	49
3.4.1.Lesion Verification.....	51
3.4.2.Lesion Dynamic Descriptors	55
3.4.3.Lesion Dynamics: B-Scan Measurements	57
3.4.4.OCTA	60
3.4.5.Immunofluorescent Staining.....	68
3.5. OCTA in Retinopathy of Prematurity.....	69
3.5.1.Development of Neovascular Tufts	69
3.5.2.Vascular Tortuosity and Density	70
3.6. Discussion.....	71
3.7. Conclusions.....	75
4. MICROGLIA NEUROINFLAMMATION BIOMARKERS.....	77
4.1. Abstract.....	77
4.2. Introduction Cx3Cr1 ^{eGFP} Mice.....	77
4.3. Methods	78
4.3.1.Injury Model	79
4.3.2.Tracking in-vivo	80
4.3.3.OCT Methods	81
4.3.4.Immunohistochemistry	81
4.3.5.Ex-vivo Microglia Morphology.....	82
4.3.6.Statistics.....	82
4.4. Results.....	83
4.4.1.OCT + FA Imaging and Analysis.....	83
4.4.2.Microglia Dynamics	88

4.4.3.Ex-vivo Validation.....	92
4.5. Conclusions.....	98
5. ROTENONE INDUCED NEURODEGENERATION	103
5.1. Abstract.....	103
5.2. Introduction.....	103
5.3. Model Development and Methods.....	104
5.3.1.Intravitreal Injections and Dose.....	104
5.3.2.Layers Thickness Analysis	106
5.3.3.Microglia Assessment.....	107
5.4. Results of Rotenone Toxicity	107
5.4.1.OCT Layer Thickness.....	108
5.4.2.Microglia Response	110
5.4.2.1. Adjusted Dose Morphology.....	110
5.4.2.2. Microglia NFL Localization.....	111
5.4.2.3. Microglia Imaging on Ex Vivo Flatmounts by Confocal Microscopy	112
5.4.3.Longitudinal Fundus Imaging	112
5.4.3.1. IR Imaging.....	113
5.4.3.2. FFA Imaging.....	113
5.4.3.3. Autofluorescent Imaging	114
5.4.4.OCTA and En-Face OCT	114
5.4.4.1. Day 7 and 14 Degeneration	115

5.5. Conclusions.....	116
6. EXPLORING THE USE OF EXOSOMES AS A BIOMARKER OF RETINAL DYSFUNCTION	118
6.1. Abstract.....	118
6.2. Introduction.....	118
6.3. Isolation and Characterization of Exosomes	119
6.3.1. Isolation of exosomes from cell supernatant	119
6.3.2. Exosomes from Blood Serum.....	120
6.3.3. Storage of Exosomes	123
6.4. Exosomes in 405nm Stressed 661W Cell Culture.....	124
6.4.1. Constitutive Release	125
6.4.2. Phototoxicity.....	126
6.5. Exosome Inhibition.....	130
6.5.1. Systemic administration.....	131
6.5.2. Control Eye Toxicity Assessment	132
6.5.3. CNV Inhibition.....	132
6.6. Conclusions.....	135
7. SUMMARY AND CONCLUSIONS.....	136
7.1. Future Directions	137
Bibliography	139
Vita (Heading 2, style: TOC 2).....	157

List of Tables

Table 3.2.3-1: Lesion Measurements	59
Table 3.2.3-1: Table of Automated Microglia Counting.....	89

List of Figures

Figure 1.1.5-1:	Exosome Isolation and Analysis.....	13
Figure 1.2.1-1:	Fundus Imaging: Color and Infrared	14
Figure 1.2.2-1:	FA and IR	15
Figure 1.2.2-2:	Fundus Imaging: Infrared and Microglia.....	17
Figure 1.2.3-2:	OCT Imaging of the Retina	19
Figure 1.2.3-3:	B-scan of the Retina Layers.....	19
Figure 2.1.2-1:	Orthographic Representation of 3D data	26
Figure 2.1.3-1:	En-Face OCTA Algorithm on ROI of a Single Slice.	28
Figure 2.2.1-1:	Sample Data of Single Frame OCTA Depth Projections.	32
Figure 2.2.3-1:	Sample Retina Showing NFL and Choroid Enhancement by Frame Averaging.	34
Figure 2.2.4-1:	Enhanced microvasculature through STDEV frame averaging 35	
Figure 2.2.5-1:	Comparison of Mean and STDEV Frame Averaging.....	36
Figure 2.2.5-2:	Comparison of CNR by Vascular Plexus and Frame Averaging Method (N=7)	37
Figure 2.2.6-1:	Comparison of Frame Averaging Method.....	38

Figure 3.2.0-1:	Samples of the Multiple Imaging Views of a Single Eye.....	50
Figure 3.2.0-2:	Comparison of the in-vivo OCTA.....	51
Figure 3.2.1-1:	Lesion Verification.....	52
Figure 3.2.1-2:	OCTA, En-Face and B-Scan.....	53
Figure 3.2.1-3:	Choroid Flatmount.....	55
Figure 3.2.2-1:	Orthographic views and lesion measurement.....	56
Figure 3.2.2-2:	Lesion Dynamics Over Time.....	57
Figure 3.2.3-1:	Lesion Dynamics Plots Over Time.....	58
Figure 3.2.4-1:	Lesion Dynamics OCTA.....	61
Figure 3.2.4-2:	OCTA at 7 and 21 Days.....	62
Figure 3.2.4-3:	OCTA Changes in the Inner Retina.....	63
Figure 3.2.4-4:	OCT Changes in the Choroid.....	64
Figure 3.2.4-5:	OCTA Frame Averaged Inner Retina.....	65
Figure 3.2.4-6:	OCTA Frame Averaged Choroid.....	67
Figure 3.3.1-1:	Day 17 ROP Mice OCTA.....	70
Figure 3.3.1-2:	ROP vs. Control OCTA.....	71
Figure 4.3.1-1:	Microglia and IR Imaging of Lesions.....	84

Figure 4.3.1-2:	OCT and OCTA Longitudinal Imaging.....	86
Figure 4.3.1-3:	Layer Thickness Analysis.....	87
Figure 4.3.1-4:	FFA of Vascular Permeability Assessment	88
Figure 4.3.2-5:	Microglia Density Changes	90
Figure 4.3.2-6:	Microglia Density Changes	91
Figure 4.3.3-7:	CNV Formation	92
Figure 4.3.2-8:	ONL Infiltration of Microglia.....	94
Figure 4.3.2-9:	Subretinal of Microglia.....	95
Figure 4.3.2-10:	Superficial Layer – Chronic Activation of Microglia.....	96
Figure 4.3.2-11:	Corresponding OCTA and Flatmount of a Lesion	97
Figure 4.3.2-12:	Samples of the Microglia Activation States	98
Figure 5.1.1-1:	Microglia Imaging at 3 Days Showing Toxicity	105
Figure 5.1.1-2:	Imaging In-Vivo Microglia Imaging on Days Showing Response to Rotenone Toxicity.....	106
Figure 5.2.1-1:	Comparison of OCT at 7 and 14 Days Showing Thinning and Degeneration.....	108
Figure 5.2.1-2:	OCT Thickness Reports Showing Changes Over Time	109
Figure 5.2.1-3:	OCT Thickness and RNFL Thickness Over Time	110

Figure 5.2.2-1:	Microglia Imaging at 7 Days Showing NFL Localization ...	111
Figure 5.2.3-1:	Longitudinal Fundus Imaging.....	113
Figure 5.2.4-1:	OCTA at Day 7 and 14	115
Figure 5.2.4-2:	OCT Thickness of the IPL.....	116
Figure 6.1.2-1:	Exosomes from Blood Samples.....	122
Figure 6.1.3-1:	Storage Temperature of Exosomes Alters Size	124
Figure 6.2.1-1:	Particle Sizing of Exosomes from 661W Cells and ARPE19 Cells	126
Figure 6.2.2-1:	Cell Culture Phototoxicity	127
Figure 6.2.2-2:	Phase Contrast Imaging of Stressed Cells	128
Figure 6.2.2-3:	Particle Sizing of Exosomes	129
Figure 6.2.2-4:	Western Blots.....	130
Figure 6.3.3-1:	DMSO and GW4869 Treated Eyes: B-scan and OCTA	133
Figure 6.3.3-2:	DMSO and GW4869 Treated Eyes: 7 Day Samples	134
Figure 6.3.3-3:	DMSO and GW4869 Treated Eyes: Measurement Plots	135

List of Illustrations

Illustration 1.1.2-1:	Mouse Eye Schematic.....	4
Illustration 1.1.3-1:	Alterations to the Retina in AMD.....	6
Illustration 1.1.4-1:	Microglia Activation States	10
Illustration 1.2.3-1:	Optical Coherence Tomography.....	18
Illustration 2.1-1:	OCT data Processing Scheme Illustrating Scan Patterns and the Potentially Extracted Information.....	24
Illustration 6.1-1:	Flow Diagram of Exosome Isolation Steps.	120
Illustration 6.1-2:	Blood Serum Processing.....	121
Illustration 6.1-3:	Serum Exosome Processing.....	123
Illustration 6.3-1:	Exosome Secretion and GW4869 Inhibition	131

List of Abbreviations

UTMB	University of Texas Medical Branch
GSBS	Graduate School of Biomedical Science
TDC	Thesis and Dissertation Coordinator
AMD	Age-related Macular Degeneration
BBB	Blood Brain Barrier
BRB	Blood Retina Barrier
CNS	Central Nervous System
CNV	Choroidal Neovascularization
OCT	Optical Coherence Tomography
OCTA	Optical Coherence Tomography Angiography
RGC	Retinal Ganglion Cell
ROS	Reactive Oxygen Species
RPE	Retinal Pigmented Epithelium
UV	Ultra Violet

1. BACKGROUND

1.1. Anatomy and Pathology of the Eye

Ocular physiology is unique in the body, anatomically isolated, yet containing a direct neuronal link to the brain. For example, during fetal development, the eye is an offshoot of the neural crest that becomes the central nervous system (CNS). While the eye contains specialized neurons and structure to allow vision, the progenitor cells and differentiated cell populations are still part of the CNS. The eye consists of two hemispheres: anterior and posterior. The anterior portion is the transparent cornea, anterior chamber, and the lens. In the anterior chamber, the Iris opens and closes the pupil allowing more regulating light. The vitreous fluid separates the lens from the posterior segment containing the retina and choroid. The functional units of the eye are the cells that make up specific layers of the retina; within the inner layers are the neuronal layers, and in the outer layers are the photoreceptors (rods and cones). The posterior layers of the outer retina consist of the Retinal Pigment Epithelium (RPE), the Bruch's membrane, the choroid space, and the sclera which is the most posterior layer. The posterior layers isolate the eye from the rest of the body. The brain and retina are immune-privileged organs, wherein they are surrounded by a selectively permeable blood barrier and have their own immune system comprised of glial cells. With the isolation of the retina, novel methodologies and biopsy surrogates to sample the biological processes are required. To be utilized as biomarkers, the retinal thickness, vascular morphology, and immune response all require non-invasive monitoring and measurement methods.

The glial cell types of interest to inflammation are astrocytes that support neurons and microglia which are the resident macrophages of the neuroretina. The glial cells provide neurotrophic factors to the neurons and help maintain the integrity of the Blood

Brain Barrier (BBB) and the Blood Retina Barrier (BRB). Both the BBB and BRB prevent many pathogens and immune cells from infiltrating the neural tissue¹.

In the vascular structure of the retina, inner layers are avascularized, and the retina relies on diffusion of oxygen and other small molecules. The retinal layers have a high metabolic rate, yet they exist in a hypoxic environment; this environment makes the neuronal layers highly susceptible to ischemic damage. ROS generation in the mitochondria can be exacerbated over a lifetime of photo toxicity with exposure to light, particularly from the portion of the spectrum ranging from ultraviolet (UV) to blue^{2,3}. The photoreceptor containing layers are avascularized, and the retina relies on diffusion of oxygen and other small molecules. The retinal layers have a high metabolic rate yet maintain a hypoxic environment^{4,5}. This hypoxic environment makes the neuronal layers highly susceptible to ischemic damage. ROS generation in the mitochondria can be exasperated over a lifetime of photo toxicity that occurs with long term exposure to light, particularly from the portion of the spectrum ranging from ultraviolet (UV) to blue^{2,3}. Low levels of inflammation and excessive ROS generation are thought to be contributing factors to neurodegeneration.

1.1.1. CELL TYPES OF THE RETINA AND CENTRAL NERVOUS SYSTEM

The cell types present in the CNS and retina specialize during neurodevelopment, but all cells derive from the neural crest. The neurons in the retina each specialize according to the function and layer in which they are found. Photoreceptors are the most unique cells in the retina as they are photosensitive. Photoreceptors initiate neuronal transmission with opsins, such as rhodopsin, causing membrane depolarization. Maintaining the cell membrane polarization and transmission of the impulse wave results in photoreceptors being one of the most metabolically active cell types in the body. Retinal Ganglion Cells (RGCs) are involved in integrating and transmitting the photoreceptor signal to the Optic Nerve Head (ONH) and then to the brain⁶.

Retinal Pigment Epithelial Cells (RPE)⁷ and glial cells (Astrocytes, Microglia, and Muller cells)⁸ support the photoreceptors and neurons. RPE cells form the barrier layer that separates the retina from the choroid and is indicated in regulation of ROS stress in retinal degeneration⁹⁻¹¹. Astrocytes are neuronal support cells that, during homeostasis, are neurotrophic and secrete anti-angiogenic factors, but the reactive state of astrogliosis can promote neuronal apoptosis¹²⁻¹⁴. Microglia are resident macrophages and regulators of phagocytosis and inflammatory response¹⁵⁻¹⁷. Muller cells are similar to astrocytes, but their morphology is different, as they span multiple retinal layers^{18,19}.

1.1.2. ANATOMICAL AND PHARMACOLOGICAL ISOLATION OF THE RETINA

Because of the relatively small volume and anatomical isolation (Illustration 1.1.2-1), the pharmacokinetics of the retina are different from other tissues²⁰. Even when the pharmacokinetics of a drug indicate it should be absorbed into the retina, efflux pumps in the BRB, and osmotic gradients prevent uptake; therefore, a new approach is required to deliver agents across the BRB²¹. For diagnostics, the challenge is to facilitate the transport of biomarkers and drugs across the intact biological barriers. Some current studies indicate that neural barriers may be temporally permeated, but the safety and efficacy currently is undetermined²².

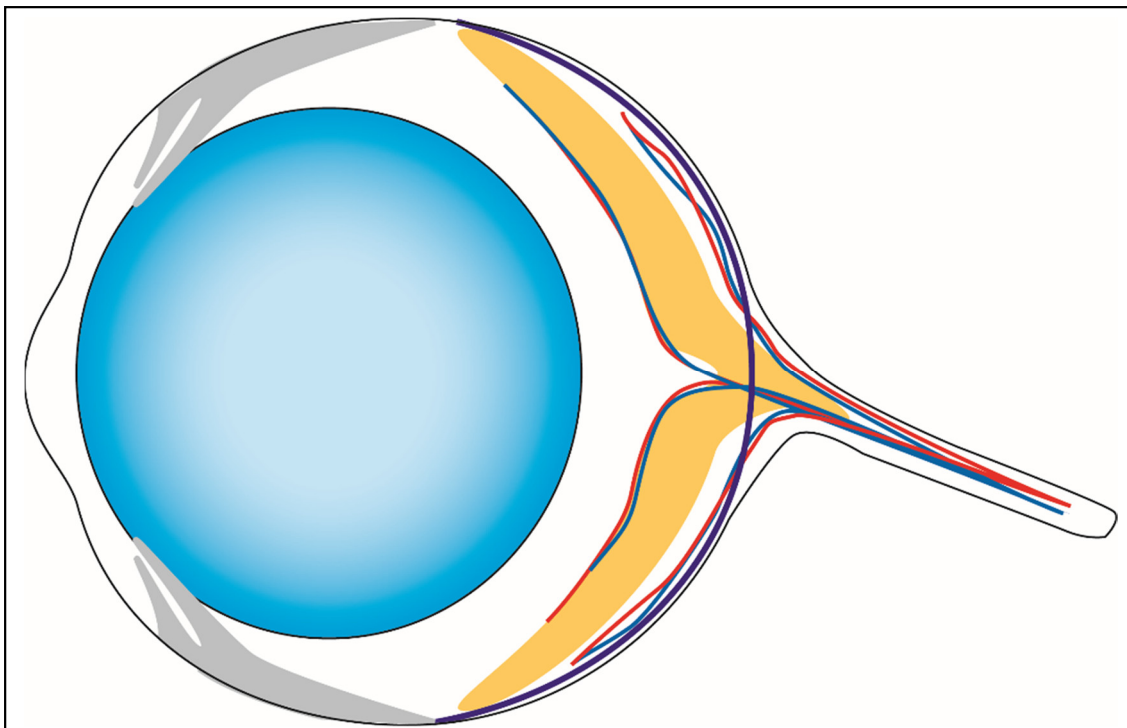


Illustration 1.1.2-1: Mouse Eye Schematic

The Murine eye is significantly smaller than a human eye; however, the basic anatomy and retinal layers are comparable.

The current direct delivery method to access the retina is an intravitreal injection, which presents the risk of cataracts, retinal detachment, infection, or increased intraocular pressure (IOP)²³⁻²⁵. In rabbit models, a sub-tenions injection for anesthetics shows similar distribution to an intravitreal injection; other drugs, however, become trapped in the choroid space^{26,27}. With the intravitreal injection, the distribution of agents in the eye is limited because of maximal dosing volume, frequency of administration, and duration of effect. Large loading volumes can increase the IOP, but concentrated loading bolus can quickly become neurotoxic. Encapsulation in synthetic nanoparticles can improve the pharmacokinetics through time release and isolation of hydrophobic drugs from the aqueous ocular environment²⁸⁻³¹. The best studied class of drugs and delivery methods to the retina are designed for treating the angiogenic and ROS in neurodegenerative retinal diseases.

1.1.3. AGE RELATED MACULAR DEGENERATION (AMD)

Age Related Macular Degeneration (AMD) is a neurodegenerative disease of the eye and one of the leading causes of loss of vision. AMD presents in two forms: the “wet” form with neovascularization and the “dry” form that presents with lipid plaques. In both forms of AMD, oxidative stress and inflammation are two of the pathological features thought to contribute to the disease progression. Chronic inflammation over a lifetime is thought to contribute to Reactive Oxidative Species (ROS) generation and subsequent stress of the neuronal mitochondria that is symptomatic of neurodegeneration. In addition to neurodegeneration in the retina, there is apoptosis of the photoreceptor cells that results in loss of light sensitivity. Lipid oxidation of lipofuscin and Amyloid- β ($A\beta$) play a role in the inflammatory progression inducing production of ROS. In later stages, the lipids accumulate on the Retinal Pigment Epithelial Layer, the boundary layer consisting of membrane cells, to form intrusive deposits called drusen. Furthermore, trafficking of neuronal survival factors and removal of damaged proteins is thought to be impaired as they also contribute to the drusen formation.

1.1.3.1. Choroidal Neovascularization

Choroidal Neovascularization (CNV), Diabetic retinopathy, and “wet” AMD are disorders whose pathogenesis may involve a progressive inflammatory response that leads to uncontrolled angiogenesis. The retinal vascularization is normally tightly regulated against angiogenesis, specifically suppressing Vascular Endothelial Growth Factor (VEGF) and Adrenomedullin (AM)^{32,33}. The RPE cells respond to stress and ROS by releasing cytokines and further ROS generation. The RPE and vascular endothelial cells also respond to systemic inflammation. Pro-inflammatory cytokines such as Tumor Necrosis Factor Alpha (TNF- α) or ischemic response to Hypoxia Inducible Factor-1 α (HIF-1 α) can promote VEGF and AM, resulting in neovascularization^{34,35}. HIF-1 α also induces glial activation in a pro-inflammatory state through the TOLL like receptor 4 (TLR4) pathway. The TLR4 in microglia can simulate NF- $\kappa\beta$ and iNOS to produce

cytokines and ROS³⁶. The pro-inflammatory cytokines contribute to neovascularization.

Illustration 1.1.3-1.

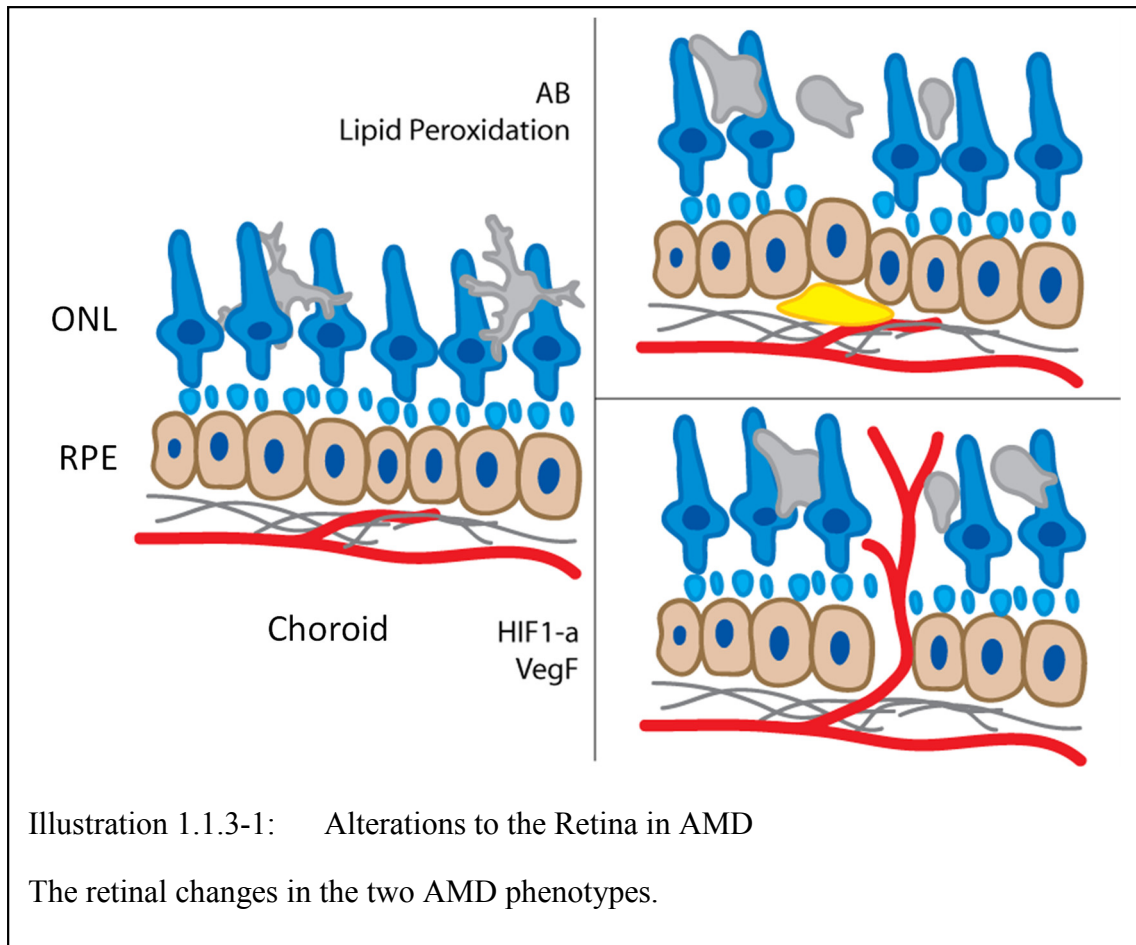


Illustration 1.1.3-1: Alterations to the Retina in AMD

The retinal changes in the two AMD phenotypes.

Neovascularization is the uncontrolled growth of immature vessels that cross into other retinal layers. When the vessels grow into other layers, they displace the functional cells and disrupt the layer morphology furthering inflammation and promoting cell loss. Furthermore, the immature vessels are weak and prone to rupturing, compromising the BRB and allowing infiltration of somatic inflammatory cells. Rupturing the Bruch's membrane and the somatic macrophages can further the glial inflammatory process or initiate neovascularization. The inflammatory processes release cytokines and ROS that promote functional cell atrophy and dysfunction.

When clinical symptoms are apparent, there is already a degree of damage, and the therapeutic goal is to halt this progression. In the treatment of the CNV, Laser Photocoagulation can help target and prevent localized angiogenesis, but it damages the surrounding cells. Pharmaceutical therapy targets VEGF, and inflammatory promoters such as HIF-1 α have shown effectiveness in reducing angiogenesis, but drug delivery routes remain problematic^{30,37}. Small lipophilic compounds may help target the retina, but bioavailability of a systemically administered compounds is low. Currently, the therapeutic approaches focus on preventing further angiogenesis; however, with an improved understanding of the early inflammatory response, we can detect and treat earlier stages of the pathogenesis of retinal diseases.

1.1.4. MICROGLIA ACTIVATION AND NEUROINFLAMMATION

In the Central Nervous System (CNS), glial cells are responsible for maintaining the cellular microenvironment including lipid cycling and neuronal survival. Because of the similarity to other neurodegenerative diseases, the pathogenesis in AMD might be attributed to microglial dysfunction or senescence, leading to increased mitochondrial stress in the neurons. Microglia are the resident immune cells in the retina and the sole resident macrophages; however, their function may be impaired by aging or repeated low-grade inflammation³⁸⁻⁴¹. Interestingly, some studies indicate³⁸ that blocking or suppressing the activation of microglia is neuroprotective and therefore a potential therapeutic target^{40,42}. Contrarily, acute activation of microglia is beneficial and required to maintain a healthy retina. Thereby, assessment of how chronic inflammation develops in-vivo is required to understand the dual role of microglia. Microglia are the key regulators of inflammation controlling canonical pathways of ROS production, alternative NLRP3 inflammasome pathways, regulation of heat shock proteins (HSPs), and homeostasis of cytokines⁴³⁻⁴⁵.

1.1.4.1. Microglia in Chronic Inflammation

Chronic low-grade inflammation is thought to be a contributing factor in the progression of AMD⁴⁶⁻⁴⁸. The disease is modeled in a mouse by laser-induced choroidal neovascularization (L-CNV)⁴⁹⁻⁵¹. In a healthy retina, the microglia are predominately localized to the inner retina in a resting or ramified state in which they extend long, thin processes with complex branching patterns. In the inflamed state, microglia become activated, and their morphology transforms into an amoeboid-like state having retracted and thickened processes, and they migrate to accumulate at the site of inflammation. Sustained microglia secrete inflammatory factors in acute and chronic injury models and may play a critical role in the pathogenesis and show that neurodegeneration is an underlying factor^{46,52}.

1.1.4.2. Microglia in CNV

In the L-CNV model, the microglia proliferation/migration to the choroid is reported to be highest 3-5 days after injury⁵³. When activated, microglia secrete proinflammatory and angiogenic factors and contribute to the production of reactive oxygen species. Sustained microglial activation may also become neurotoxic and increase autophagy of healthy neurons^{54,55}. In disease, such as neurodegenerative disease, chronic inflammation can sustain microglial activation and signaling, and microglia remain in the amoeboid morphology⁵⁶. Microglial activation and dynamics during the progression of CNV are poorly understood, and more rigorous studies are needed to determine microglia activity and localization at different stages of inflammation and retina remodeling. Such knowledge will contribute to understanding the pathogenesis of CNV, identify potential interventional targets, and define time points for treatment such as suppression of activation.

1.1.4.3. Microglia Activation

Because photoreceptors are the most metabolically active cells, their ROS production is constitutive. Microglia, however, are usually in a resting state surveying the microenvironment, unless they are activated where they secrete the additional ROS⁴⁵. The morphology of microglia is altered with activation, moving from ramified to ameboid⁵⁷⁻⁵⁹(Illustration 1.1.4-1). The ramified morphology has long, thin, highly branched processes. Hypertrophied morphology is the retraction and thickening of the process; the branches are fewer but larger and soma can enlarge. Migrating microglia may have an elongated body or simple process. Activated microglia are ameboid, often circular, and are actively secreting cytokines to modulate an inflammatory response. There are several markers to differentiate each activation state, but increased binding of isolectin is a general marker of activation⁶⁰.

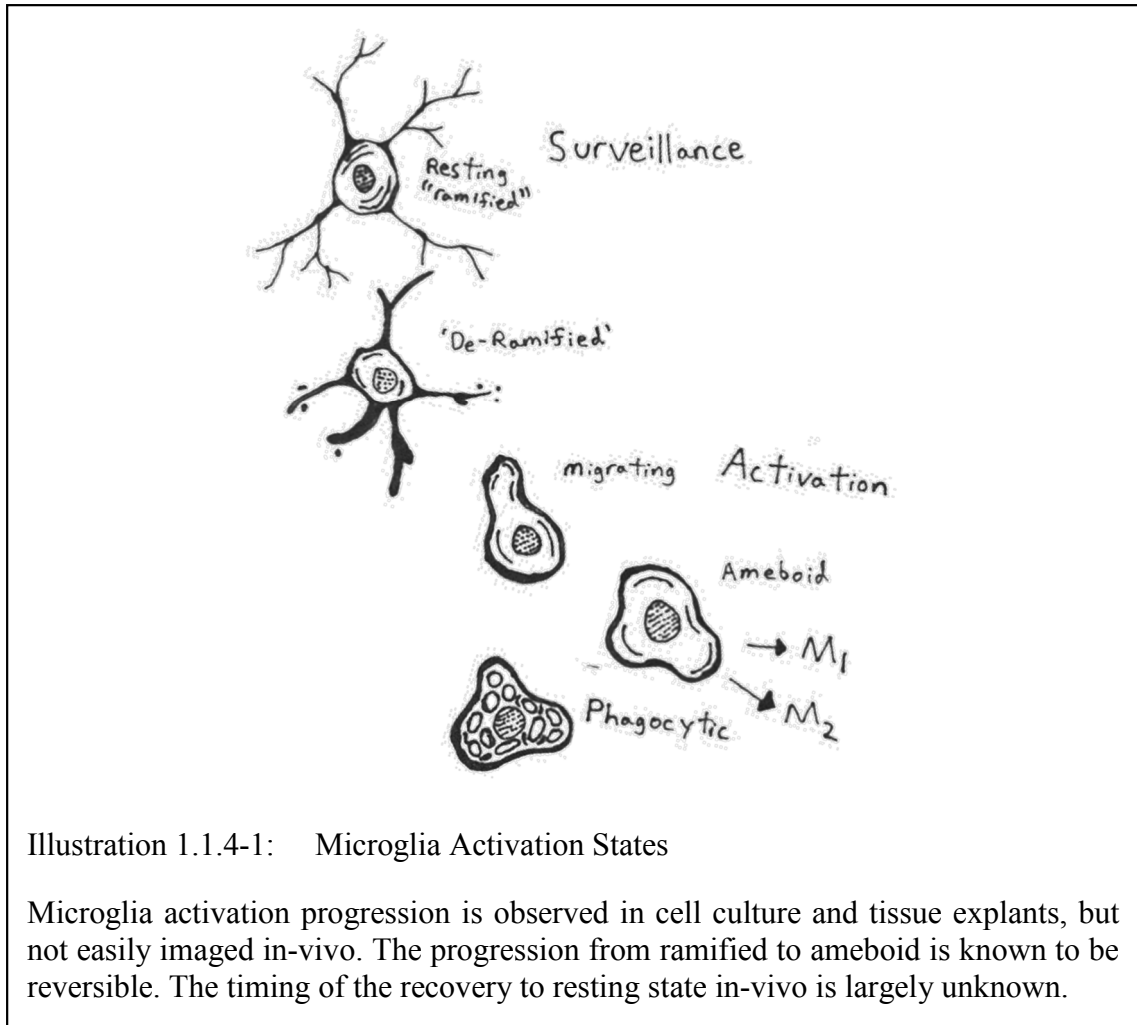


Illustration 1.1.4-1: Microglia Activation States

Microglia activation progression is observed in cell culture and tissue explants, but not easily imaged in-vivo. The progression from ramified to ameboid is known to be reversible. The timing of the recovery to resting state in-vivo is largely unknown.

1.1.4.4. Known Pathways and Markers of Neuroinflammation

HSPs are important molecular chaperones with several key roles: helping proteins maintain proper conformation, preventing aggregation, maintaining complexes, and protein trafficking. HSPs are key regulators of apoptosis^{61,62} and affect the inflammation pathways^{63,64}. Hsp70 and Hsp90 are known to be neuroprotective under stress conditions, and Hsp27 is vital to regulating apoptosis^{65,66}. In AD and possibly in AMD, neurons are protected from A β accumulation by Hsp70. To further protect neurons, Microglia are activated for A β clearance by Hsp90⁶⁷. In this process of glial activation, Hsp90 induces production of IL-6 and TNF α ⁶⁸, while Hsp70 increases expression of TGF- β ⁶⁹.

While this balance of HSPs and cytokines needs to be maintained, the progression of inflammation in the diseased retina indicates that TNF- α , IL-1 β and INF- γ are elevated in endothelial cells. Correspondingly, in early disease stages, HSPs are upregulated and later downregulated in association with neurodegeneration.⁷⁰ The cytokine production can activate the NF- κ B and MAPK pathways, and while in initial stages this low grade inflammation serves to protect the eye, over time it can induce apoptosis. While HSPs cannot be directly sampled in-vivo, the inflammatory regulation is important to consider.

1.1.5. EXOSOMES AS A NOVEL FORM OF CELLULAR COMMUNICATION

Neurons, glial cells, and RPE cells communicate in interconnected cell-cell communication feedback loops via direct contact and extracellular release. Cell derived membrane vesicles (CMVs) are endogenously secreted by many cell types in order to shuttle molecular cargo to effect other cells. In many inflammatory responses, cytosolic proteins and RNA are trafficked from cell to cell through the use of extracellular membrane vesicles⁷¹. Exosomes are small enough to diffuse readily, and the double membrane has surface markers from the source cells for receptor specificity.

1.1.5.1. Exosome Origin

Exosomes are generated and sequestered in multivesicular bodies (MVBs) that originate from invagination of endolysosomal vesicles. When triggered by a Ca²⁺ wave, the MVBs fuse to the cell membrane, and exosomes are released outside the cell⁷². Investigation of the mechanisms of exosome release has indicated that there is a link between synthesis specified by lipid rafts and targeted protein localization prior to release^{73,74}. Exosomes can be inhibited with neutral sphingomyelinase inhibitor GW4869, which prevents MVB fusion and release of exosomes^{12,75}. The cell state and type determine the protein and miRNA content of exosomes released in the retina.

It is believed that exosomes act as an inter-organ transport of protective factors in conditioning therapies. Remote ischemic reperfusion conditioning elicits a cardioprotective and neuroprotective effect despite the distant organ systems, as exosomes are the transporters of the protective factors^{76,77}. Exosomes from the brain of AD patients have been found in the blood serum being co-released with the A β oligomers⁷⁸. Furthermore, the exosomes have been characterized and identified in AD patients at preclinical stages⁷⁹. Similarly, exosomes may play a critical role in inter organ communication of the retina. Within the retina, RPE secretion of $\alpha\beta$ -crystalline along with other anti-angiogenic factors was shown to be selectively released by exosomes^{74,80}.

1.1.5.2. Standardization of Exosome Isolation Procedures

The current protocols for exosome isolation are combinations or variations of the following methods: ultracentrifugation, size exclusion filtration, antigen binding assays, and buoyancy gradient assays⁸¹. It is desirable to isolate the exosomes by differential centrifugation to ensure a larger fraction of CMVs⁸². Isolated exosomes can be analyzed for their proteomics and miRNA. The release of exosomes is modulated by cell signaling, where the composition of the exosomes is both specific to origin cell type and dependent on cell state. The expression profiles are being investigated as a diagnostic tool for cancer and diabetes to differentiate normal and inflammation signaling associated with disease states⁸³. Exosomes are typically verified as being small macrovesicles 10-150nm and are positive for some typical markers as follows: HSP70, CD63, CD9, and ALIX⁸⁴⁻⁸⁶. Isolation and Sizing shown in Figure 1.1.5-1.

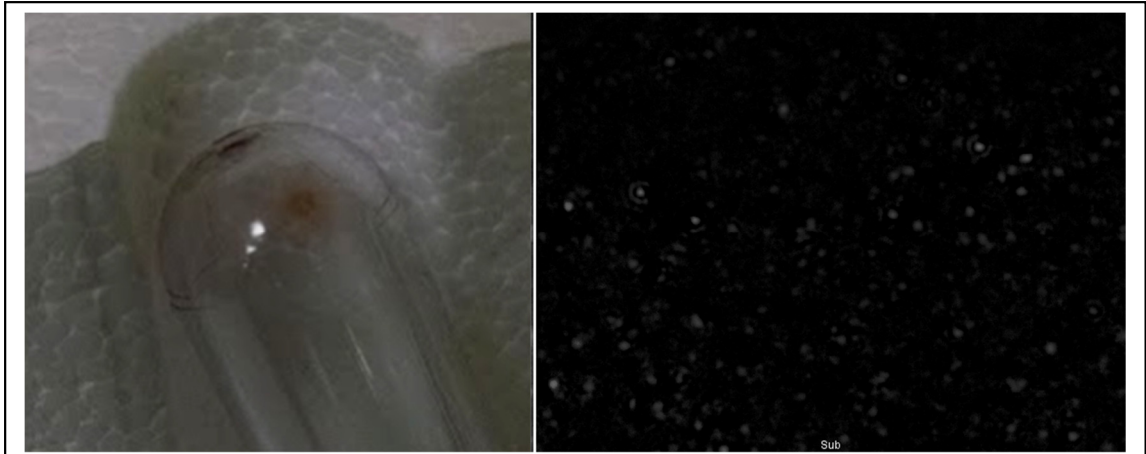


Figure 1.1.5-1: Exosome Isolation and Analysis

Exosomes isolated by ultracentrifugation form a pellet in the bottom of the tube (left). The diffraction pattern of each exosome can be seen in the Nanosight NS300 tracking system (right). The diffraction appears as small spots with the airy disk or “halos” around the larger particles. The diffraction size and motion are tracked over time to calculate density and particle size.

1.2. Imaging of the Eye

Since the cornea and lens are transparent to allow vision, the retina can be directly visualized through the pupil. The simplest and most common screening is white light fundus imaging where the surface can be visualized. Current screening of retinal health is measured by visual acuity (with correction for lens and ocular geometry), Inter-Ocular Pressure (IOP), and direct visualization of the retina for morphological disruptions.

Current screening for AMD, Glaucoma, and Diabetic Retinopathy relies on visual acuity and confirmation by retinal imaging to show disruption in morphology or vascular defect. For each of these diseases, detection and intervention of early retinal inflammation is desirable. Optical Coherence Tomography (OCT), discussed below, is now a widely used tool for imaging the cross section of the retinal layers to scan for defects.

1.2.1. FUNDUS IMAGING

Fundus imaging of the retina involves capturing a reflectance image of the retina following illumination of the eye through the pupil and lens. A slit-lamp ophthalmoscope is used to shine white light onto the retina and capture reflected light from structures such as arteries, veins, and RPE, thereby providing a morphological map of the retinal surface. A color fundus camera operates in a similar manner to a widefield microscope, illuminating a field of view and recording it on a digital sensor. With optics called diopters, the corrective power can adjust the focal plane. For clinical use, the slit lamp is standard for basic exams; the Micron series of color fundus cameras are the equivalent for preclinical research.

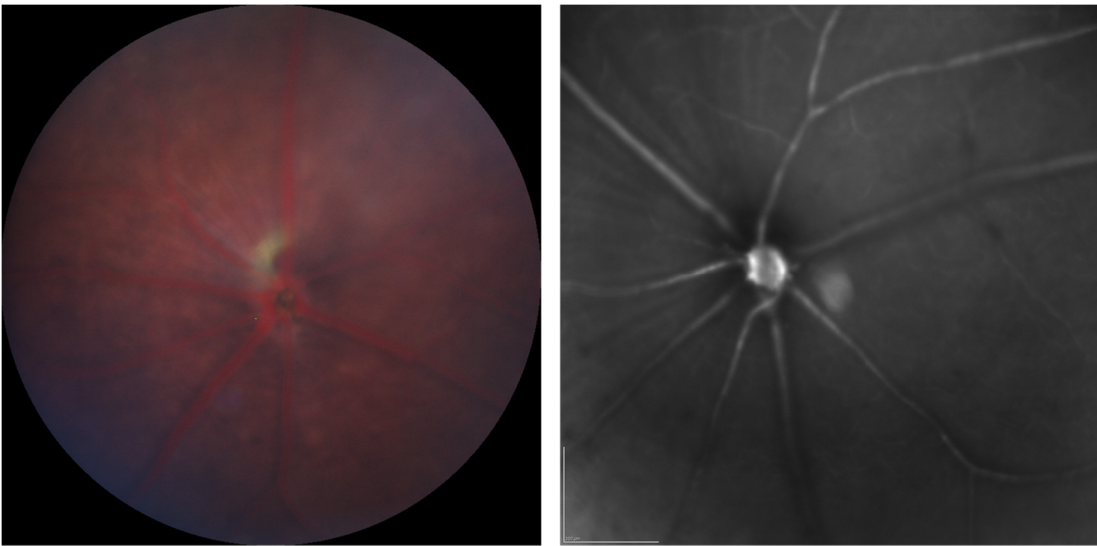


Figure 1.2.1-1: Fundus Imaging: Color and Infrared

The color and IR imaging can detect gross morphology of the retina. In the two images, the Optic Nerve Head and major vasculature can be observed. The RPE reflectivity is uniform in both, providing a preliminary indication that it is a healthy retina.

Fundus cameras can be built with more advanced optics. When used in a Scanning Laser Ophthalmoscope (SLO) configuration, the laser and pinhole setup deliver a low resolution confocal type imaging through the pupil. The selectable wavelength can be focused on different structures, but the axial (depth) resolution is on the order of $\sim 50\mu\text{m}$. Infrared light is used to see the structure of the eye as the longer wavelength allows imaging of the inner retina to RPE. Red-free imaging is a green filter that blocks longer red

wavelengths to enhance vessels, nerve fiber bundles, and retinal infiltrations. With the laser excitation, the fundus camera can detect fluorescence, such as peroxidized lipids or a delivered contrast agent. This specialized mode is reviewed next in its own section.

1.2.2. FLUORESCENT IMAGING AND ANGIOGRAPHY

Vascular changes in the retina are clinically diagnosed with a variety of methods but most commonly with Fluorescent Angiography (FA) using either Fluorescein or Indocyanine green (ICG) dyes delivered intravascularly as a contrast agent^{87,88}. The fluorescent imaging of the dyes allows for an assessment of the retina vasculature and its integrity, specifically the permeability to high molecular weight compounds. Fluorescein is a low molecular weight dye and rapidly diffuses out of the vasculature at a site of increased permeability. ICG is a high molecular weight compound that is slower to perfuse and leak from the vasculature beds unless the wall is severely compromised.

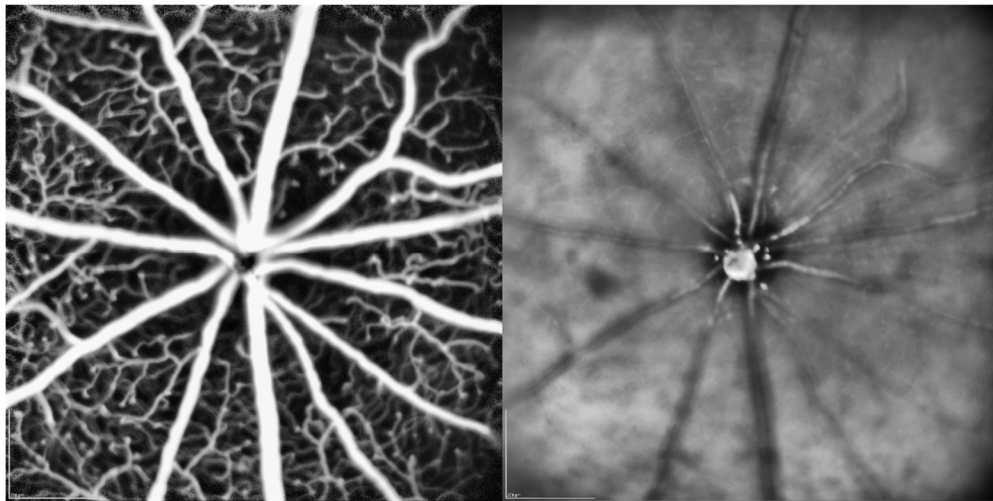


Figure 1.2.2-1: FA and IR

The FA image (left) shows the inner retinal vasculature, including some of the intermediate vasculature. With standard fluorescent slit lamp or fundus imaging, the depth of the signal is unknown. The matching IR image on the right is acquired at the same time and vasculature is not as pronounced.

With the rate of perfusion and diffusion timed after injection, estimates of permeability can be determined. For diagnosis of neovascularization, retinal vessels and

their leakage of dye from the immature vessels can be observed and used for diagnosis of retina pathology or assessment of the effectiveness of therapeutic interventions for the treatment of retina disorders such as retinopathy. In animal models, the leakage is confirmed with choroidal flatmounts.

In addition to the requirement for the injection of a dye that may lead to complications, this image-based diagnostic technique provides an indirect measure of the retina vasculature integrity as measured by vascular permeability, and the resolution for deep vessels is poor. The FA leakage only indicates there is vascular permeability; the leakage cannot resolve the neovascular capillary response or determine the layers affected. Furthermore, serious, albeit rare, cases of anaphylaxis may occur with Fluorescein or ICG injections⁸⁹. The power of OCT (discussed in Section 1.2.3) is the non-invasive ability to create high resolution depth profiles of the retinal structure without any contrast agent.

Fundus fluorescent imaging can detect other agents besides fluorescein. The 488nm excitation wavelength is common in fluorescent imaging. Two notable sources excited by 488nm light are peroxidized lipids and added Green Fluorescent Protein (GFP). In both research and clinical use, retinal autofluorescence is used to detect neurodegeneration, especially RPE and photoreceptor stress^{90,91}. In RPE stress, the lipid aggregate is referred to as lipofuscin. Transgenic induced fluorescence is most often from the jellyfish derived GFP. The protein sequence can be inserted as a reporter gene or constitutively expressed in a target cell.

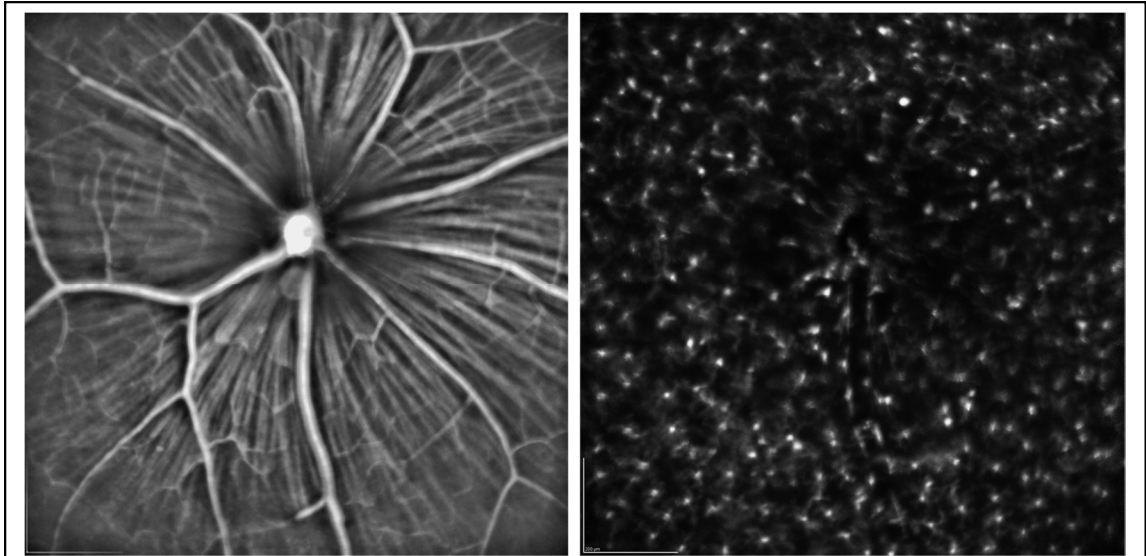
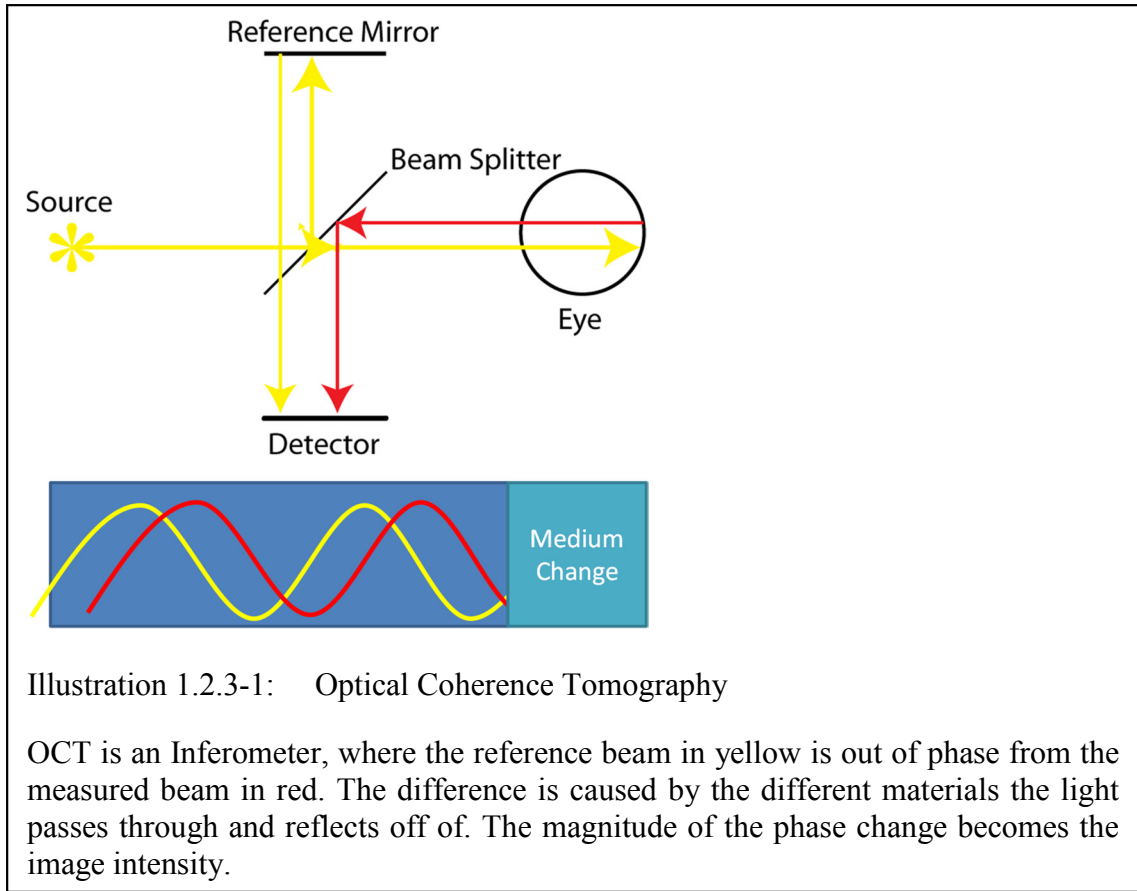


Figure 1.2.2-2: Fundus Imaging: Infrared and Microglia

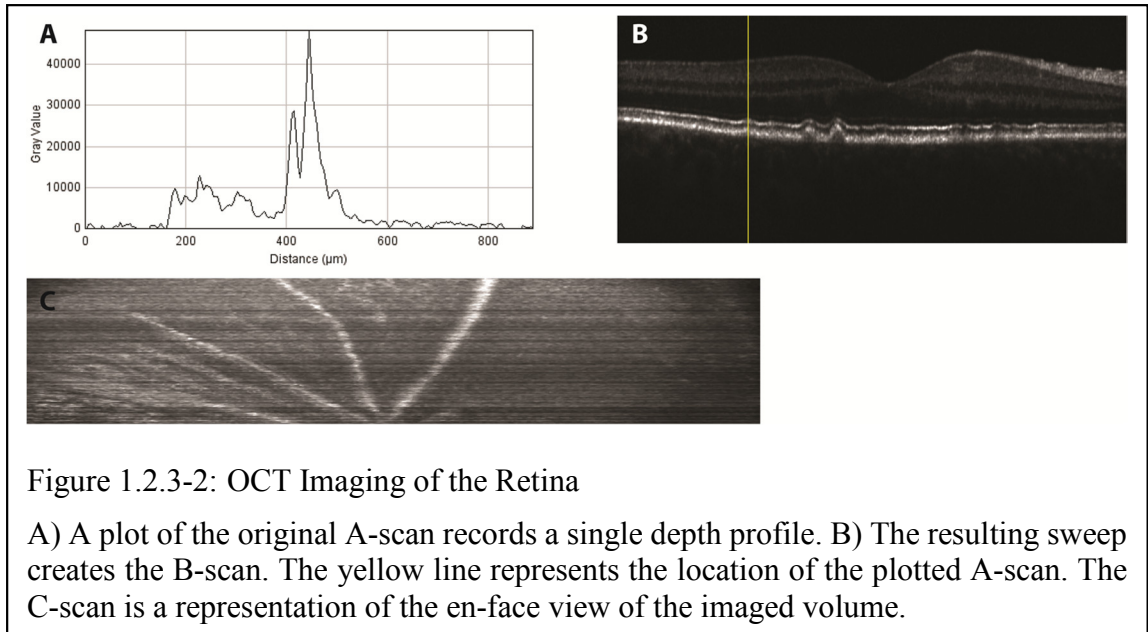
IR imaging can detect the Optic Nerve Head, and in the inner retina, major vasculature and nerve fiber tracks can be observed. The Fluorescent image shows the microglia labeled with eGFP in the inner retina.

1.2.3. OPTICAL COHERENCE TOMOGRAPHY (OCT)

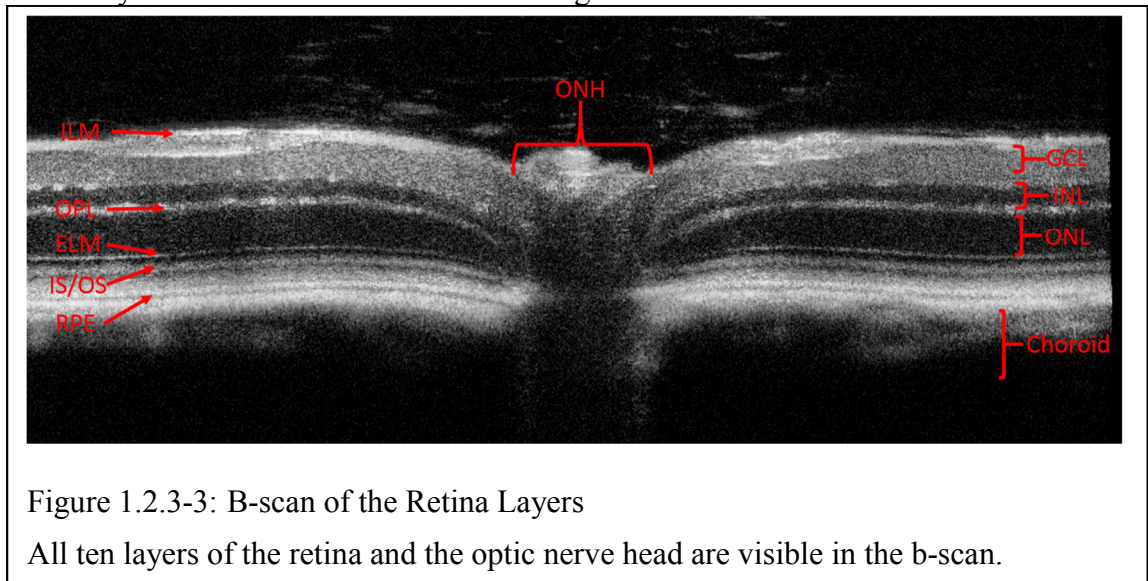
OCT is an interferometer-based imaging system. As the imaging beam passes through the sample, each optical boundary shifts the light out of phase as it is reflected back to the sensor. The imaging beam is compared to a reference beam, traveling along a known path length where the calculated magnitude of the phase delay is transformed (typically fast Fourier transform) into a 3D depth scan. OCT imaging is comparable in the resolving power to measure retinal layers via traditional histology. En-face OCT is a method of creating a volume with the OCT scan, then selecting specified layers for analysis in a fundus view^{92,93}. The use of en-face OCT allows for optical sectioning of the retina at a higher resolution than that afforded by scanning laser ophthalmoscopes (SLO).



A-scan is an individual OCT depth profile produced by the interference pattern of the sampling beam to a reference beam Figure 1.2.3-1. The image is adjustable to compensate for the curvature of the eye by changing the reference arm length in proportion to the axial distance. The image beam in the sensor is out of phase to the reference beam; the Fourier transform of this data results in a pseudo-intensity plot of the depth profile (Figure 1.2.3-2 A).



The B-scan is a cross section of the retinal volume produced by shifting consecutive A-scans in a line. As the consecutive depth profiles are aligned, edge gradients become more apparent (Figure 1.2.3-2 B). To scan a volume, the scanning head defines a pattern of b-scans thus defining the number of repeated frames before the scanner shifts the location and repeats the scan. The B-Scan pattern can be linear or radial, but for our purposes, we will be using rectangular volumes of consecutive B-scans. With the B-scans, all ten layers of the retina can be resolved Figure 1.2.3-3.



The C-scan, or en-face OCT scan, is a slice through the volume providing a more traditional fundus like view (Figure 1.2.3-2 C). The C-scans can be combined via projection methods as an OCT “slab” or a portion of the depth volume containing capillaries of the relative retinal layer. The projection methods or other processing steps can determine the ability to resolve microstructure in the retina.

1.2.4. OPTICAL COHERENCE TOMOGRAPHY ANGIOGRAPHY (OCTA)

OCTA is the analysis of the variance of the measured signal to discriminate fluid from static elements in tissue, with constituents that are moving (e.g. red blood cells in vessels) providing a speckle pattern that is discernable from static elements due to differences in variance of light intensity. In addition to the en-face data, the blood flow in the vasculature results in a detectable speckle pattern. When a fluid, such as blood, is flowing through a vessel, the local speckle pattern increases in phase difference and variance. A Fourier transform is performed on the data, which increases the contrast of the vessel from the surrounding tissue. The vessel can be detected with the appropriate processing.

Clinical OCTA systems have been used to characterize DR and CNV in human patients after diagnosis by traditional methods⁹⁴⁻⁹⁶. In the DR, the retraction of the capillaries from the perimeter of the foveal avascular zone is a symptom of the increased ischemia. Recently, OCTA was used to monitor capillary response and choroid vasculature⁹⁷ in Laser photocoagulation therapy, which is used to modulate the oxidative demand in diabetic macular retinopathy.

Although OCTA is being rapidly adopted in the clinic, few animal models have been studied with OCTA⁹⁸ or high-resolution en-face imaging. OCTA is used in a diabetic mouse model⁹⁹ and L-CNV¹⁰⁰⁻¹⁰², but longitudinal studies are limited to the chronic phase. Furthermore, previous proof of concept studies focused on the neovascularization and did not correlate the lesion dynamics to changes in the inner retina. Although these studies

have proven the feasibility of monitoring capillaries, they have not studied the blood-retinal barrier and angiogenic changes in the inner retina capillaries.

Implementation of OCTA methods are optimized to either extract functional data, such as blood flow, or widefield high-resolution structural data in-vivo¹⁰³. To develop OCTA algorithms for resolving the capillary beds, the nature of the imaging system must be considered. Most OCTA systems approach the speckle variance as either a spatial transform or as the temporal transform of an A-scan. With all methodologies, fluid movement enhances the signal variance in the imaging beam. Laminar flow is the highest contrast and aids in Doppler methods for estimating flow rate, but the signal is lost when movement is parallel to the imaging axis; so therefore, vessels perpendicular to the imaging axis are best resolved^{104,105}.

The results of OCTA microvasculature in comparison with alternative enhanced resolution techniques such as Adaptive Optics SLO (AO-SLO) combined with FA has not yielded any significant differences in area calculation¹⁰⁶. However, OCT as a volumetric modality offers optical slicing in the retinal layers and does not require fluorescein as a contrast agent. AO-SLO, while becoming widely adopted, is still slower in scanning than new OCT systems.

2. OPTICAL COHERENCE TOMOGRAPHY (OCT) AND IMAGE BIOMARKERS

2.1. Abstract

With the recent development of the OCT and OCTA techniques discussed in Chapter 1, adaptation to animal models are required. Currently, OCTA methods in rodents require either a custom built OCTA system or adaptation of a clinical device. To that end, a customizable and generalized solution to managing and interpreting the OCT data was required. Once developed, the screening methods were developed for longitudinal studies enabling the tracking of retinal inflammation. The focus of the studies was to identify the feature of inflammation that may be predictive of the final pathology. The models utilized here for method development were laser induced inflammation resulting in either an acute injury or Choroidal Neovascularization. A further proof of concept study included a model of Retinopathy of Prematurity (ROP) to track rapid vascular changes in another established disease model.

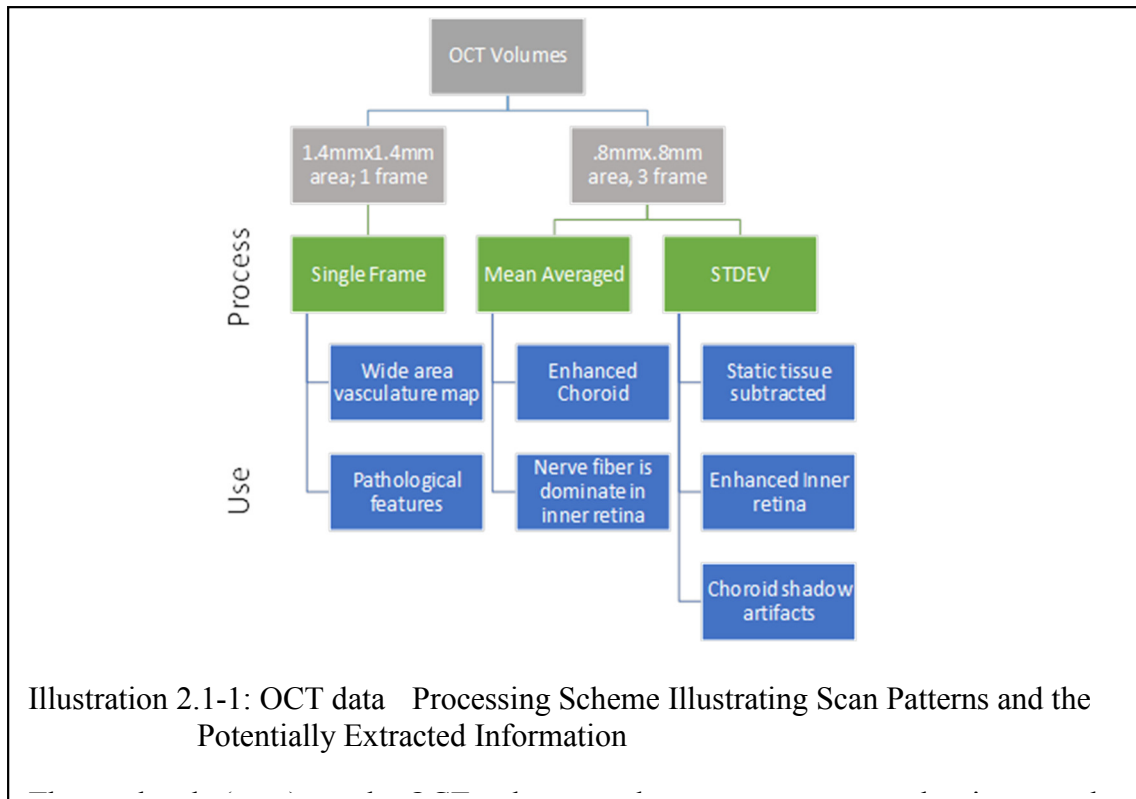
2.2. Introduction

As discussed in Chapter 1, OCT is an interferometric-based noninvasive imaging modality which allows depth (layer-by-layer) assessment of the retina *in vivo*. It is analogous to ultrasound in that it uses time-gated detection of light from backscattered tissue constituents in depth. As light waves, rather than sound waves, are used, the resolution of OCT is much higher than that of ultrasound, albeit at the cost of shallower penetration (1-2 mm). Its most basic form, the A-scan, is the depth profile of the light wave's phase change at a single point, where changes in the scattering properties at boundaries in the material slow the reflected beam.

Over the past 25 years, OCT use in the field of ophthalmology has changed the way we detect and analyze retinal pathology. With early systems, even the comparatively low axial resolution was sufficient to detect changes in retinal layer thickness. Specific layers such as the NFL have a strong correlation of thinning and neurodegeneration. More recent systems have improved the acquisition speed and resolution. The new OCT systems have resolution on the same order of histology (2-7 μm) and the ability to detect all ten layers of the retina. With increased data collection capability, novel scan patterns and processing procedures are now available. Of the two, most importantly to this chapter is A) the near isotropic resolution and B) the ability to analyze speckle variance for blood flow contrast. The near isotropic resolution allows for digital re-slicing through the volume. The fast acquisition allows scan patterns to be optimized for detecting flow.

2.3. Method Development

Adapting OCT for preclinical trials requires development of standardized methods. Each alteration of the experimental and imaging acquisition parameters affects the quantity and quality of recorded data. With the data volume, the speckle variance can be utilized as a contrast to detect blood flow. Movement and heterogeneity of the tissue results in excess scattering that presents as “speckle.” In most applications laser speckle is considered noise and averaging or other noise reduction methods are employed to reduce the speckle effect on image quality^{107,108}. However, this speckle can be advantageous for detecting motion, such as in blood vessels. For OCTA, the contrast of the speckle pattern is enhanced by the turbidity of moving fluids, i.e., blood flow. The increased scattering of blood in vasculature and the presence of large scattering particles, such as blood cells, creates transient and localized speckle. Decorrelation algorithms can detect the intensity ‘flicker’ caused by blood flow, especially in capillaries, by rapidly resampling the A-scan phase variance^{109,110}.



The speckle in a fundus scope can be mapped to detect flow in speckle variance angiography^{111,112}. Alternatively, a high-density scan pattern, such as provided by modern OCT systems, can detect flow, through speckle variance, as increased spatial intensity in the en-face view^{109,113,114}. By digitally re-slicing the rectangular B-scan (x-z) volume to the en-face (x-y) or C-scan view, the speckle and OCT intensity of the vasculature can be seen to be higher than surrounding tissue¹¹⁵. However, since the reflected wave contains both the phase and speckle data, the vasculature is fragmented across the 3D volume and cannot be directly visualized^{116,117}. 3D visualization and projection resolved methods have been utilized to interpolate and resolve vascular morphology. Recent literature shows, OCTA as a volumetric modality can differentiate between the vascular layers in the inner and outer retina and, more specifically, localize a vessel in the inner retina to the different vascular plexuses¹¹⁸.

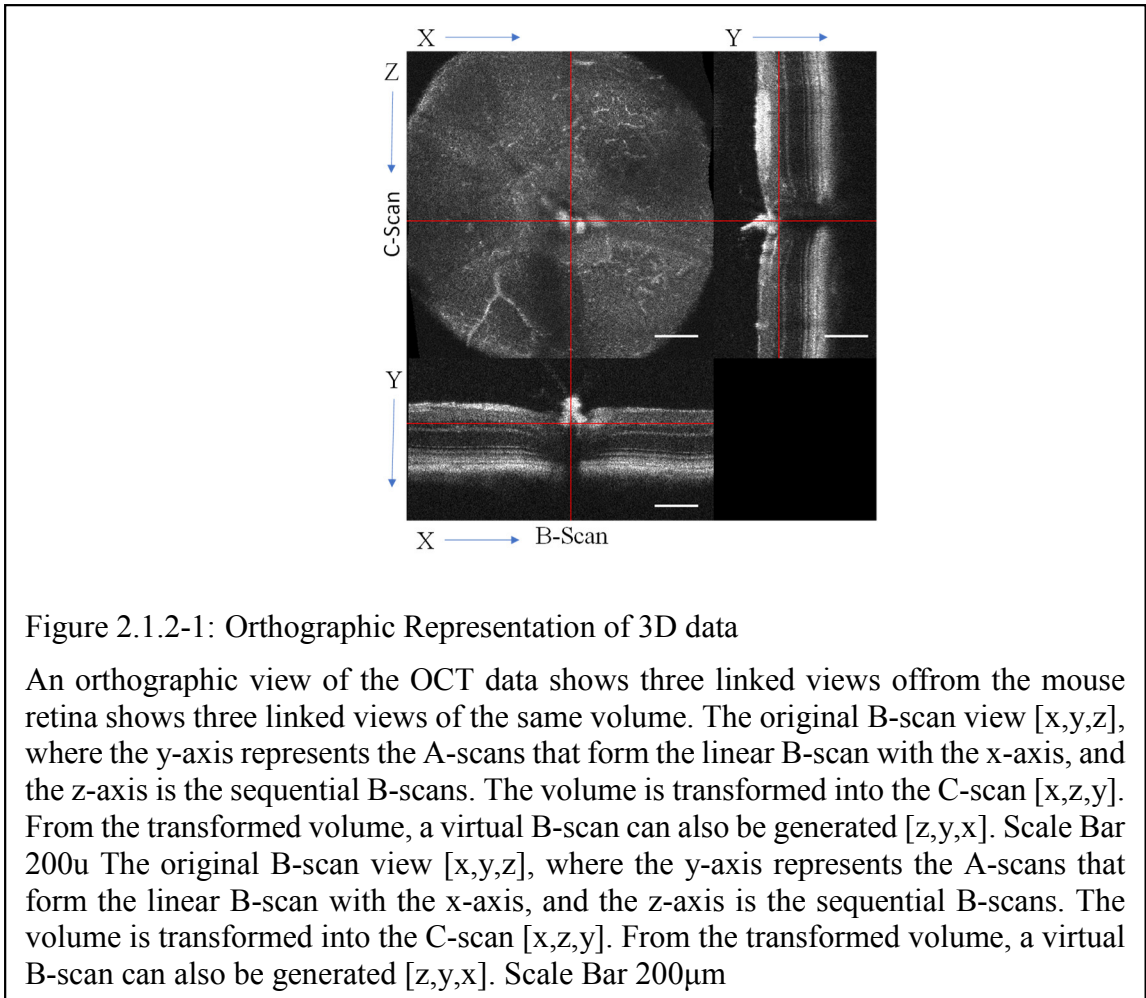
2.3.1. IMAGE ACQUISITION

To extract OCTA data from the intensity image, a near-isotropic high-density scan is required. For smooth transitions, the C-scan needs to be isotropic in the lateral plane, i.e. the same number of A-scans per both axes in the C-scan. In this experiment, the OCT was imaged using a Bioptigen R2200 sdOCT (Leica) with the appropriate mouse retinal lens.

Briefly, to prepare the data, an automated image processing routine was developed in ImageJ to handle the raw data Bioptigen OCT reader and generate the registered 3D data cube. Image registration is a critical step to minimize bulk motion and imaging artifacts and was used to register the b-scans¹¹⁹. The data cube was digitally resliced (Figure 2.1.2-1) and projected as necessary to produce the required data structure for the angiography algorithm. Optimization of the convolution kernels for processing was completed in MATLAB (MathWorks). For wider distribution of this prototype algorithm, all further image processing was performed on the OCT intensity data in ImageJ.

2.3.2. A METHOD FOR DIGITAL BIOPSY

For consistency, all coordinate systems will be referenced to the raw data format with the matrix indices labeled $[x,y,t,z]$ (Figure 2.1.2-1), where x is the number of A-scans per B-scan, y is the A-scan, t is the frames (same repeated B-scan), and z is the number of B-scans in the volume. Widefield OCTA was achieved by using a scan density of 1000x1000 A-scans, with a lateral resolution (x and z -axis) of $1.4\mu\text{m}$, as a single volume. Axial resolution (y -axis, depth) of the system is $1.9\mu\text{m}$, so the resulting data cube of the scanned volume has near isotropic resolution. Averaging of multiple consecutive B-scans (matrix index t) decreases the area to a smaller region of interest; therefore, the scans were optimized for a wide view or repeated scans.



The OCT volume was optimized for a single frame and larger area $XZ = 1.4\text{mm} \times 1.4\text{mm}$ $[x=1000, y = 1024, t = 1, z=1000]$ or for three repeated frames at $.8\text{mm} \times .8\text{mm}$ $[x=572, y = 1024, t = 3, z=572]$. With the Bioptigen system, the scanning acquisition rate is 1 million A-scans in 34 seconds; therefore, the imaging duration is sufficiently short for the acquisition of multiple regions or scan parameters without losing fixation or corneal clarity.

With the custom scan parameters of the Bioptigen system, a high-resolution data cube can be captured and processed for multiple analysis techniques in cross sections and en-face views. Simply put, one single scan volume can replicate the information of multimodal scanning, but with depth-resolved angiography and perfect co-registration between views. As scan density increases, en-face OCT is increasingly more useful. From

the data, an orthographic view display can provide linked views of the point with different cross-sectional orientations. The en-face and both b-scan views are generated at the same point of reference, and morphology can easily be interpreted.

The major benefit is that morphological features, such as branch points, can be used as landmarks to ensure repeated measurements. As pathology may change over time, this provides the ability to repeatedly locate the same physiological point becomes critical to accurately identifying phenotypic modifications associated with disease progression and/or treatment.

2.3.3. A NEW ALGORITHM FOR EN-FACE OCTA

Previously, the spatial-temporal relationship of the speckle variance was developed for fundus angiography for flow measurements; however, the transitive property of this relationship has not been applied to OCTA algorithms. Instead, OCTA algorithms have solely calculated the variance by either a spatial or temporal approach, with the majority using a multi-frame calculation for detecting speckle variation over time. The principles of speckle-variance angiography and the preprocessing steps of fundus vessel tracing utilize local gradients to enhance the contrast of tubular structures. Reflectance imaging and fluorescein angiography cannot resolve both the contrast agents and the depth of the vessels, leaving OCTA with clear advantages in this regard^{120,121}.

Therefore, we hypothesized that by combining the theory and processing of fundus vasculature imaging in a 2.5D manner, the vessel data can be reliably extracted from a single en-face frame. Through the implemented methodology, we have developed a method by which to detect the relationship of structural and functional changes in the microvascular network in the inner murine retina which traditional angiography methods cannot resolve in 3D. The novelty of this algorithm is that the spatial-temporal relationship optimizes the tradeoffs in speed and resolution and can be optimized to use 1 frame, or an averaging as low as 3 frames, to provide the sensitivity needed to detect microvasculature.

2.3.3.1. The Basis of an En-Face Spatial-Temporal Contrast OCTA Algorithm

In the en-face view, the vasculature is extracted using peak-detecting strategies akin to fundus vasculature tracing. Both the tubular structure of large vessels and the blood flow in all vessels act as a contrast agent for the vasculature, so microvasculature that has no flow will either not appear or be fragmented. This algorithm works by exploiting the spatial-temporal relationship of the speckle variance to enhance the localized contrast in the en-face image. The resulting volume is a vessel enhanced image suitable for visualizing slice-by-slice, rendering in 3D, or projecting into optical slabs.

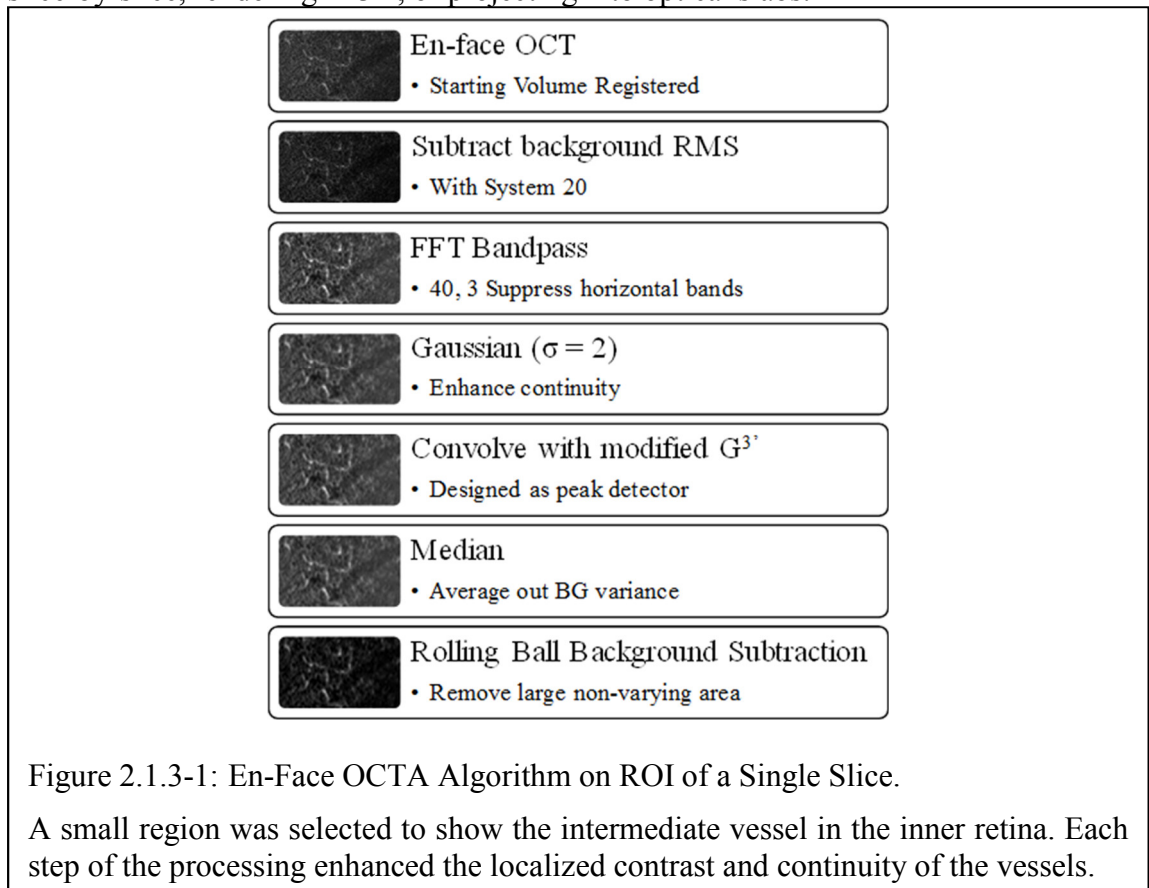


Figure 2.1.3-1: En-Face OCTA Algorithm on ROI of a Single Slice.

A small region was selected to show the intermediate vessel in the inner retina. Each step of the processing enhanced the localized contrast and continuity of the vessels.

This algorithm follows the six steps outlined and runs on each slice of the en-face volume. The data processing utilizes the 2.5D approach¹²² by applying 2D image processing for peak and edge detection to each slice of a 3D volume. The 2.5D approach takes the volume [X, Z] plane to enhance the vasculature, and then enhances continuity

between the slices [Y] axis. First, from the en-face OCT, the background that was measured as the root mean squared (RMS) was subtracted as a constant offset. Secondly, the high- and low-frequency banding caused by bulk motion, such as the mouse's breathing rate (~1-4 Hz), the heart rate (5-13Hz), or registration errors was compensated for with a bandpass filter with horizontal stripe suppression [17]. Through the 2.5D processing and registration, the bulk motion resulted in a contiguous frame registration error while blood flow results in the localized "flicker." The third step was to improve the continuity of the image gradients using a Gaussian with a $\sigma=2$ scaling. The fourth step was ridge enhancement, with a modified 2D peak detector based on a third derivative gaussian kernel scaled for detecting the microvasculature. The fifth stage was a median filter to suppress errors in the ridge detection caused by background variance. The final stage was to use a rolling ball background subtraction algorithm as an adaptive localized method to remove large areas of non-varying background intensity of the static tissue.

2.3.3.2. OCTA Volume

When all stages are complete, the tubular structures of the en-face view are enhanced in contrast from the static tissue and is more continuous than the raw data. The 2.5D process outputs a vessel-enhanced volume with the coordinates system co-registered with the original C-scan. This portion of the algorithm allows for multiple outputs depending on the highlighted pathology. The alternative processing and visualization outputs may be adapted to suit the varying imaging conditions.

2.3.4. IMPROVING SPECIFICITY WITH PROJECTIONS

To visualize the angiogram, the data can be reviewed slice-by-slice through the volume, rendered as a 3D object, or projected with color-coded depths. Currently, the OCT slab requires manual selection to define the starting limit for projections. Orthographic projections, as used as in Figure 2.1.3-1, are utilized to select slabs for analysis. For

consistency in data analysis, a routine was written to start from the selected slice and project consecutive 60 μ m slabs through the end of the stack. The color-coded projection provides depth information of the vascular beds.

Projections are an established approach to reduce the dimensionality of data. How they are applied to imaging data is less uniform as each projection method alters the starting data in subtle but systematic ways. With projections, the data alterations follow the mathematical principles of the central value limit theorem. Projections alter not only depth information of the projected axis but also the steepness of the edge gradients on the other two axis. In choosing projections, the way the data is altered can enhance or hide different features in the structure of the data, i.e. an average projection (mean) will blend a small structure into the background whereas a maximum intensity projection (MIP) may enhance it.

2.3.4.1. Standard Deviation (STDEV) Projection

The standard deviation projection (STDEV) allows for mapping the variance in an image. In the methods development, the mean and STDEV are explored as ways to enhance the contrast of specified structures. STDEV highlights areas of increased variance. Flow contrast is enhanced; however, motion artifacts are also exacerbated.

2.3.4.2. Mean Intensity Projection (MIP)

The mean intensity projection method (MIP) works to minimize localized variance. For b-scans and differentiating static structures from the background tissue, this method reduces noise in the image at the cost of smoothing out the edge gradients of small structures. MIP is an adjunct to the method used to enhance the edge gradients on the B-scans, reducing variance in both re-sliced views.

2.3.4.3. Color-Encoded Depth Projection

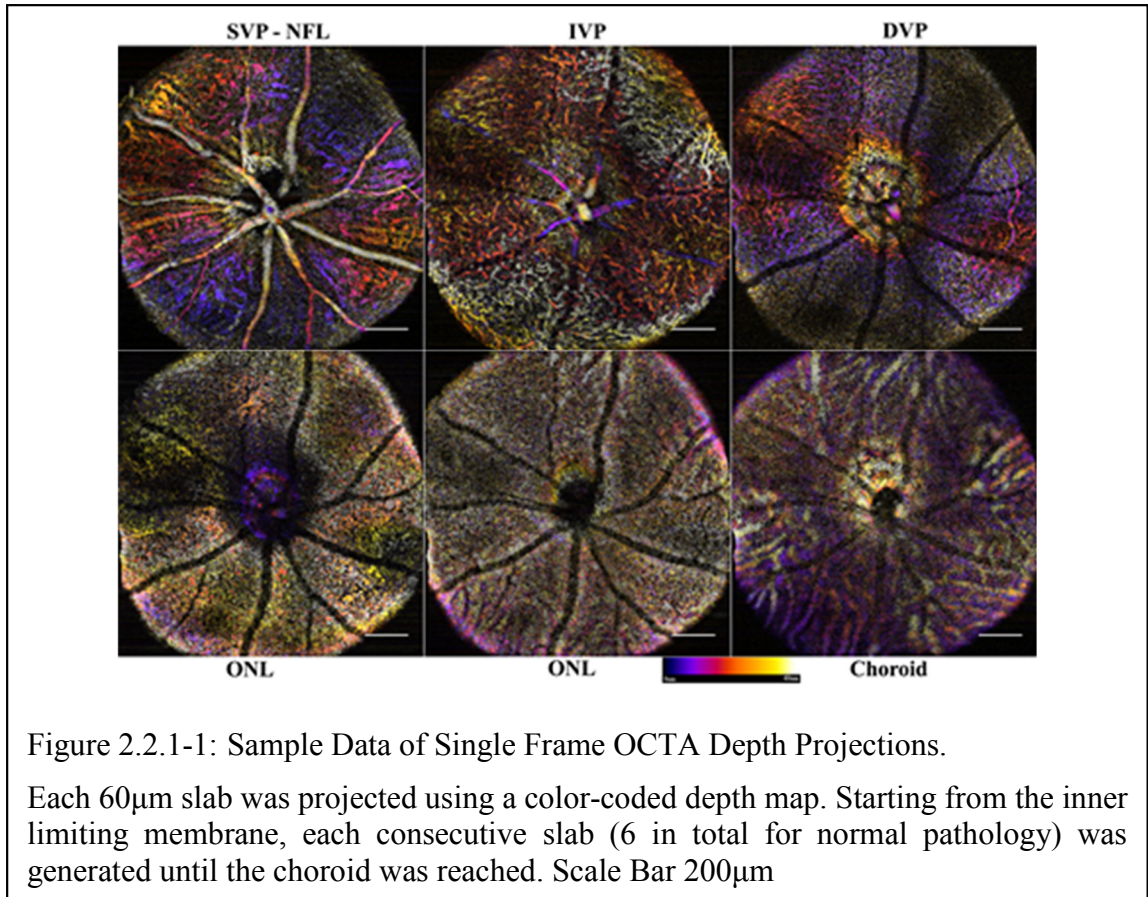
To visualize the angiogram, the data can be reviewed slice-by-slice through the volume, rendered as a 3D object, or projected with color-coded depths. The color coding allows the heatmap to represent the depth data on a 2D image plane. Currently, the OCT slab requires manual selection to define the starting limit for projections. Orthographic projections are utilized to select slabs for analysis. For consistency in data analysis, a routine was written to start from the selected slice and project consecutive 60um slabs through the end of the stack. The color-coded projection provides depth information of the vascular beds while the localized contrast of a MIP is unchanged.

2.4. Results

Through the algorithm presented, tubular objects were reliably detected. With the sampling resolution, the vessels in the inner retina were detected in the separate microvascular beds. The enhanced views allowed choroidal vascular imaging.

2.4.1. SINGLE FRAME VOLUME: A DIGITAL BIOPSY

With the high-resolution volume, the data cube is reliably digitally re-sliced and processed. From the same volume B-scans, Orthogonal Views, 3D visualization, OCTA, and composite visualizations are all possible. For localizing regions of interest and landmarks, the Orthographic view proved most useful. The original B-scan and En-face view are usually linked; however, adding in the virtual B-scan allows precise localization of features. The ambiguity of seeing the cross section of a vessel or pathology is resolved in the three 2d representations. The views can also be rendered in 3D to provide a more intuitive sense of depth.



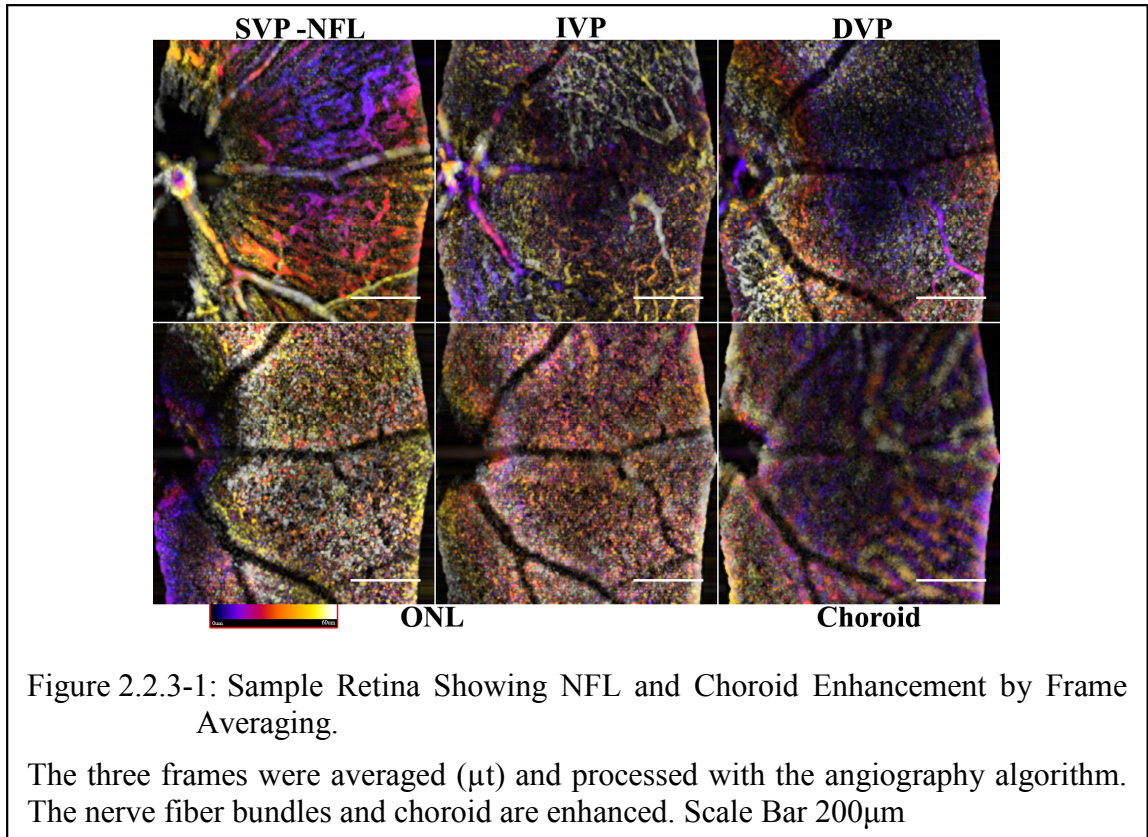
2.4.2. OCTA: FLOW DEPENDENT SIGNAL

The specificity of the vascular signal is related to both structure and variance, with 1) structure being visually evident by the contrast differences in backscattered intensity that occur between the blood vessel (impacted by the optical property differences between the blood and surrounding tissue) and 2) the variance providing an alternate contrast to differentiate areas with flow from static areas. It is advantageous to explore use of both to enhance contrast for the vasculature. Thus, in the single frame method, static structures and vascular flow needs to be differentiated. Since the algorithm uses a ridge detection kernel for vessel-like objects, the nerve fiber tracts are also visible. A simple experimental design using imaging before and after euthanasia collects the necessary data to demonstrate that the signal is flow dependent. As the heart stops, the signal in small vasculature is

immediately lost, and large vessels lose their main source of contrast leaving only the nerve fiber tract visible. See Lu. et. al. for details¹²³.

The 1.4mm 'large-area' field-of-view provides the ability to scan a sufficient area to cover the optic nerve head (ONH) and the vasculature surrounding it. With a single frame, the full scan was acquired in 34 seconds, and with stack registration before reslicing, the motion artifacts were minimized. The remaining bulk motion was compensated for with the bandpass filter, allowing clear resolution of the nerve fiber layer (NFL), intermediate vascular plexus (IVP), and deep vascular plexus (DVP). With the single frame view, a wide area can be imaged rapidly and the microvasculature of the IVP and DVP visualized. The microvasculature of the superficial vascular plexus (SVP), however, cannot be distinguished from the NFL. An example of a naive or defect-free retina of an adult mouse is shown in Fig. 2.2.1-1. Through the layers, the vasculature can be well established. The ONL-containing slabs show no vasculature or intrusions; however, the shadowing artifacts of the superficial vasculature are clearly visible.

2.4.3. FRAME AVERAGE BY MEAN



Averaging the mean value of three or more consecutive frames is the traditional way to limit speckle variation and improve the signal to noise ratio (SNR) or Contrast to Noise Ratio (CNR). This variation of the processing is typically employed to improve the SNR in the B-scans, but, for OCTA, the sensitivity to detect nerve fibers and choroid vessels is enhanced.

Both the NFL and choroid contain large tubular structures, whose static component of the signal can be detected as a ridge. The utility of enhancing the NFL is that neurodegeneration and the contour of the inner retinal layers can be assessed. The NFL slab of the angiography shows the nerve bundles that correlates to traditional red-free fundus imaging. The microvasculature in the SVP, however, are obscured by the nerve bundles Figure 2.2.3-1.

Frame averaging can improve image quality; however, the longer dwell time and smaller area assessment is more prone to motion artifacts. A second registration step may be required if motion drift was not fully compensated for in the initial registration.

2.4.4. OCTA: STDEV

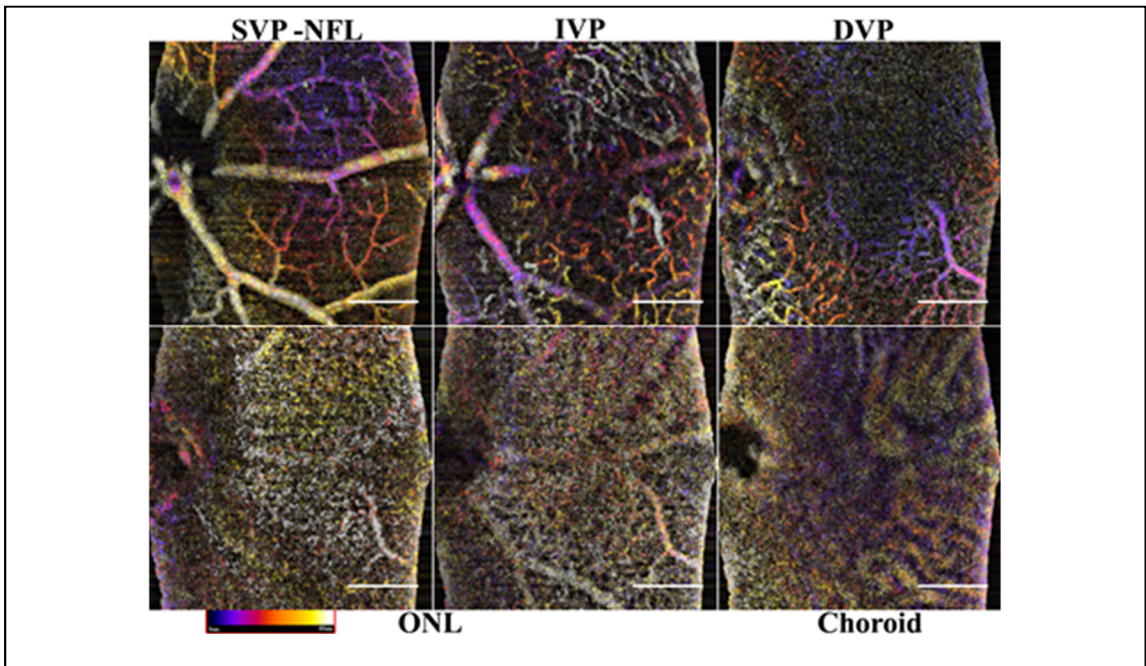


Figure 2.2.4-1: Enhanced microvasculature through STDEV frame averaging

The alternative processing of the same volume used to generate Fig 5, shows the increased specificity of the microvasculature. The SVP, IVP, and DVP are enhanced showing all microvasculature. The ONL and Choroidal slabs show artifacts of the superficial vasculature. Scale Bar 200 μ m.

The improved the vessel specificity of OCTA using STDEV projections is shown in Figure 2.2.4-1. The standard deviation of the frames is, by transitive properties, the complex signal consisting of phase variance and speckle variation. Instead of decorrelation, however, the STDEV is computed during frame averaging, enhancing the specificity of the algorithm to see small flowing vessels in the inner retina. Static tissue, such as the nerve fiber bundles, have lower variance compared to the turbidity of flowing fluids. Unlike the mean averaging method shown in Figure 2.2.3-1, the static component of the NFL and choroid is rejected. Through this flow enhanced discrimination, the inner plexiform layer

increases the improves that can be resolved, although the flow in the choroid the signal is decreased. Figure 2.2.4-1 shows the same retina as Figure 2.2.3-1; however, the vasculature of the inner retina is enhanced. The frame averaging increased the specificity of the OCTA algorithm and explicitly differentiates SVP microvasculature over the nerve fiber bundles in the NFL. The shadow artifacts in the ONL are inverted and could lead to false positives.

2.4.5. COMPARISONS OF PROJECTION METHODS

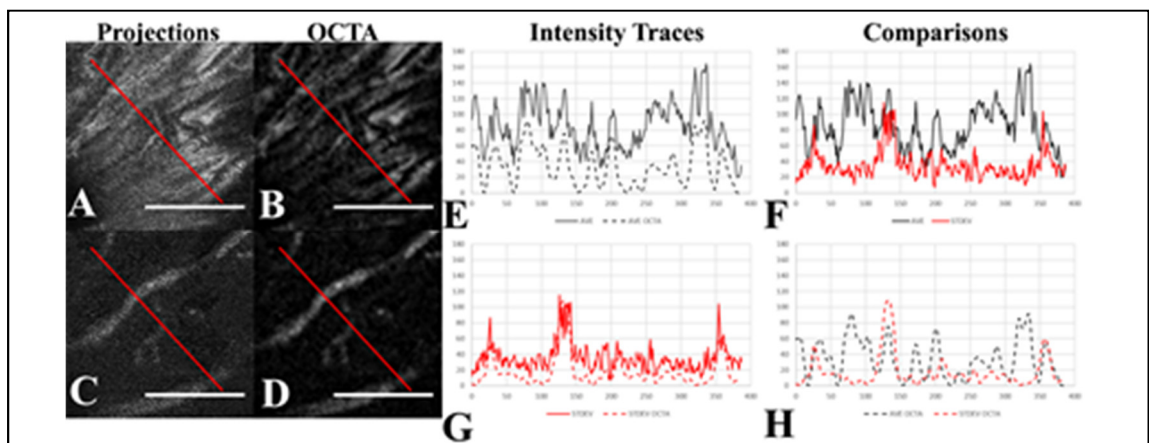


Figure 2.2.5-1: Comparison of Mean and STDEV Frame Averaging

Lines were drawn over the projections of the same retinal slice with (A) mean and (C) STDEV frame averaging, as well as the corresponding OCTA slice (B, D), for line intensity profile measurement (red line). The line profiles for the projections and OCTA for (E) mean averaging and for (G) STDEV averaging are shown. Comparisons between the two averaging methods' line profiles are also shown for both (F) the projections and (H) the OCTA slice.

Figure 2.2.5-1 compares the two frame averaging methods with line profiles across the same retinal slice as either a projection or an OCTA image. The improved specificity of the STDEV frame averaging towards flowing features (i.e., vessels) is clearly visualized (Figure 2.2.5-1 C, D), while stationary features (e.g., nerves, fiber layers) are detected well by the mean frame averaging (Figure 2.2.5-1 A, B). In the line profiles, the vessels manifest as distinct peaks in STDEV frame averaging (Figure 2.2.5-1G), while the fibers present in the same layer appear as a pattern of ridges (Figure 2.2.5-1). Through the line profiles in

Figure 2.2.5-1 H, the specificity of the STDEV averaging method is evident as the nerve fiber bundles are rejected. As each post-processing routine is run on the same scan, this provides fixability in the contrast enhancement for data analysis depending on the structures to be isolated.

$$CNR = \frac{\mu_s - \mu_n}{\sqrt{\sigma_s^2 + \sigma_n^2}} \quad \text{Equation 1}$$

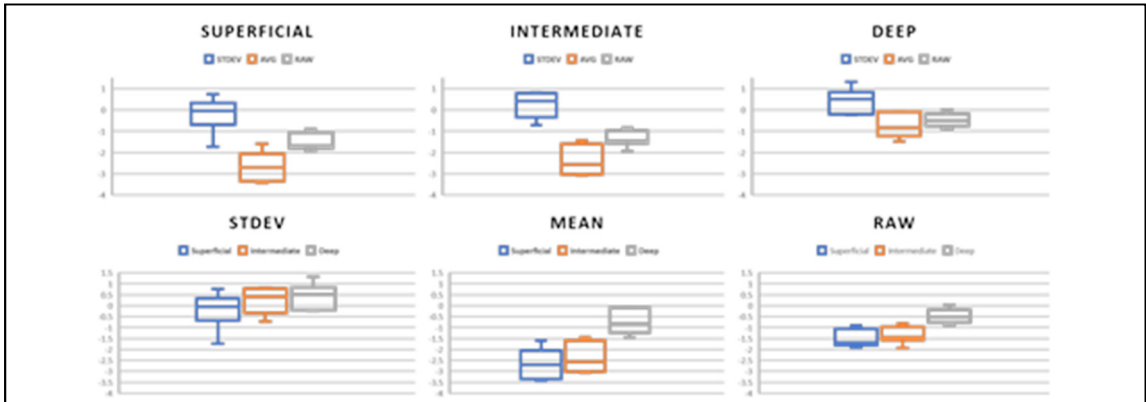


Figure 2.2.5-2: Comparison of CNR by Vascular Plexus and Frame Averaging Method (N=7)

Boxplots of the CNR of the vascular plexuses separated by frame averaging methods (top), showing the highest CNR with the STDEV averaging, followed by the raw images, and finally the mean averaging. Boxplots for the CNR of the frame averaging methods were plotted as well (bottom), displaying the highest CNR in the deep vascular plexus, followed by the intermediate and superficial vascular plexuses.

The contrast-to-noise ratio (CNR) was calculated (n=7) at each vascular plexus (i.e., superficial, intermediate, deep) and for each frame averaging method (i.e., STDEV, mean, raw). The CNR (Equation 1) was calculated with the signal (s) being the vessel, and noise (n) being the background tissue. STDEV frame averaging had the highest CNR across the vascular plexuses, demonstrating its higher vessel specificity, while mean frame averaging had the CNR lower than even the raw images, showing its higher specificity towards non-vessel structures (e.g., nerve fibers) Figure 8. Overall, the superficial vascular plexus had the lowest CNR, likely due to the presence of the NFL causing a higher background and increased noise, while the deep vascular plexus had the highest CNR, presumably due to the reduced influence of the NFL on the background.

2.4.6. OCTA: MIP

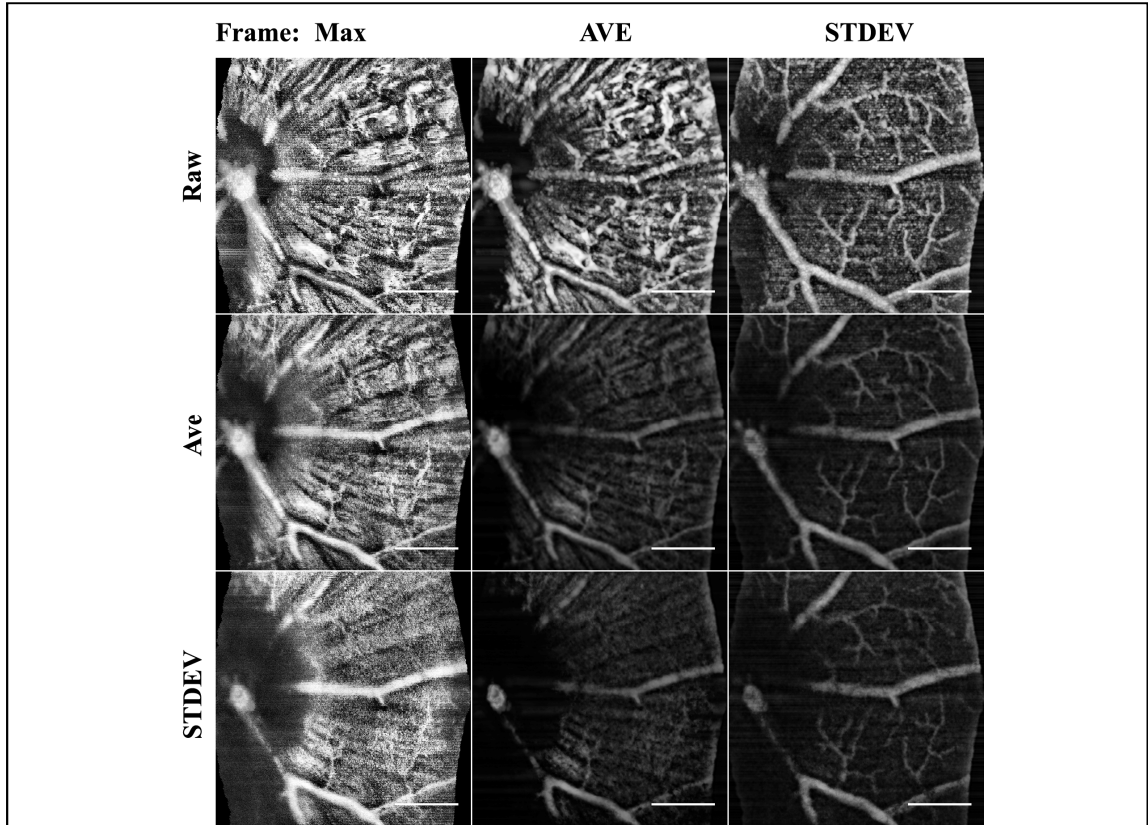


Figure 2.2.6-1: Comparison of Frame Averaging Method

Columns are the Frame Averaging method and the rows are the depth projections used. By altering the combinations, the specificity to detect different the morphology is selectable. STDEV frame averaging improved vessels, where mean AVE enhanced NFL. MAX intensity projections only captured the ILM. Scale bar 200 μ m.

Averaging the mean value of three or more consecutive frames is the traditional way to limit speckle variation and improve the signal to noise ratio (SNR) or Contrast to Noise Ratio (CNR). This variation of the processing is typically employed to improve the SNR in the B-scans, but for OCTA, the sensitivity to detect nerve fibers and choroid vessels is enhanced.

Both the NFL and choroid contain large tubular structures, whose static component of the signal can be detected as a ridge. The utility of enhancing the NFL is that neurodegeneration and the contour of the inner retinal layers can be assessed. The NFL

slab of the angiography shows the nerve bundles that correlate to traditional red-free fundus imaging. The microvasculature in the SVP, however, are obscured by the nerve bundles.

Frame averaging can improve image quality; however, the longer dwell time and smaller area assessment is more prone to motion artifacts. A second registration step may be required if motion drift is not fully compensated for in the initial registration.

2.5. Conclusions

As adoption of OCTA in the clinic continues, there is a growing need for robust and efficient algorithms to increase the prevalence of this technique in both pre-clinical and clinical studies. OCTA, as a label-free modality, can identify the layer-specific changes in the microvasculature. The novel algorithm presented in this Chapter improves upon traditional OCTA by removing the need for computation-heavy decorrelation algorithms to detect vasculature. Furthermore, the algorithm can be adapted for any en-face OCT data where the sampling density approaches the Nyquist criterion for the microvasculature. The algorithm is also flexible to user needs, capable of using a single frame or multiple frames, depending on the desired target. Specifically, to visualize vasculature in various layers of the retina, our approach is adequate with only a single frame for every layer except for the superficial. For the superficial layer, frame averaging is required to reduce the artifacts introduced by the nerve fiber layer.

In the future, we plan to develop the algorithm towards easing the difficulty of automated 3D segmentation, by reducing the processing complexity through the 2.5D methodology. The spatial-temporal relationship and 2.5d processing optimize the efficiency by allowing the application of established vessel segmentation algorithms to the OCT image volumes, as well as optimize the overall algorithm for improved computation speed through slice-by-slice parallelization on a GPU. With the contrasting specificity for flowing and stationary features offered by the two complementary frame-averaging

methods, the algorithm presented has great potential for improving our understanding of retinal diseases and their progression. The prototype ImageJ algorithm will be released for further development. With the established methodology, OCT and OCTA is produced from the same volume. The benefit is twofold: first the acquisition time is minimized and secondly, all processing modalities are perfectly registered. As all of the methodology advancement is post-processing, the algorithm is generalizable to any system.

3. OCT LONGITUDINAL STUDIES OF INFLAMMATION

3.1. Abstract:

Tracking inflammation over time is important to understanding the pathogenesis of neurodegeneration and determining the efficacy of new treatments. In a typical study, a new drug is tested on cell cultures and eventually animal models where FA and histology validate the outcome. In the animal models for AMD, the laser induced CNV is currently accepted for the wet form, but there are debates over the suitability of proposed dry AMD models.

Recent advances in the field of cellular and molecular biology have determined that the biological and pathophysiological processes involved in the onset and the progression of retina neuroinflammatory and degenerative diseases involve inflammation accompanied by tissue and vascular remodeling. An important aspect related to the understanding of retina neurodegeneration that can be studied in animal models is making a distinction between how an injury transitions from acute to either a resolving phase or a chronic response¹²⁴⁻¹²⁶. The resolving response is defined as the pro-inflammatory acute or early phase that lasts only a few days before transitioning to the resolving phase where processes such as wound repair and scarring occur. In contrast, in chronic inflammation, the resolving phase does not occur, and instead, the pro-inflammatory progression of the acute phase persists long after the initial insult is removed. In the retina responses of various capillary beds in response to injury has not previously been studied in-vivo, particularly with attention to comparison of acute and chronic phases.

3.2. Introduction

CNV is clinically diagnosed with a variety of image-based methods, but most commonly with fluorescent angiography (FA) using either fluorescein or indocyanine green (ICG) dyes delivered intravascularly as a contrast agent^{87,88}. Vascular leakage visualized by ICG or FA indicates the presence of altered vascular permeability and are considered safe; although, rare cases of anaphylaxis may occur with Fluorescein or ICG injections⁸⁹. While FA has utility to be used in the clinic as the procedure is established, the correlation and interpretation of OCTA are not yet fully understood; however, OCTA can be used in situations where FA cannot, therefore, OCTA can provide unique information as in some cases such as relative flow measures and depth assessments.

The murine laser-induced model of CNV (L- CNV) induces an inflammatory response in the Retinal Pigment Epithelial Layer (RPE) that is known to be neurodegenerative and promote pathological neovascularization¹²⁷. Low dose laser photocoagulation that is below the CNV threshold can cause photoreceptor ablation, an acute injury. In the acute injury dose range, there are two key thresholds; first is the safety threshold (subvisible¹²⁸) in which photoreceptors are stressed but there is no immediately observable lesion and secondly when the intensity is sufficient to ablate both the photoreceptors and the RPE cells inducing CNV. Currently, the CNV model is used in preclinical treatment efficacy studies, including anti-VEGF³⁷ and anti-TNF α ¹²⁹ therapies, where FA and histology are the current gold standards to measure the impact of drug treatment on limiting the severity of CNV. It is important to note that the low dose laser photocoagulation and photoablation, such as used in surgery, results in acute inflammation that may affect the contralateral eye¹³⁰ but does not develop into chronic inflammation¹³¹. Acute injury lesions lead to permanent photoreceptor ablation and a subsequent scarring without directly affecting the vasculature^{132,133}. Accurate data models that can differentiate between acute and chronic phase are needed to be able to predict the effect of laser injury modulating inflammation^{134,135}, as the subsequent retinal thickness changes may occur days or weeks later^{136,137}.

As shown in Chapter 2, OCT provides the non-invasive ability to create high-resolution depth profiles of the retinal structure without any contrast agent. OCT B-scan imaging is comparable in the resolving power to measure retinal layers via traditional histology^{92,93}. In mouse models, the histological findings are well correlated to measurements with the OCT B-scans^{138,139}. The C-scan, or en-face OCT scan¹⁴⁰, is a slice through the volume providing a more traditional ‘fundus like’ view. The C-scans can be combined via projection methods as an OCT ‘slab’, or a portion of the depth volume, containing capillaries of the relative retinal layer.

Clinical OCTA systems have been used to characterize Diabetic Retinopathy (DR) and CNV in human patients after diagnosis by traditional methods⁹⁴⁻⁹⁶. Recently, OCTA was used to monitor capillary response and choroid vasculature⁹⁷ in laser photocoagulation therapy, which is used to modulate the oxidative demand in proliferative diabetic retinopathy^{141,142} and diabetic macular edema (DME). The photoreceptor damage of modern photocoagulation is at the limit of detection using conventional fundus imaging, and OCT only detects macular thinning after several weeks¹³⁶. FA and OCTA have been well correlated in the inner retina when OCTA was used in a diabetic mouse model⁹⁹. Few trials were performed with OCTA in L-CNV¹⁰⁰⁻¹⁰², but longitudinal studies were limited to only the chronic phase’s impact on the choroid.

To better understand the difference in vascular response between the acute injury and neuroinflammation, we used two irradiation exposure parameters. In these procedures, a surgical photoablation laser operating at 532nm was used. The first dose is a classical L-CNV model and is used here to study the chronic phase of the inflammatory response¹⁴³. The second dose is an acute injury that studies the photoreceptor ablation with a predominantly acute inflammatory response¹⁴⁴. Histological analysis of lesions precludes monitoring the dynamics of lesion formation in longitudinal studies; therefore, the method we developed uses high-resolution data cubes that were processed for multiple co-registered analysis techniques orthogonal (cross sections and en-face views)¹²³ and OCTA.

Simply put, one single scan replicates the information of multimodal scanning, providing depth-resolved angiography and perfect co-registration between views. While previous CNV studies focused solely on visualization of the choriocapillaris^{49,101}, in the current study we screened for image markers of the phases of retinal injury. This work builds upon previous work in the field to show that high-resolution orthogonal OCT and OCTA are a multimodal combination that's highly suitable for longitudinal retinal imaging studies.

3.3. Methods

All animal procedures were performed according to the IACUC regulations. For retinal imaging, wild-type C57BL/6 mice (The Jackson Laboratory) were used. Both male and female mice were randomly assigned into Acute Injury and L-CNV groups. Aged mice were used for two reasons: an increase in RPE autofluorescence, and aged female BL6 mice present with a more severe response to L-CNV. The experimental groups were chosen as litters of 4 female and 4 male mice. At 81 weeks the aged group subjects were screened for any apparent retinal disruptions or defects. Mice were anesthetized with a ketamine dexmedetomidine mixture, and their eyes were dilated. Corneal hydration was maintained with lubricating drops (Alcon).

Laser lesions were induced with an image guided laser system (Micron III Phoenix Research Laboratories, Pleasanton, CA), to guide a photocoagulation laser (Meridian Merilas) to the precise location on the retina. The focused 532nm laser onto the retina reliably induced 4 lesions in the right eye of each subject, typically at the 3,6,9, and 12 o'clock positions corresponding to the retinal quadrants, as previously described by Gong et. al.¹⁴³. Prior to this experiment, a dosing study was used to determine threshold parameters, for reliably inducing Acute Injury lesions and L-CNV, using the Micron III. The L-CNV model^{145,146}, was induced with 180mW for 70ms, and Acute Injury with

46mW of power for 200ms. Following the laser treatment, we imaged the lesions at the timepoints of 1h, 1 day, 2 days, 1 week, 2 weeks, and 3 weeks.

3.3.1. LESION VERIFICATION

Each lesion was verified as acute injury or CNV using traditional in-vivo ophthalmology modalities of the Spectralis HRA +OCT imaging system. White light, Infrared (IR), and FA fundus imaging modes were all used to image the retina (discussed in detail in the Section 3.4.2, and shown in Figure Figure 3.2.2-1). In conjunction with the fundus imaging, volumetric scans were acquired with the Bioptigen OCT. Prescreening of each subject was used to establish baseline health; specifically scanning for preexisting retinal degeneration or physiological abnormalities. Any signs of bleeding or redness were noted, as they could be symptomatic of choroidal bleeding or retinal detachment. As an adjunct to Color fundus, IR imaging was used to confirm lesions. FA imaging was used to scan for vascular leakage from day 3 to 21. Reference IR images were acquired for comparisons to ensure the focus and accuracy of the FA images. Images were calibrated and pertinent measurements are in μm or μm^2 .

As an adjunct to color fundus imaging, IR SLO imaging was used to confirm lesions. For FA imaging, 100 mg/kg of 10% Sodium Fluorescein (AK-FLUOR, Akorn, Decatur, IL) was diluted 1:20 in normal saline for intraperitoneal injection prior to fluorescence fundus imaging with the Spectralis HRA. Multiple FA images were captured through the late stage of perfusion. FA imaging was used to validate vascular leakage from day 3 to 21. Reference IR images were acquired concurrently for comparisons to ensure the focus and accuracy of the FA images. Images were calibrated, and pertinent measurements are in μm or μm^2 . Acute injury lesions were verified as transient hyperreflectivity and the low autofluorescent signal on fundus imaging. The lesions were then verified with FA to show they were not leaking, and OCT for assessment of layer involvement.

3.3.2. EN-FACE OCTA PROCEDURE

Implementation of OCTA methods are optimized to either extract functional data, such as blood flow, or widefield high-resolution structural data in-vivo⁵. In this study, for wide field analysis, we are prioritizing analyzing structural data over flow data, as the accuracy of flow rate is currently undetermined. To develop OCTA algorithms for resolving the capillary beds, the nature of the imaging system must be considered. An individual OCT depth profile is the A-scan, produced by the interference pattern of the sampling beam to a reference beam. The image is adjustable to compensate for the curvature of the eye by changing the reference arm length in proportion to the axial distance. The B-scan is a cross-section of the retinal volume produced by shifting consecutive A-scan in a line. The B-Scan pattern can be linear or radial, but for our purposes, we will be using rectangular volumes of consecutive B-scans.

To extract OCTA data from the intensity image, a high-density scan is required. For smooth transitions, the C-scan needs to be isotropic in the lateral plane, i.e. the same number of A-scans per both axes in the C-scan. En-face OCTA can be achieved by using a scan density of 1000x1000 A-scans, with a lateral resolution of 1.4 μ m, as a single volume. The axial resolution of the system is 1.9 μ m. Averaging or multiple consecutive scans decreases the area to a smaller region of interest, while samples of the lesions were acquired in this manner, a widefield scan was used for analysis. In the en-face scan, the blood flow in the vasculature increases both scatter (phase) and intensity and has been proposed for use in multi-functional OCT imaging to extract angiography and high-resolution structural information from a single scan volum¹⁴⁷. With the single high-density volume, post-processing producing multiple outputs including high-resolution B-scans and en-face OCTA (Figure 3.2.1-2). Our custom automated image processing routine was developed in ImageJ to handle the raw data Bioptigen OCT reader and generate the

registered 3D data cube that compensated for motion artifacts and misalignment of the B-scans.

From the data cube, high-resolution B-scans were resliced through the center of lesions for analysis of lesion morphology. The measurements recorded in μm , are self-normalized for each lesion and reported as percent change. The percent change in the dynamics takes the first measurements at one hour and normalizes the subsequent measurements as expansion (positive values) or reduction (negative values). Additionally, OCTA was generated by further processing with a custom algorithm on the entire data cube or a VOI (Volume of interest, a 3D region of interest). Our algorithm uses structural enhancement and segmentation of the en-face intensity images to produce the 3D angiography. This method is a distinct approach to the implementation of the theory behind J. Wang, et al method of reflectance-based projection-resolved (rbPR) OCTA algorithm to reduce shadow artifacts¹⁴⁸. The rbPR algorithm is a probabilistic approach to histogram equalization and segmentation, whereas our approach is a sequential set of localized structural enhancement iterators. Both approaches enhance the capillary network and are robust to rejecting shadow artifacts in the projections of the retinal layers.

3.3.3. LESION DYNAMIC DESCRIPTORS:

The longitudinal imaging with the OCT system produced data cube (Figure 3.2.1-2) for each timepoint that was processed for en-face images and B-Scans. The qualitative description of the lesion dynamics defined the critical measurements used to differentiate the influence of the light dose on the degree of retinal injury and identify the extent of retinal layers that were disrupted. The lesions were numbered and B-scans that crossed through the lesion midpoint were identified for measurements, exemplars in (Figure 3.2.2-2).

3.3.4. LESION DYNAMICS: B-SCAN MEASUREMENTS:

Lesion growth measurements were compiled as an individual lesion by treatment group and gender. Measurements were recorded to capture the lesion growth dynamics, dimensions from the layers were: A lateral line across the boundary of the outer nuclear layer and outer plexiform layer (Label: ONL). A line is drawn laterally across the Retinal Pigment Epithelium (Label: RPE) layer from edge to edge of visible disruptions. The height of the lesion (Label: Height) measured as the maximum point of OPL-RPE disruption. The final measurement is the widest point across the Exterior Limiting Membrane to Inner Segment/Outer Segment (ELM-IS/OS) protrusion into the ONL (Label: PR).

3.3.5. RETINAL AND CHOROID FLATMOUNTS:

As traditional validation of CNV injury, choroidal flatmounts were prepared for both doses. The corresponding inner retinal was also extracted for flatmounts to show the vascular morphology. Retinas were prepared for confocal imaging by perfusion and/or direct staining with the appropriate fluorescent label. The vasculature was perfusion labeled with Fluorescein-labeled Concanavalin A (Con A) through the carotid artery¹⁴⁹. All eyes were fixed in 4% PFA and micro-dissected for both retinal and choroid flatmounts. Flatmounts, that were not perfused, were incubated with 594 AlexaFluor-labeled Isolectin B4 for 2 hours 1:500 dilution. All samples were stained with 1:200 DAPI solution for 30 minutes. The flatmounts were imaged on the confocal microscope to validate the CNV model.

3.3.6. STATISTICS:

For the in-vivo visualization with OCTA there were 8 mice of mixed sexes and two groups of old and young for each condition. To prevent errors from variable group size effects, a constant 16 lesions that were verified imaged at all time points were used. For immunofluorescent Staining, there were an additional 16 mice used to verify the in-vivo

findings. The standard deviation σ and average μ were computed for individual groups. Because the normalcy and repeated measures conditions were violated for the T-test and ANOVA analysis for significance, the percent change, and C_v was calculated for both sex and age before pooling into the measurement tables. For dimensionality reduction in the longitudinal analysis, the first and second derivatives were computed for the change over time for each lesion and combined into the plotted data model. The significance of the percent change is $> 5\%$ from the initial value. The second derivative assesses for asymptotes, or steady state, where they are no further significant changes $\lim_0 y$. The second derivative as an event detection model detect the trends to describe the multi-parametric longitudinal data. The C_v within groups and between groups was assessed to ensure the trends were consistent within each condition.

3.4. Results

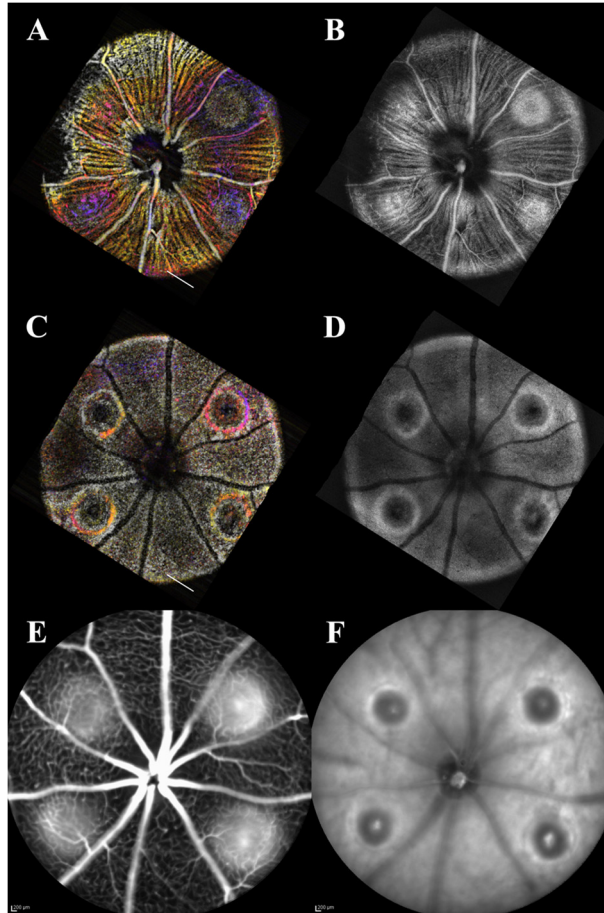


Figure 3.2.0-1: Samples of the Multiple Imaging Views of a Single Eye

A,B is the OCTA and en-face OCT of the inner limiting membrane and superficial vascular plexus. C,D is the OCTA and en-face view of the highlighting Retinal Pigment Epithelium and choroidal disruption. E,F are the fluorescein angiography and IR imaging of the showing the CNV leakage. The landmarks in the en-face image D and fundus F allowed comparisons of the vasculature in the OCTA and FA images. Leakage in the CNV was correlated to the OCTA image in all cases.

The fundus screening could be replicated with en-face OCT/OCTA combination that was suited for non-invasive longitudinal studies (Figure 3.2.0-1). The CNV model showed not only neovascularization but loss of perfusion in the Deep Vascular Plexus that can be confirmed with immunofluorescent staining. (Figure 3.2.0-2). Orthogonal OCT allowed precise landmarking and quantification of the lesions (Figure 3.2.2-1) to build a mathematical model of the changes over time.

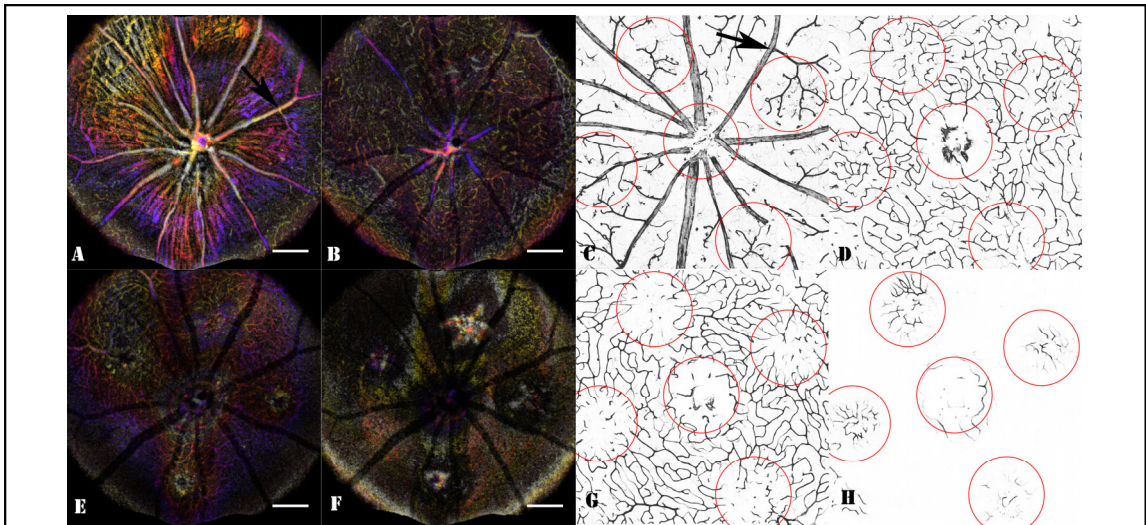
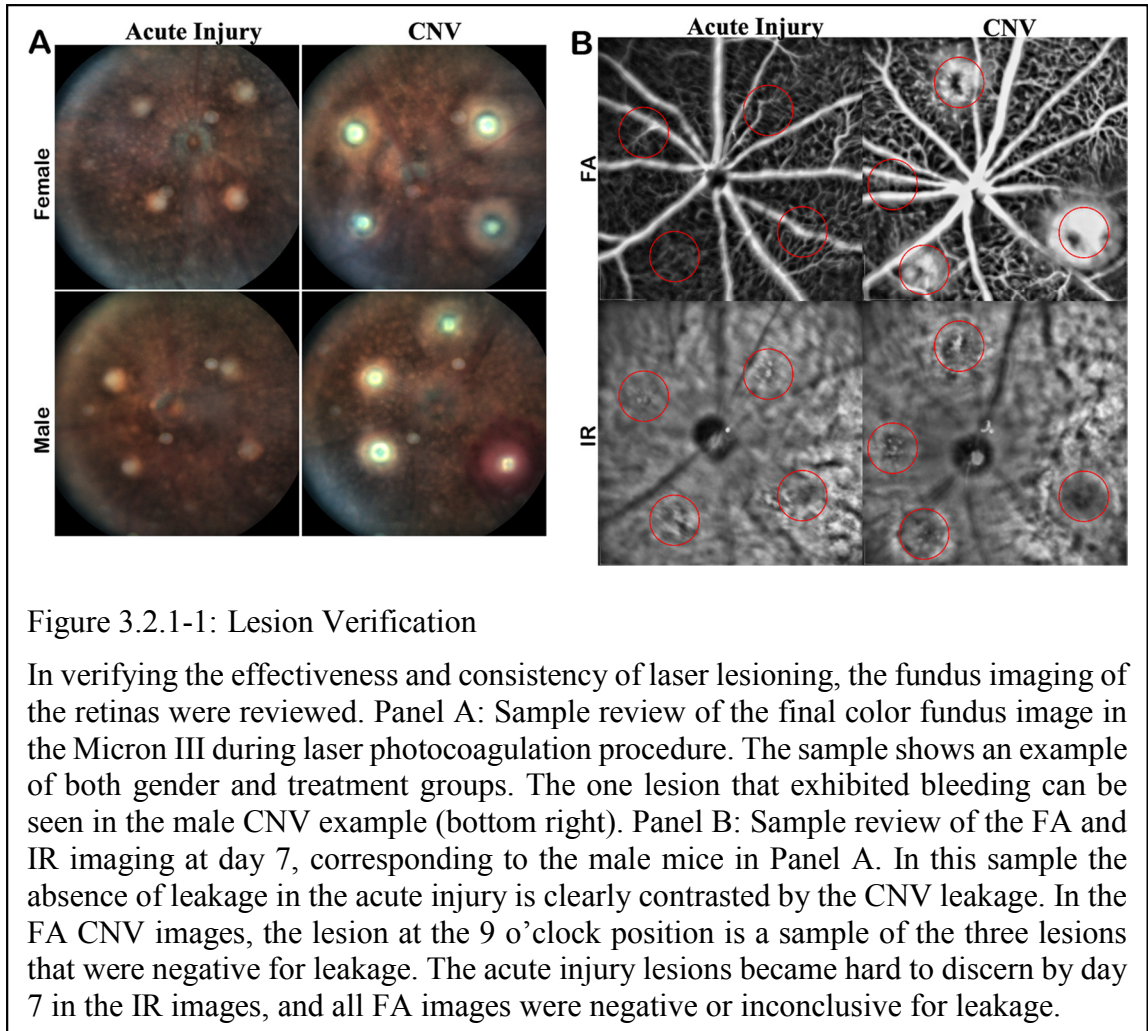


Figure 3.2.0-2: Comparison of the in-vivo OCTA

Comparisons of the in-vivo OCTA (color depth map) and retinal flatmounts (binary mask) demonstrate the correlation between findings for the SVP, IVP, DVP, and ONL. At day 14 of the CNV induction, the final OCTA was generated, then perfused with Con A and extracted for flatmount. The left panel is the OCTA images represented as depth maps through the different layers. The right panel is corresponding flatmount images labeled with Con A. The Black arrow denotes a landmark vascular branch in the superficial layer (A, C) used to compare lesion locations. The superficial (A, C) and IVP (B, D) are intact with perfused vasculature at day 14. The DVP shows a clear disruption of the vasculature where areas of non-perfusion are clear in both OCTA and confirmed in the flatmount. The ONL (F, H) should be avascular, however, at this stage of CNV there is a signal in the OCTA and vascular staining in the flatmounts.

3.4.1. LESION VERIFICATION

Each lesion was classified, and measurements were compiled using the following order of assessment: fundus validation, OCT qualitative description, OCT measurements, and OCTA visualization. Following laser irradiation, all animals presented with hyperreflective lesions in the color fundus images. Acute injury dose showed no signs of bleeding or vascular leakage. The initial OCT images confirmed the presence of the lesion for both doses by the presence of a disruption in the ONL. CNV dose presented with a clear vaporization bubble in all lesions, and only one lesion had severe bleeding, samples in panel 'A', (Figure 3.2.1-1).



The IR imaging tracked the lesions and helped guide the FA. Autofluorescence baseline imaging before FA shows an inconsistent severity of the hyperfluorescent response, some CNV lesions fluorescing brightly while others were not detectable even with maximum gain for detector sensitivity. The maximum fluorescent intensity in either model remains below the detectors threshold with the sensitivity gain used for FA. Because of the low autofluorescence intensity, is therefore not a major confounding factor when assessing the leakage of the CNV.

While the CNV had clear evidence of retinal disruptions, the boundaries of the acute injury lesions were hard to discern from the rest of the retina. Photoreceptor damage observed in the Outer Nuclear Layer (ONL) of the B-scan OCT imaging was often

undetectable in the fundus images and unable to determine the extent of the damage of the acute injury lesions. The orthogonal views were used to landmark the optimal B-scans for the lesions, however, any single en-face slice was insufficient to determine the morphology of the lesion.

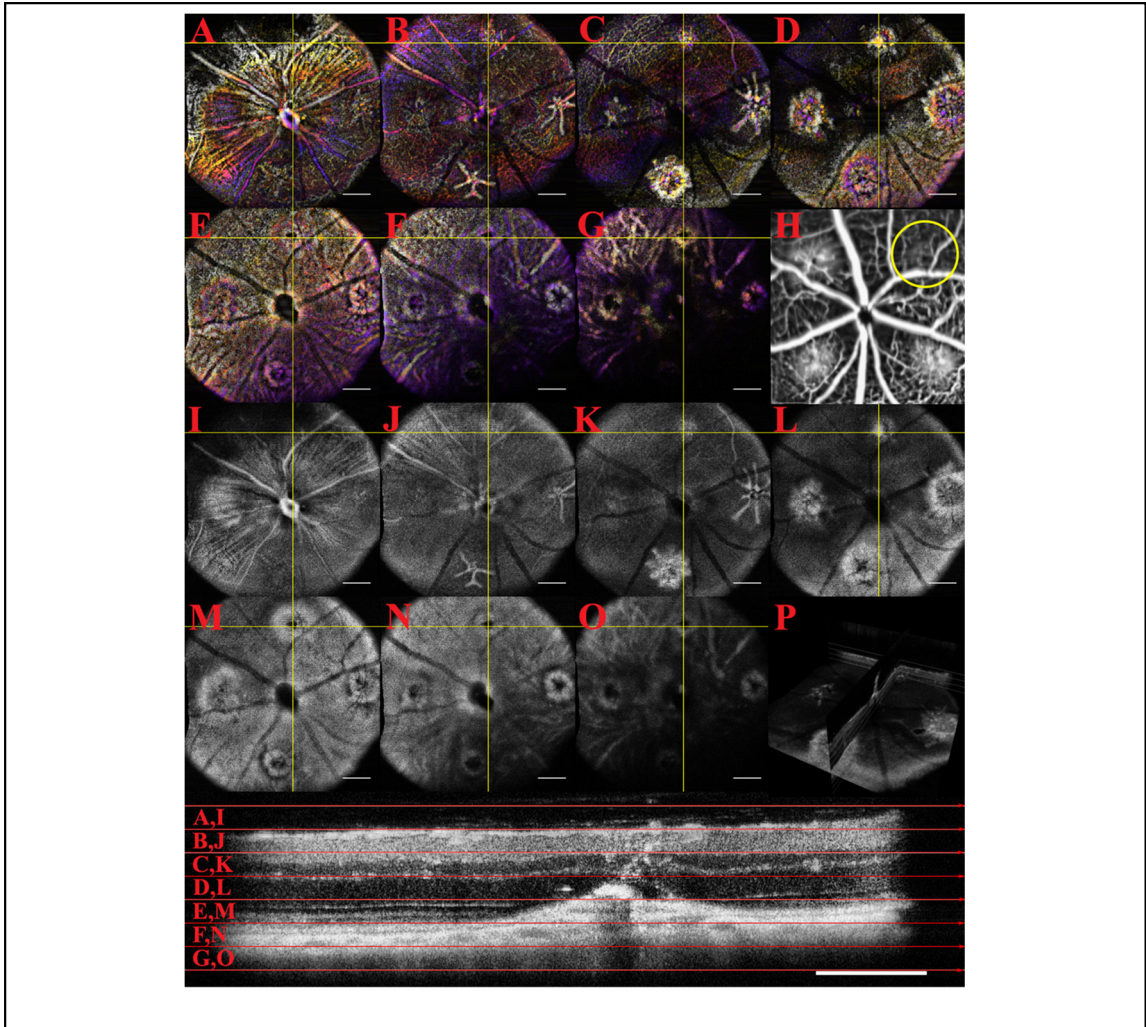


Figure 3.2.1-2: OCTA, En-Face and B-Scan

The OCT volume was sequentially re-sliced for en-face views with 60 μ m thick optical slabs. The OCTA projections (A-G) track the lesion marked with yellow crosshairs and circled in the Fluorescence Angiography (H). The same optical slabs are presented as traditional en-face views (I-O) however the edge gradients of the lesions are not well defined, and the boundaries are difficult to determine. (P) is the three-dimensional visualization of the orthographic views cutting through the center of the lesion. The bottom B-scan is the horizontal slice through the center of the lesion marked. The Superficial Vascular Plexus is highlighted in A, The Intermediate Vascular Plexus in B, and the Deep Vascular Plexus in C. The Retinal pigment epithelial layer is ruptured as seen as evidenced by the altered structure (E,F). Scale bar 200 μ m.

From day 3, the FA scans verified the vascular leakage in the CNV lesions. The acute injury lesions showed no apparent leakage at any timepoint. In contrast, all but three of the CNV lesions clearly showed signs of leakage at all time points and could be imaged with OCT (Figure 3.2.0-1). The three CNV lesions that were indeterminate were noted as potentially not CNV in the continued evaluation. While three lesions did not show the characteristic pooling in FA, the normal vasculature could not be resolved either (Figure 3.2.1-2). All three lesions were verified as CNV with lectin in the flat mounts. The lesion could be bleeding, and the absorption characteristics of blood severely increasing attenuation the 488nm fluorescence, IR light as used in OCTA is not attenuated by and therefore can still resolve the lesion. Consistent with previous literature, female CNV mice developed larger initial lesions that grew proportionately to the males¹⁴³. For longitudinal analysis 16 sample lesions for each group (CNV and acute injury) with every imaging modality imaged at all timepoints were included for all quantitative analysis. Follow up subjects used for validation of microvascular vasculature morphometry (Figure 3.2.0-2) and their choroids imaged (Figure 3.2.1-3), and verified for consistency, but were not included in the pooled quantitative longitudinal analysis to keep group size (n =16) consistent between time points for valid differential analysis.

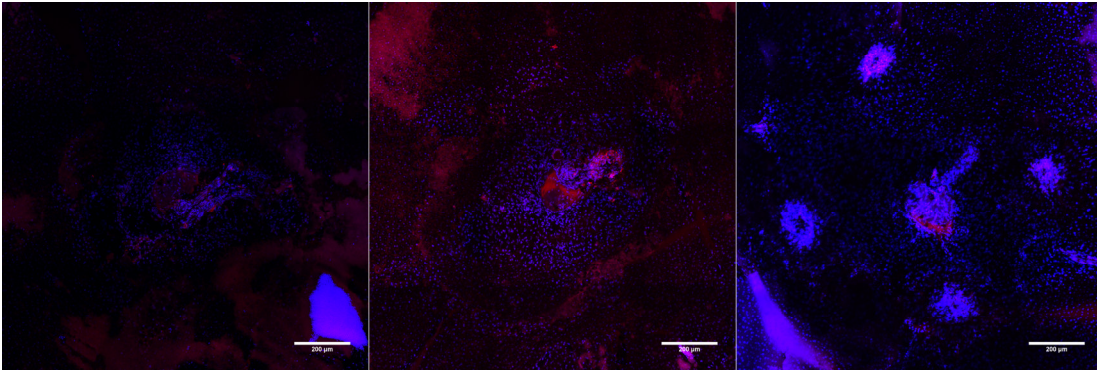


Figure 3.2.1-3: Choroid Flatmount

Choroid flatmounts at 1 week show the difference between the acute injury and control lesions. The acute injury choroid (left) is intact without visible disruptions and is comparable to the control eye (center). The CNV choroid (right) is clearly marked by four lesions and the disrupted zone around them. The DAPI (blue) and Isolectin (red) colocalize on the optic nerve head and the lesions. The control and acute injury eye have dispersed patterns of lectin and no accumulation of nuclei (note that a piece of the ONL adhered to the acute injury choroid). Scale bar 200μm.

3.4.2. LESION DYNAMIC DESCRIPTORS

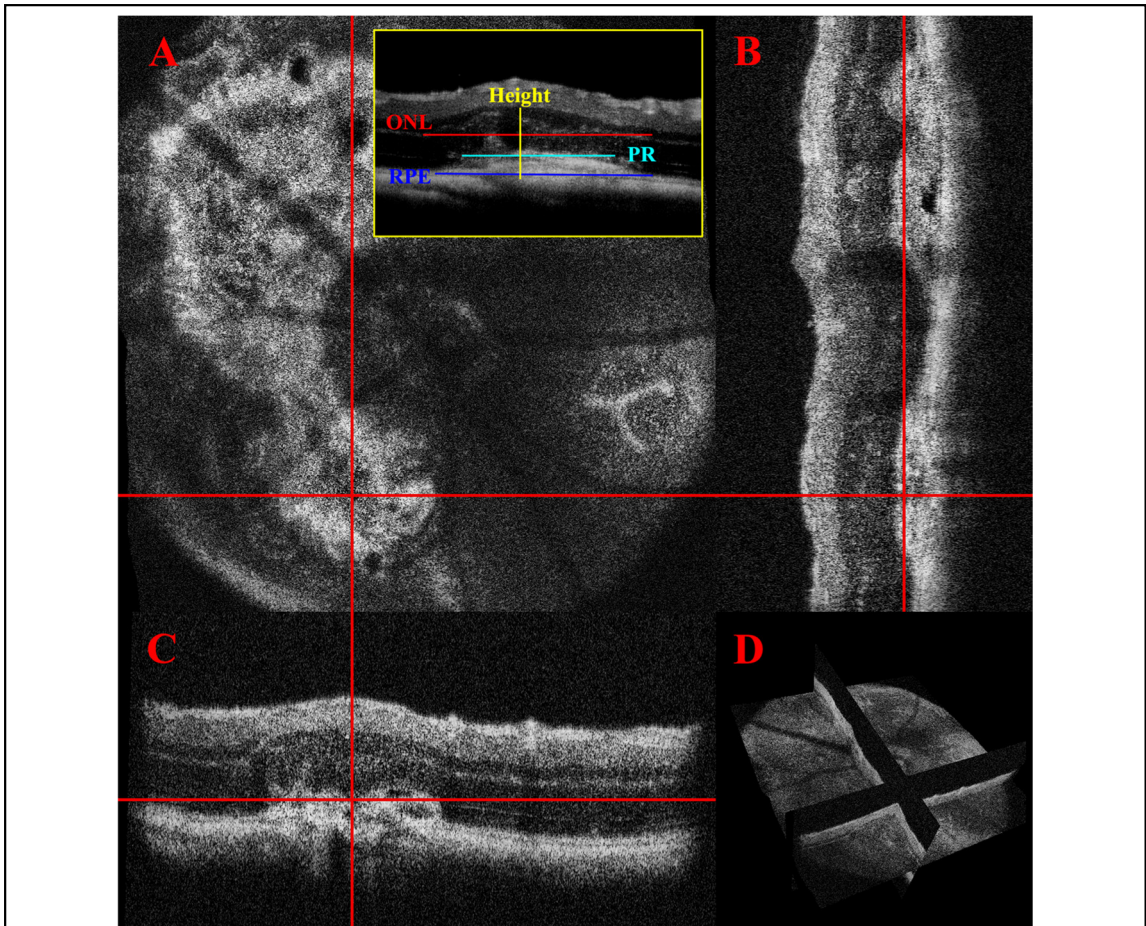


Figure 3.2.2-1: Orthographic views and lesion measurement

The en-face view (A) is aligned with two B-scans (B, C) to determine the center of the lesion. The red registration lines show corresponding coordinates. (D) is the three dimensional view of the projections illustrating that the linked views are digital slices of the volume from the same scan. The inset is the measurement scheme for the key layers of the lesion.

Orthographic views of the lesions were used to landmark and accurately extract the B-scans over time (Figure 3.2.2-1). Acute injury lesions exhibited a cylindrical shape, showing disruption throughout the Outer Nuclear Layer (ONL) and by day 3 began to assume an hourglass shape (Figure 3.2.2-2). Eventually, the hourglass neck would split, and the disruptions would form a pyramidal scar. While there was swelling, the Inner Nuclear Layer (INL) remained relatively undisturbed. It should be noted that although the RPE boundary was distorted, it remained continuous.

Early CNV lesions had less definitive borders, until day 3 when the swelling was noticeable in all layers. On day 7 there was the formation of edemas with clearly defined layer separation (Figure 3.2.2-2). However, the lesions that did not present with clear leakage or severe edema. By day 14 a reduction in edema and scarring of RPE-ONL was more pronounced. Day 21 was marked by scarring and disruption of RPE. While all the acute injury lesions followed a predictable progression, the CNV lesions size and features were highly variable when evaluated qualitatively.

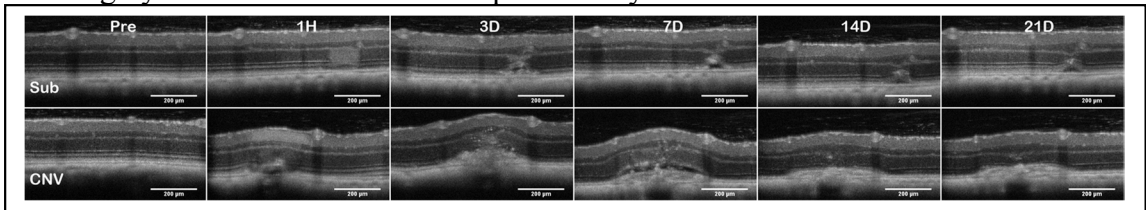


Figure 3.2.2-2: Lesion Dynamics Over Time

Lesion dynamics imaged by OCT over time (1h-21 days) shows the progression of two exemplars of acute injury and CNV lesions. The larger lesions and RPE disruptions in CNV differ substantially from the subthreshold in both magnitude and temporal characteristics. Females developed more severe CNV at all time points, however, all measured trends of the pathology followed the same time course. Scale bar 200µm.

3.4.3. LESION DYNAMICS: B-SCAN MEASUREMENTS

The female subjects in the CNV group had more severe lesions, however, the growth trends were consistent with the males and pooled for analysis 3.2.3-1 Panel A. There was no significant statistical difference found in the male-female dynamic, especially once the percent change plots were calculated. The resulting dynamics traces, plotted in 3.2.3-1 Panel B, were generated from pooled data of treatment groups.

The acute injury lesion is confined to the ONL with the major changes seen in the RPE distortions. (Table 3.2.3-1, 3.2.3-1 Panel A) The acute injury lesion expands from $136^{\pm 21}\mu\text{m}$ to $196^{\pm 44}\mu\text{m}$ (50% change) along the RPE layer at day 3, when the trend reverses. The scar reaches steady state between day 7 and 14 with a $146^{\pm 45}\mu\text{m}$ lesion diameter occurring in the RPE. The PR scar is reduced from $129^{\pm 10}\mu\text{m}$ to $78^{\pm 13}\mu\text{m}$ at day 3 and

reduces to a steady state at day 7. The height of the lesions shows minimal change $121 \pm 10 \mu\text{m}$ to $131 \pm 10 \mu\text{m}$; therefore, the inner layers' integrity remains continuous.

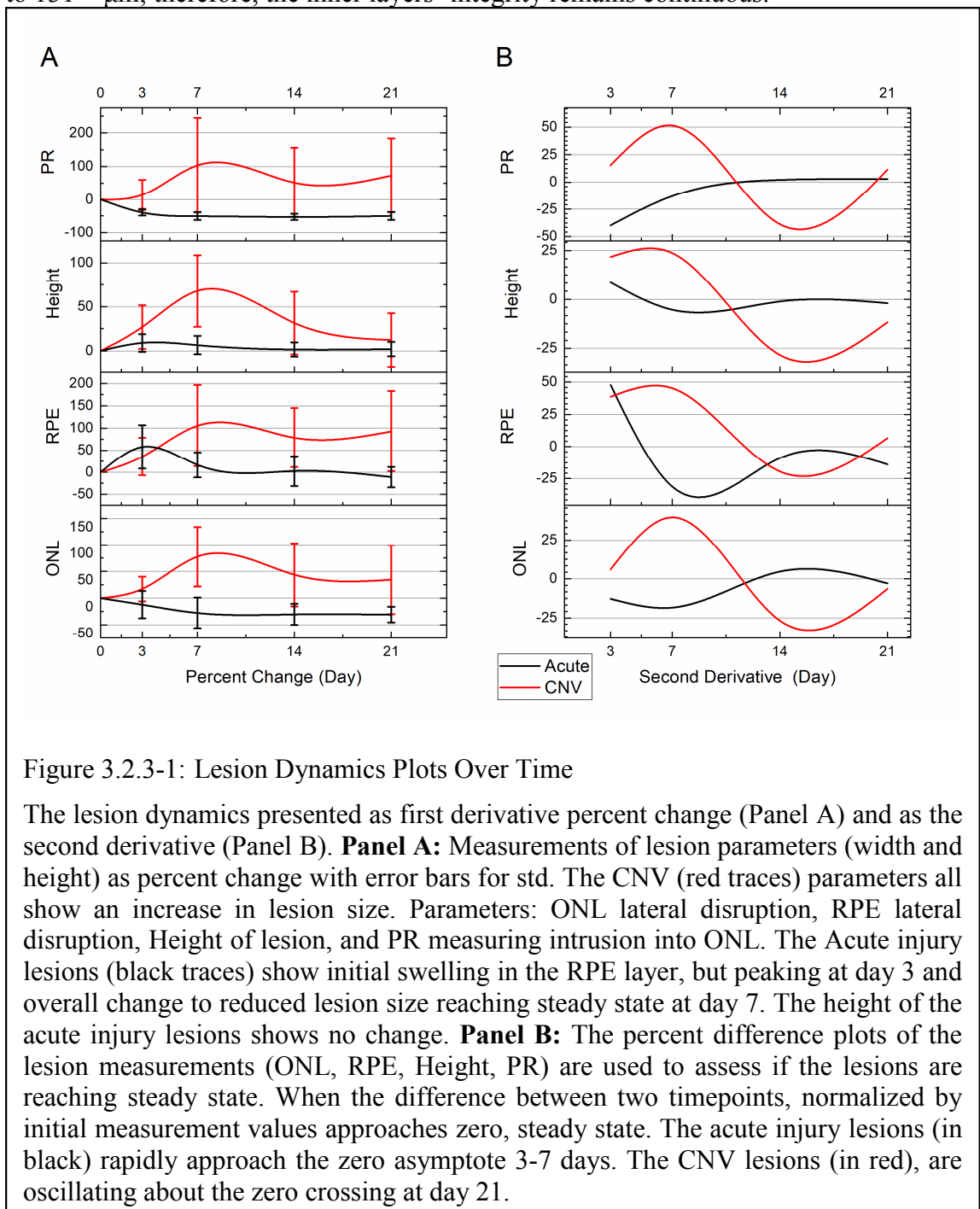


Figure 3.2.3-1: Lesion Dynamics Plots Over Time

The lesion dynamics presented as first derivative percent change (Panel A) and as the second derivative (Panel B). **Panel A:** Measurements of lesion parameters (width and height) as percent change with error bars for std. The CNV (red traces) parameters all show an increase in lesion size. Parameters: ONL lateral disruption, RPE lateral disruption, Height of lesion, and PR measuring intrusion into ONL. The Acute injury lesions (black traces) show initial swelling in the RPE layer, but peaking at day 3 and overall change to reduced lesion size reaching steady state at day 7. The height of the acute injury lesions shows no change. **Panel B:** The percent difference plots of the lesion measurements (ONL, RPE, Height, PR) are used to assess if the lesions are reaching steady state. When the difference between two timepoints, normalized by initial measurement values approaches zero, steady state. The acute injury lesions (in black) rapidly approach the zero asymptote 3-7 days. The CNV lesions (in red), are oscillating about the zero crossing at day 21.

The CNV lesion show lesion dynamics with a clear transition into chronic inflammation. At day 3, all parameters are showing expansion. The lesion growth

continues, and peaks around day 7. The edemas at day 7 mark the maximal vertical expansion of the lesions (Figure 3.2.2-2). While eventually as the swelling and edema volume subsides, only the height of the lesions returns to baseline. All other layers show clear lateral expansion of the lesion border from the first timepoint.

Acute injury								
Day	ONL	C _v	RPE	C _v	Height	C _v	PR	C _v
1	128.31	0.10	136.59	0.16	121.39	0.06	129.71	0.08
3	110.90	0.22	196.09	0.23	131.55	0.08	78.07	0.18
7	87.86	0.36	156.98	0.19	125.08	0.10	60.96	0.20
14	94.38	0.32	146.75	0.31	123.95	0.11	64.52	0.25
21	94.50	0.28	137.17	0.33	121.55	0.08	69.13	0.24
CNV								
Day	ONL	C _v	RPE	C _v	Height	C _v	PR	C _v
1	408.75	0.24	345.66	0.50	170.38	0.19	276.72	0.43
3	418.96	0.24	428.85	0.13	204.83	0.19	278.93	0.25
7	566.08	0.34	566.49	0.32	246.35	0.32	401.73	0.50
14	457.69	0.39	520.06	0.30	197.74	0.29	314.71	0.49
21	433.87	0.43	528.33	0.37	178.06	0.26	342.27	0.52

Table 3.2.3-1: Lesion Measurements

Table of average lesions dimensions, measurement in μm , as the lesions change over time. The Coefficient of Variation (C_v) is standard deviation normalized by the mean, σ/μ , is used to compare the measurement consistency. The Acute injury measurements show that the lesions are substantially smaller at day 1, 128 μm compared to 408 μm . At 21 days, acute injury measurements show a decrease while CNV has expanded.

Table 3.2.3-1 lists the measurements and variance analysis for each condition. The variance measured as standard deviation was predictably higher for CNV than acute injury treatment (124 μm vs. 21 μm), so Coefficient of Variation (C_v) was used to ensure consistency in comparisons. When compared, the C_v of .19 acute injury and .33 CNV indicate that both sample populations were internally consistent.

When only considering inter-gender variance, the males exhibited less severe CNV and had less variance in size measurements, i.e. RPE Female $659^{\pm 179}\mu\text{m}$ vs. Male $397^{\pm 66}\mu\text{m}$ but no significant change. While the discrepancy in size increased the variance of the measurement of a discrete time point, the longitudinal analysis was proportional and did not reveal any significant changes. The trends indicate that the variance is due to a bi-modal distribution of lesion severity, with the females having a higher proportion of the more severe phenotype. The C_v analysis results in comparable variance (.28-.24); therefore, when analyzed as percent change, the trends were consistent in all lesions despite variance in size (Table 3.2.3-1). The acute injury showed no sex discrepancy in lesion dynamics and C_v was low in all measurements. Because the lesion growth across gender is proportional to initial lesion size, the longitudinal analysis of individual lesions as percent change negates the concern of gender induced variance in lesion size.

3.4.4. OCTA

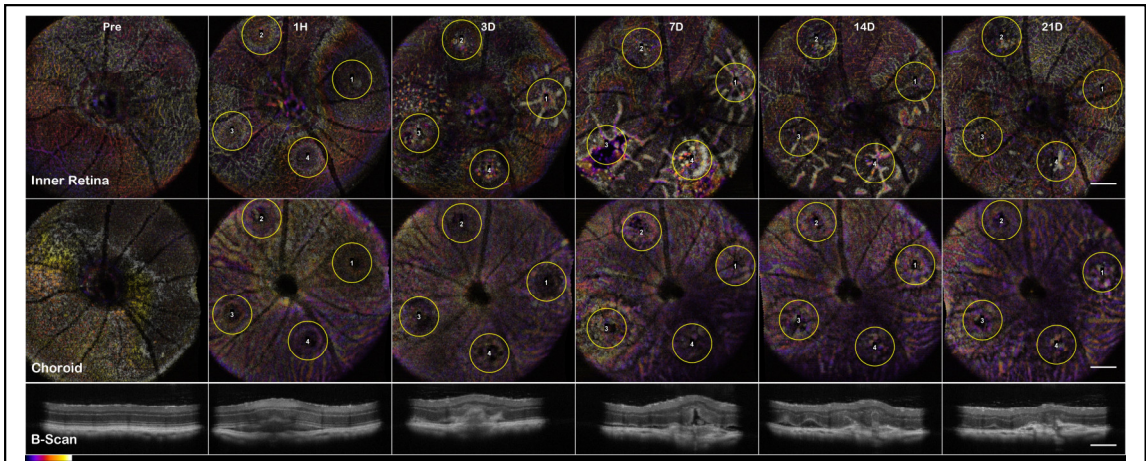


Figure 3.2.4-1: Lesion Dynamics OCTA

The longitudinal analysis of CNV as seen through both OCTA and High-Resolution B-Scans of lesion 1 reveals the inflammatory progression. Top row: The progression of inner retinal capillaries shows the day 3-14 non-perfusion of the vasculature as the inner layers are displaced by the edema and protrusions from the choroid. Middle Row: The choroidal layers show the lesion disruption that allows the vasculature infiltration of the retina. Bottom Row: The B-Scans of individual lesions over time tracks the swelling and edema formation in the early stage, then the neovascularization and scarring in the chronic phase. Scale bar 200 μ m

The C-scan of the data cubes were processed with a custom algorithm¹²³ to spatially enhance the microvasculature. The en-face volume was assessed for morphology changes throughout the depth (Figure 3.2.1-2). Once features were identified, 60 μ m optical slabs were projected into color depth-coded OCTA images for qualitative analysis (Figure 6). The inner retinal capillary layers identified were the Superficial Vascular Plexus (SVP), Intermediate Vascular Plexus (IVP), Deep Vascular Plexus (DVP), The DVP was most affected and analyzed in the following section (Figure 3.2.1-2 C). In the final images, motion artifacts still appear as banding, but the registration step minimizes the net effect. In the depth projections, the microvasculature is discernable from the background.

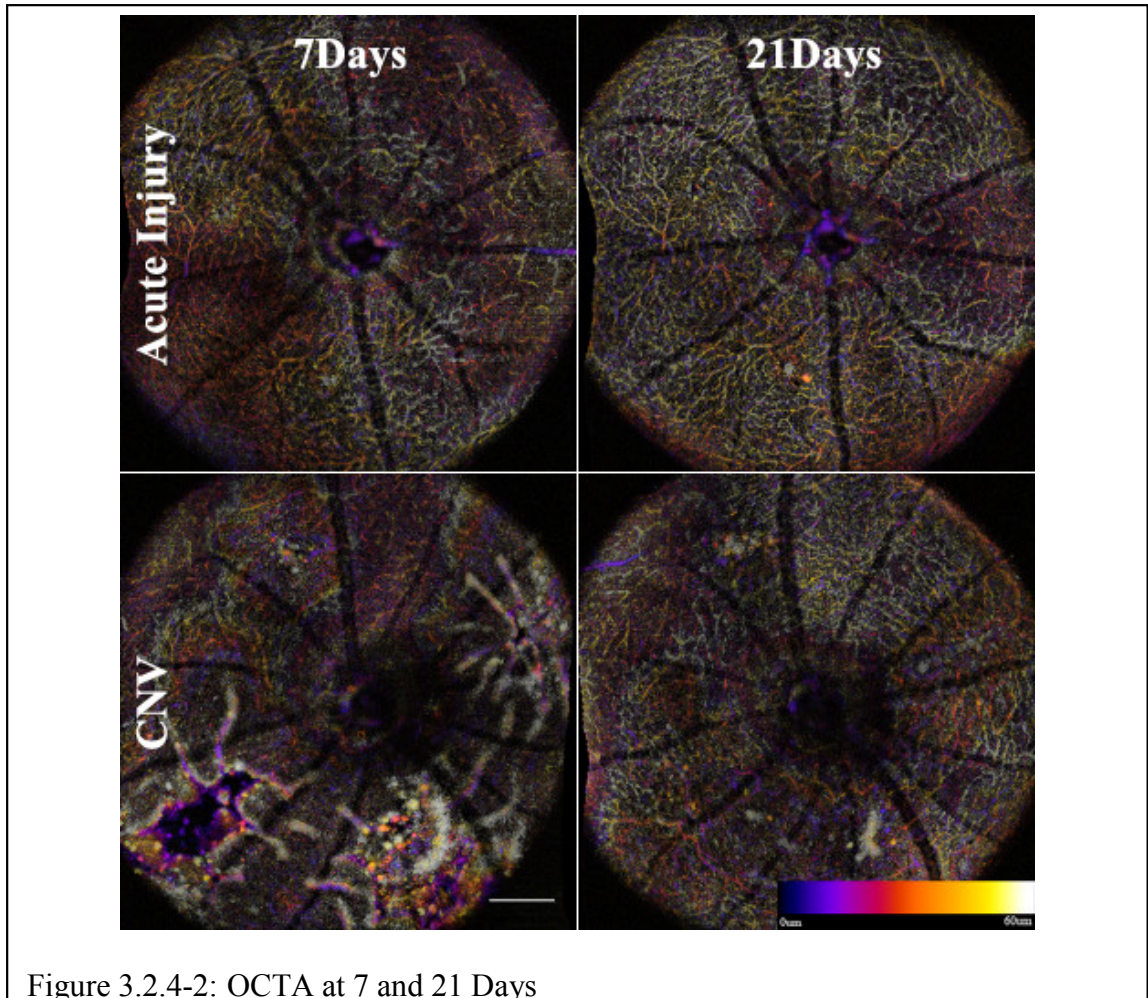


Figure 3.2.4-2: OCTA at 7 and 21 Days

Disruptions of the inner retina capillaries are apparent when comparing the acute injury to CNV lesions. Though the progression, the acute injury capillary bed is not disrupted. The formation of edema at day 7 in CNV corresponds with the displacement of capillaries. At day 21 most capillaries have returned to a normal distribution. Scale bar 200 μ m

The acute injury lesion followed the predictable progression of an early inflammatory phase response, peaking at 3 days and reaching steady-state around day14 (Figure 3.2.3-1 Panel A). The phenotype of the lesions showed initial lateral growth of the hourglass shape, before collapsing into a pyramidal scar in the ONL. The en-face OCTA data in conjunction with the B-scan data show that acute injury lesions may acutely distort the RPE layer while the Bruch's membrane appears to remain intact. The inner retinal capillaries appear unaffected by the acute injury lesion, and not an induced angiogenic response¹⁵⁰. Moreover, for acute injury lesions, the scarring is confined to the

photoreceptor layers, presenting as the lesion from the IS/OS that protrudes into the ONL yet are asymptomatic of vascular leakage when analyzed with FA. Comparing the baseline to 1-hour lesion response using the combination of B-scan and OCTA visualization, the damage of the acute injury lesions is confined to the photoreceptor layer and has not disrupted the choroid (Figure 3.2.4-4) or inner retinal vasculature (Figure 3.2.4-3). The acute injury lesions showed no gross changes in the capillary network in the OCTA scans. The acute injury lesion and scarring in the ONL slab were apparent and did not penetrate the choroid slab.

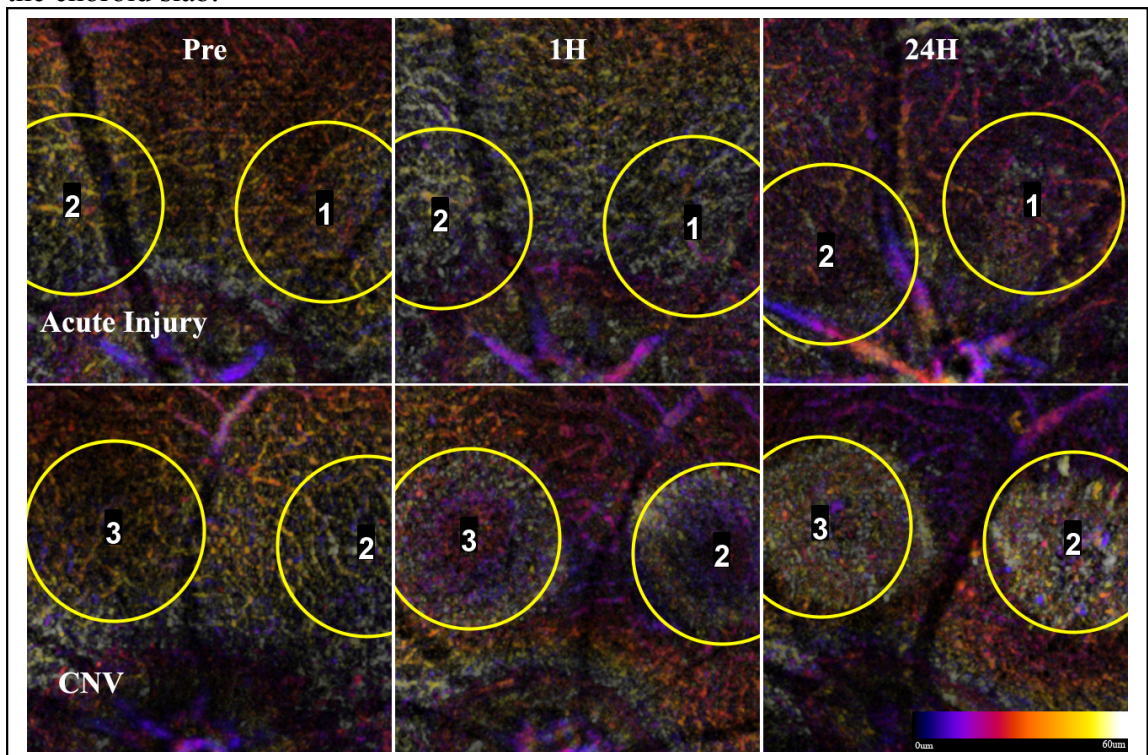


Figure 3.2.4-3: OCTA Changes in the Inner Retina

Color-coded depth-resolved projections of the SVP and DVP in the initial 24 hours of lesion induction. For each condition, the lesions were labeled in order of induction (counterclockwise) for reference. The acute injury response (top row) does not indicate a loss of capillaries. Throughout the initial 24hours, there was no net loss of SVP or DVP capillaries. The transient response of the Inner retina vasculature in the CNV lesions (bottom row) shows that non-perfusion is immediate. The CNV conditions show that the DVP capillaries are immediately disrupted at 1H, and the displacement area expands with increased swelling at 24 hours.

To confirm the RPE rupture and capillary non-perfusion, a repeat experimental OCTA group was set with time points 1h, 24h, and 72h. With the short time points, the choroid disruption was visible immediately and inner retina capillary non-perfusion apparent at 24h. (Figure 3.2.4-3) The inner retina at 1h in CNV shows displacement of layers, and at 24h the signal from the vasculature is undetectable. The acute injury samples and surrounding areas do not lose optical signal, demonstrating this is a localized disruption (Figure 3.2.4-4). Importantly, the integrity of the choroid slab can be immediately assessed for RPE rupture. At 1h the acute injury lesions distort the RPE but do not penetrate through and protrude into the choroid. At 24h the initial distortion from the localized inflammation is minimized showing choroid as a continuous layer.

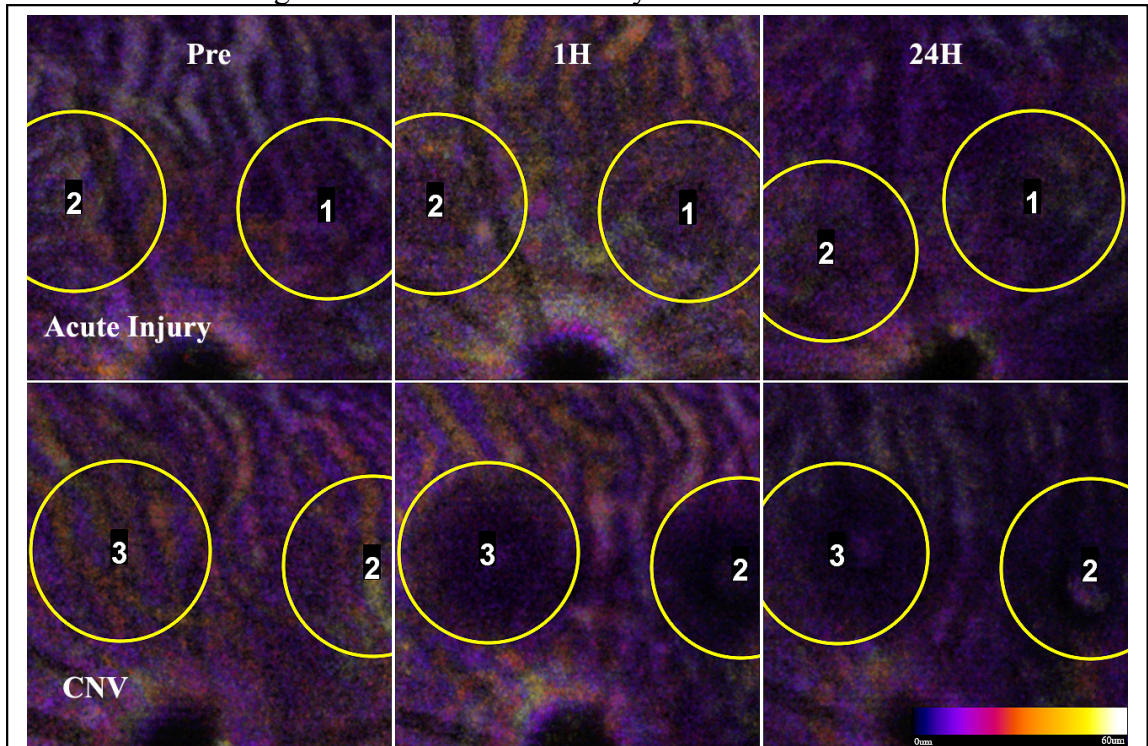


Figure 3.2.4-4: OCT Changes in the Choroid

OCTA images of the Choroidal layer for acute injury lesions and CNV. While the choroid below the acute injury lesions (L1 and L2) appears to be intact, the CNV lesions (L2 and L3) clearly penetrate Bruch's membrane appearing as a void in OCTA images. Assessment is immediate, and the separation differentiates acute insults that do not form CNV.

In L-CNV clear rupture of the RPE and Choroid were observed at 1 hour while the retinal layers are not continuous and the damage from the vaporization bubble is apparent. The CNV lesions affected all retinal layers by displacing the inner layers and disrupting the continuity of the outer retina. The en-face view of the OCTA highlighted several key features, the rupture of the choroid, the infiltration into the (ONL disruption circled in Figure 3.2.4-4), and the non-perfusion of capillaries in the IPL/INL. The choroid rupture was directly correlated to the presence of leakage in the FA. None of the acute injury lesions had choroidal disruption, while the CNV lesions had disruptions proportional to the FA leakage.

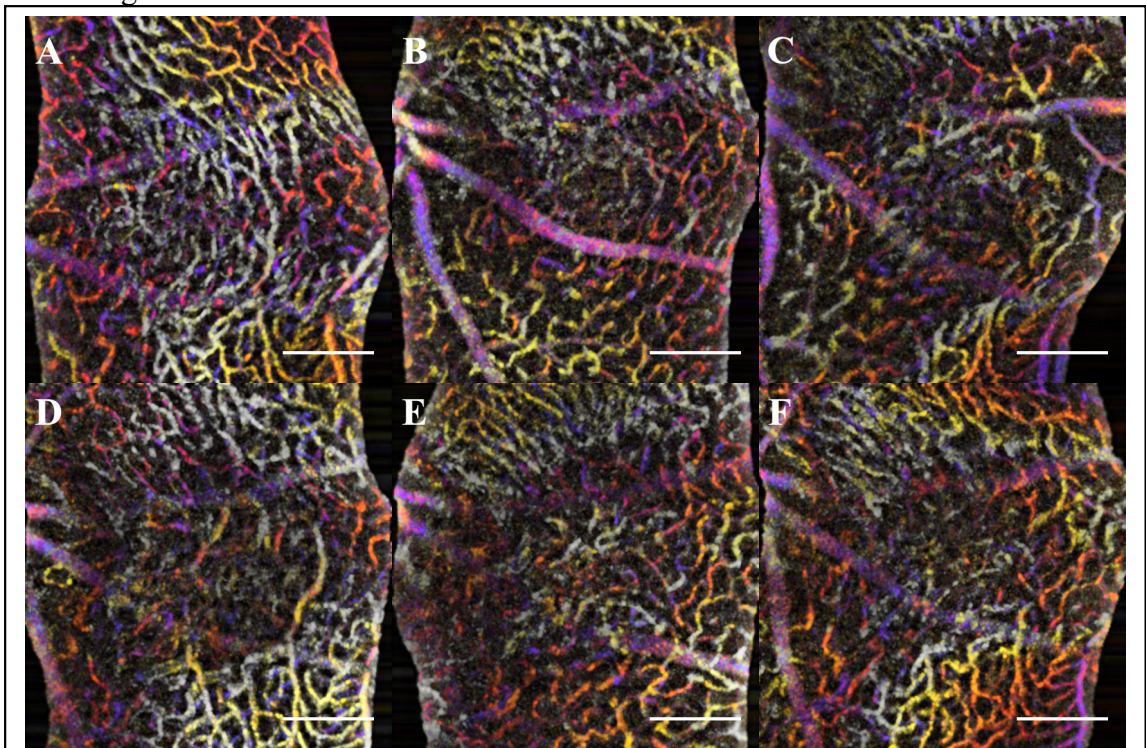


Figure 3.2.4-5: OCTA Frame Averaged Inner Retina

Alternative processing of the OCTA data to show the changes in the Deep Vascular Plexus over time. A single lesion was isolated in the center of the scan. A) pretreatment, the entire field has clear vessels. B) 1 hour, vessels in center are not well visualized. C) 3 days, the vessels are disorganized or non-perfused as lesion height increases. D) 7 days, vascular perfusion is low. E) 14 days, perfusion can be visualized, however the capillary organization has changed. F) 21 days, a full field of capillaries returned with remodeling of the lesion.

Visualizing the CNV model through longitudinal en-face OCTA reveals that the lesions exhibit early microvascular changes before a prolonged lesion growth phase that indicates the development of chronic inflammation could be observed (Figure 3.2.4-5), as the lesions dimensions failed to reach steady state at day 21 (Figure 3.2.1-3 Panel B). While most rodent CNV studies focus on days 7-21, relying on histology to confirm neovascularization¹⁵¹, our results indicate there is an early dynamic process on a scale of hours to 3 days that influences both layer morphology and microvasculature. The implication is that photoreceptor layer swelling causes a deflection of the inner retina during a critical period of 1h to 3d. This early vascular change is important to study how the severity of early inflammation affects the transition from acute to chronic phase 3-7days. It should be noted that the critical periods for CNV are the early acute phase 1h-3d, 3-7days for the transition to the chronic phase, and 7-21 days of the chronic phase neovascularization.

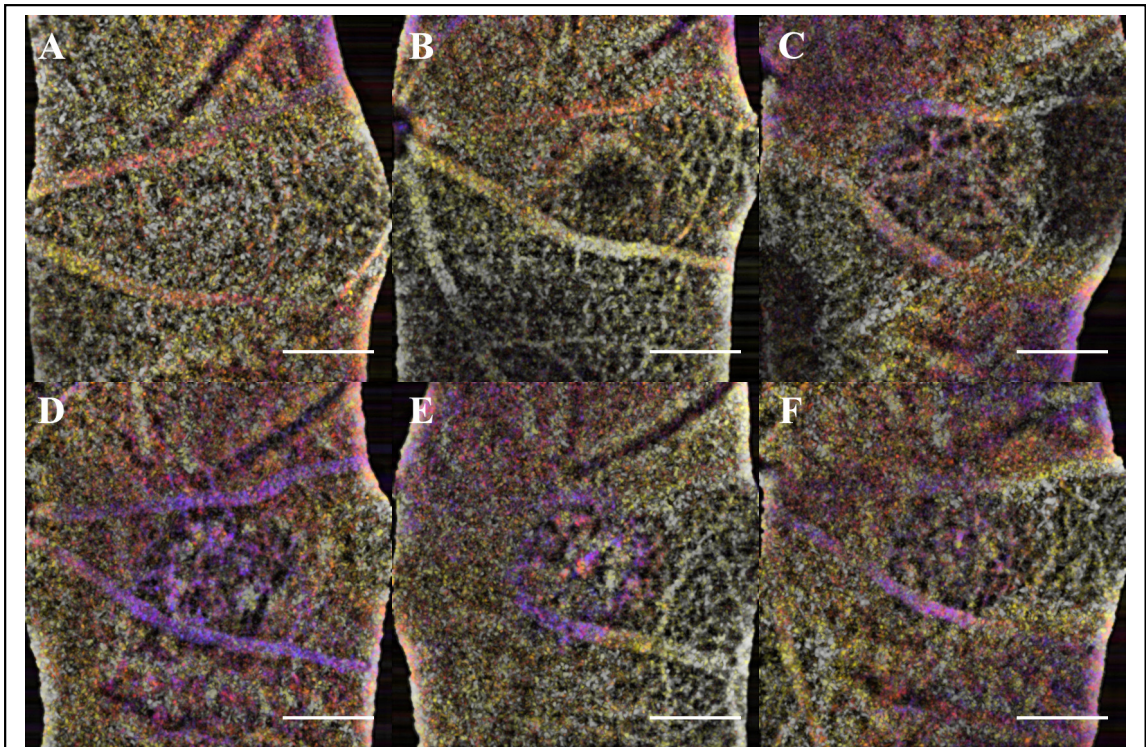


Figure 3.2.4-6: OCTA Frame Averaged Choroid

Alternative processing of the OCTA data to show the changes in the Retinal Pigment Epithelium/Choroid over time. A) pretreatment, shows no vasculature. B) 1 hour, the initial lesion is a dark void. C) 3 days, the distorted vasculature and fluid can be seen in the center of the lesion. The fluid was verified with correlation to suspected edemas visible in the b-scans and tissue voids in the retinal flatmounts. D) 7 days, A ring of neovascularization begins to form. E) 14 days, The lesion forms scar and ring patterns typical of flatmounts of angiogenesis. F) 21 days, the border ring is no longer visualized but infiltrating vasculature can be seen.

As evidenced by OCT assessment of the lesion, the vaporization bubble begins to swell and displace the inner retinal layers immediately following the lesion induction (Figure 3.2.1-2). The RPE disruption is apparent at the 1h timepoint in the en-face OCT, corresponding to the discontinuous layers seen in the B-scan, and is an early sign of successful CNV induction (Figure 3.2.4-6). In non-pathogenic conditions, the acute phase response ends, and the lesion would enter the resolving phase between day 3 and 7; however, in that period the CNV development continues forming sub-retinal edemas (fully apparent at day 7) indicative of the transition into the chronic inflammatory response.

The ONL view identified the early sign of inflammation, edema formation at day 7, and the eventual scarring (Figure 7). The optical slab containing the IPL/INL was most affected by the retinal swelling and edema. The region above and around the lesion was displaced, and moreover, the IVP and DVP showed regions of capillary non-perfusion. The non-perfusion was obvious on days 3 and 7, the reperfusion was not apparent until day 14 (Figures 6,7,10). This capillary non-perfusion or loss of flow was not directly observable through FA, as the inner retina presents as either a void or obscured by the leakage from the choroid vasculature.

3.4.5. IMMUNOFLUORESCENT STAINING

A final group of age-matched mice was utilized for producing the retinal and choroidal flatmounts. To assess the OCTA findings in the inner retinal layers, the SVP, IVP, DVP, and ONL were mapped with OCTA projections and ConA Lectin stained flatmounts at day 14 (Figure 2). The vascular features disrupting the IVP and DVP were confirmed in the ConA Staining. Additionally, the CNV vascular intrusion into the ONL was validated in the flatmount. Neither the OCTA nor Lectin staining in the acute injury and control conditions exhibited abnormal vasculature.

Isolectin staining was used to validate the en-face OCT assessment of the integrity of the RPE layer with choroidal flatmounts (Figure 3.2.1-3). The flatmounts were co-stained with isolectin and DAPI to visualize the choroid. At one week, the choroid of the acute injury lesions was comparable to the naive control eyes, neither showing signs of disruptions or abnormal vasculature. The CNV choroids showed clear neovascular scarring.

While the swelling in CNV is consistent with the previously published histopathological studies showing cellular infiltration and wound healing in the chronic phase¹⁵², the early impact on the inner retina has not been explored. Our data shows that the early swelling and capillary non-perfusion precede edema and neovascularization. We found that the en-face OCTA provides new information on the early inner retina capillary

non-perfusion in CNV (Figure 3.2.4-3). The severity of edema and swelling between days 3-14 correspond to the area of capillary non-perfusion that may lead to ischemia prolonging inflammation. While the choroid infiltration in CNV is expected, the inner retinal capillary non-perfusion was previously unreported.

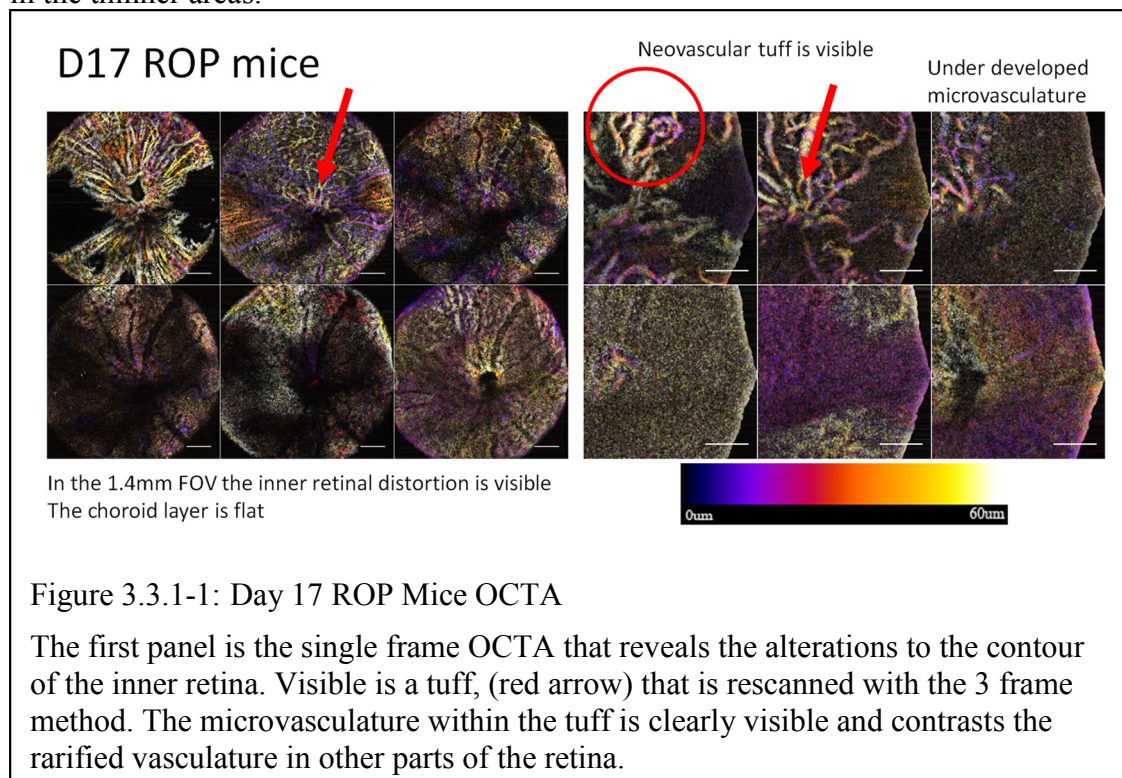
3.5. OCTA in Retinopathy of Prematurity

Retinopathy of Prematurity (ROP) is a neurodegenerative state where treatment for prematurity causes disruption of the angiogenesis of the retinal vasculature. In-vivo, these rapid changes occur as retinal vasculature undergoes angiogenesis and pruning and therefore require a different approach to tracking than the slow changes in an adult. As human retinal vasculature develops late into the third trimester (nasal 36 weeks, temporal after), premature babies are born with among other ailments underdeveloped lungs and retinas^{153,154}. Maintaining proper or supplemental oxygen to premature babies assists in offsetting the compromised lung function, however the retina becomes a hyperoxia environment compared to the womb. With the alteration in oxygenation the vascular pruning and angiogenic process are disrupted.

In this study ROP was induced in mouse pups and OCTA method from the CNV study was utilized to monitor the abnormal angiogenesis. A rodent model called oxygen induced retinopathy (OIR) induces ROP like phenotype in neonatal pups when placed her a hyperoxia environment¹⁵⁵. With mouse pups age P14-P24 (14 to 24 days) the pupil is too small to focus a fundus camera. The OCT system however is adaptable by changing the reference arm distance that is suitable for mouse pups. Furthermore the Bioptigen system we utilized is already approved for clinical trials investigating the detrimental effects of oxygen therapy in premature infants¹⁵⁶.

3.5.1. DEVELOPMENT OF NEOVASCULAR TUFTS

The main feature is neovascular tufts that develop into tortuous vasculature with low branching density. Early tufts are protruding from the ILM and SVP. The surface contour of the ILM is disrupted with clear evidence of non-uniform retinal thickness. The IVP and DVP in underdeveloped in the thinner areas or completely absent. Retinal vasculature was comprised of few, large diameter, and highly tortuous vessels were there were no tufts. The large single frame view also showed that there was less NFL structure in the thinner areas.

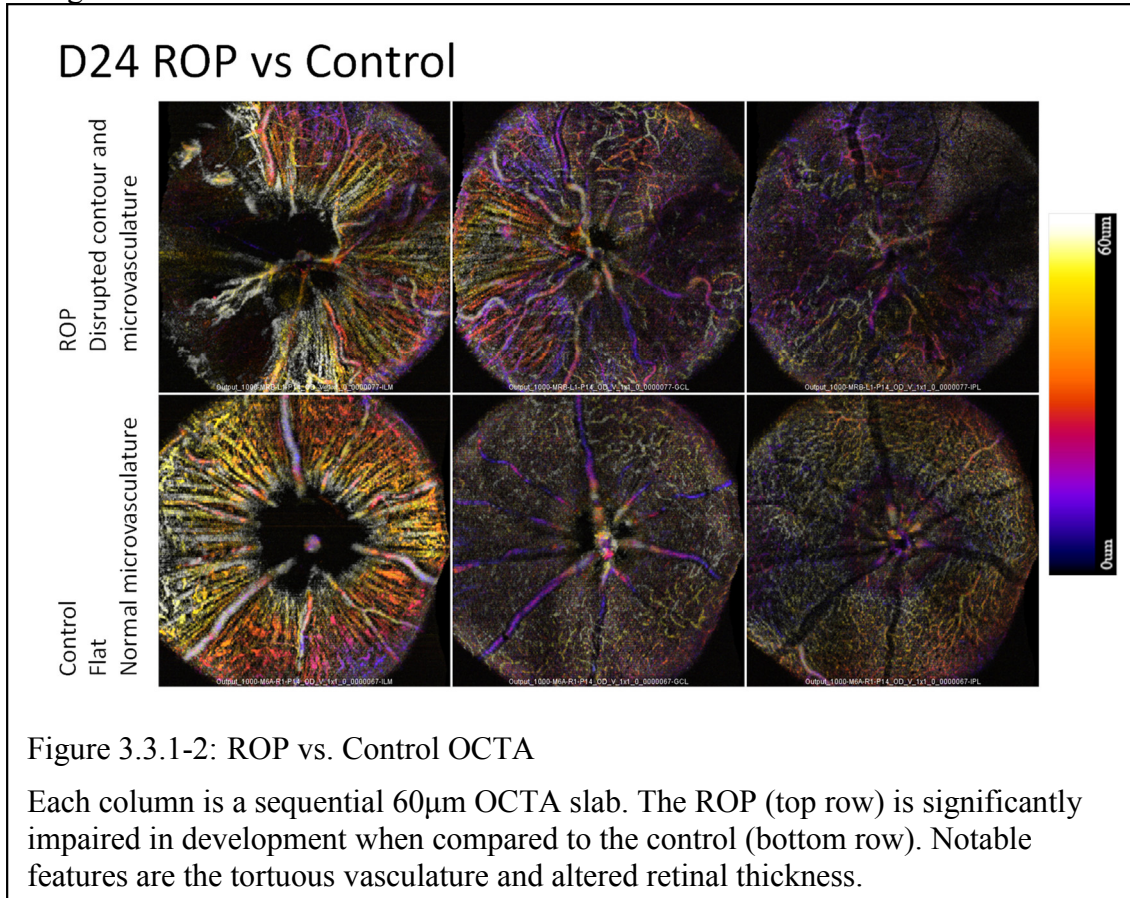


The projection method using 3-frame variance clearly highlights the morphology of the tufts. Single frame or 3-frame average were better suited to show the alterations in retinal thickness, specifically the contour of the ILM and NFL where retinal development was impaired.

3.5.2. VASCULAR TORTUOSITY AND DENSITY

The large vessel normally generates into branching patterns. While each pattern is a unique combination of branches and segments, the development is typically regulated by

balancing the oxygen demand and vascular density^{154,157}. While the vasculature shows gross morphological changes, further development is required to accurately quantify the changes.



3.6. Discussion

In retinal diseases, vascular defects are coupled with glial (see chapter 4) and neuronal dysfunction. The ischemic environment of the retina is easily perturbed by an inflammatory insult. Loss of vasculature or increased ischemia can dysregulate the normal anti-angiogenic signaling and instead, promote neovascularization^{146,158}. The laser lesions used in this study with an acute injury, and the progressive inflammation that induces choroidal neovascularization. The acute injury is a predictable model for the early pro-inflammatory phase of lesion formation and progression^{133,159}, as supported by the low

variance in the lesion sizes (measured by C_v in Table 1) in contrast to the uncontrolled angiogenesis characteristic of CNV. Determining the features of the inflammation progression and alterations to the vascularization are of important to understanding neuroinflammation. Specifically, when changes might occur that transform an injury into neurodegeneration.

In CNV model, the physical damage and retinal infiltration vasculature displacing the photoreceptors are well established^{145,160}, but the progression of the vascular inflammatory response and inner retinal neurons is unknown. Traditional angiography methods cannot assess how laser injury in the two models affects the remodeling of inner retinal capillaries or implications to the degree of ischemia in the eyes. The en-face OCT scans provide a non-invasive approach to assess how outer retinal swelling associated with an inflammatory stimulus affects the inner retina. This longitudinal study of an acute and chronic injury reveals how the progression of layer disruption corresponds to vascular changes.

With the non-invasive nature of OCT, we successfully demonstrated the ability to track individual lesions in a longitudinal study designed to identify key timepoints in the progression of lesion morphology that differentiates an acute injury lesion from CNV pathology (Figure 3.2.2-2). Through the high resolution, B-scan images were generated from the registered volume (Figure 3.2.2-1) enabling optical sectioning of the center of each of the lesions so that for each timepoint repeatable lesion dimensions were reliably calculated^{140,161}. From these measurements, we determined that the laser irradiation parameters (~0.01 Joules) induced not only increased lesion size but changes in both pathology and duration of inflammatory response. Plotting the derivative, the percent difference between timepoints for each of the lesion measurement data (Figure 3.2.3-1), the peak response and transition into the resolving phase begins by day 3 in the acute injury model, although the CNV response continues as both inner and outer vascular networks are remodeling in the chronic phase. The features seen in the B-scan images indicate that

the CNV lesions all have swelling that displaces the inner retina, and edema is formed at day 7. In addition, this method allows for digital re-sectioning yielded simultaneous lesion measurements and OCTA visualization. The combination provided improved capability for assessing the impact of swelling upon layer morphology and the subsequent disruptions to the capillary network.

While the chronic inflammation and leaky vasculature are well-established features of wet AMD, the inner retinal changes are not well characterized. At 21 days, the OCTA images of the choroid were consistent with the leakage area in FA (Figure 3.2.1-1), however, in the early response at 3-14 days, the OCTA of the inner retina exhibited capillary non-perfusion and reperfusion that directly correlates with the swelling and edema in CNV when the lesion height $\geq 200\mu\text{m}$. OCTA survey of macular edema due to retinal branch vein occlusion, supporting correlation but not indicative of causality between edema and vascular rarefaction¹⁶². With the loss of continuous flow to generate contrast in the en-face OCT, the vasculature signal becomes fragmented or completely lost. Although inner capillary dropout is a known contributing factor to retinal ischemia in glaucoma and diabetic retinopathy visible through OCTA¹²⁰, it has not previously been attributed as a feature of CNV or AMD. With the swelling and edema in the early phases of CNV, the displacement of the inner layers may cause the vasculature to be pinched, restricting or stopping blood flow altogether.

The CNV lesion dynamics of the RPE and PR layers in the chronic phase correlate to the in-vivo findings of previous studies^{97,163} indicating that the resulting pathology exhibits similar features in all studies. Therefore, the combined orthogonal OCT and OCTA imaging approach allow for the study of how the swelling and edema in inflammation progression causes displacement that affects the microvasculature of the inner retina. Furthermore, the method of post-processing allows for comparison of the dynamics of acute vs. chronic injury and specifically offers a longitudinal method to non-invasively correlate the edema formation to vascular changes.

The contrast of the vasculature visualized with OCTA is dependent on the spatial/temporal speckle pattern of erythrocytes in blood flow. The algorithm we developed utilizes the spatial domain component of OCT speckle patterns to highlight and extract the angiogram from an en-face OCT volume^{123,164}. The high-density volumetric scanning of en-face OCT allows for digital re-slicing and processing with a custom 3D vessel enhancement algorithm extending the principles of vessel detection strategies for fundus images¹⁶⁵. Our OCTA methodology allowed the findings in this study to be confirmed across subjects by re-slicing the volumes to focus on the inner retina vasculature that was perfectly registered to the high-resolution B-scans of the lesions. Additionally, by using a single high-density scan and the spatial portion of the speckle pattern, instead of repeated scans, the algorithm covers a wider area. The tradeoff to the approach is that the flow rate cannot be calculated through this method. However, currently flow rate cannot be validated, thereby large area screening of vascular morphology was a better utilization of the data. As a variant of the speckle decorrelation algorithm, our en-face OCTA methodology is capable of resolving the microvascular morphology comparable to that which was observed in the previous rodent studies¹⁰¹.

In human CNV studies using OCTA, only the choriocapillaris was compared to the FA imaging^{97,166}, and OCTA is highly correlated to the leakage. While FA is used clinically to determine the presence or absence of vascular leakage or edema, lectin staining is used in pre-clinical trials for measuring vascular dysfunction indirectly as leakage area. Lectin staining on rat retinal flatmount has shown that there is no increase in lesion growth after day 10, however, such methods cannot assess the functional aspect microvasculature perfusion under in-vivo conditions⁴⁹. Our longitudinal analysis of the inner retina non-perfusion and reperfusion was only possible using an OCTA methodology. OCTA with blood flow velocity analysis or new oximetry techniques^{167,168} is required to verify that there is a temporary loss of the blood perfusion increasing localized hypoxia.

The finding of the CNV model translate to the methodology needed to assess the ROP model. OCTA is able to non-invasively detect microvascular development. This method also showed the capability of imaging juvenile mice reliably. While only a proof of concept study, the ROP data indicated the feasibility to track the development of the abnormal angiogenesis. Further work would require developing a mathematical model to correlate retinal thinning and tufts to the late stage abnormal tortuosity.

3.7. Conclusions

Longitudinal studies with OCT/OCTA allow for precise and repeated measurements without a traditional tissue biopsy. With the advancement of sensors and signal processing efficiency, the digital biopsy offers a more flexible method to reinvestigate the data cube, without needing to reimage the sample. In the samples, when an abnormality was spotted, the data processing could highlight multiple tissue aspects. For example, in the CNV studies, choroidal vessels infiltrating the inner retinal space through neovascularization is the main focus, yet, DVP disruptions were observed, a finding not previously described.

Retinal vasculopathy is the key cause of vision loss and blindness in many retinal diseases such as diabetic retinopathy, age-related macular degeneration, and retinopathy of prematurity. Fluorescein angiography (FA) and indocyanine green angiography (ICGA) are the gold standards to diagnose vascular changes in these diseases, but have significant limitations⁵¹. They are considered invasive because a special dye needs to be injected into a vein to visualize retinal vessels. In addition, the resolution of retinal vessels is dramatically reduced when there is vascular leakage, making it difficult to resolve detailed vessel structure in the leakage site; and FA and ICGA have relatively short imaging time windows following dye injection.

Histological analysis of vascular beds provides higher resolution. Nevertheless, this technique uses fixed tissue and the detection and visualization of some of the vascular changes occurring *in vivo* could be masked or lost during *ex vivo* tissue processing and labeling. The recent development of OCT-A technique overcomes several limitations of the above current methods of vascular imaging. It can be performed to image and analyze retinal and choroid vessels *in vivo*, non-invasively and longitudinally. Moreover, OCT-A provides information for blood flow. In the past two years, OCT-A has been actively utilized on studies aimed at determining retinal vascular changes in human patients suffering from age-related macular degeneration, diabetic retinopathy and vascular occlusion.

4. MICROGLIA NEUROINFLAMMATION BIOMARKERS

4.1. Abstract

Structural changes to the retina alone cannot determine cellular response. Because retinal tissue cannot be directly sampled without further damaging the retina, transgenic microglia are potential in-vivo biomarkers of inflammation. As resident macrophages and regulators of homeostasis, not every cell can perform all functions simultaneously; therefore, each microglia morph to play a specific role depending on their microenvironmental state. The morphology and role of each microglia is linked. Thereby, if microglia are tagged, their functional state can be inferred from the morphology.

In inflammatory response, the role of microglia is inferred from cell culture studies. Photoreceptor health is maintained by auxiliary cells, such as the RPE and Muller cells. However, the regulation of the microenvironment is a function of macrophages. As neuroinflammation is investigated based on the classical time points, this study's aim is focused on assessing the phases of inflammation. Before more specify studies can be performed, an assessment of microglia localization, density, and activation state is required.

4.2. Introduction Cx3Cr1^{eGFP} Mice

Cx3Cr1 is the fractalkine receptor expressed on all myeloid derived macrophages. This is the binding sight of Cx3CL1 or the Fractalkine receptor. In inflammatory response regulation, Cx3Cr1 contributes to macrophage activation, and in the brain, Cx3CL1 is expressed by neurons. Since Cx3Cr1 is constitutively expressed on the surface of macrophages, including microglia, the cell morphology will be labeled when conjugated

to eGFP. With confocal image analysis, the reporter gene can be confirmed to label the morphology of the microglia.

For the many neurodegenerative diseases where microglia are implicated in contributing to pathogenesis, vascular morphology and microglia activation need to be assessed non-invasively, so the technologies and protocols need to be made compatible. Cx3Cr1^{eGFP} mice (The Jackson Labs) are a transgenic strain with the green fluorescent protein (eGFP) driven by an endogenous promoter of Cx3Cr1, a chemokine receptor specifically expressed in microglia/macrophage. This strain has been widely used to track microglia/macrophage in-vivo. Because the eGFP has similar fluorescence properties to fluorescein, alternative methods to verify neovascularization are required. The latest generation of OCT imaging has previously been demonstrated to have a comparable resolution to histology measurements. Therefore, with high-resolution volumes^{161,169,170} and speckle variance for angiography contrast¹⁷¹, the orthogonal views (en-face view and two cross-sectional B-scans)¹⁶⁶ can be used to precisely monitor pathology.

While many microglia pathways and vascular imaging capabilities have been independently explored, to date no study has tracked differences in microglia activation correlated to angiogenesis and acute injuries in-vivo. To understand when to collect retinas for traditional metrics, we propose an imaged based solution whose methodology can be applied to tracking inflammation progression in various models.

4.3. Methods

In this study, we examined the microglia dynamics in retina non-invasively by Scanning Laser Ophthalmoscopy (SLO) after laser-induced acute-injury lesions and CNV, together with high-resolution en-face OCT/OCTA, to examine structural changes in the retina. This complementary methodology is a non-invasive way to precisely generate functional and structural models of inflammation progression. Our in-vivo findings in

inflammation models were confirmed with confocal microscopy. With these techniques, we demonstrate that microglia exhibit different distribution and dynamics in response to acute-injury vs. chronic inflammatory condition, suggesting different roles of microglia in resolving vs. promoting retinal pathological changes in the two different conditions.

4.3.1. INJURY MODEL

Two laser injury models were induced resulting in differing acute and chronic inflammatory responses. The L-CNV model induces a neuroinflammatory response in the chronic phase of inflammation. The acute-injury lesion replicates the conditions used in previous Cx3Cr1^{eGFP} laser lesion studies¹⁷² and is intended to transition into the resolving phase, leaving only a scar in the photoreceptor layer. Age-matched C57-BL/6 and Cx3Cr1^{eGFP} mice were assigned to acute-injury or the neuroinflammatory L-CNV groups. Four mice of each strain were assigned to matched groups for each of the experimental groups (acute injury C57-BL/6, CNV C57-BL/6, acute injury Cx3Cr1^{eGFP}, and CNV Cx3Cr1^{eGFP}).

Lesions were induced in the right eye, and the contralateral eye served as an internal control. Laser lesions were induced using a Micron III system with Meridian 532nm photocoagulation laser⁸⁸ to induce a chronic neuroinflammatory injury (CNV) and an acute-injury so that the phases of inflammation could be independently assessed. The L-CNV model¹⁰⁰ was induced with a fixed 50 µm beam, using a laser output of 180mw with 70ms exposure, whereas the acute-injury¹⁴⁴ was induced with a lower laser power of 46mW and 200ms exposure. These parameters and the timepoints chosen for study (1h, 1 day, 3 days, 7 days, 14 days, and 21 days) were chosen based on an initial standardization trial in a group of 8 wild-type and 8 age-matched Cx3Cr1^{eGFP} mice in which lesions were made in the right eye, half of each strain randomly assigned to acute-injury or CNV, and imaged with OCT (details below) and AF.

Autofluorescence image parameters were optimized to ensure that baseline autofluorescence of lesions in the Cx3Cr1^{eGFP} would not overwhelm the signal from the eGFP due to lesion autofluorescence. With the established procedure, a second experimental group was longitudinally measured for 21 days. A third follow-up group was used to collect histology at the corresponding time points. In C57BL/6J mice, SLO in FA mode was performed with intraperitoneal injection of fluorescein for visualizing the vasculature.

4.3.2. TRACKING IN-VIVO

Using a standard 30deg lens, fluorescent images of transgenic mice eyes were acquired through Spectralis SLO in AF mode or simultaneous AF/IR to image the microglia. All mice were prescreened and had clear corneas with no apparent retinal defects. The quantitative results were presented for the 30deg lens (1.2x1.2mm area, 1.44mm²) where the sampling resolution imaging the murine eye was calibrated at 0.77 μm per pixel. The Cx3Cr1 fractalkine receptor subtype was constitutively expressed on the cell membrane of macrophage-derived cells. While all somatic macrophages express Cx3Cr1, only the microglia in the naive retina express the gene¹⁷³. Early evidence from neurodegenerative models, such as glaucoma, show the tagged microglia allow tracking of early microgliosis that has demonstrated to predict the severity of neurodegeneration¹⁷⁴. The Cx3Cr1^{eGFP} stain has previously been used for in-vivo imaging with SLO to track microglia activation^{172,174-177}.

Microglia were identified through an automated image segmentation macro in ImageJ, yielding image features calculated with the cell count analysis in the following routine. Briefly, a duplicate mask was created, and adaptive contrast enhancement and smoothing were applied before the mask was binarized and eroded. The mask was fed into the “Analyze Particles” routine to create a table containing centroids and shape descriptors of each segmented cell. The cell position was calculated as Euclidian distance to the optic

nerve head, which was manually denoted. The automated cell counting was normalized to the naive eye, and if low image quality resulted in fragmentation of the segmentation, the results were excluded.

4.3.3. OCT METHODS

The OCT image processing was designed such that, from a single scan, we could generate orthographic views, high-resolution B-scans, and OCTA. The Bioptigen R2200 SD-OCT system was programmed for volumetric OCT scans that were recorded from a 1.4x1.4mm area, with a lateral resolution of 1.4 μ m and an axial resolution of 1.9 μ m. The raw OCT data were imported into ImageJ and B-scans registered to reduce motion artifacts in the volume. Orthogonal views in ImageJ were utilized to interactively explore the 3D dataset and locate the laser lesion morphology. Orthographic views which simultaneously displayed OCT en face views with two cross-sectional views in x-z (B-scan) and y-z, allowed for localization of lesions. The orthographic views were the most effective method to assess the 3D morphology. The en-face OCT landmarked and located the lesion center for reliable and repeatable measurements in the B-scans. Landmarks such as the Optic Nerve Head (ONH) and superficial vasculature branch points were not rapidly altered and provide registration points for the time series. B-scans were averaged for high-resolution cross-sectional images of the lesions. Furthermore, high-resolution OCT B-scans were generated for each region of interest across the maximal lesion width identified in the en-face scan. From the same volume, the spatial-temporal speckle variance was utilized as contrast for extracting vascular data directly from the en-face view to produce OCTA projections¹²³. The spatial-temporal speckle variance is related to the laser speckle variance^{111,112} but uses vascular extraction methods from fundus imaging^{165,178} directly on the en-face OCT slices¹⁶⁴. Then the projections are color coded for depth to provide additional information to visualize the structure of the retina and pathology.

4.3.4. IMMUNOHISTOCHEMISTRY

Retinas were enucleated and fixed in 4% paraformaldehyde before both the retina and choroid were flat-mounted. Flatmounts were prepared using standard microdissection techniques under a stereoscope. The flatmounts were stained with DAPI (1:500) and Isolectin B4 with Alexa 594 (1:300) for 2 hours. After mounting on slides, they were imaged with a confocal Olympus FlowView fv1000, with a 20x .72NA lens and 60x 1.4NA oil immersion lens. The 20x image settings provided 0.621 μ m lateral resolution with slice spacing of 1.14 μ m.

4.3.5. EX-VIVO MICROGLIA MORPHOLOGY

Microglia in the flat mounts were manually located and identified in each retinal layer in the confocal imaging. Their morphology was traced in ImageJ, resulting in branching information, after a thresholding routine was applied where the channels were first unmixed to minimize spectral bleed-through. It was found that ramified microglia have long, thin cell processes with a range of about 200 microns. When the microglia suspect they have encountered a threat to the Central Nervous System, they go through the de-ramified state and the processes become shorter and thicker. When activated, the microglia go into a migrating state with minimal processes and an elongated soma as they move to the site of the threat. Fully activated and phagocytosing microglia are amoeboid with fully circular cell bodies.

4.3.6. STATISTICS

Analysis of microglial counts (and density) included a percent change calculation as well as ANOVA tests as follows. For statistical analysis, measurements were compiled with a minimum n=4 for each timepoint, and the average (μ) and standard deviation (σ) for each group were calculated. The inter-group variance was computed using the coefficient of variance (C_v) which is σ/μ . The C_v was used to determine if a finding was consistent within the experimental group and to show that the changes were distinguishable from

other conditions. Once compiled by the group, the longitudinal assessment was self-normalized to the preliminary number of microglia and represented as percent change $\frac{V_t - V_0}{V_0} \times 100$ over time (t). With the $C_v < .3$, a percent change $>5\%$ is considered significant.

The statistical significance was tested in an ensemble fashion to test the multivariate changes over time. Two-way ANOVA was used with the interaction test to determine the independence and significance of the factors (variables of area, counts, location, time, and treatment group), while single-factor ANOVA was used to test for significant change between timepoints within individual treatment groups. Post hoc tests were performed using Fisher's and Tukey's methods as applicable. T-test between factors and across timepoints were assessed and correlated to the ANVOA.

4.4. Results

Imaging by fundus SLO, OCT, and OCTA together provided a complementary integrated platform for monitoring and quantifying structural and inflammatory responses of the retina in the two injury models up to 21 days. Fluorescent fundus imaging modality enabled us to clearly visualize and count the number of GFP expressing microglia present in the retina at the baseline (Row 1, Figure 4.3.1-1), while IR mode allowed lesion localization. Figure 4.3.1-1 shows representative SLO microglia and IR images at baseline and 3 days following low and high laser doses. These results demonstrate the ability of complementary imaging to visualize microglial distribution combined with retinal morphology that cannot be determined in-vivo by traditional fundus imaging.

4.4.1. OCT + FA IMAGING AND ANALYSIS.

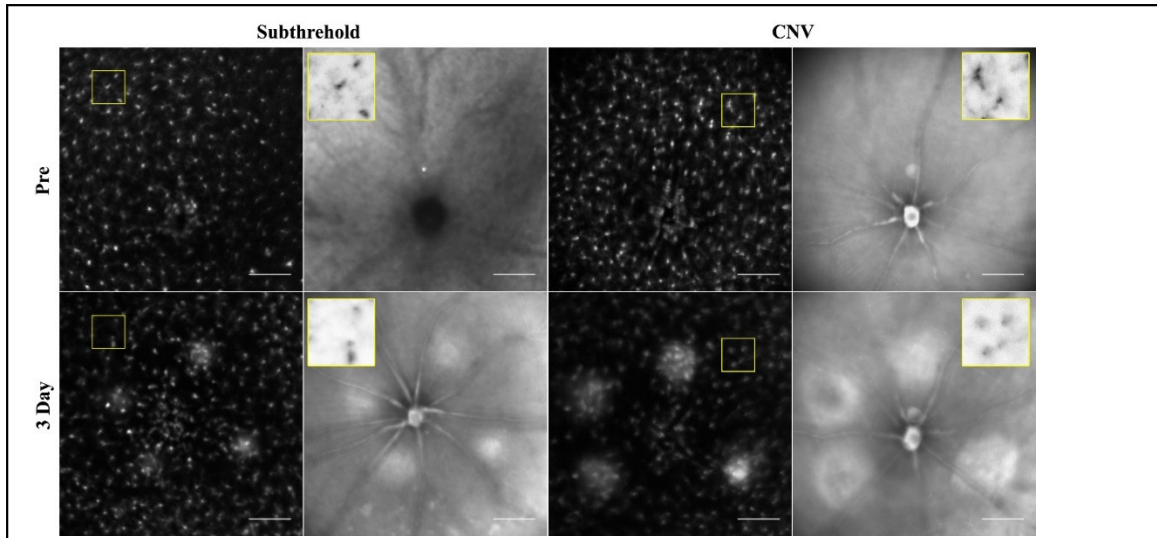
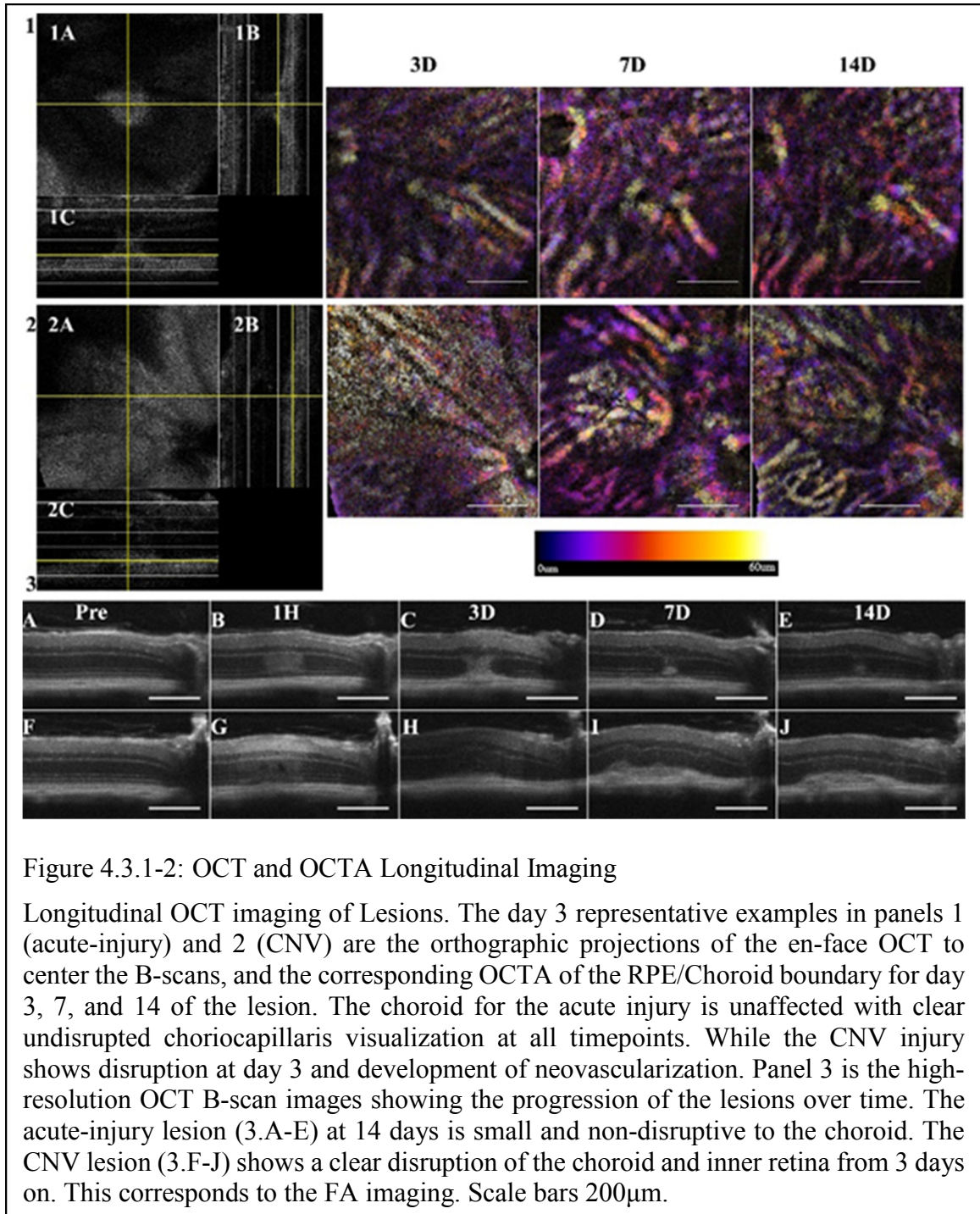


Figure 4.3.1-1: Microglia and IR Imaging of Lesions

Representative in-vivo fundus imaging. Matched imaging pairs of the microglia and Infra-Red fundus images of acute-injury and CNV eyes before and three days after lesions. In the preliminary scans, the microglia are distinguished by the small soma and surrounding ramifications as seen in the color inverted inset. At 3 days, the microglia somas were enlarged, processes retracted, and, as seen in the respective inserts, may localize together. The acute-injury lesions activate and migrate at 24h, with examples of the clustering at the four lesion sites shown at day 3. The CNV microglia, however, are slow to migrate until day 3 where they are almost totally localized to the CNV. Scale bar is 200 μ m.

OCT imaging of the lesions over multiple timepoints provides an indication of the progression of lesions. The OCT volume was visualized with orthographic projections from the en-face view to select the depth and B-scans for analysis. The orthographic projections allowed for precise localization and measurement of the lesions across the widest point. Through the projections, morphology trends of the lesion pathology were clearly visualized and measured in the B-scans. Figure 4.3.1-2 shows the OCT imaging of the lesions over multiple timepoints providing an indication of the progression of lesions. Additionally, depth-projected OCTA was performed. From the OCT B-scans, we determined that the acute-injury inflammation peaks at 24h and begins resolving at 72hrs, whereas the chronic response continues with clear CNV formation at 7-14 days. Additionally, the orthographic views defined the OCTA slabs to visualize the

neovascularization and determine layer involvement. Retinal layer thickness measurements obtained from OCT (B-scans) show the dynamics of lesion growth. A comparison of lesion thicknesses over time for the CNV vs. acute-injury lesions is shown in Figure 4.3.1-3, with total retinal thickness and the lesion thickness from the IPL to the photoreceptor layer plotted. In the CNV model, the thickness and lesion size peak at 7 days and subside days 14-21, whereas in the acute-injury lesion (green traces), thicknesses remain within measurement variance throughout the 21 days.



Fluorescein Angiography, shown in Figure 4.3.1-4, revealed vascular leakage in the CNV model visible beginning on day 3 and continuing to day 14. In contrast, vascular leakage was absent in both the acute-injury model and age-matched controls at all time

points assessed. The leakage of CNV at day 3 is consistent with the known angiogenic response and corresponding vascular leakage shown in previous studies¹⁴⁵.

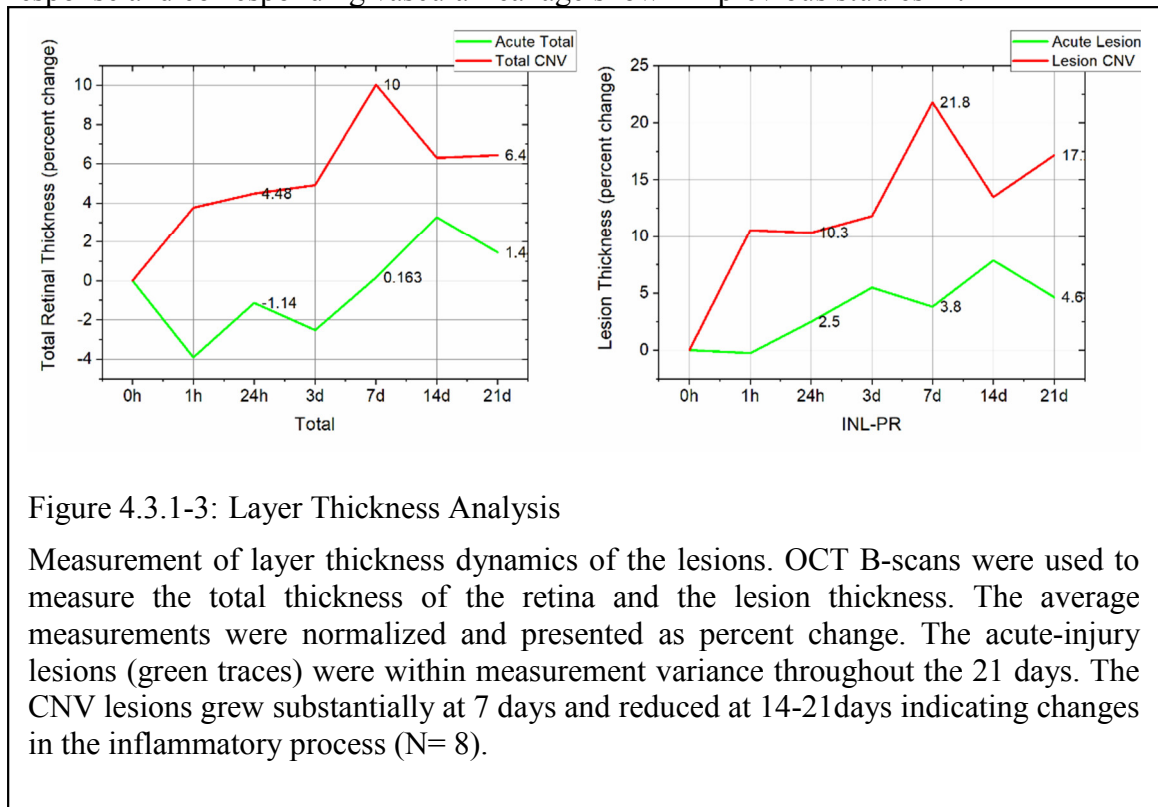


Figure 4.3.1-3: Layer Thickness Analysis

Measurement of layer thickness dynamics of the lesions. OCT B-scans were used to measure the total thickness of the retina and the lesion thickness. The average measurements were normalized and presented as percent change. The acute-injury lesions (green traces) were within measurement variance throughout the 21 days. The CNV lesions grew substantially at 7 days and reduced at 14-21days indicating changes in the inflammatory process (N= 8).

Further disruption of the vasculature seen in FA is corroborated by the OCTA changes of the CNV lesion at day 3 as shown in Figure 4.3.1-2 (panels), showing a loss in integrity of the choriocapillaris. Given that OCT revealed the lesion features beginning within 1 hour (Figure 4.3.1-2, panel 3) and damage was consistent with FA finding of damage, orthogonal OCT was used to ensure pathology in the Cx3cr1^{eGFP} model.

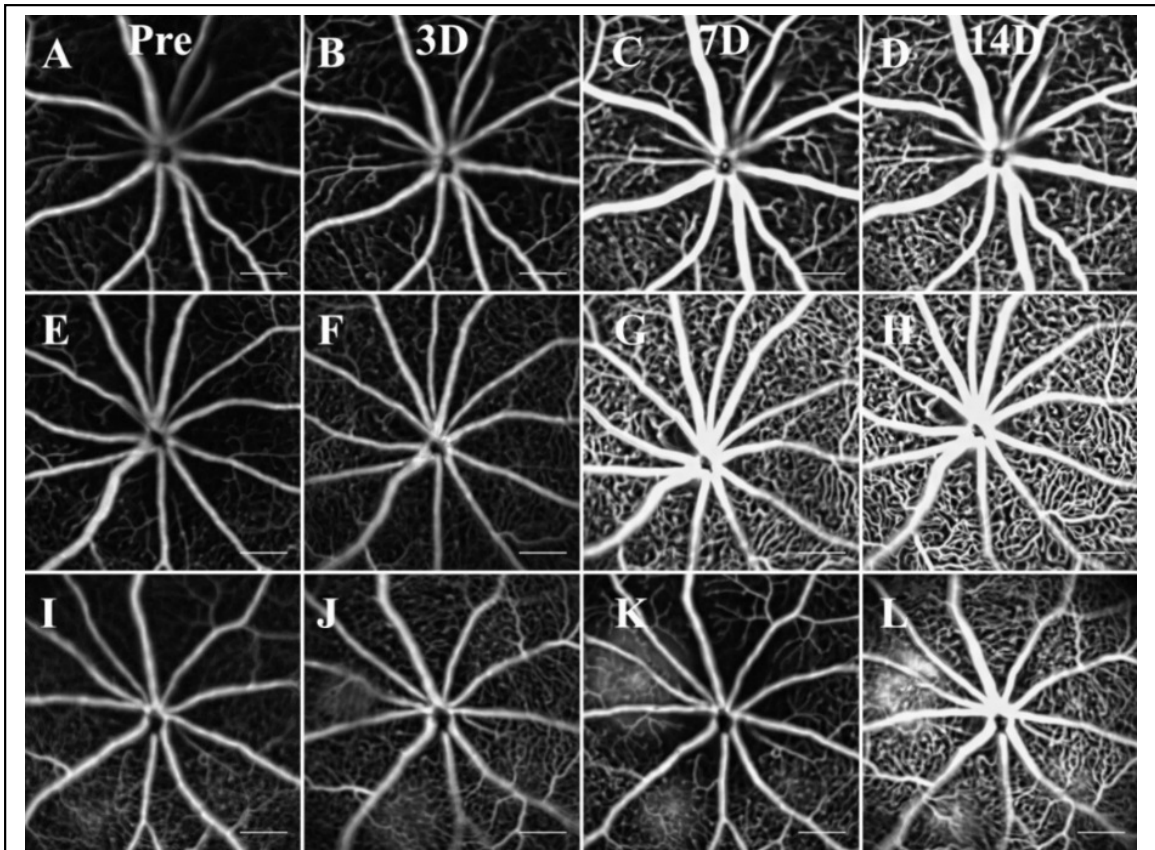


Figure 4.3.1-4: FFA of Vascular Permeability Assessment

CNV model results in vascular leakage. Control (A-D), Acute (E-H), and CNV (I-L) fluorescein angiography are shown at four timepoints: pretreatment, 3, 7, and 14 days after induction of lesions. The control and acute-injury conditions show intact vasculature with no clear signs of leakage or vascular remodeling. In contrast, CNV retinas show signs of leakage at 3 days (J) which continues to 4 days. Scale bars 200 μ m.

4.4.2. MICROGLIA DYNAMICS

For quantification of microglia obtained by fundus imaging, we used an automated segmentation algorithm to count the number of microglia that were imaged using the 30-degree fundus lens. This analysis yielded an average of 350-381 microglia per field in scans taken at baseline prior to laser exposure (Day 1) (Table 4.3.2). Throughout the study, the untreated control retinas had a range of 273-451 ($\mu = 364.9$ and $\sigma = 34.8$) microglia in the field of view. The microglia seen in-vivo at the baseline prior to laser photocoagulation exhibited small somas, and thin processes were observable. From the inflammatory

progression, the timing of morphological changes accompanying the microglia activity was assessed non-invasively and validated with histopathological analysis at various times following the induction of laser lesions (1h, 1 day, 3 days, 1 week, 2 weeks, and 3 weeks).

Time	Acute	σ	C_v	CNV	σ	C_v	CTRL	σ	C_v
pre	345.33	15.01	0.04	344.00	41.00	0.12	381.14	12.88	0.03
1h	474.67	177.11	0.37	381.25	66.03	0.17	380.14	39.17	0.10
24h	292.00	24.88	0.09	260.00	24.12	0.09	338.86	38.76	0.11
3d	290.00	32.05	0.11	296.25	99.23	0.33	335.86	22.88	0.07
7d	388.00	9.00	0.02	324.00	39.60	0.12	357.71	34.07	0.10
14d	387.33	68.41	0.18	488.00	235.56	0.48	377.86	29.03	0.08
21d	390.33	47.08	0.12	410.00	114.14	0.28	382.86	31.15	0.08

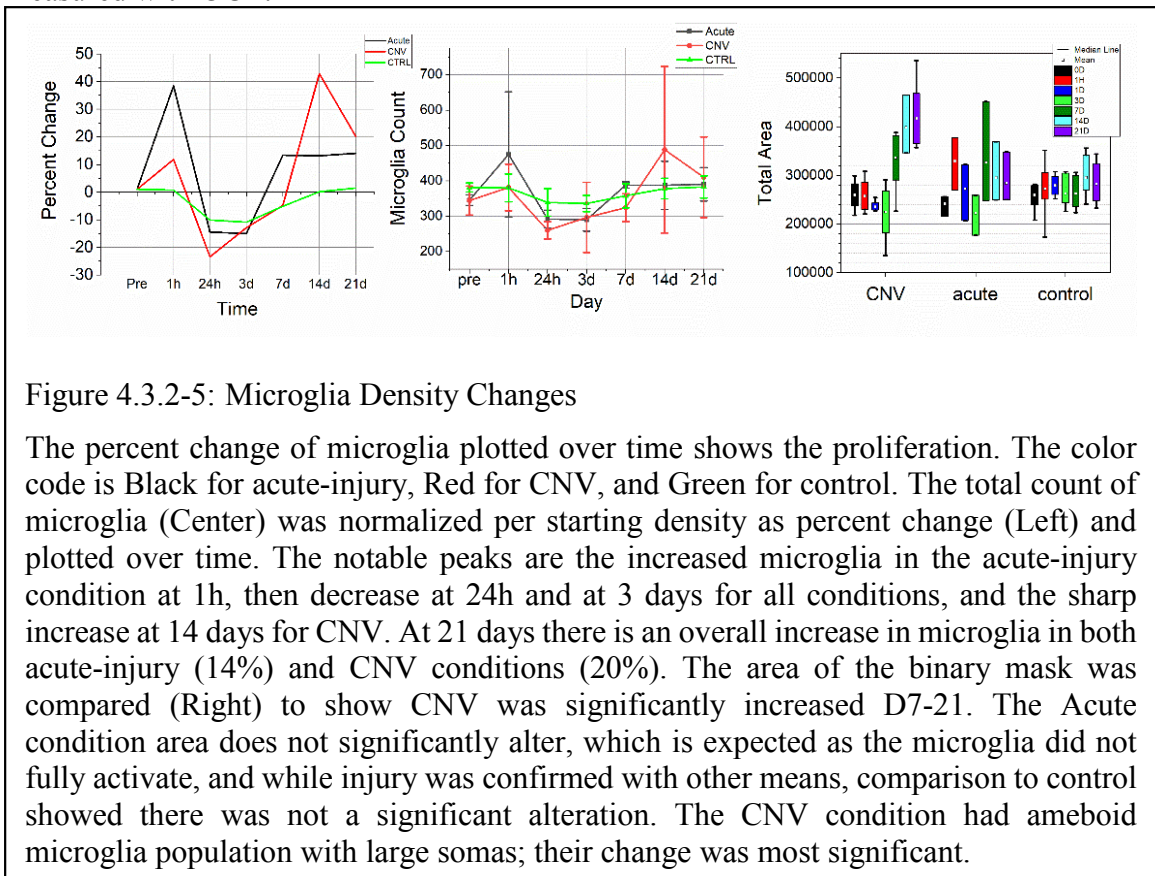
Table 3.2.3-1: Table of Automated Microglia Counting

Average microglia count, and standard deviation as measured from the in-vivo imaging system. Groups are listed as Acute (Acute-injury), CNV, and CTRL (combined left eyes for both groups). Control eyes microglia count distribution was $\mu = 364.9$ and $\sigma = 34.8$ thereby computing a coefficient of variation (C_v) of 0.095. N=8.

Microglia in the acute-injury model show evidence of activation and reach peak migration at day 3 (Row 2, Figure 4.3.2-1), returning to a resting state around day 14. However, in CNV, the microglia exhibit delayed migration and remain activated at the site of injury through day 21. In this model, we observed a correlation between the delay of microglia activation and the severity of chronic injury leading to CNV.

Table 4.3.2 summarizes the average microglia cell counts for the three groups over the seven timepoints assessed. Following CNV induction, the immediate acute phase of inflammation was marked by lesion swelling and activation of microglia; however, the migration response was delayed compared to the acute-injury. At 1h, the average number of acute-injury retina microglia was $474^{\pm 177}$ while the control and CNV eyes were $380^{\pm 39}$ and $381^{\pm 66}$ respectively. To compare between the groups, each individual eye was self-normalized and represented as percent change. While the microglia show signs of process retraction and activation at 24h in both groups, the predominant migration to the lesions did not occur until day 3 with the CNV eyes (see Figure 4.3.2-5). The microglia in the

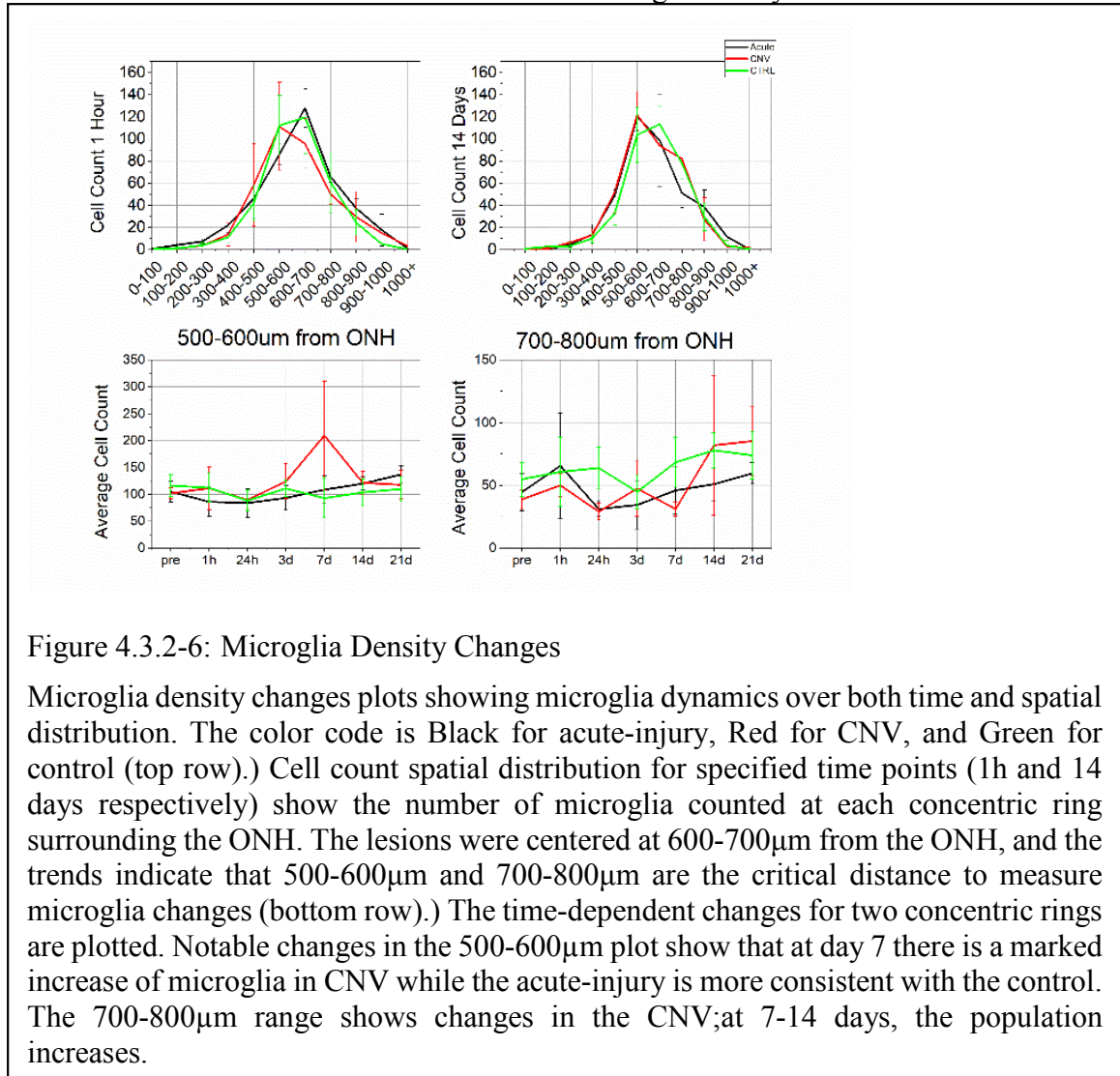
acute-injury group follows an activation and migration pattern aligning to the dynamics measured with OCT.



The plots in Figure 4.3.2-5 illustrate the key aspects of the relationship regarding how microglia density changes both spatially and temporally. When the microglia migrated to the inner retinal site of injury, the overall density of microglia decreased (day 1 to day-3 Table 1). The acute-injury lesions' peak densities occurred at 1h +40% and 7 days, demonstrating a rapid migration and repopulation of the retina (see Figure 4.3.2-5). The microglia at CNV lesions were slower to migrate at 3-7 days and peaked in density at 14 days. At 21 days, there was an overall increase in microglia in both acute-injury (+14%) and CNV (+20%) conditions plotted as percent change indicating increased density.

Ameboid microglia are differentiated by having larger somas; therefore, the area of the binary mask is different. Area analysis (see right panel in Figure 4.3.2-5) of the binary image shows that the conditions variance is significant ($P < 0.001$); however, time series

only approaches significance with $P=0.05$. The two-way ANOVA shows that the different size distribution of the CNV condition is significant to both acute and control eyes. The size difference between acute and control was not significantly different.



From the overall density, the spatial distribution for the peaks was 1h and 14 days; therefore, the spatial density was plotted as the cell count for each 100 μ m concentric ring surrounding the ONH (Figure 4.3.2-6). The lesions were targeted to be centered between 600-700 μ m from the ONH, and the adjacent rings showed the greatest change in density. The region of 500-600 μ m was between the ONH and lesion, and the ring 700-800 μ m was the boundary for the periphery; both were further analyzed for density changes over time.

The CNV condition in the 500-600 μ m plot shows that on day 7 there was an increase in microglia from 100 to 200 cells, but the 700-800 μ m decreases in density overall. While the periphery densities varied over time, the trend indicates a late phase increase in total microglia density.

4.4.3. EX-VIVO VALIDATION

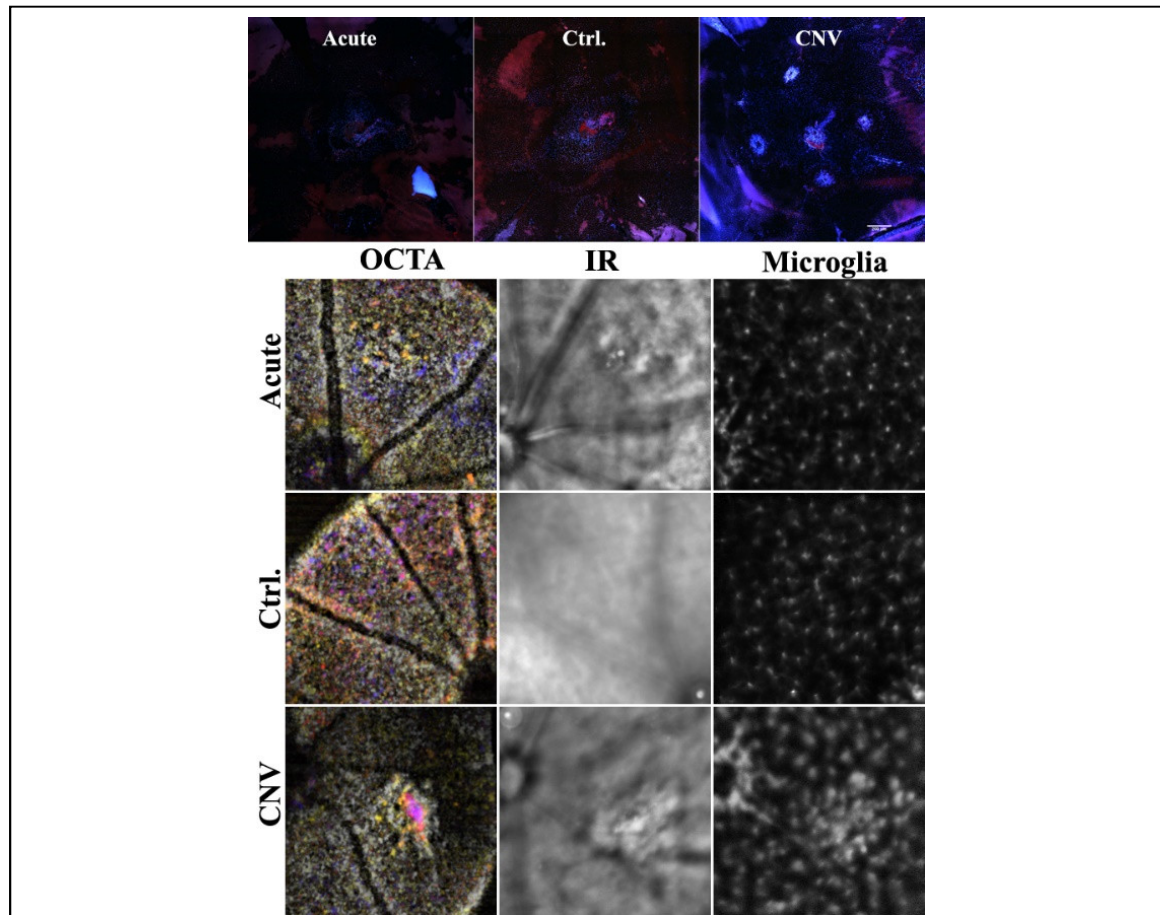
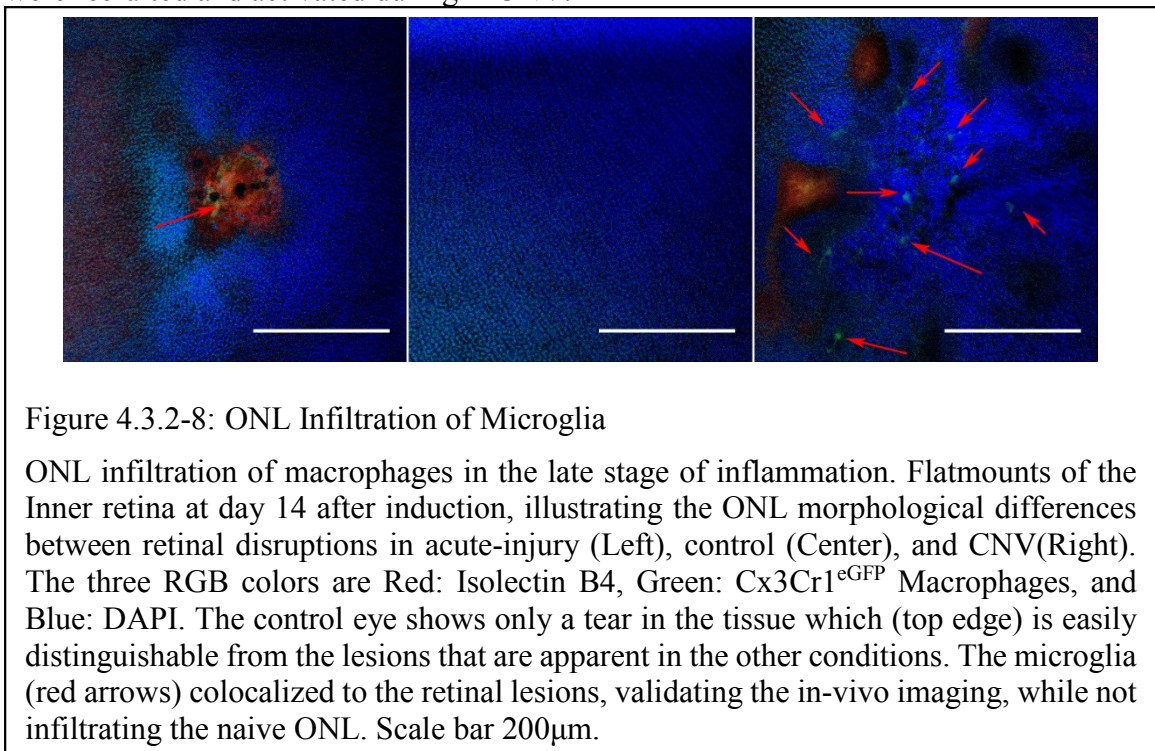


Figure 4.3.3-7: CNV Formation

Imaging of early CNV formation and subretinal macrophages. Flatmounts of the 7-day post-lesion choroid comparing acute-injury, control, and CNV. The three RGB colors are Red: Isolectin B4, Green: Cx3Cr1^{eGFP} Macrophages, and Blue: DAPI. Flatmounts confirmed that there were no disruptions to the choroid in the acute-injury or control eyes and that macrophages were not normally present. The CNV eye is disrupted with a DAPI/isolectin positive lesion (cyan color). The CNV lesion and surrounding area also contain macrophages. Below is the late stage at day 21, showing OCTA, infrared, and microglia imaging in-vivo. The acute-injury and control are comparable; however, the CNV injury has a scar and recruitment of microglia. Scale bar 20 μ m.

Immuno-histological verification of the microglia pathology was compiled using choroid (example day-7, Figure 4.3.2-7) and retinal flatmounts (example day-14, Figure 4.3.2-8) imaged in a mosaic across a wide area with the low magnification lens to identify sites of clustering. While the IR and microglia imaging in Figure 4.3.2-7 show the CNV injury at day 21 with a continued trend of the microglia localized to the lesion, only the OCTA definitively separates the inner retina portion of the lesion from the choroid with the confidence of depth resolution. Without a flatmount, the microglia are only imaged from the superficial retina, and IR reflectance does not have a defined boundary. Throughout the choroid flatmounts (Figure 4.3.2-7 Top, Figure 4.3.2-9), the control and acute-injury lesions showed no accumulation of lectin-positive (activated microglia or vessels) or Cx3Cr1⁺ macrophages. However, the CNV lesion shows colocalization of both lectin and Cx3Cr1^{eGFP} on the choroid site of the lesion from day 3 on, indicating microglia were recruited and activated during L-CNV.



In both dose responses, microglia migrated into the ONL within the lesion and were verified with the retinal flat mount (Figure 4.3.2-8). The CNV lesion developed a “star-

like” scar pattern with apparent edemas and microglia colocalization. The lesions were reimaged with a 63x oil immersion lens to identify cellular level morphology in regions of interest (ROI). To assess the early change seen in the fundus images, day 3 choroid flat mount (Figure 4.3.2-9) was imaged to show that the lesion identified (Figure 4.3.2-9 Right) shows the early formation of CNV and infiltration of microglia. At the late stage, the microglia in the acute-injury condition returned to a resting and ramified morphology.

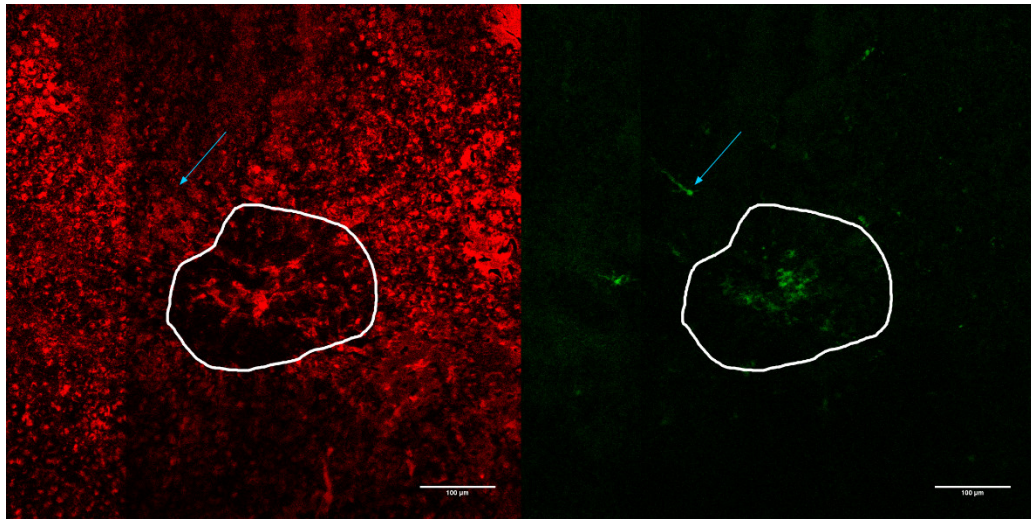


Figure 4.3.2-9: Subretinal of Microglia

Subretinal accumulation during the acute phase. Choroid flatmount at day 3 of CNV induction, showing lectin (red) to identify the early lesion and CxeCr1eGFP (green) labeling infiltrating macrophages. The lectin staining of the choroid highlights the lesion area, although the neovascular tuft is not yet fully formed. Since Cx3Cr1 is present on all the myeloid-derived macrophages, the somatic macrophages and microglia cannot be differentiated, but the elongated processes suggest (blue arrow) the lesion periphery is microglia or dendritic cells. Scale bar 100µm

Day 21 was a specific timepoint of interest of the CNV condition because it demonstrated the presence of lectin positive-amoeboid microglia in the inner retina (Figure 4.3.2-10), validating that the microglia imaged in-vivo (Figure 4.3.2-7) were amoeboid and not out of the focal plane. The microglia were all simple with thick branching structures or fully amoeboid and lectin-positive. Taken together, this is an indication of chronic microglial activation in the CNV condition, as the acute-injury returned to resting state at 14 days. Furthermore, on day 21, the neovascularization imaged in the ONL contained

lectin-positive macrophages and was surrounded by lectin negative microglia with simple branching morphology (Figure 4.3.2-11). The morphology of the lesion in the ONL was best monitored in-vivo by OCTA, where the fluid accumulation provided contrast to see the star pattern morphology (Figure 4.3.2-11 A-E). The en-face OCTA morphology corresponded to the alterations seen in the nuclei stained with DAPI.

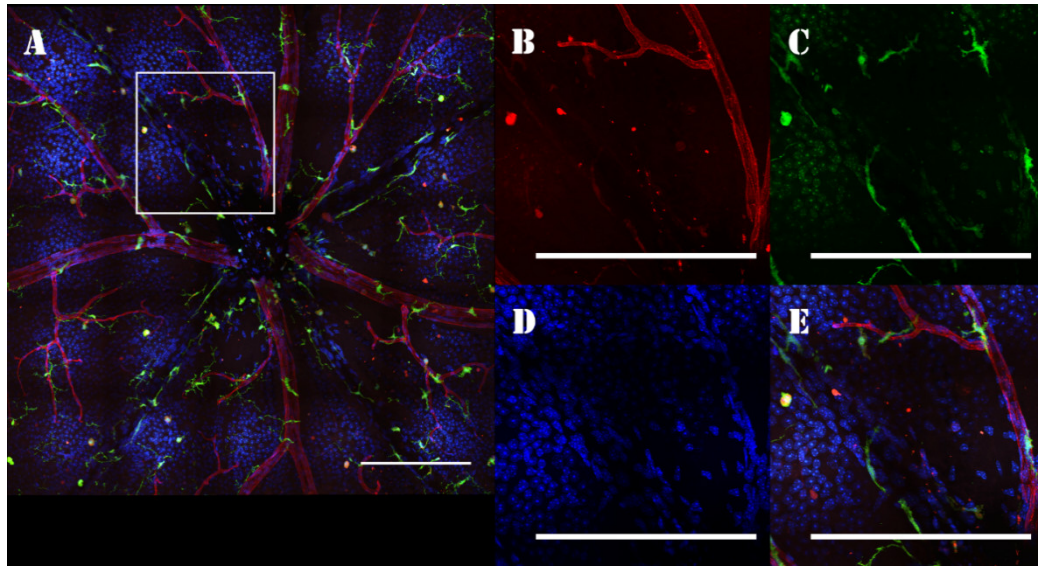


Figure 4.3.2-10: Superficial Layer – Chronic Activation of Microglia

Superficial microglia remain activated in CNV. Day 21 inner retinal Flatmount of CNV showing the vasculature and microglia. The three RGB colors are Red: Isolectin B4, Green: Cx3Cr1eGFP microglia, and Blue: DAPI. A) is the mosaic showing the ONH and the surrounding tissue of the NFL-IPL, also the white box is the inset shown (B-E). B) Isolectin stains the vasculature and activated microglia. The elongated microglia in C) do not colocalize to the lectin staining in B). The amoeboid microglia are lectin-positive with the highest expression appearing yellow in A) and E). Also, often several microglia are vascular associated and show an elongated but low ramification morphology. Scale bars 200 μ m

After screening the normal and pathological condition, the microglia morphology was classified into the subtypes: ramified, de-ramified, migrating, amoeboid, vessel-associated, and among nuclei (Figure 4.3.2-12). The CNV lesions altered the localization and morphology of the microglia with activated (both amoeboid and isolectin positive) and increased vessel-associated microglia at 21 days. Vessel-associated microglia were also found on the confocal images usually with two ramifications and an elongated cell body

attached to or formed around a blood vessel. Finally, there were activated microglia found among densely packed nuclei in the INL and ONL. This placement is unusual because the microglia are generally only activated when at the site of a threat and return to a ramified state as they move away from it. While the acute-injury demonstrated the acute inflammatory response, the prolonged ONL localization and activation of microglia in the CNV condition may be linked to the continued pathogenesis.

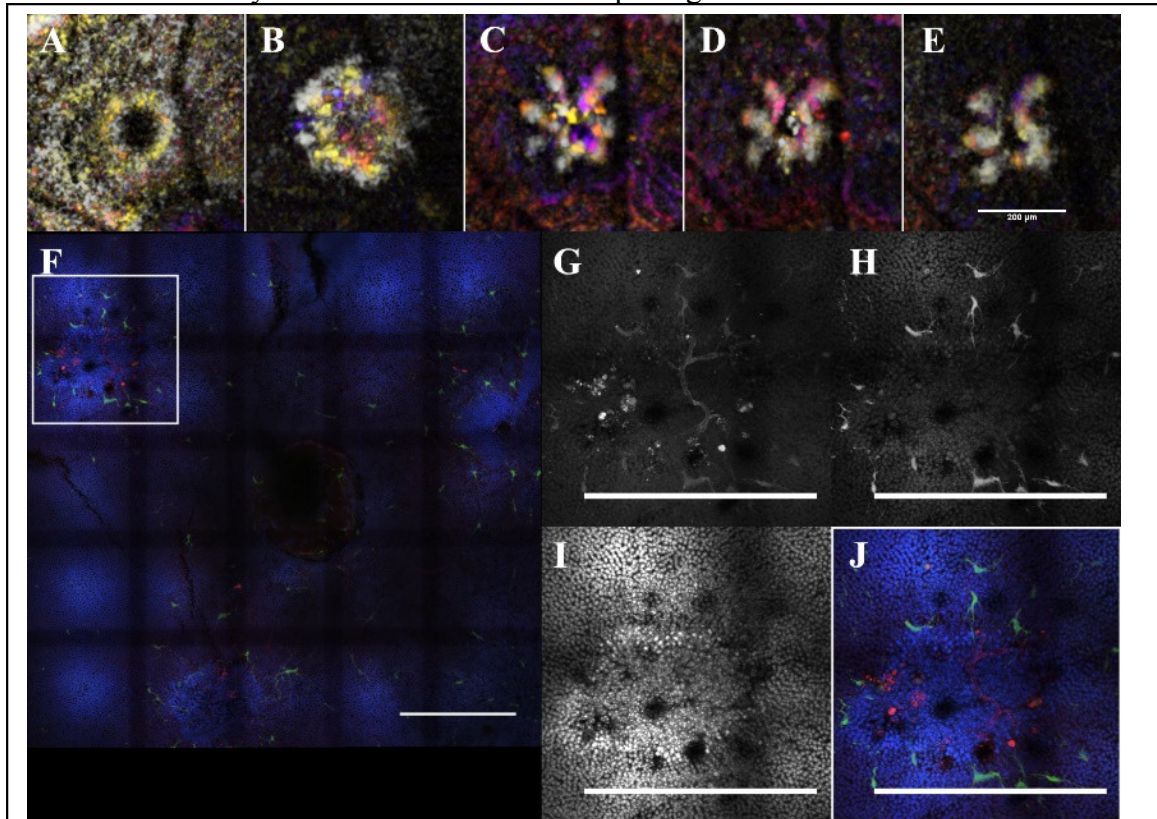


Figure 4.3.2-11: Corresponding OCTA and Flatmount of a Lesion

OCTA of the lesion (A 1H, B 3D, C 7D, D12D, E 21D) shows the progression. CNV lesion shows microglia infiltration at 21 days in the chronic phase. The ONL showing the CNV lesions surrounding the ONH. The three RGB colors are Red: Isolectin B4, Green: Cx3Cr1eGFP microglia, and Blue: DAPI. F) is the mosaic showing the ONH and the surrounding tissue of the ONL, also the white box is the inset shown (B-E). While the isolectin G) and Cx3Cr1eGFP H) are cell-specific, DAPI I) shows the scar. The composite J) shows only moderate colocalization; the vessels and microglia infiltrating the ONL are apparent. This aberrant localization of vasculature is a hallmark characteristic of CNV; the microglia morphology and cell state within the lesion is not as well understood. The enlarged somas and short thick processes are makers for glial stress. Scale bars 200 μ m.

States of Microglia

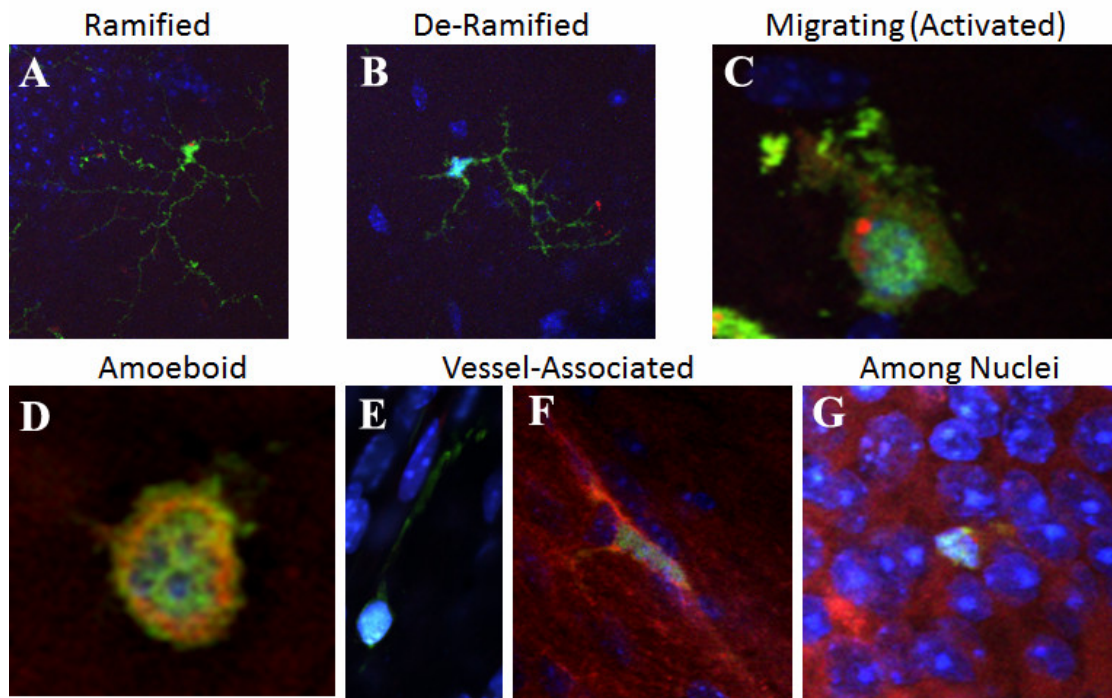


Figure 4.3.2-12: Samples of the Microglia Activation States

The samples of Microglia morphology were assessed with three RGB colors; Red: Isolectin B4, Green: Cx3Cr1^{eGFP} microglia, and Blue: DAPI. The naive retinal microglia maintained a Ramified (A) morphology until insult occurred. The activation progression (B-D) demonstrated that the microglia retract and migrate to the site of injury. At day 21, the Activated (D) microglia were stained with isolectin on their surface and localized within the lesion and inner retina. In the inner retina, there was also a prevalence of vessel-associated (E, F) microglia. Displaced microglia (G) were found in the INL and ONL and appear to be amoeboid as no processes could be resolved.

4.5. Conclusions

In understanding the role of microglia in pathogenesis neuroinflammation, the location, activation state, and density need to be assessed over time. The multimodal imaging approach consisting of the orthographic OCT enface, OCTA, and SLO techniques used in the current study allows for the visualization of both structural and functional changes in laser-induced retina lesions as well as quantification and correlation of

microglia activation to stages of retinal inflammation. Through this approach, the spatial and temporal dynamics of both the progression of lesion morphology and microglia activation were non-invasively imaged in the same eye. The only current way to utilize high resolution optical imaging to study microglial involvement in acute and chronic inflammation of retina is through the use of flatmounts preparation. However, this technique is not suitable for characterizing the longitudinal aspects of retina remodeling from an acute to chronic inflammatory response.

We validated the findings of the in-vivo imaging studies by using conventional immunohistopathological studies. The combination of non-invasive imaging techniques utilized in the current study enabled collection of “digital biopsy,” allowing for repeated measures of the retina with digital re-slicing of the tissue as needed. Traditional FA of the CNV indicates vascular dysfunction, while the combination of en-face OCT/OCTA and microglia imaging made it possible to develop a better understanding of the role of microglia activation associated with retina neuroinflammation and remodeling. Furthermore, OCTA is an increasingly acceptable surrogate for FA, therefore allowing for use of alternative contrast agents. For example, in this study, use of OCTA replacing fluorescein angiography allowed the imaging of GFP expressing microglia, so that indicators of inflammation, lesion microstructure, and vascular dysfunction may be imaged together.

Fluorescent imaging of the CX3CR1 model allowed for in-vivo visualization of microglia with the clear advantage of allowing longitudinal dynamics to be assessed. While microglia are in the resting or ramified state, they extend long, thin processes with complex branching patterns (Figure 11). The features of thin processes extending beyond the soma were clearly evident in-vivo and confirmed by the immunohistochemistry. When stimulated, microglia progressed through the de-ramified morphology where the processes retract and thicken as the cells prime for migration and activation (Figure 9). The migrating morphology is mostly amoeboid but may have a few thick processes and an elongated cell

body. These features were seen in cases of activation as bright round somas with blurred edges but clearly as amoeboid in the flatmounts. These dynamics indicate the CNV lesions undergo changes according to the phases of the inflammation process and tracking the OCT measurements of the lesion correlated to the timing of vascular leakage.

The microglial response in the acute-injury model followed the predicted transitions of the acute inflammatory response. The OCT imaging indicated that between 3 and 7 days the acute-injury lesions transitioned into the resolving phase and were not changing or further developing at 14-21 days. The histology at day 21 showed most acute-injury microglia to be in a ramified morphology with low levels of lectin staining. The spatial distribution of the microglia indicated that the proliferation and migration were regional and comparable to the control retina. This contrasts the CNV model at 21 days where many microglia were lectin-positive and fully amoeboid or in the de-ramified state with an enlarged soma and thick processes. At 7 and 14 days, the microglia increased overall; however, in the 500-600 μ m band between the ONH and lesion, there was the highest density: 200 cells at 7 days. The increase in microglia at day 21 may indicate immune response potentiation, but in the CNV condition, the amoeboid microglia indicate the inflammatory response is not fully resolved.

From the OCT data, it can be observed that an acute inflammatory response can transition to the resolving phase at 3-7 days and correlates to an increased number of resting microglia in the retina by 14 days. Furthermore, the acute-injury lesions had no significant impact (<5% change) on retinal thickness as measured by OCT B-scans, and the OCTA showed no indication of inner retinal vascular disruption or choroidal infiltration; therefore, it can be concluded that the damage was confined to the photoreceptor layer. The chronic response was seen in the CNV condition as measured by the retinal thickness changes, with significant thickness change at 7 days, corresponding to the drastic increases in the number and migration of microglia. While both conditions had +10-20% higher microglia density

at 14 days, the microglia in the CNV model remain activated through day 21 as evidenced by their amoeboid morphology and lectin-positive staining.

While this study allows for longitudinal studies of microglia migration and activation in both an acute and chronic inflammatory injury, the cytokines and other signaling factors were not assessed. Other studies have used either acute or chronic models to assess microglia expression of known activation markers. In the activated state, the microglia have an amoeboid morphology with two distinct cytokine expression states M1 (classical) or M2 (alternative macrophage activation)¹⁷⁹⁻¹⁸¹. The amoeboid morphology and overexpression of isolectin B4 are established markers of activation but cannot differentiate between M1/M2 profiles¹⁸². One study of the initiation phase (up to day 7) showed that there are different distributions of microglia polarization, with more M2 in the superficial retina and more M1 infiltrating the choroid⁵³. Further studies are required as M2 is thought to be more proangiogenic^{183,184}, while M1 is associated with the acute activation and the choroidal infiltration^{53,185}. During the inflammatory progression, modulating the balance and duration of M1/M2 activation may offer new targets and therapeutic potential for inhibiting neurodegeneration. It should be noted that the source of variance in lesion size and glia activation state may be gender, as estrogen levels is shown to affect M1/M2 glial activation in mouse models of neurodegeneration^{179,186,187}.

The increase in microglia density and evidence of stressed morphology are indicators of potentiation of the inflammatory response. The acute-injury lesion shrinkage measured by OCT is an indicator of the resolving phase and correlates to the microglia returning to resting morphology. The potentiation by increasing the number of microglia and altering their localization to the ONL and Choroid could be evidence of priming in the retinal immune response. One drawback to the fundus imaging of the microglia is that while the lateral resolution showed the activation and density changes, flatmounts were required to accurately determine the depth of microglia. En-face OCT and OCTA, however, can visualize the vascular and pathological morphology at any layer providing

an in-vivo surrogate for a biopsy. The data from this study and others indicate that the inflammatory progression in the CNV model is not simply an increased severity but a drastically different response than to an acute injury. Through this study, the timing and localization of microglia activation can be better understood in-vivo by combining the transgenic reporter and OCT imaging, thereby allowing the design of further studies to determine the specific activation states (M1/M2) throughout the inflammatory progression.

5. ROTENONE INDUCED NEURODEGENERATION

5.1. Abstract

Rotenone, a pesticide and toxicant, is used for its specificity as an electron transport chain (ETC) complex 1 inhibitor. As a small lipophilic molecule, rotenone can be readily absorbed into all tissue, including crossing the BBB into the CNS and irreversibly binding to the ETC complex 1, inhibiting further electron gradient potential and exchange in the mitochondria. While rotenone affects the mitochondria in all cells, sustained low dose exposure in farmers has specifically resulted in Parkinson's disease-like symptoms¹⁸⁸. The neurotoxicity of this neurodegeneration is notable because of the specificity in the loss of dopaminergic neurons; furthermore, the mechanism of susceptibility is currently unknown. For retinal research, the specificity of the mechanism of action is utilized to induce ROS stress in photoreceptor cell cultures as a model of AMD. As such, systemic exposure is used to model Parkinson's disease^{189,190}.

5.2. Introduction

While rotenone does not directly activate microglia¹⁹¹, it has been found to enhance neuronal toxicity¹⁹²⁻¹⁹⁴ and can interact synergistically with other toxicants to increase neuronal oxidative stress. While this neuronal damage is usually attributed to NF- κ B activation¹⁹², the multiple functional states of microglia activation show classical M1/M2 polarization^{179,180,184,195}. In acute studies of microglia activation to rotenone, the M1 phenotype was dominant, and the PD model showed that microglia, not astrocytes, were activated^{196,197}. In late stages of the PD model, microglia were found in the M2 state¹⁹⁸, with a link to NADPH Oxidase^{45,199-201} and NLRP3^{45,202,203}. In acute toxicity studies, rotenone toxicity induced a M1 polarization^{196,204}.

While many studies into potential mechanisms of rotenone induced microglia activation have been performed with primary cell cultures, the in-vivo progression of inflammation has not been established. The direct route of exposure to neural tissue and the ability to monitor progression in the eye may help elucidate the link between chronic neuroinflammation and neurodegeneration as is it recognized that as neuroinflammation persists, toxic products lead to neurodegeneration. Therefore, we believe use of the rotenone may help model the microglia response in that transition.

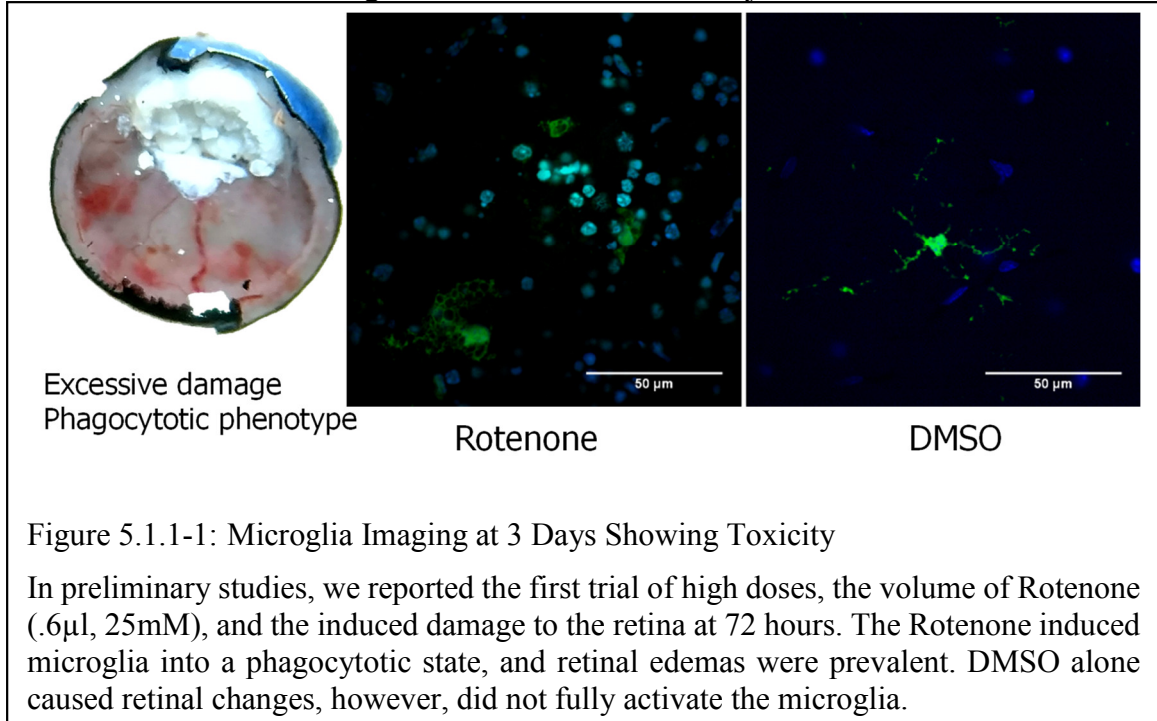
5.3. Model Development and Methods

All animal procedures were approved and performed according to the UTMB IACUC regulations and the IOVS guidelines for use of animals in ophthalmic research. For microglia imaging, transgenic B6.129-Cx3cr1^{tm1Litt}/J mice (Cx3Cr1^{GFP}) were used (The Jackson Laboratory). The eGFP fluorophore was imaged in-vivo using the fluorescent fundus imaging mode of Heidelberg Spectralis HRA+OCT. A Bioptigen r2200 SD Optical Coherence Tomography (OCT) system was used to gather B-scans, using a custom algorithm to generate OCT Angiography (OCTA) maps of the retina. The retinal microglia migration and activation state were correlated to the OCTA using the optic nerve head and the branching of inner retinal vasculature as landmarks.

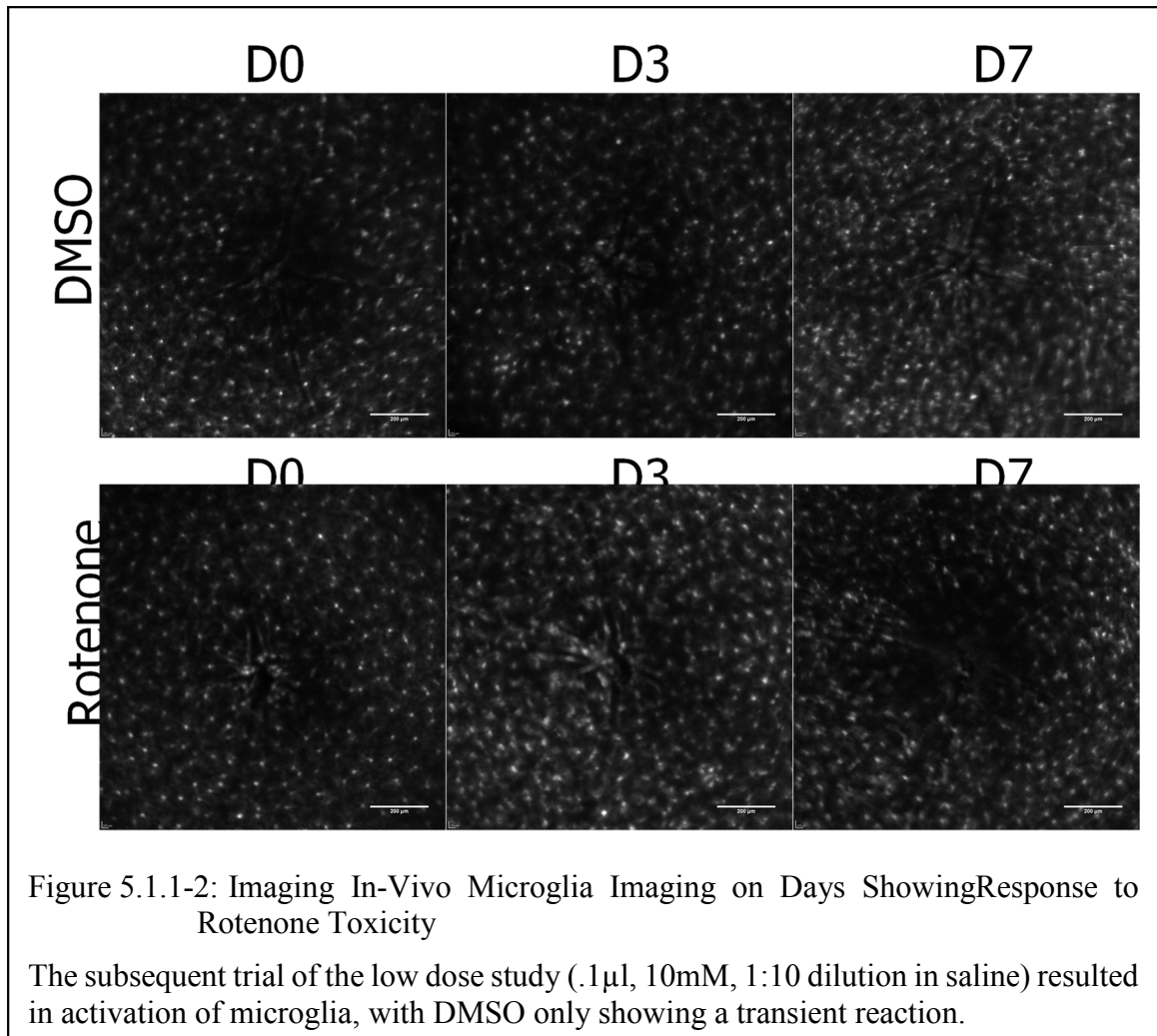
5.3.1. INTRAVITREAL INJECTIONS AND DOSE

The rotenone or DMSO was injected into the retina with a 35g needle and Hamilton type syringe. Volumes 0.1 to 0.6ul of DMSO or a mix of DMSO and rotenone were intravitreally injected. The initial dose of 0.6ul 25mM Rotenone, which was calculated from published literature, was not diluted so DMSO vehicle toxicity could be assessed. The intravitreal injection was expected to cause RGC thinning compared to the DMSO eyes²⁰⁵. While DMSO is the chosen solvent for many intravitreal injection experiments, there is

known toxicity in the retina and degeneration of the RGC layer that could confound the analysis²⁰⁶. In the first experiments, we aimed to determine how much retinal damage occurred and if lens clouding could be avoided with an adjustment to the dose.



In follow-up experiments, adjustments were made to minimize DMSO toxicity based on the volume of other drugs delivered and a safety factor by dilution while maintaining a soluble rotenone concentration. For reduction of toxicity, 100mM Rotenone/DMSO was vortexed into sterile PBS with a 1:10 dilution factor for 10mM. A final volume of 0.1-0.3 μ L was intravitreally injected. This volume was an approximation as backflow is an uncontrolled variable. Loading volume was 0.3 μ L, and delivered retained volume was at least 0.1 μ L. These dilutions were agitated before injection to prevent precipitation.



5.3.2. LAYERS THICKNESS ANALYSIS

The retinal layer thickness was calculated using the built-in segmentation reports algorithm found in the commercial instrument (Bioptigen). The thickness reports generated provided data in µm for the Total thickness (Total), Retinal Nerve Fiber Layer (RNFL), Inner Plexiform Layer (IPL), Inner Nuclear Layer (INL), Outer Plexiform Layer (OPL), Outer Nuclear Layer (ONL + IS), Outer Segment (OS), and Retinal Pigment Epithelium (RPE). Annular and radial scans were utilized for the Bioptigen automated mouse layer segmentation and thickness report. The annular scans provided average layer thickness. Radial scans were better suited for individual quadrant analysis in the standard template of the Early Treatment Diabetic Retinopathy Study (ETDRS) subfield area format.

To provide input for the en-face OCTA algorithms, a second high-resolution OCT scan was recorded from a 1.4x1.4mm area, with a lateral resolution of 1.4 μ m and axial resolution of 1.9 μ m. The volumes were registered to reduce motion artifacts and then processed for high resolution B-scans and OCTA.

5.3.3. MICROGLIA ASSESSMENT

After the total microglia population was plotted over time, the spatial distribution was calculated with respect to the optic nerve head. The microglia localization and density was computed using an automated soma detection algorithm akin to other in-vivo algorithms^{177,207}. The density was plotted in a sholl-like analysis centered on the optic nerve head with increasing bins of 100 μ m. The images were assessed for glial morphology.

Retinas were enucleated and fixed in 4% paraformaldehyde before flatmounting both retina and choroid using standard microdissection techniques. The flatmounts were counterstained with DAPI (1:500), and then functional targets were stained using Isolectin 4B with Alexa 594 (1:300) for vasculature and activation, M1 marker CD80(1:250), or M2 marker CD 206(1:200) with 2hours incubation⁵³. The retina and choroid flatmounts were both imaged using a confocal microscope. Microglia morphology and localization was noted. Activation state was assessed by the colocalization of CD80 or CD206 within the ameboid microglia.

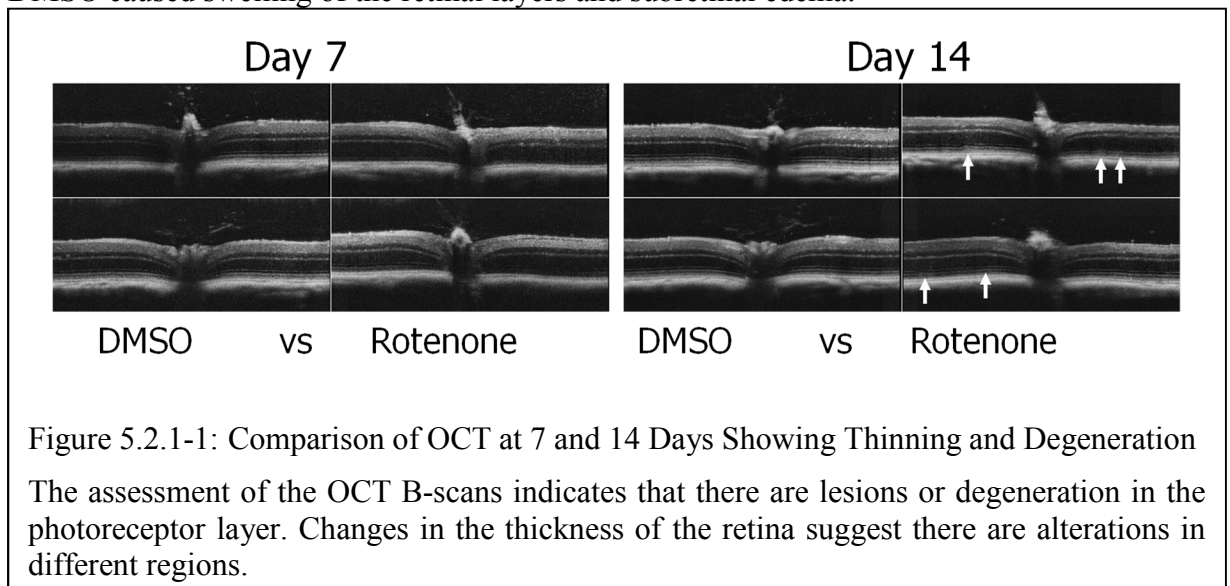
5.4. Results of Rotenone Toxicity

With the initial dose tests, we determined the high volume and high concentration of DMSO caused toxicity and degeneration. At 3 days, the high dose of DMSO caused retinal detachment. In both conditions, lens clouding occurred; this clouding suggests that DMSO toxicity alone can cause lens epithelial toxicity. The rotenone dose, however, resulted in microglia activation and phagocytotic microglia. With the excessive damage

involved in both doses, the contribution of the features of neurodegeneration could not be attributed to either DMSO or Rotenone with confidence. Lowering the injection volume and using dilutions yielded minimal perturbations in the DMSO condition, so the rotenone effects were differentiated from the vehicle. The solutions of DMSO and Rotenone + DMSO were diluted by a safety factor of 1:10 into sterile PBS. This high concentration low volume injection allowed for diffusion through the vitreous while avoiding risk of increased IOP. The lens clarity of the test animals was maintained after injection, facilitating longitudinal imaging studies.

5.4.1. OCT LAYER THICKNESS

In the first assessment, the OCT B-scans were segmented automatically to determine if global alterations to layer thickness existed. In initial studies published with rat models, the findings indicated that retinal degeneration of the RGC layer was pronounced when compared to DMSO and controls at 3 days²⁰⁸. High volume 0.6µL DMSO caused swelling of the retinal layers and subretinal edema.



When adjusted for toxicity, the low volume diluted DMSO produced minimal changes. Through OCT thickness analysis, the average thickness of the rotenone treated retinal layers between 3-7 days increased in the RNFL with greater variance at day 14.

Using the orthogonal views, the cross sections showed that in the 7 and 14-day images, one hemisphere was thinner than the other. The orthographic views allowed assessment of the surface contour of the inner and outer retinal layers. With the linked views and registration to ensure the choroid was flat, it was verified as localized thinning and not an off-axis imaging artifact.

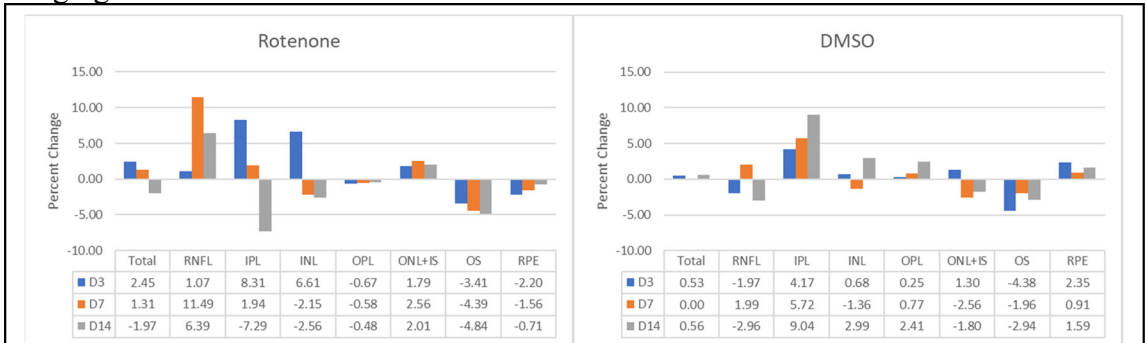


Figure 5.2.1-2: OCT Thickness Reports Showing Changes Over Time

The assessment of the OCT B-scans provide thickness measurements. The OCT B-scans thickness of the retina were computed for all layers. For analysis, the layers were normalized to the starting thickness as percent change. While the total thickness failed to reach significance, the variance and layer specific changes indicated regional alterations. Values greater than 5% are considered significant. It should be noted, the RNFL changes in the Rotenone treatment group.

With the automated thickness reports, the average layer thickness was assessed. The average total thickness of the retina did not substantially change over time; however, the variance increased. Individual layer alterations identified that the RNFL and IPL exhibited the largest changes. With the variance in thickness, further analysis at day 7 and 14 indicated that there may be two response phenotypes: a mild degenerative response and a severe degeneration. The mild phenotype shows RNFL degeneration in one hemisphere with minimal change to the overall thickness. The RNFL increased in thickness, and the IPL decreased in thickness. The severe phenotype had a greater change to the RNFL and increased the variance in the thickness measurements.

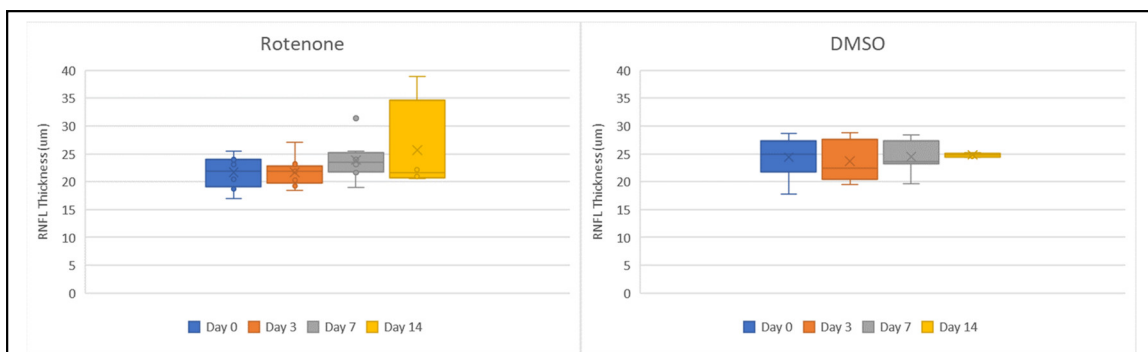


Figure 5.2.1-3: OCT Thickness and RNFL Thickness Over Time

The thickness assessment of the OCT B-scans reveals that the RNFL is significantly impacted in the rotenone treatment group. The high variance on day 14 is directly related to the localized changes. One hemisphere is degenerating while the other maintains a close to normal thickness.

RNFL thickness changes are seen in the Rotenone model. While the DMSO thickness is not substantial, the rotenone treatment group increases in thickness and variance. Again, the severity of degeneration indicates a multimodal distribution of thicknesses. With increased trials and more specific ROI thickness profiles, the multiple phenotypes can be compared.

5.4.2. MICROGLIA RESPONSE

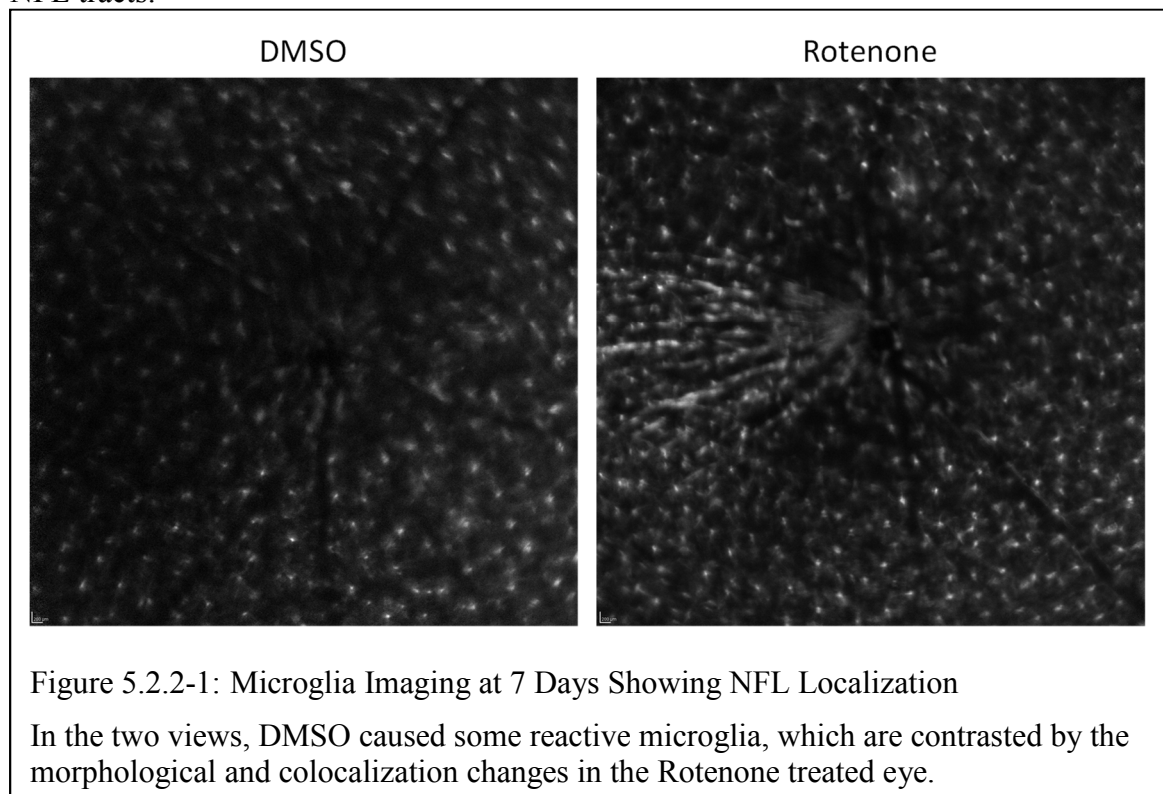
With the higher dose of Rotenone, the microglia entered a phagocytotic phenotype which was abundant in the superficial layers. With the excessive retinal damage, microglia could not be tracked in-vivo. DMSO with the .6μL volume caused retinal degeneration, but the microglia did not show an increase in ameboid pathology. The Rotenone exposed microglia were ameboid in morphology and contained many visible vacuoles. The DMSO treated eyes were in a mix of ramified and hypertrophied microglia. DMSO is known to delay or impair astrogliosis through mitochondrial membrane defects²⁰⁹, however the full effect on gliosis regulation has not been reported.

5.4.2.1. Adjusted Dose Morphology

The dose adjustment for volume and dilution maintained a clear cornea and lens, and therefore, the microglia could be tracked in-vivo. Both DMSO and Rotenone caused a decrease in microglia population imaged in the retina at day 3. By day 7, the cell count returned. The microglia morphology, however, was altered in the rotenone treatment group. The somas were larger, and the process area could not be clearly visualized.

5.4.2.2. Microglia NFL Localization

In a subset of the fundus images, the microglia can be clearly associated with the nerve fiber tracts. At day 7, the microglia followed the bundles and aligned tangentially. Traditionally this morphology is most often associated with adhesion to vasculature. This phenomenon was not present in any of the DMSO treated animals. In the DMSO treatment, small clusters might form, but there was not alignment to any anatomical feature. At 14 days, the rotenone treated eyes showed signs of activation, however, no colocalization of NFL tracts.



While microglia co-localization with the NFL bundles is a unique feature, specific cell state is undetermined by Cx3Cr1^{eGFP} imaging alone. The alterations at day 7, but not at day 14, indicate this response is transient. Further studies of the protective or neurodegenerative potential of microglia activation to rotenone are required. With this group of Cx3cr1 mice, the sample population was predominately expressing the mild phenotype. An expanded study to increase the probability of the severe phenotype would be required.

5.4.2.3. Microglia Imaging on Ex Vivo Flatmounts by Confocal Microscopy

The flatmounts of the retina were stained for DAPI, CD80, and CD206 in addition to the transgenic eGFP. The glia showing reactivity were positive for M1 markers at day 7. The M2 phenotype was not readily identified at day 7; however, there was not a readily available positive control. Rotenone is known to induce an M1 response; therefore, the result is expected; nevertheless, the lack of M2 transition could be a contributing factor to the pathology. As inflammation progresses in other injury induced disease models, the M2 phenotype is expected at day 5¹⁸⁵. The lack of a switch in phenotypes may indicate an initiation of a chronic inflammatory response.

5.4.3. LONGITUDINAL FUNDUS IMAGING

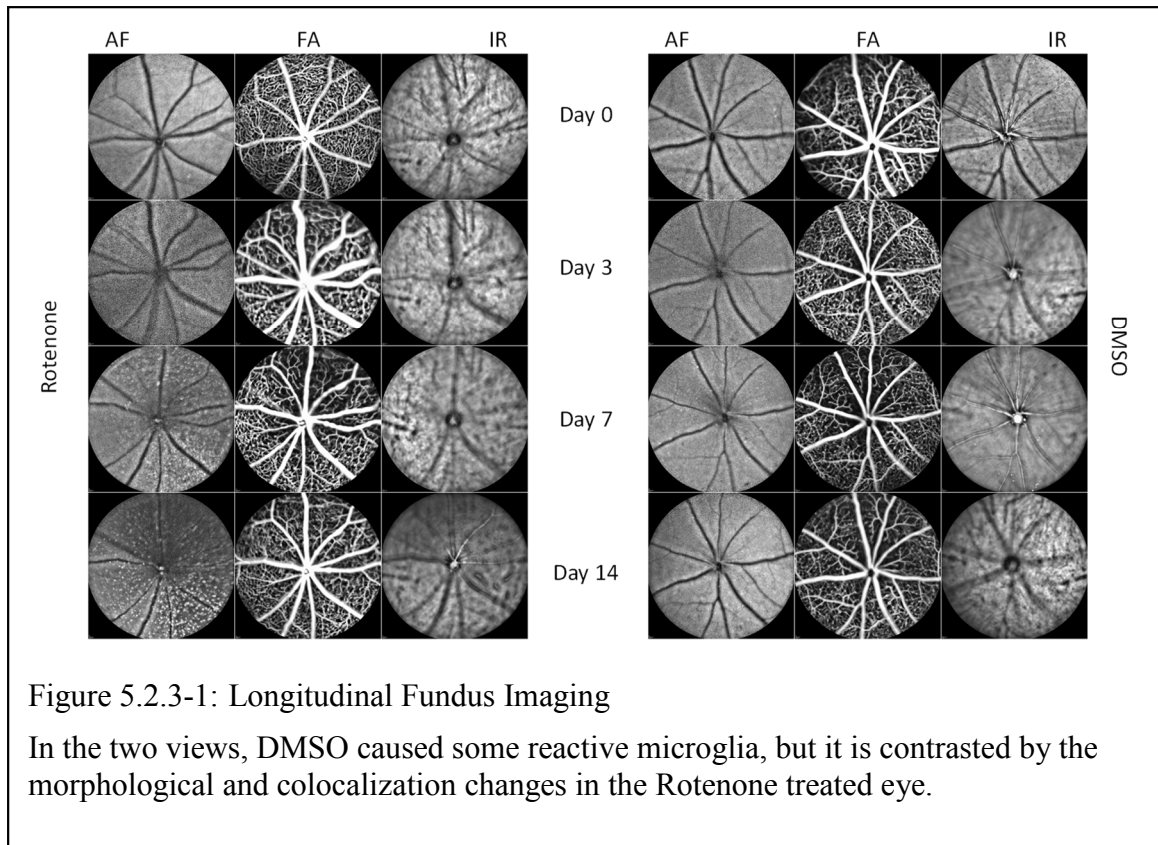


Figure 5.2.3-1: Longitudinal Fundus Imaging

In the two views, DMSO caused some reactive microglia, but it is contrasted by the morphological and colocalization changes in the Rotenone treated eye.

Wild type C57-BL/6 mice were screened with all applicable fundus modes on the Heidelberg Spectralis system. The longitudinal findings were set to replicate a traditional clinical exam. The data were assessed for the three key modalities: Infrared (IR), Fundus Fluorescein Angiography (FFA), and Autofluorescent (AF) imaging.

5.4.3.1. IR Imaging

Infrared imaging did not reveal any pronounced abnormalities in the DMSO treatment of the back of the RPE/Choroid images. The field of view was relatively uniform. The rotenone treated animals did not show obvious changes except in the 14-day images of severe degeneration. Although the alterations were subtle, an indication exists that there were RPE/Choroid alterations. Further texture analysis could be run on the IR images; however, the OCTA/En-Face imaging provides more capability.

5.4.3.2. FFA Imaging

Furthermore, the fundus imaging did not reveal vascular leakage when screened with FFA. In both injection groups, perfusion was rapid and uniform. There was no appearance of vascular dropout or vascular permeability. This control assessment ruled out vascular impairment with the intravitreal route of delivery. Systemic administration may impact the epithelial walls in late stages of the PD model; however, that pathology may be linked to route of exposure and not inherent mechanism.

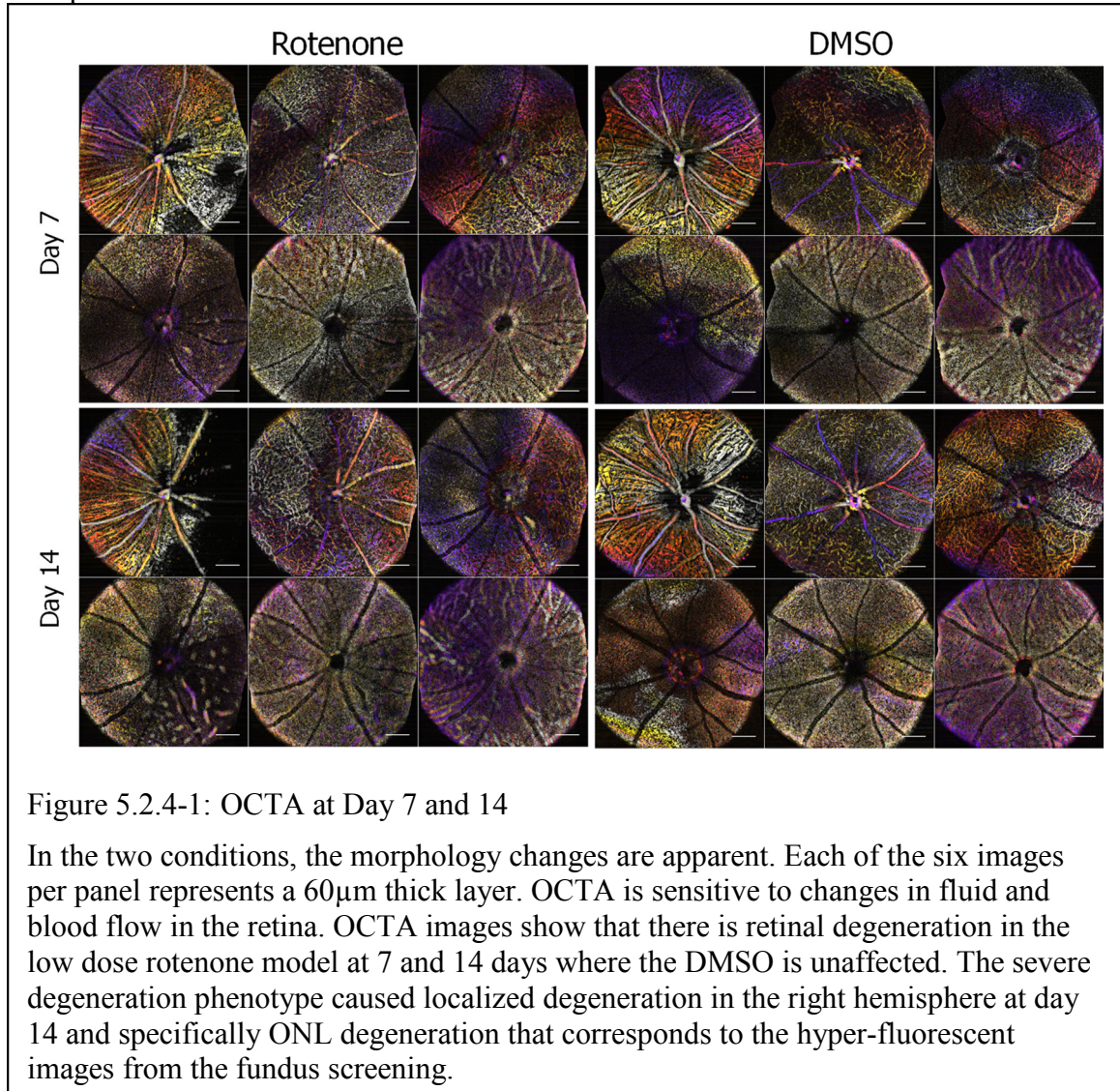
5.4.3.3. Autofluorescent Imaging

As a control step before FFA, autofluorescence images are taken. Normally in short studies, these scans do not rapidly change and are used as calibration for the fundus camera. Surprisingly, at 14 days, hyperfluorescent foci appeared; the foci mimicking dry AMD pathology localized in the ONL. The hyperfluorescent spots were peripheral to the ONH and more abundant in the severe degeneration subjects. As autofluorescence at 488nm is typically a sign of lipid peroxidation, this occurrence is also a feature of dry AMD that is not typically reproducible in-vivo. Although the foci were first observable at day 7, they could easily be attributed to imaging artifacts. At day 14, moderate degeneration showed moderate hyperfluorescent foci, while the severe degeneration had many bright foci.

5.4.4. OCTA AND EN-FACE OCT

The depth of the hyperfluorescent spots cannot be determined with fundus imaging; therefore, the OCT volumes were reassessed. The OCT volumes were resliced, and OCTA projections of the ONL were generated. The hyperfluorescent spots corresponded to lesions in the ONL-RPE. With OCTA and en-face imaging, the ONL-RPE lesions were most apparent in the severe degeneration condition, and the moderate degeneration was clear of lesions. In all samples, the topology of the inner retina was disrupted. The vascular beds remained intact, in both area and permeability measured by FA. In the severe degeneration, the localized thinning of the inner retina and hyperfluorescence preceded the degeneration

and was definitively detectable on B-scan OCT. However, early degeneration was visible on the OCTA/En-Face views. Further studies could help determine sensitivity to early disruptions.



5.4.4.1. Day 7 and 14 Degeneration

By day 7, there was thinning localized to one hemisphere in the Rotenone treated eyes that was not present in the DMSO. In the example of the severe degeneration, the OCTA slabs showed degeneration in a single hemisphere. This finding is supported by automated thickness reports and aligns to the hyper-fluorescence. The variance in both

severity and impacted layers suggests there may be sub-populations in the neurodegenerative phenotype. The clinical relevance is that certain individuals may be more susceptible to the neurotoxicity. With this improved understanding of the progression, further dose-response studies can be designed to predict the neurodegeneration based off of early changes in the retina.

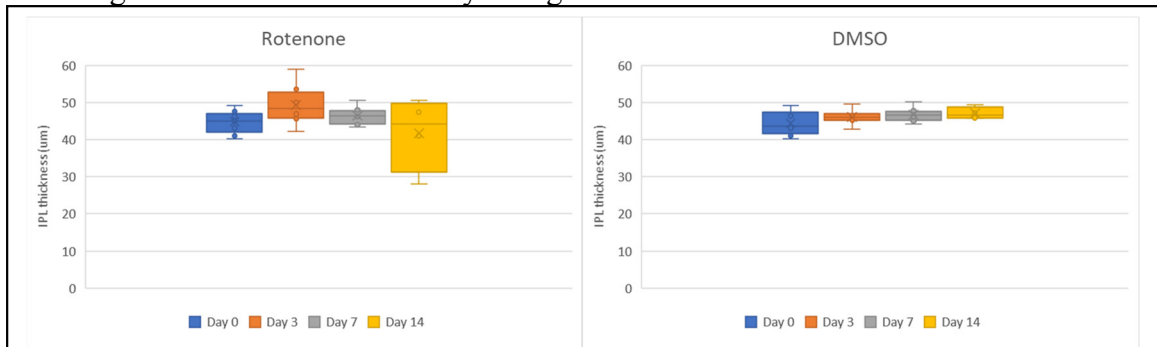


Figure 5.2.4-2: OCT Thickness of the IPL

With the alterations in the OCTA, the IPL and ONL thickness is revisited. The thinning in the rotenone treated eyes at 14 days is highly variable. This variance is likely due to the moderate and severe degeneration in half the retina. The DMSO treated eyes showed no alterations to the thickness.

5.5. Conclusions

By applying the principles of toxicological assessment, we improved our understanding of how a known agent with known mechanism of action could produce different phenotypes. Low doses of rotenone induced a rapid loss in GCL thickness and a slower loss of photoreceptors. Given that the distribution and diffusion of a highly lipophilic compound within the retina is not easily determined, the degeneration pattern can be attributed to either diffusion or a cascade of localized degeneration. With a limited trial, the 7-day microglia were only M1 positive. The amoeboid morphology was apparent even with a lower dosage.

The microglia activation and retinal degeneration with low dose rotenone will require further studies into the secondary inflammatory signaling pathways. Prime candidates include the NLRP3 pathway, NADPH Oxidase involvement, and bioactivity between 7-14 days. The potential for glial migration from ILM to ONL further implicates the dual role of glia response as critical for both homeostasis and neurodegeneration.

Microglia response to the rotenone-induced ocular toxicity resulted in an early inflammation response, with a delayed neurodegeneration. A unique factor is that the microglia role could be protective to the early neuronal injury but turn neurotoxic if activation is sustained. The lack of an M2 phenotype may be a critical factor in sustained activation and degeneration. The power of this method showed that, through the OCT/OCTA and microglial imaging combination, the retinal inflammation and degeneration can be monitored non-invasively. Where previous studies relied solely on histology, the longitudinal methods reveal the inflammatory to degenerative stages. This is especially important to differentiate between the DMSO and Rotenone toxicity. While in the previous studies the histology indicated day 3 degeneration with the high dose, the in-vivo data indicated that the cytokines should be assessed at days 7 and 14 for low dose neurotoxicity.

6. EXPLORING THE USE OF EXOSOMES AS A BIOMARKER OF RETINAL DYSFUNCTION

6.1. Abstract

In this chapter an optimized methodology to extract and store exosomes from cell cultures of different sources is described which addresses a common problem in the field that traditional exosome isolation methods are not uniform and will alter the size and/or content of the exosomes. As an emergent field, the biological pathways regulated by exosome mediated signaling is not currently understood. With implications for both diagnostic and therapeutic applications, standardized procedures for isolation, storage, and analysis are required.

In these proof-of-concept studies, exosome alterations during oxidative stress are known to alter the inflammatory pathway. Our cell culture results show that photoreceptors (661W cells) secrete more exosomes under stress conditions. In a study of the in-vivo role of exosomes, a blockade of exosome release inhibited CNV inflammation. In a novel therapeutic approach, the systemic administration of the exosome inhibitor (GW4869) blocked the shift to pro-inflammatory signaling via exosome release.

6.2. Introduction

In the biomarker discovery process, exosomes have yielded both significant diagnostic power and significant challenges to the isolation and characterization procedures. The aim of a portion of this study was to determine how to consistently isolate and process exosomes from different biological fluids. Currently, changes to the profile of the content of exosomes in retinal diseases are not fully known. However, early studies suggest RPE cells and microglia can be either pro-inflammatory or neuroprotective.

Astrocytes, as well as normal RPE exosome secretion, have been suspected to be anti-angiogenic.

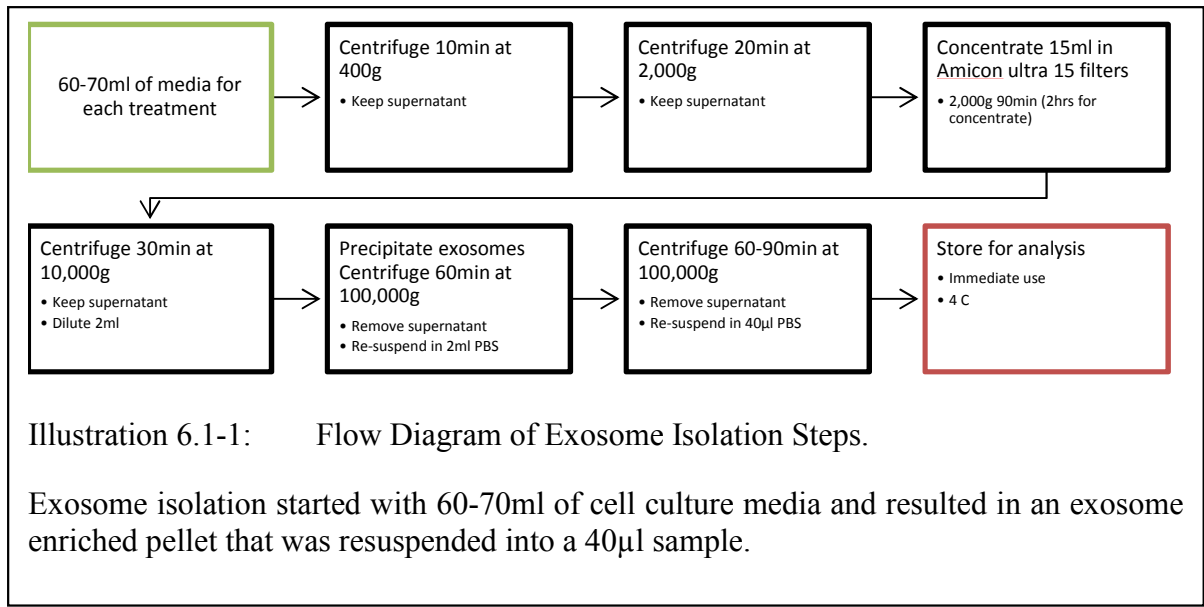
Methods development for exosome characterization is as important as their content profile to basic science research. Ultracentrifugation gradient assays, profiling techniques, and even storage conditions can impact the validity of the results. Through this section, repeatability of experiments and modulation techniques were developed for future studies.

6.3. Isolation and Characterization of Exosomes

Isolation of exosomes from cell culture works on the basic premise that in a fluid environment, exosomes will diffuse into the media and then isolate with established methods for analysis. The current reality is that isolation methods are not uniform and will alter the size and/or content of the exosomes. With this goal in mind, an optimized methodology to extract and store exosomes from cell cultures of different sources was developed. Initial sizing was performed with the Malvern High Performance Particle Sizer (HPPS). Later studies were tested with the Malvern Nanosight NS300 system.

6.3.1. ISOLATION OF EXOSOMES FROM CELL SUPERNATANT

Exosomes from cell supernatant is a common procedure with many alterations and variants²¹⁰⁻²¹². Exosome precipitation kits, such as ExoQuick, yielded impure or non-soluble exosome pellets^{213,214}. Exosomes have been reliably isolated from RPE cell lines, so for protocol development, we utilized the ARPE-19 cell line. With the optimization of each protocol, it was found that ultracentrifugation was the most reliable at yielding an exosome pellet; however, it was likewise the most laborious process.



Using the process for ultracentrifugation, exosome pellets were reliably isolated from cell culture media. A key step in the process was using Amicon ultra 15 filters to concentrate the 2,000g supernatant for the next steps. With the concentration steps, small proteins and aggregates were removed while reducing the volume for resuspension into PBS. When performed carefully, this process reduces the aggregates potential in the final ultracentrifugation. Once pooled and diluted, the first ultracentrifugation of 1h was followed by a wash and then a final 1.5h run for a reliable pellet.

6.3.2. EXOSOMES FROM BLOOD SERUM

Blood is another important biological fluid from which exosomes can be sampled. In the mouse species, the low blood volume yields 0.5-1mL with a cardiac puncture. Using a 22g needle, the cardiac puncture is a reliable method for mice; with larger species, however, non-terminal procedures will yield a sufficient volume. From the cardiac puncture, the whole blood was coagulated, then centrifuged to isolate the plasma (Illustration 6.1-2). With this procedure, each .7mL of blood yielded 200-400µL of serum. After the partial coagulation of the whole blood, the tube was centrifuged at 1k RPM so

that the clear serum would separate. The serum was then removed and diluted into PBS for storage.

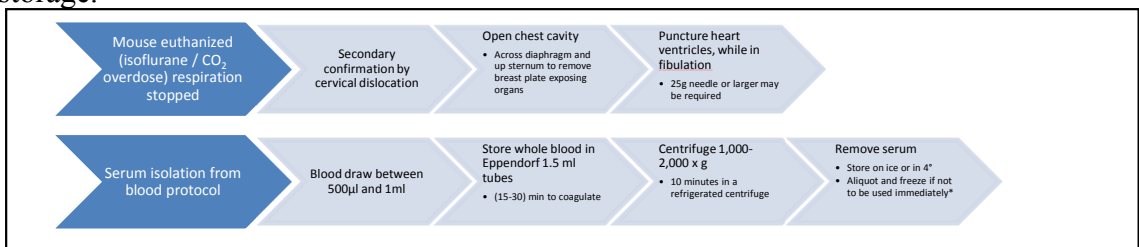


Illustration 6.1-2: Blood Serum Processing

Blood serum was isolated in a manner to preserve the exosomes and microvesicles. From 0.5-1ml of whole blood, 200-400µL of serum could be isolated per mouse. From that fraction, sufficient microvesicles existed for analysis.

Once the serum was collected, a modified ultracentrifugation protocol (Illustration 6.1-3) could be followed. The serum was first spun at low speed to remove cells and then resuspended into PBS. The sequential centrifugation steps result in a pellet in the ultracentrifugation steps. Comparison of the supernatant data before and after the final ultracentrifugation step shows that a large yield remains suspended. Fine tuning the duration final spin up to 2 hours allows for higher recovery of the exosomes but with a potential tradeoff in purity and damage.

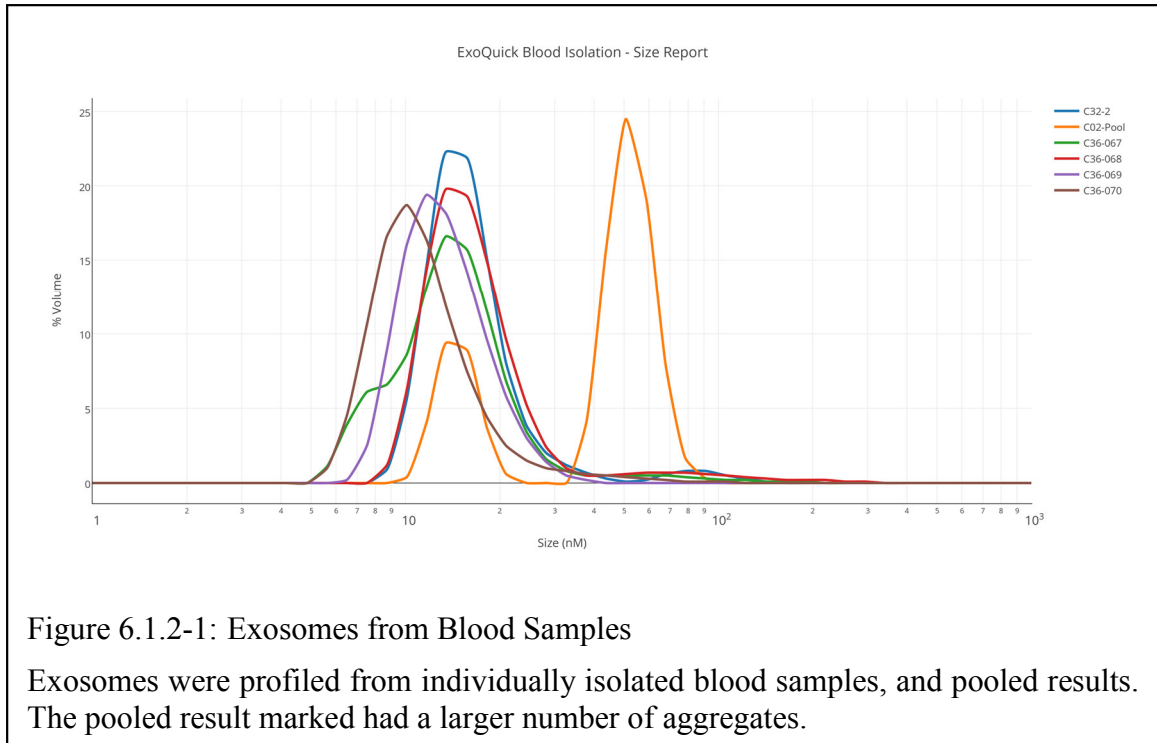
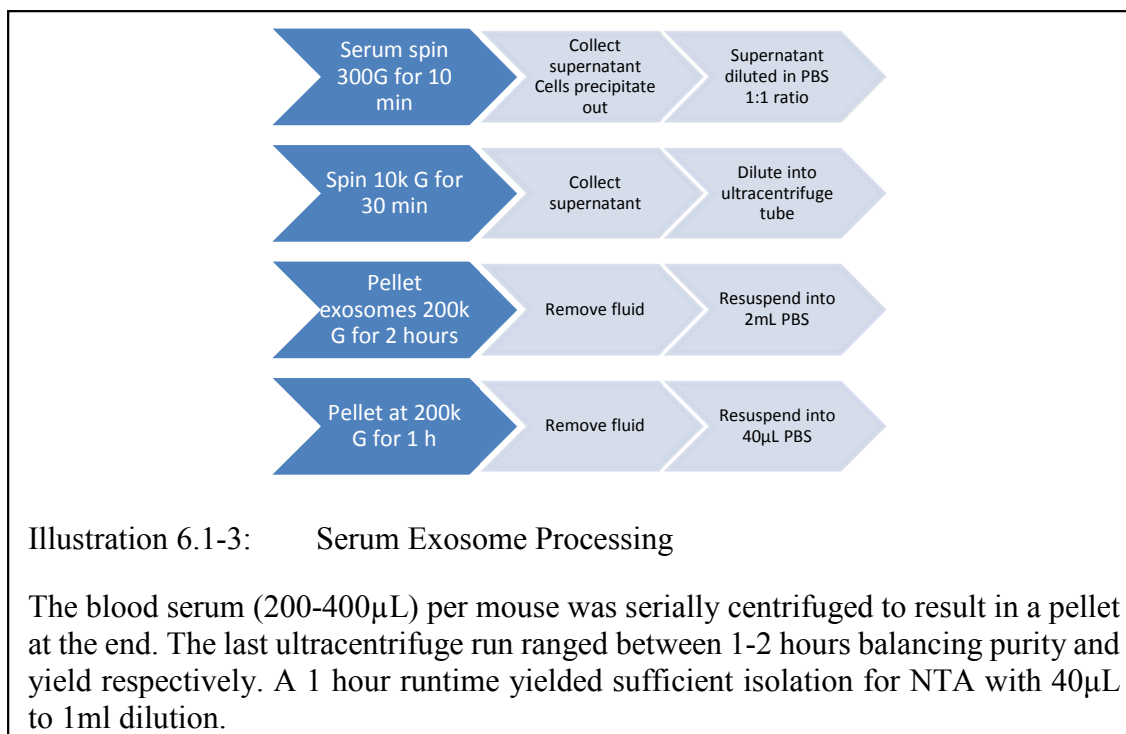


Figure 6.1.2-1: Exosomes from Blood Samples

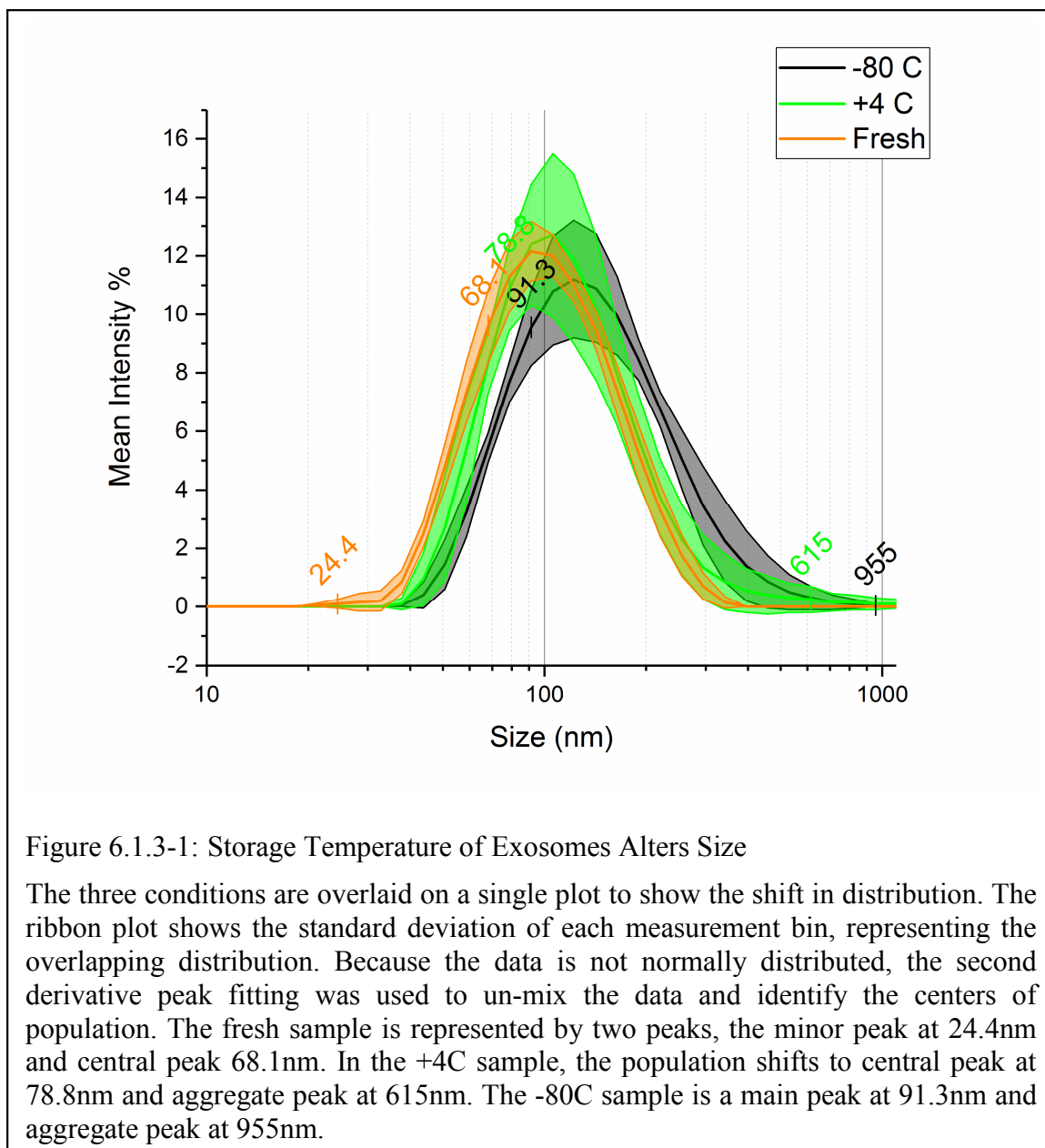
Exosomes were profiled from individually isolated blood samples, and pooled results. The pooled result marked had a larger number of aggregates.

Exosomes isolated from blood were suited for analysis. Each run was analyzed individually using the HPPS system. Each individual blood draw was sized and compared. An additional pooled sample was compared against the source blood draws. The pooled sample appears to contain more aggregates than the individual samples.



6.3.3. STORAGE OF EXOSOMES

In several isolation protocols, freezing exosomes is often recommended if samples cannot be immediately analyzed. However, the initial studies did not assess the potential changes a freeze thaw cycle could have on size and content. While freezing exosomes at -20°/-80°C is often recommended, we found that storage at 4°C was less disruptive. Exosomes were isolated with the centrifugation method developed in section 6.3.1. The sample was aliquoted for each test condition. Except for storage temperature, all other reagents/materials and methods were kept consistent.



With the study, exosomes that were stored at 4°C were more consistent in size and content than fresh samples. All samples stored for longer periods would swelled and fragment. Aggregates above 200µm were common as freezing increased both fragmentation and aggregates in the sample.

6.4. Exosomes in 405nm Stressed 661W Cell Culture

An immortalized photoreceptor cell line, 661W, was utilized for two objectives: A) to demonstrate photoreceptors constitutively release exosomes, and B) to stress that conditions modulate the exosome release. For the retina, exosome release by RPE cells is widely studied for alterations under oxidative stress conditions, switching from anti-angiogenic ($\alpha\beta$ -crystallin release) to pro-angiogenic and inflammatory signaling^{74,80,215}. A particular stressor, near-UV to Blue light, has been shown to cause oxidative damage and exosome secretion in ARPE-19 cells that in turn can be damaging to photoreceptors²¹⁶. The direct effect of blue light oxidative stress on photoreceptors has not been studied, and as previously mentioned, changes to exosome release have not been determined.

6.4.1. CONSTITUTIVE RELEASE

With normal growth conditions until the final 24h incubation in exosome depleted FBS, the 661W cells were healthy and adhered to the plates. A constant of 10 plates were pooled per experimental repetition to harvest a sufficient yield of exosomes. ARPE-19 cells were used as a positive control, as the secretion of exosomes in those cells is already known. Samples were compared to the SAE cells used in the prior isolation and storage experiment²¹⁷.

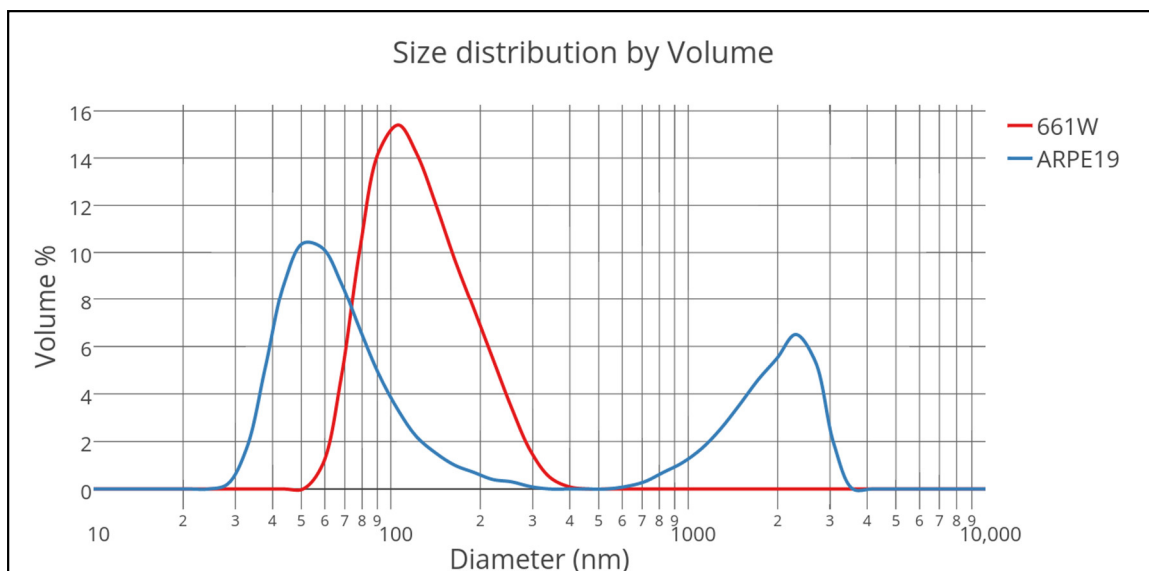


Figure 6.2.1-1: Particle Sizing of Exosomes from 661W Cells and ARPE19 Cells

661W cells produced exosomes with larger average size than ARPE 19 cells. The difference in size was consistent for multiple trials. The only alteration to the 661W cells profile in the subsequent studies was the number of aggregates above 1000nm.

The 661W cells secreted a comparable amount of exosomes to the ARPE 19 cells and the SAE cells. The size distribution, however, demonstrated that the population of microvesicles was unique for each cell type. The peaks of 661W cells are consistent in all experiments. Multimodal distributions can be separated with Gaussian-mixture models. The other alternative method is the NTA tracking with the Malvern NanoSight system.

6.4.2. PHOTOTOXICITY

The cell cultures were grown as the controls, except the final incubation with exosome depleted media which was incubated under 405nm led sources. The 405nm led array was built to provide uniform illumination across each petri dish. The intensity was designed to be adjustable and measured with a photometer before each experiment. The led setup array in Figure 6.2.2-1 provides even illumination. The voltage and distance is adjustable to control light output power.

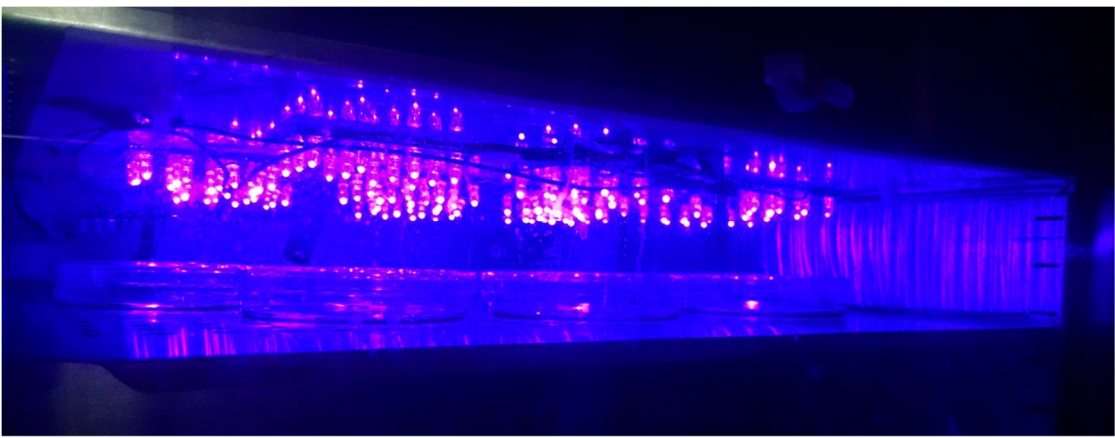


Figure 6.2.2-1: Cell Culture Phototoxicity

An array of 405nm leds were built to evenly illuminate the entire dish. The dosage was controllable by time, and fluency W/M^2 . The distance from the LED to the dish and the voltage were both adjustable to control light output.

Phototoxicity was induced first with $4mw/cm^2$ for 24 hours; this dosage was chosen as it is known for its anti-bacterial effect and ROS damage. The toxicity was assessed with a live-dead assay using phase contrast microscopy, Hoechst 33342 staining of nuclei, and Propidium Iodide (PI) for nuclear permeability. With the 4mw dose, the 661W cell morphology showed clear distress, apoptosis, and cell loss with phase contrast microscopy. With this cell stress, the apoptotic cells formed clusters.

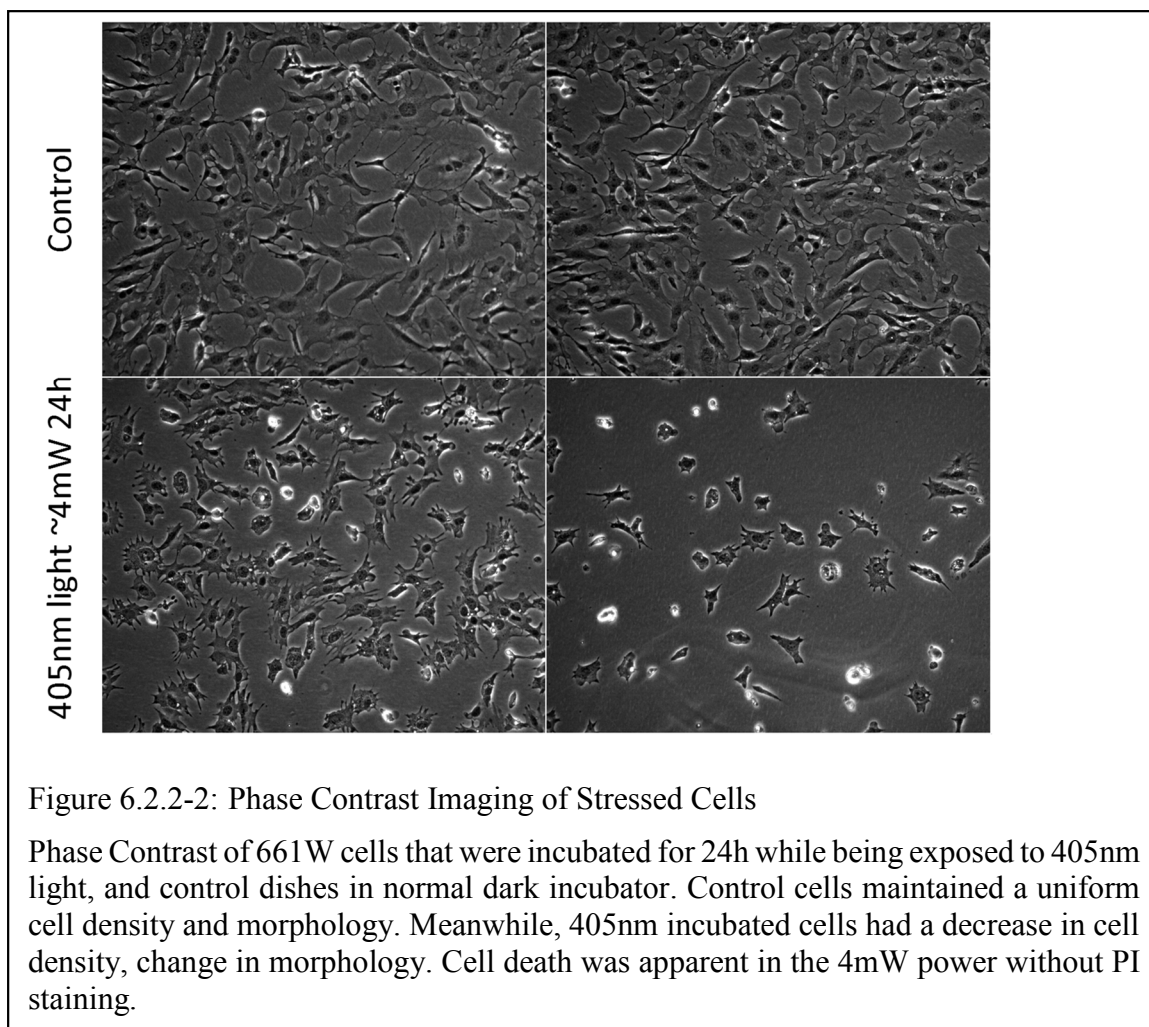


Figure 6.2.2-2: Phase Contrast Imaging of Stressed Cells

Phase Contrast of 661W cells that were incubated for 24h while being exposed to 405nm light, and control dishes in normal dark incubator. Control cells maintained a uniform cell density and morphology. Meanwhile, 405nm incubated cells had a decrease in cell density, change in morphology. Cell death was apparent in the 4mW power without PI staining.

A second dosage of $2\text{mw}/\text{cm}^2$ was used to induce stress without causing cell death. The cells maintained a uniform distribution and density comparable to the control. With the cell cultures exposed, the live dead assay showed that the nuclei, while stressed, were not permeable as seen in the 4mw dose. The Phase Contrast imaging shown in Figure 6.2.2-2 illustrates the phototoxic stress and apoptotic pathway's effect at 4mW. By reducing the power to 2mW, the dosage still induced some apoptosis, however most cells survived. We believe this dose is closer to the clinically relevant exposure.

The HPPS was used to quantify the size distribution profile of the isolated exosomes and plotted in figure 6.2.2-3. With 405nm exposure, the central peak of the exosomes remained between 70-100nm. The average size was 120nm. The control may

consist of three distributions: ~100nm, 120nm and >1000nm. The largest distribution is the aggregates; however, the other two distributions are the populations of interest. For the 405nm treated exosomes, there may be an additional distribution 40-50nm range. Further testing with the NTS system would count the number of exosomes and identify the peaks.

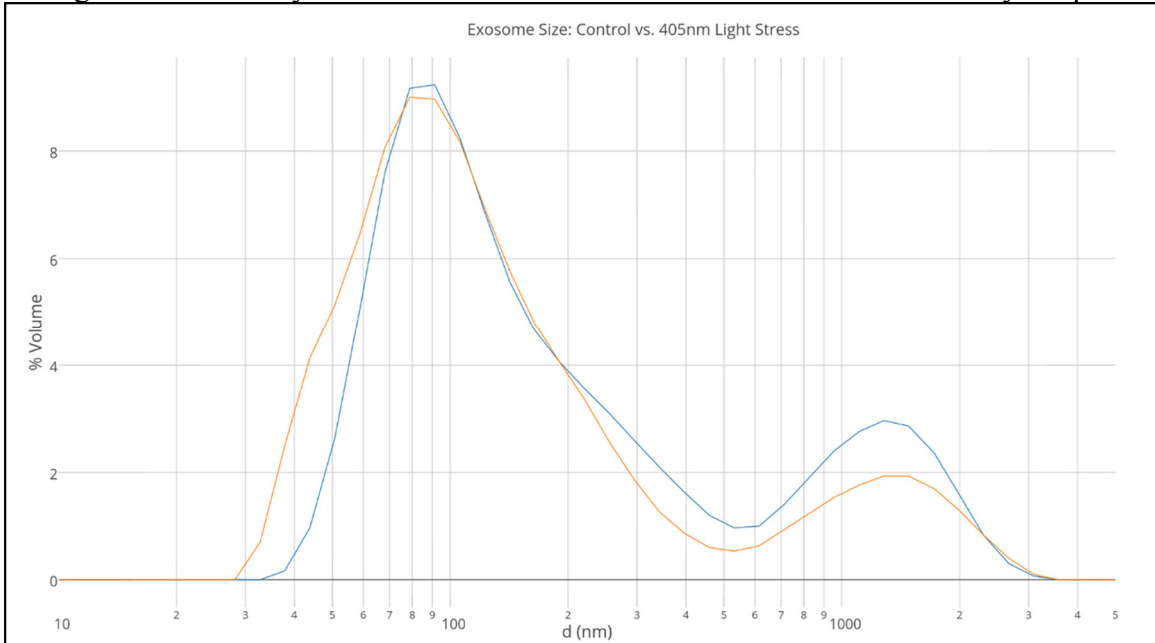
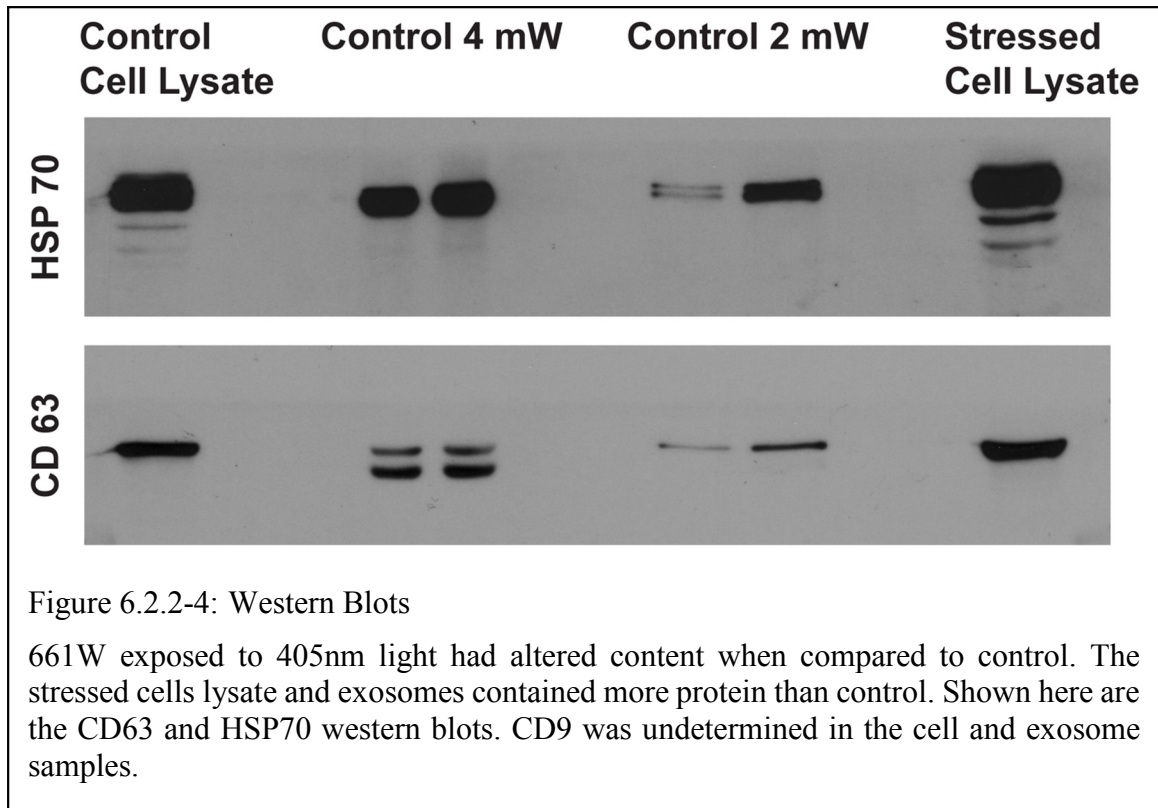


Figure 6.2.2-3: Particle Sizing of Exosomes

661W exposed to 405nm light (orange) had altered size distribution when compared to control (blue). With the peak in between 70-100nm was unchanged, the aggregates and fragments were altered.

Western Blots of the samples show that there was an increase in protein in the samples. CD63 and HSP70 western blots were used as standard markers of exosomes. The 661W exposed to 405nm light had altered protein content when compared to control. The stressed cells lysate and exosomes contained more surface marker proteins than control. CD9 was undetermined in the cell and exosome samples.



Particle Sizing with the HPPS showed an altered distribution of exosome sizes, but no alterations in the peaks. That is, the average size produced does not change, but the content and number released does. The constitutive level of exosome release is below that of the stressed photoreceptors. To understand the state dependent content, Proteomics and mRNA sequencing is required.

6.5. Exosome Inhibition

GW4869 is a non-competitive neutral sphingomyelinase inhibitor. As the MVB is generated from an intracellular vesicle and exosomes from the clathrin coated pit, fusion to the exterior cell membrane is required to release the exosomes. GW4869 inhibits the fusion/release step but not exosome generation^{75,218,219}. In this way, GW4869 inhibits changes to exosome signaling as the content released is cell state dependent. For retinal diseases, it is strongly implicated that exosome signaling is key to maintaining homeostasis of the retina. In theory, exosomes that carry pro-inflammatory or pro-angiogenic signals

would be inhibited. The alternative hypothesis is that exosome inhibition would prevent the proper homeostasis of anti-angiogenic signaling and wound healing response. This inhibition could also disrupt the normal signaling; therefore, control eyes are required to assess the potential for off target effects.

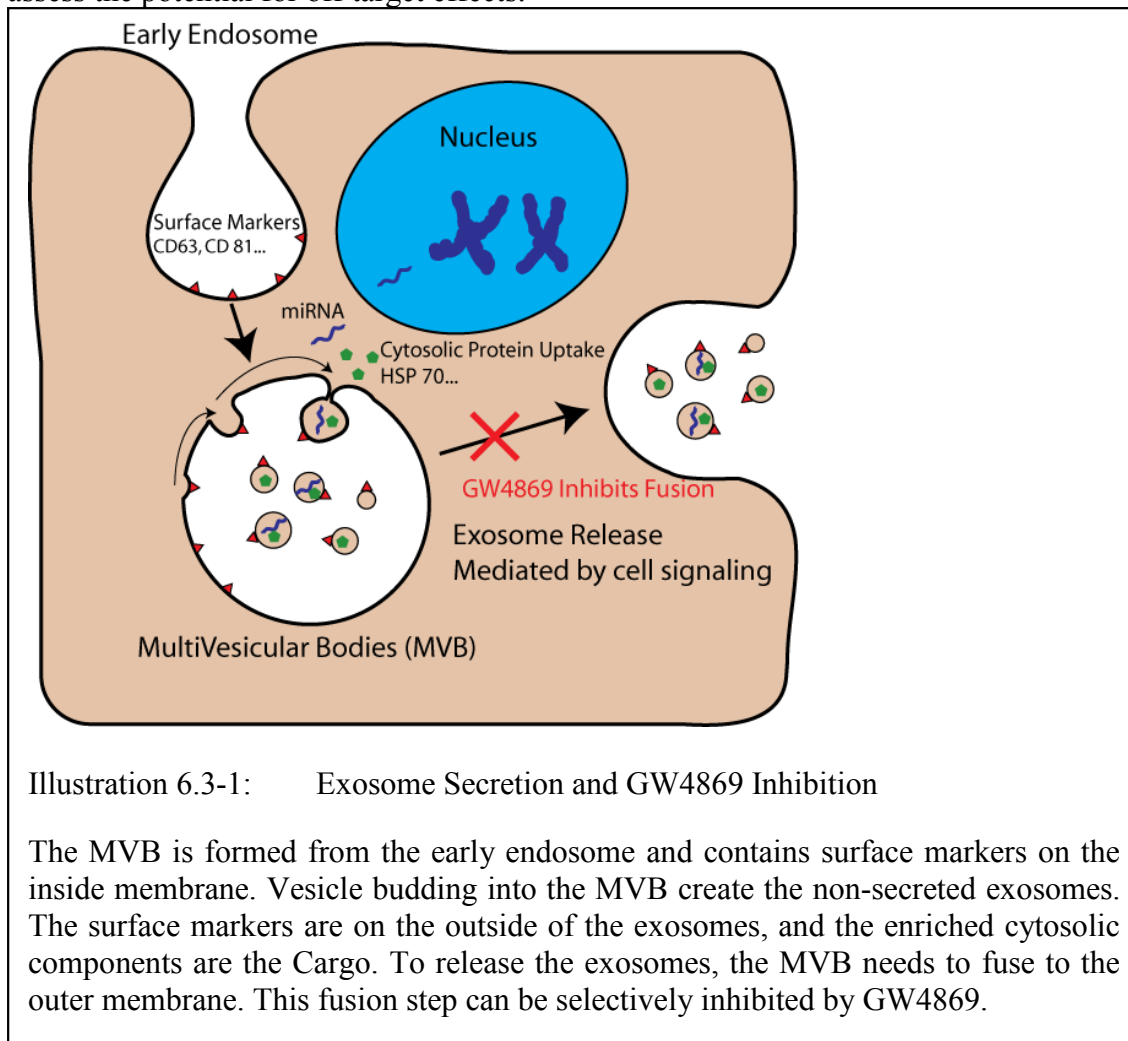


Illustration 6.3-1: Exosome Secretion and GW4869 Inhibition

The MVB is formed from the early endosome and contains surface markers on the inside membrane. Vesicle budding into the MVB create the non-secreted exosomes. The surface markers are on the outside of the exosomes, and the enriched cytosolic components are the Cargo. To release the exosomes, the MVB needs to fuse to the outer membrane. This fusion step can be selectively inhibited by GW4869.

6.5.1. SYSTEMIC ADMINISTRATION

A pilot experiment was designed to determine the effects of exosome inhibition on GW4869. Systemic delivery through interperitoneal injection with as a vehicle (2.5% DMSO dissolved in saline) that was shown to be effective in the literature. The dose of 1.25mg/kg was determined from sources^{75,220,221}.

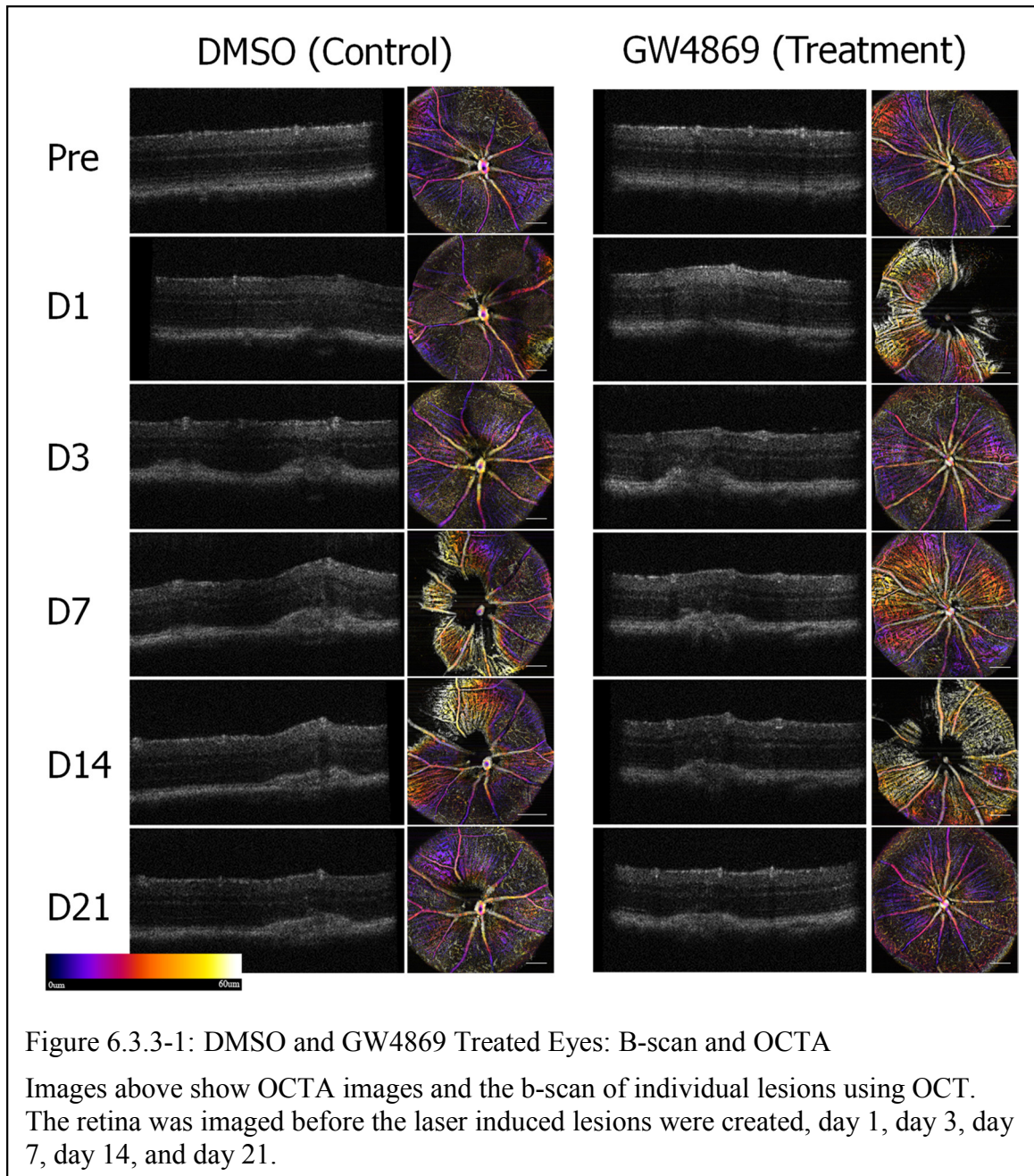
Systemic administration of GW4869 showed no major deficits to animal health when compared to DMSO, and other short periods of systemic administration did not show detrimental effects^{75,222}. Animal health was monitored, and no differences between DMSO and GW4869 were observed.

6.5.2. CONTROL EYE TOXICITY ASSESSMENT

The control eyes were screened for abnormalities. With the screening, there were no obvious deficits in the contralateral eye with either DMSO or GW4869 treatment. While administration may be cytotoxic in higher doses²²³, neither low doses nor systemic administration alters retinal pathology. Given the susceptibility of eyes to neurodegeneration and accumulation of small lipophilic compounds, this finding is encouraging. Through the studies, the control eyes showed no change in morphology or vascular impairment. With longitudinal tracking, there were no associated thinning, vascular impairment, or alteration in autofluorescence foci. Chronic studies may differ; however, two-week daily injections showed no ill effects.

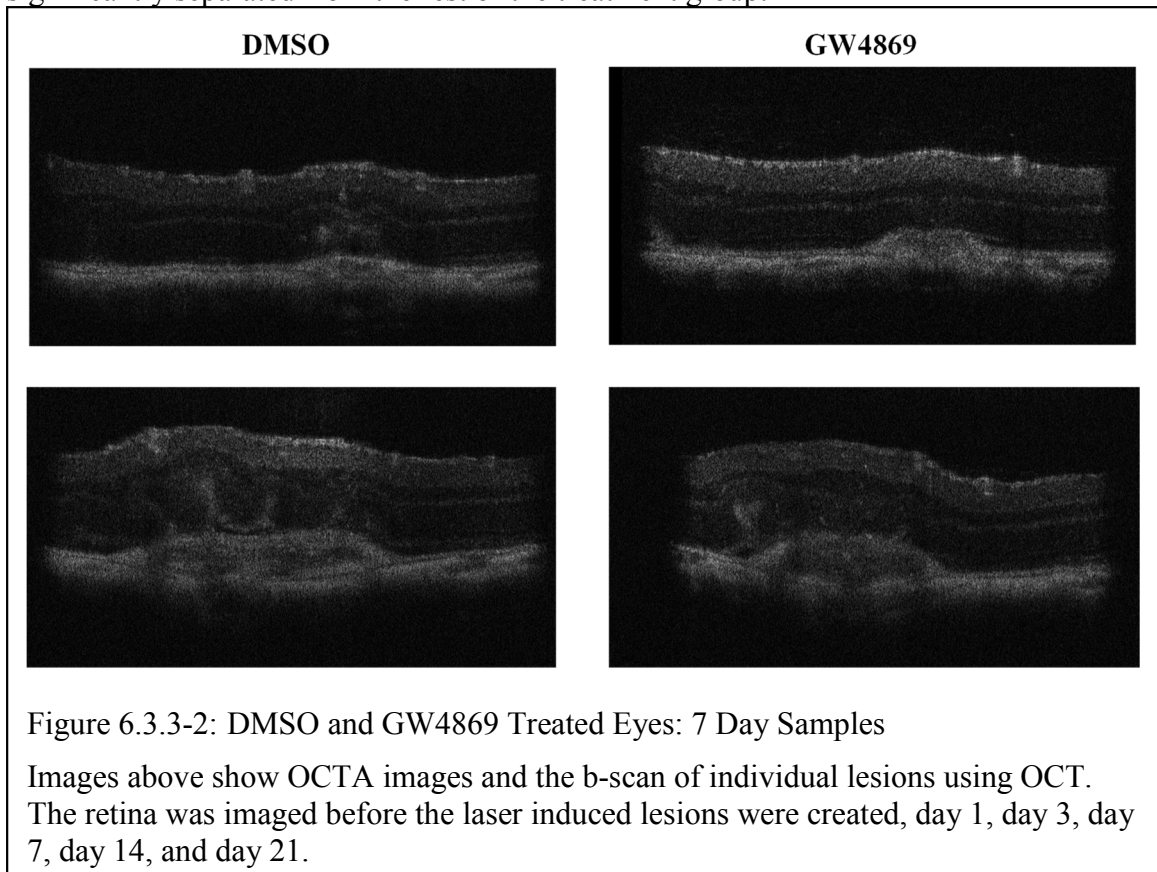
6.5.3. CNV INHIBITION

The retinas were assessed for alterations in the CNV pathology. In the time course of the study, the initial inflammation and subsequent neovascularization was measured *in vivo* following the protocols developed in Chapter 3. The study design put CNV and DMSO sham injections in longitudinal comparison to DMSO/GW4869 treatments. In the study, the dynamics of the lesion growth were altered at both early and late stages.

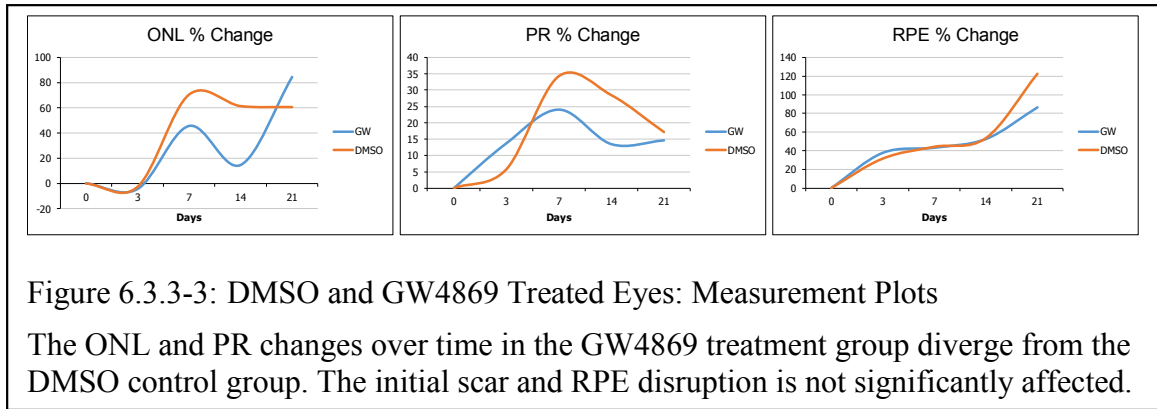


Control DMSO treated subjects showed no alteration to the inflammatory progression than other CNV experiments. Their lesion maturation progressed as expected. The GW4869 treated eyes demonstrated more variable alterations to the wound healing progression. While the most severe DMSO lesions showed bleeding that may match exclusion criteria, the most severe GW4869 lesions were significantly smaller.

Furthermore, the GW treated eyes indicated that the more efficacious treatments were significantly separated from the rest of the treatment group.



The variance in CNV lesion severity is apparent in the two conditions. The B-scans illustrate the edema formation and lesion height alterations. At day 7 the edemas were less numerous and were associated with smaller lesions when GW4869 was compared to DMSO. The B-scans were measured, and results compiled into plots to quantify the changes in lesion dynamics. The lesions were also smaller at 14 days, specifically noticeable in the ONL measurement. The scarring on the RPE was not altered, and FFA would not show the alterations seen through OCT/OCTA.



While preliminary, the data suggest that GW4869 can limit the neuronal damage in CNV. The proposed mechanism is early inflammatory signals cannot be secreted through exosome signaling and damage is limited. In the late stage, GW4869 is a specific inhibitor for nSMases (Neutral Sphingomyelinase) and can inhibit fibrosis. With this study, ERG or specific apoptotic/ROS stress markers need to be assessed. The indication is that the more nerves preserved, the more eyesight may be retained.

6.6. Conclusions

Exosomes are important mediators of cellular communication and are an infant field of research. As further studies progress, the role of exosome signaling during inflammation will be further understood. In our initial studies, exosome alterations during oxidative stress are known to alter the inflammatory pathway. Our cell culture results show that photoreceptors (661W cells) secrete more exosomes under stress conditions. Along with known contributions of RPE cells, the exosome content under stress remains an open question. The systemic administration of the exosome inhibitor (GW4869) blocked the shift to pro-inflammatory signaling via exosome release. The effect of exosome inhibition showed a decrease in damage with CNV induction. In future tests, increased specificity of the exosome inhibition agent and dosage/timing could impart more efficacious results.

7. SUMMARY AND CONCLUSIONS

Throughout this dissertation, the overarching goal is to explore new methodologies in tracking the progression of neuroinflammation and their role in neurodegeneration. The screening methodology presented utilized the non-invasive aspects of the digital biopsy to facilitate longitudinal studies. The exosome isolation research complements the in-vivo imaging by providing a more specific way to design studies for sampling the inflammatory signaling. With the initial methods development, the primary focus was to determine the features of inflammation pathology that were detectable at each stage of the inflammatory progression.

With the use of the in-vivo screening, the pathology in several models was assessed. In the development of the OCTA methodology, the improvements of the projection methods and combined orthographic views allowed visualization of not only the CNV but also alterations to the vascular profusion of the DVP. The microvascular alterations are a previously undescribed pathology of the CNV model. As each of the experiments were performed, the utility of the digital biopsy was apparent by the ability to digitally re-slice or re-process the data to find unexpected pathology. The microvascular disruption in the CNV model and the photoreceptor abnormalities in the rotenone model are both examples of this pathology discovery. The traditional fundus imaging was not sensitive enough to differentiate these alterations from a control eye.

The microglia assessment showed that the acute injuries induced a rapid response. Chronic activation started in each model with a delayed response. For both the CNV and rotenone model, microglia activation was slower to respond or migrate than an acute injury. This delayed activation may suggest the role in inflammation is closer to adaptive immunity. Furthermore, the proliferation of microglia in the laser models is indicative of immune potentiation. The measured response in each lesion varied but was consistent in the shape of the dynamic plots and pathology observed. The variance in both OCT

measurements may be indicative of sub-populations within the dataset. As an inflammatory response, this could be due to prior inflammation or differences in susceptibility.

7.1. Future Directions

Imaging advancements for a digital biopsy would include an integrated platform for multi-modal imaging of neuroinflammation. With the ability to co-register the data, we can develop improved inflammation dynamics models for longitudinal analysis of subpopulations. Potential improvements to OCTA include flow analysis to quantify the velocity of blood flow. Besides quantification, visualization can be improved with orthographic and 3D image fusion, providing more intuitive ways to interpret and explore features of pathology.

Microglial activation in inflammation is still poorly understood in-vivo. One major question this research raises is the effect of M1/M2 activation at day 7 vs 14. Where previous studies relied on terminal endpoints, this assessment asks if microglia in each state are beneficial or detrimental. For each model, activation differs, but the differences highlight how acute inflammation may turn into the chronic activation seen in the CNV model. For future studies, Cytokine expression I.E. TNF- α IL1, IL10, and IL18 are required at the new timepoints to determine inflammatory pathways

Other models of retinal degeneration can benefit from the same methodology. A non-invasive way to assess inflammation in longitudinal studies can help diagnose systemic diseases. An additional benefit is that in using the longitudinal imaging, one subject replaces eight in traditional studies (7 time points). For slow progressing diseases, like PD, this may be a way to assess neurodegeneration and vascular defects.

Finally, repeated “dose” studies using the laser models explored would be useful to examine inflammation potentiation. The inflammation dynamics and microglia activation could help indicate mechanisms that lead to pathogenesis of retinal degeneration in humans.

The theory of inflammation potentiation or priming would suggest that wound healing and microglia response may be exacerbated with repeated doses. With longitudinal studies, these alterations can be assessed without the use of terminal procedures and inferences from large cohorts.

Bibliography

1. Cayrol R, Haqqani AS, Ifergan I, Dodelet-devillers A, Prat A, Walker JM. *The Blood-Brain and Other Neural Barriers*. Vol 686. (Nag S, ed.). Humana Press; 2011. doi:10.1007/978-1-60761-938-3.
2. Ambati J, Anand A, Fernandez S, et al. An animal model of age-related macular degeneration in senescent Ccl-2- or Ccr-2-deficient mice. *Nat Med*. 2003;9(11):1390-1397. doi:10.1038/nm950.
3. Denton ML, Foltz MS, Schuster KJ, Estlack LE, Thomas RJ. Damage thresholds for cultured retinal pigment epithelial cells exposed to lasers at 532 nm and 458 nm. *J Biomed Opt*. 2007;12(3):034030. doi:10.1117/1.2737394.
4. Linsenmeier RA, Zhang HF. Retinal oxygen: from animals to humans. *Prog Retin Eye Res*. 2017;58:115-151. doi:10.1016/j.preteyeres.2017.01.003.
5. Sakai M, Sakai H, Nakamura Y, Fukuchi T, Sawaguchi S. Immunolocalization of heat shock proteins in the retina of normal monkey eyes and monkey eyes with laser-induced glaucoma. *Jpn J Ophthalmol*. 47(1):42-52. <http://www.ncbi.nlm.nih.gov/pubmed/12586177>.
6. Schlamp CL, Montgomery AD, Mac Nair CE, Schuart C, Willmer DJ, Nickells RW. Evaluation of the percentage of ganglion cells in the ganglion cell layer of the rodent retina. *Mol Vis*. 2013;19(March):1387-1396. <http://www.pubmedcentral.nih.gov/articlerender.fcgi?artid=3695759&tool=pmcentrez&rendertype=abstract>.
7. Claybon A, Bishop AJR. Dissection of a mouse eye for a whole mount of the retinal pigment epithelium. *J Vis Exp*. 2011;(48):3-7. doi:10.3791/2563.
8. Dinet V, Bruban J, Chalour N, et al. Distinct effects of inflammation on gliosis, osmohomeostasis, and vascular integrity during amyloid beta-induced retinal degeneration. *Aging Cell*. 2012;11(4):683-693. doi:10.1111/j.1474-9726.2012.00834.x.
9. Li CP, Yao J, Tao ZF, Li XM, Jiang Q, Yan B. Epigallocatechin-gallate (EGCG) regulates autophagy in human retinal pigment epithelial cells: A potential role for reducing UVB light-induced retinal damage. *Biochem Biophys Res Commun*. 2013;438(4):739-745. doi:10.1016/j.bbrc.2013.07.097.
10. Schuele G, Rumohr M, Huettmann G, Brinkmann R. RPE damage thresholds and mechanisms for laser exposure in the microsecond-to-millisecond time regimen. *Investig Ophthalmol Vis Sci*. 2005;46(2):714-719. doi:10.1167/iovs.04-0136.
11. Sparrow J, Duncker T. Fundus Autofluorescence and RPE Lipofuscin in Age-

- Related Macular Degeneration. *J Clin Med*. 2014;3(4):1302-1321. doi:10.3390/jcm3041302.
12. Sobue A, Ito N, Nagai T, et al. Astroglial major histocompatibility complex class I following immune activation leads to behavioral and neuropathological changes. *Glia*. 2018;66(5):1034-1052. doi:10.1002/glia.23299.
 13. Pekny M, Wilhelmsson U, Pekna M. The dual role of astrocyte activation and reactive gliosis. *Neurosci Lett*. 2014;565:30-38. doi:10.1016/j.neulet.2013.12.071.
 14. Hajrasouliha AR, Jiang G, Lu Q, et al. Exosomes from retinal astrocytes contain antiangiogenic components that inhibit laser-induced choroidal neovascularization. *J Biol Chem*. 2013;288(39):28058-28067. doi:10.1074/jbc.M113.470765.
 15. Lückoff A, Scholz R, Sennlaub F, Xu H, Langmann T. Comprehensive analysis of mouse retinal mononuclear phagocytes. *Nat Protoc*. 2017;12(6):1136-1150. doi:10.1038/nprot.2017.032.
 16. Mitchell DM, Lovel AG, Stenkamp DL. Dynamic changes in microglial and macrophage characteristics during degeneration and regeneration of the zebrafish retina. *J Neuroinflammation*. 2018;15(1):1-20. doi:10.1186/s12974-018-1185-6.
 17. Zhao L, Zabel MK, Wang X, et al. Microglial phagocytosis of living photoreceptors contributes to inherited retinal degeneration. *EMBO Mol Med*. 2015;7(9):1179-1197. doi:10.15252/emmm.201505298.
 18. Zhou KK, Benyajati S, Le Y, Cheng R, Zhang W, Ma J-X. Interruption of wnt signaling in müller cells ameliorates ischemia-induced retinal neovascularization. *PLoS One*. 2014;9(10):e108454. doi:10.1371/journal.pone.0108454.
 19. Wang M, Ma W, Zhao L, Fariss RN, Wong WT. Adaptive Müller cell responses to microglial activation mediate neuroprotection and coordinate inflammation in the retina. *J Neuroinflammation*. 2011;8(1):173. doi:10.1186/1742-2094-8-173.
 20. Brunton L. Goodman & Gilman 's The Pharmacological Basis of Therapeutics. In: Bruce C, Knollmann B, eds. *Goodman & Gilman's The Pharmacological Basis of Therapeutics*. ; 2010:417-455.
 21. Hosoya KI, Tachikawa M. Inner blood-retinal barrier transporters: Role of retinal drug delivery. *Pharm Res*. 2009;26(9):2055-2065. doi:10.1007/s11095-009-9930-2.
 22. Fulmer T. Breaching the retinal barrier. *Sci Exch*. 2009;2. doi:10.1038/scibx.2009.1554.
 23. Falavarjani KG, Nguyen QD. Adverse events and complications associated with intravitreal injection of anti-VEGF agents: a review of literature. *Eye (Lond)*. 2013;27(7):787-794. doi:10.1038/eye.2013.107.
 24. Pearls O. How to Give Intravitreal Injections. *EyeNet*.:45-47.
 25. Sampat KM, Garg SJ. Complications of intravitreal injections. *Curr Opin Ophthalmol*. 2010;21:178-183. doi:10.1097/ICU.0b013e328338679a.
 26. Kompella U, Edelhauser H. *Drug Product Development for the Back of the Eye*.;

2011.

<http://books.google.com/books?hl=en&lr=&id=uSquDH4aRwYC&oi=fnd&pg=PR5&dq=Drug+Product+Development+for+the+Back+of+the+Eye&ots=aDPinf3XJ&sig=NgRYvI-q4C-l6hmMjtlYdBYUkg>.

27. Kambhampati SP, Clunies-Ross AJM, Bhutto I, et al. Systemic and intravitreal delivery of dendrimers to activated microglia/macrophage in ischemia/reperfusion mouse retina. *Investig Ophthalmol Vis Sci*. 2015;56(8):4413-4424. doi:10.1167/iovs.14-16250.
28. Xu Q, Kambhampati SP, Kannan RM. Nanotechnology approaches for ocular drug delivery. *Middle East Afr J Ophthalmol*. 2013;20(1):26-37. doi:10.4103/0974-9233.106384.
29. Sahoo SK, Dilnawaz F, Krishnakumar S. Nanotechnology in ocular drug delivery. *Drug Discov Today*. 2008;13(3-4):144-151. doi:10.1016/j.drudis.2007.10.021.
30. Iwase T, Fu J, Yoshida T, et al. Sustained delivery of a HIF-1 antagonist for ocular neovascularization. *J Control Release*. 2013;172(3):625-633. doi:10.1016/j.jconrel.2013.10.008.
31. Iezzi R, Guru BR, Glybina I V., Mishra MK, Kennedy A, Kannan RM. Dendrimer-based targeted intravitreal therapy for sustained attenuation of neuroinflammation in retinal degeneration. *Biomaterials*. 2012;33(3):979-988. doi:10.1016/j.biomaterials.2011.10.010.
32. Lukiw WJ. Coordinate Activation of HIF-1 and NF- B DNA Binding and COX-2 and VEGF Expression in Retinal Cells by Hypoxia. *Invest Ophthalmol Vis Sci*. 2003;44(10):4163-4170. doi:10.1167/iovs.02-0655.
33. Isaacs JS, Jung Y-J, Mimnaugh EG, Martinez A, Cuttitta F, Neckers LM. Hsp90 regulates a von Hippel Lindau-independent hypoxia-inducible factor-1 alpha-degradative pathway. *J Biol Chem*. 2002;277(33):29936-29944. doi:10.1074/jbc.M204733200.
34. Weidemann a, Johnson RS. Biology of HIF-1alpha. *Cell Death Differ*. 2008;15(4):621-627. doi:10.1038/cdd.2008.12.
35. Garayoa M, Martinez A, Lee S. Hypoxia-inducible factor-1 (HIF-1) up-regulates adrenomedullin expression in human tumor cell lines during oxygen deprivation: a possible promotion mechanism of. *Mol* 2000;1(November):848-862. <http://press.endocrine.org/doi/abs/10.1210/mend.14.6.0473>. Accessed November 13, 2014.
36. Yao L, Kan EM, Lu J, et al. Toll-like receptor 4 mediates microglial activation and production of inflammatory mediators in neonatal rat brain following hypoxia: role of TLR4 in hypoxic microglia. *J Neuroinflammation*. 2013;10(1):23. doi:10.1186/1742-2094-10-23.
37. van der Loos CM, Meijer-Jorna LB, Broekmans MEC, et al. Anti-human vascular endothelial growth factor (VEGF) antibody selection for immunohistochemical staining of proliferating blood vessels. *J Histochem Cytochem*. 2010;58(2):109-118. doi:10.1369/jhc.2009.954586.

38. Damani MR, Zhao L, Fontainhas AM, Amaral J, Fariss RN, Wong WT. Age-related alterations in the dynamic behavior of microglia. *Aging Cell*. 2011;10(2):263-276. doi:10.1111/j.1474-9726.2010.00660.x.
39. Ross RJ, Zhou M, Shen D, et al. Immunological protein expression profile in Ccl2/Cx3cr1 deficient mice with lesions similar to age-related macular degeneration. *Exp Eye Res*. 2008;86(4):675-683. doi:10.1016/j.exer.2008.01.014.
40. Karlstetter M, Scholz R, Rutar M, Wong WT, Provis JM, Langmann T. Retinal microglia: Just bystander or target for therapy? *Prog Retin Eye Res*. 2015;45:30-57. doi:10.1016/j.preteyeres.2014.11.004.
41. Flowers A, Bell-Temin H, Jalloh A, Stevens SM, Bickford PC. Proteomic analysis of aged microglia: shifts in transcription, bioenergetics, and nutrient response. *J Neuroinflammation*. 2017;14(1):96. doi:10.1186/s12974-017-0840-7.
42. Peng B, Xiao J, Wang K, So KF, Tipoe GL, Lin B. Suppression of microglial activation is neuroprotective in a mouse model of human retinitis pigmentosa. *J Neurosci*. 2014;34(24):8139-8150. doi:10.1523/jneurosci.5200-13.2014.
43. Kakimura J-I, Kitamura Y, Takata K, et al. Microglial activation and amyloid-beta clearance induced by exogenous heat-shock proteins. *FASEB J*. 2002;16(6):601-603.
44. Gustin A, Kirchmeyer M, Koncina E, et al. NLRP3 inflammasome is expressed and functional in mouse brain microglia but not in astrocytes. *PLoS One*. 2015;10(6):1-19. doi:10.1371/journal.pone.0130624.
45. Bordt EA, Polster BM. NADPH oxidase- and mitochondria-derived reactive oxygen species in proinflammatory microglial activation: A Bipartisan affair? *Free Radic Biol Med*. 2014;76(1):34-46. doi:10.1016/j.freeradbiomed.2014.07.033.
46. Chen M, Xu H. Parainflammation, chronic inflammation, and age-related macular degeneration. *J Leukoc Biol*. 2015;98(5):713-725. doi:10.1189/jlb.3RI0615-239R.
47. Jousseaume AM, Poulaki V, Le ML, et al. A central role for inflammation in the pathogenesis of diabetic retinopathy. *FASEB J*. 2004;18(12):1450-1452. doi:10.1096/fj.03-1476fje.
48. Madeira MH, Boia R, Santos PF, Ambrósio AF, Santiago AR. Contribution of microglia-mediated neuroinflammation to retinal degenerative diseases. *Mediators Inflamm*. 2015;2015. doi:10.1155/2015/673090.
49. Edelman JL, Castro MR. Quantitative image analysis of laser-induced choroidal neovascularization in rat. *Exp Eye Res*. 2000;71(5):523-533. doi:10.1006/exer.2000.0907.
50. Sheets KG, Zhou Y, Ertel MK, et al. Neuroprotectin D1 attenuates laser-induced choroidal neovascularization in mouse. *Mol Vis*. 2010;16(March):320-329. <http://www.pubmedcentral.nih.gov/articlerender.fcgi?artid=2834569&tool=pmcentrez&rendertype=abstract>.
51. Park JR, Choi W, Hong HK, et al. Imaging Laser-Induced Choroidal Neovascularization in the Rodent Retina Using Optical Coherence Tomography

- Angiography. *Investig Ophthalmology Vis Sci.* 2016;57(9):OCT331. doi:10.1167/iovs.15-18946.
52. Bai Y, Dergham P, Nedev H, et al. Chronic and acute models of retinal neurodegeneration TrkA activity are neuroprotective whereas p75NTR activity is neurotoxic through a paracrine mechanism. *J Biol Chem.* 2010;285(50):39392-39400. doi:10.1074/jbc.M110.147801.
 53. Zhou Y, Yoshida S, Kubo Y, et al. Different distributions of M1 and M2 macrophages in a mouse model of laser-induced choroidal neovascularization. *Mol Med Rep.* 2017;15(6):3949-3956. doi:10.3892/mmr.2017.6491.
 54. Block ML, Hong JS. Microglia and inflammation-mediated neurodegeneration: Multiple triggers with a common mechanism. *Prog Neurobiol.* 2005;76(2):77-98. doi:10.1016/j.pneurobio.2005.06.004.
 55. Langmann T. Microglia activation in retinal degeneration. *J Leukoc Biol.* 2007;81(6):1345-1351. doi:10.1189/jlb.0207114.
 56. Li L, Eter N, Heiduschka P. The microglia in healthy and diseased retina. *Exp Eye Res.* 2015;136:116-130. doi:10.1016/j.exer.2015.04.020.
 57. Lee JE, Liang KJ, Fariss RN, Wong WT. Ex vivo dynamic imaging of retinal microglia using time-lapse confocal microscopy. *Investig Ophthalmol Vis Sci.* 2008;49(9):4169-4176. doi:10.1167/iovs.08-2076.
 58. Fernández-Arjona M del M, Grondona JM, Granados-Durán P, Fernández-Llebrecz P, López-Ávalos MD. Microglia Morphological Categorization in a Rat Model of Neuroinflammation by Hierarchical Cluster and Principal Components Analysis. *Front Cell Neurosci.* 2017;11(August):1-22. doi:10.3389/fncel.2017.00235.
 59. Kettenmann H, Hanisch U-K, Noda M, Verkhratsky A. Physiology of microglia. *Physiol Rev.* 2011;91(2):461-553. doi:10.1152/physrev.00011.2010.
 60. Campos M, Amaral J, Becerra SP, Fariss RN. A novel imaging technique for experimental choroidal neovascularization. *Investig Ophthalmol Vis Sci.* 2006;47(12):5163-5170. doi:10.1167/iovs.06-0156.
 61. Lanneau D, Brunet M, Frisan E, Solary E, Fontenay M, Garrido C. Heat shock proteins: essential proteins for apoptosis regulation. *J Cell Mol Med.* 2008;12(3):743-761. doi:10.1111/j.1582-4934.2008.00273.x.
 62. Takayama S, Reed JC, Homma S. Heat-shock proteins as regulators of apoptosis. *Oncogene.* 2003;22(56):9041-9047. doi:10.1038/sj.onc.1207114.
 63. Stocki P, Dickinson AM. The immunosuppressive activity of heat shock protein 70. *Autoimmune Dis.* 2012;2012:617213. doi:10.1155/2012/617213.
 64. Wilhelmus MMM, De Waal RMW, Verbeek MM. Heat shock proteins and amateur chaperones in amyloid-beta accumulation and clearance in Alzheimer's disease. *Mol Neurobiol.* 2007;35(3):203-216. doi:10.1007/s12035-007-0029-7.
 65. Windisch BK, LeVatte TL, Archibald ML, Chauhan BC. Induction of heat shock proteins 27 and 72 in retinal ganglion cells after acute pressure-induced ischaemia.

- Clin Experiment Ophthalmol.* 2009;37(3):299-307. doi:10.1111/j.1442-9071.2009.02032.x.
66. Li Y. Retinal Preconditioning and the Induction of Heat-Shock Protein 27. *Invest Ophthalmol Vis Sci.* 2003;44(3):1299-1304. doi:10.1167/iovs.02-0235.
 67. Takata K, Kitamura Y, Tsuchiya D, Kawasaki T, Taniguchi T, Shimohama S. Heat shock protein-90-induced microglial clearance of exogenous amyloid- β 1-42 in rat hippocampus in vivo. *Neurosci Lett.* 2003;344(2):87-90. doi:10.1016/S0304-3940(03)00447-6.
 68. Ou J, Tan M, Xie A, Yu J, Tan L. Heat Shock Protein 90 in Alzheimer 's Disease. 2014;2014:6-8.
 69. Lu R, Tan M, Wang H, Xie A, Yu J, Tan L. Heat Shock Protein 70 in Alzheimer 's Disease. 2014;2014.
 70. Nahomi RB, Palmer A, Green KM, Fort PE, Nagaraj RH. Pro-inflammatory cytokines downregulate Hsp27 and cause apoptosis of human retinal capillary endothelial cells. *Biochim Biophys Acta.* 2014;1842(2):164-174. doi:10.1016/j.bbadis.2013.11.011.
 71. EL Andaloussi S, Mäger I, Breakefield XO, Wood MJ a. Extracellular vesicles: biology and emerging therapeutic opportunities. *Nat Rev Drug Discov.* 2013;12(5):347-357. doi:10.1038/nrd3978.
 72. Lakkaraju A, Rodriguez-Boulan E. Itinerant exosomes: emerging roles in cell and tissue polarity. *Trends Cell Biol.* 2008;18(5):199-209. doi:10.1016/j.tcb.2008.03.002.
 73. Svensson KJ, Christianson HC, Wittrup A, et al. Exosome uptake depends on ERK1/2-heat shock protein 27 signaling and lipid raft-mediated endocytosis negatively regulated by caveolin-1. *J Biol Chem.* 2013;288(24):17713-17724. doi:10.1074/jbc.M112.445403.
 74. Bhat SP, Gangalum RK. Secretion of α B-Crystallin via exosomes: New clues to the function of human retinal pigment epithelium. *Commun Integr Biol.* 2011;4(6):739-741. doi:10.4161/cib.4.6.17610.
 75. Essandoh K, Yang L, Wang X, et al. Blockade of exosome generation with GW4869 dampens the sepsis-induced inflammation and cardiac dysfunction. *Biochim Biophys Acta - Mol Basis Dis.* 2015;1852(11):2362-2371. doi:10.1016/j.bbadis.2015.08.010.
 76. Wei M, Xin P, Li S, et al. Repeated remote ischemic preconditioning protects against adverse left ventricular remodeling and improves survival in a rat model of myocardial infarction. *Circ Res.* 2011;108(10):1220-1225. doi:10.1161/CIRCRESAHA.110.236190.
 77. Giricz Z, Varga Z V, Baranyai T, et al. Cardioprotection by remote ischemic preconditioning of the rat heart is mediated by extracellular vesicles. *J Mol Cell Cardiol.* 2014;68:75-78. doi:10.1016/j.yjmcc.2014.01.004.
 78. Rajendran L, Honsho M, Zahn TR, et al. Alzheimer's disease beta-amyloid

- peptides are released in association with exosomes. *Proc Natl Acad Sci U S A*. 2006;103(30):11172-11177. doi:10.1073/pnas.0603838103.
79. Fiandaca MS, Kapogiannis D, Mapstone M, et al. Identification of preclinical Alzheimer's disease by a profile of pathogenic proteins in neurally derived blood exosomes: A case-control study. *Alzheimer's Dement*. 2014;11(6):1-8. doi:10.1016/j.jalz.2014.06.008.
 80. Sreekumar PG, Kannan R, Kitamura M, et al. α B crystallin is apically secreted within exosomes by polarized human retinal pigment epithelium and provides neuroprotection to adjacent cells. *PLoS One*. 2010;5(10). doi:10.1371/journal.pone.0012578.
 81. Théry C, Amigorena S. Isolation and characterization of exosomes from cell culture supernatants and biological fluids. *Curr Protoc ...* 2006:1-29. <http://onlinelibrary.wiley.com/doi/10.1002/0471143030.cb0322s30/full>. Accessed December 7, 2014.
 82. van Dommelen SM, Vader P, Lakhil S, et al. Microvesicles and exosomes: opportunities for cell-derived membrane vesicles in drug delivery. *J Control Release*. 2012;161(2):635-644. doi:10.1016/j.jconrel.2011.11.021.
 83. Hood J, Pan H, Lanza G, Wickline S. Paracrine induction of endothelium by tumor exosomes. *Lab Invest*. 2009;89(11):1317-1328. doi:10.1038/labinvest.2009.94.Paracrine.
 84. Takeuchi T, Suzuki M, Fujikake N, et al. Intercellular chaperone transmission via exosomes contributes to maintenance of protein homeostasis at the organismal level. *Proc Natl Acad Sci U S A*. 2015;112(19):E2497-506. doi:10.1073/pnas.1412651112.
 85. Suetsugu A, Honma K, Saji S, Moriwaki H, Ochiya T, Hoffman RM. Imaging exosome transfer from breast cancer cells to stroma at metastatic sites in orthotopic nude-mouse models. *Adv Drug Deliv Rev*. 2013;65(3):383-390. doi:10.1016/j.addr.2012.08.007.
 86. Ng YH, Rome S, Jalabert A, et al. Endometrial Exosomes/Microvesicles in the Uterine Microenvironment: A New Paradigm for Embryo-Endometrial Cross Talk at Implantation. *PLoS One*. 2013;8(3). doi:10.1371/journal.pone.0058502.
 87. Hui F, Nguyen CTO, Bedgood P a., et al. Quantitative Spatial and Temporal Analysis of Fluorescein Angiography Dynamics in the Eye. *PLoS One*. 2014;9(11):e111330. doi:10.1371/journal.pone.0111330.
 88. Wigg JP, Zhang H, Yang D. A Quantitative and Standardized Method for the Evaluation of Choroidal Neovascularization Using MICRON III Fluorescein Angiograms in Rats. *PLoS One*. 2015;10(5):e0128418. doi:10.1371/journal.pone.0128418.
 89. Ha SO, Kim DY, Sohn CH, Lim KS. Anaphylaxis caused by intravenous fluorescein: Clinical characteristics and review of literature. *Intern Emerg Med*. 2014;9(3):325-330. doi:10.1007/s11739-013-1019-6.

90. Boretzky A, Mirza S, Khan F, Motamedi M, van Kuijk FJGM. High-resolution multimodal imaging of multiple evanescent white dot syndrome. *Ophthalmic Surg Lasers Imaging Retina*. 2013;44(3):296-300. doi:10.3928/23258160-20130503-18.
91. Rossberger S, Ach T, Best G, Cremer C, Heintzmann R, Dithmar S. High-resolution imaging of autofluorescent particles within drusen using structured illumination microscopy. *Br J Ophthalmol*. 2013;97(4):518-523. doi:10.1136/bjophthalmol-2012-302350.
92. Lau T, Wong IY, Iu L, et al. En-face optical coherence tomography in the diagnosis and management of age-related macular degeneration and polypoidal choroidal vasculopathy. *Indian J Ophthalmol*. 2015;63(5):378-383. doi:10.4103/0301-4738.159860.
93. Wolff B, Matet A, Vasseur V, Sahel JA, Mauget-Faÿsse M. En face OCT imaging for the diagnosis of outer retinal tubulations in age-related macular degeneration. *J Ophthalmol*. 2012;2012. doi:10.1155/2012/542417.
94. Inoue M, Jung JJ, Balaratnasingam C, et al. A Comparison Between Optical Coherence Tomography Angiography and Fluorescein Angiography for the Imaging of Type 1 Neovascularization. *Invest Ophthalmol Vis Sci*. 2016:1-3. doi:10.1167/iovs.15-18900.
95. Spaide RF, Klancnik JM, Cooney MJ, et al. Volume-Rendering Optical Coherence Tomography Angiography of Macular Telangiectasia Type 2. *Ophthalmology*. 2015;122(11):2261-2269. doi:10.1016/j.ophtha.2015.07.025.
96. Costanzo E, Miere A, Querques G, Capuano V, Jung C, Souied EH. Type 1 Choroidal Neovascularization Lesion Size: Indocyanine Green Angiography Versus Optical Coherence Tomography Angiography. *Investig Ophthalmology Vis Sci*. 2016;57(9):OCT307. doi:10.1167/iovs.15-18830.
97. Cole ED, Novais EA, Louzada RN, et al. Visualization of Changes in the Choriocapillaris, Choroidal Vessels, and Retinal Morphology After Focal Laser Photocoagulation Using OCT Angiography. *Investig Ophthalmology Vis Sci*. 2016;57(9):OCT356. doi:10.1167/iovs.15-18473.
98. Giannakaki-Zimmermann H, Kokona D, Wolf S, Ebnetter A, Zinkernagel MS. Optical Coherence Tomography Angiography in Mice: Comparison with Confocal Scanning Laser Microscopy and Fluorescein Angiography. *Transl Vis Sci Technol*. 2016;5(4):11. doi:10.1167/tvst.5.4.11.
99. Zhi Z, Chao JR, Wietecha T, Hudkins KL, Alpers CE, Wang RK. Noninvasive imaging of retinal morphology and microvasculature in obese mice using optical coherence tomography and optical microangiography. *Investig Ophthalmol Vis Sci*. 2014;55(2):1024-1030. doi:10.1167/iovs.13-12864.
100. Park JR, Choi W, Hong HK, et al. Imaging Laser-Induced Choroidal Neovascularization in the Rodent Retina Using Optical Coherence Tomography Angiography. *Investig Ophthalmology Vis Sci*. 2016;57(9):OCT331. doi:10.1167/iovs.15-18946.
101. Alnawaiseh M, Rosentreter A, Hillmann A, et al. OCT angiography in the mouse:

- A novel evaluation method for vascular pathologies of the mouse retina. *Exp Eye Res.* 2016;145:417-423. doi:10.1016/j.exer.2016.02.012.
102. Zhi Z, Yin X, Dziennis S, et al. Optical microangiography of retina and choroid and measurement of total retinal blood flow in mice. *Biomed Opt Express.* 2012;3(11):2976. doi:10.1364/BOE.3.002976.
 103. Gao SS, Jia Y, Zhang M, et al. Optical Coherence Tomography Angiography. *Investig Ophthalmology Vis Sci.* 2016;57(9):OCT27. doi:10.1167/iovs.15-19043.
 104. Pechauer AD, Tan O, Liu L, et al. Retinal Blood Flow Response to Hyperoxia Measured With En Face Doppler Optical Coherence Tomography. *Investig Ophthalmology Vis Sci.* 2016;57(9):OCT141. doi:10.1167/iovs.15-18917.
 105. Hong YJ, Makita S, Ju MJ, Lee BH, Miura M, Yasuno Y. Non-invasive three-dimensional angiography of human eye by Doppler optical coherence tomography. *2011 Int Quantum Electron Conf, IQEC 2011 Conf Lasers Electro-Optics, CLEO Pacific Rim 2011 Inc Australas Conf Opt Lasers Spectrosc Aust Conf.* 2011;(September):769-771. doi:10.1109/IQEC-CLEO.2011.6194122.
 106. Mo S, Krawitz B, Efstathiadis E, et al. Imaging Foveal Microvasculature: Optical Coherence Tomography Angiography Versus Adaptive Optics Scanning Light Ophthalmoscope Fluorescein Angiography. *Investig Ophthalmology Vis Sci.* 2016;57(9):OCT130. doi:10.1167/iovs.15-18932.
 107. Alonso-Caneiro D, Read S a., Collins MJ. Speckle reduction in optical coherence tomography imaging by affine-motion image registration. *J Biomed Opt.* 2011;16:116027. doi:10.1117/1.3652713.
 108. Mayer M a, Borsdorf A, Wagner M, Hornegger J, Mardin CY, Tornow RP. Wavelet denoising of multiframe optical coherence tomography data. *Biomed Opt Express.* 2012;3(3):572-589. doi:10.1364/BOE.3.000572.
 109. Jia Y, Bailey ST, Hwang TS, et al. Quantitative optical coherence tomography angiography of vascular abnormalities in the living human eye. *Proc Natl Acad Sci.* 2015:201500185. doi:10.1073/pnas.1500185112.
 110. Ang M, Cai Y, Shahipasand S, et al. En face optical coherence tomography angiography for corneal neovascularisation. *Br J Ophthalmol.* 2015:bjophthalmol-2015-307338. doi:10.1136/bjophthalmol-2015-307338.
 111. Choi B, Kang NM, Nelson JS. Laser speckle imaging for monitoring blood flow dynamics in the in vivo rodent dorsal skin fold model. *Microvasc Res.* 2004;68(2):143-146. doi:10.1016/j.mvr.2004.04.003.
 112. Liu Q, Chen S, Soetikno B, Liu W, Tong S, Zhang H. Monitoring acute stroke in mouse model using laser speckle imaging-guided visible-light optical coherence tomography. *IEEE Trans Biomed Eng.* 2017;9294(c):1-1. doi:10.1109/TBME.2017.2706976.
 113. Mahmud MS. Speckle Variance Optical Coherence Tomography (svOCT). 2013.
 114. Shi W, Gao W, Chen C, Yang VXD. Differential standard deviation of log-scale intensity based optical coherence tomography angiography. *J Biophotonics.*

- 2017;10(12):1597-1606. doi:10.1002/jbio.201600264.
115. Wang J, Zhang M, Hwang TS, et al. Reflectance-based projection-resolved optical coherence tomography angiography [Invited] ". *Biomed Opt Express*. 2015;112(3):2395-2402. doi:10.1364/BOE.8.001536.
 116. Lee P, Chan C, Huang S, Chen A, Chen HH. Extracting Blood Vessels from Full-Field OCT Data of Human Skin by Short-Time RPCA. *IEEE Trans Med Imaging*. 2018;0062(c). doi:10.1109/TMI.2018.2834386.
 117. Le N, Song S, Zhang Q, Wang RK. Robust principal component analysis in optical micro-angiography. *Quant Imaging Med Surg*. 2017;7(6):654-667. doi:10.21037/qims.2017.12.05.
 118. Spaide RF, Klancnik JM, Cooney MJ. Retinal Vascular Layers Imaged by Fluorescein Angiography and Optical Coherence Tomography Angiography. *JAMA Ophthalmol*. 2014;10022(1):45-50. doi:10.1001/jamaophthalmol.2014.3616.
 119. Xiao M, Zou C, Sheppard K, Krebs M. OCT Image Stack Alignment: one more important preprocessing step. *BioImage Informatics Conf*. 2015:3-5.
 120. de Carlo TE, Romano A, Waheed NK, Duker JS. A review of optical coherence tomography angiography (OCTA). *Int J Retin Vitre*. 2015;1(1):5. doi:10.1186/s40942-015-0005-8.
 121. Chen C-L, Wang RK. Optical coherence tomography based angiography [Invited]. *Biomed Opt Express*. 2017;8(2):1056. doi:10.1364/BOE.8.001056.
 122. Sherfuddin M, Vijay K, Prashanthi HMG, Sathya G. Skeletonization of 3D Images using 2.5D and 3D Algorithms. 2015;(September):4-5.
 123. Liu W, Luisi J, Liu H, Motamedi M, Zhang W. OCT-Angiography for noninvasive monitoring of neuronal and vascular structure in mouse retina: Implication for characterization of retina neurovascular coupling. *EC Ophthalmol*. 2017;3(2017):89-98.
 124. Nussenblatt RB, Ferris F. Age-related Macular Degeneration and the Immune Response: Implications for Therapy. *Am J Ophthalmol*. 2007;144(4). doi:10.1016/j.ajo.2007.06.025.
 125. Cuenca N, Fernández-Sánchez L, Campello L, et al. Cellular responses following retinal injuries and therapeutic approaches for neurodegenerative diseases. *Prog Retin Eye Res*. 2014;43(July):1-59. doi:10.1016/j.preteyeres.2014.07.001.
 126. Ding X, Patel M, Chan C-C. Molecular pathology of age-related macular degeneration. *Prog Retin Eye Res*. 2009;28(1):1-18. doi:10.1016/j.preteyeres.2008.10.001.
 127. Shah RS, Soetikno BT, Lajko M, Fawzi AA. A Mouse Model for Laser-induced Choroidal Neovascularization. *J Vis Exp*. 2015;(106):1-7. doi:10.3791/53502.
 128. Tode J, Richert E, Koinzer S, et al. Thermal Stimulation of the Retina Reduces Bruch's Membrane Thickness in Age Related Macular Degeneration Mouse

- Models. *Transl Vis Sci Technol*. 2018;7(3).
129. Shi X, Semkova I, Mütther PS, Dell S, Kociok N, Jousseaume AM. Inhibition of TNF- α reduces laser-induced choroidal neovascularization. *Exp Eye Res*. 2006;83(6):1325-1334. doi:10.1016/j.exer.2006.07.007.
 130. Nonaka A, Kiryu J, Tsujikawa A, et al. Inflammatory response after scatter laser photocoagulation in nonphotocoagulated retina. *Investig Ophthalmol Vis Sci*. 2002;43(4):1204-1209.
 131. She H, Li X, Yu W. Subthreshold transpupillary thermotherapy of the retina and experimental choroidal neovascularization in a rat model. *Graefes Arch Clin Exp Ophthalmol*. 2006;244(9):1143-1151. doi:10.1007/s00417-005-0042-3.
 132. Park YG, Kim EY, Roh YJ. Laser-based strategies to treat diabetic macular edema: History and new promising therapies. *J Ophthalmol*. 2014;2014. doi:10.1155/2014/769213.
 133. Brinkmann R, Roider J, Birngruber R. Selective retina therapy (SRT): a review on methods, techniques, preclinical and first clinical results. *Bull Soc Belge Ophthalmol*. 2006;(302):51-69.
 134. Koinzer S, Hesse C, Caliebe A, et al. Photocoagulation in rabbits: Optical coherence tomographic lesion classification, wound healing reaction, and retinal temperatures. *Lasers Surg Med*. 2013;45(7):427-436. doi:10.1002/lsm.22163.
 135. Chidlow G, Shabeeb O, Plunkett M, Casson RJ, Wood JPM. Glial cell and inflammatory responses to retinal laser treatment: Comparison of a conventional photocoagulator and a novel, 3-nanosecond pulse laser. *Investig Ophthalmol Vis Sci*. 2013;54(3):2319-2332. doi:10.1167/iovs.12-11204.
 136. Ohkoshi K, Tsuiki E, Kitaoka T, Yamaguchi T. Visualization of subthreshold micropulse diode laser photocoagulation by scanning laser ophthalmoscopy in the retro mode. *Am J Ophthalmol*. 2010;150(6):856-862.e2. doi:10.1016/j.ajo.2010.06.022.
 137. Ohkoshi K, Yamaguchi T. Subthreshold Micropulse Diode Laser Photocoagulation for Diabetic Macular Edema in Japanese Patients. *Am J Ophthalmol*. 2010;149(1):133-139.e1. doi:10.1016/j.ajo.2009.08.010.
 138. Knott EJ, Sheets KG, Zhou Y, Gordon WC, Bazan NG. Spatial correlation of mouse photoreceptor-RPE thickness between SD-OCT and histology. *Exp Eye Res*. 2011;92(2):155-160. doi:10.1016/j.exer.2010.10.009.
 139. Berger A, Cavallero S, Dominguez E, et al. Spectral-domain optical coherence tomography of the rodent eye: Highlighting layers of the outer retina using signal averaging and comparison with histology. *PLoS One*. 2014;9(5). doi:10.1371/journal.pone.0096494.
 140. Zhang P, Zam A, Jian Y, et al. In vivo wide-field multispectral scanning laser ophthalmoscopy-optical coherence tomography mouse retinal imager: longitudinal imaging of ganglion cells, microglia, and Müller glia, and mapping of the mouse retinal and choroidal vasculature. *J Biomed Opt*. 2015;20(12):126005.

doi:10.1117/1.JBO.20.12.126005.

141. Luttrull JK, Musch DC, Spink CA. Subthreshold diode micropulse panretinal photocoagulation for proliferative diabetic retinopathy. *Eye*. 2008;22(5):607-612. doi:10.1038/sj.eye.6702725.
142. Wilkinson CP, Ferris FL, Klein RE, et al. Proposed international clinical diabetic retinopathy and diabetic macular edema disease severity scales. *Ophthalmology*. 2003;110(9):1677-1682. doi:10.1016/S0161-6420(03)00475-5.
143. Gong Y, Li J, Sun Y, et al. Optimization of an Image-Guided Laser-Induced Choroidal Neovascularization Model in Mice. *PLoS One*. 2015;10(7):e0132643. doi:10.1371/journal.pone.0132643.
144. Boretsky A, Motamedi M, Bell B, van Kuijk F. Quantitative evaluation of retinal response to laser photocoagulation using dual-wavelength fundus autofluorescence imaging in a small animal model. *Investig Ophthalmol Vis Sci*. 2011;52(9):6300-6307. doi:10.1167/iovs.10-7033.
145. Lambert V, Lecomte J, Hansen S, et al. Laser-induced choroidal neovascularization model to study age-related macular degeneration in mice. *Nat Protoc*. 2013;8(11):2197-2211. doi:10.1038/nprot.2013.135.
146. Wang H, Han X, Wittchen ES, Hartnett ME. TNF-alpha mediates choroidal neovascularization by upregulating VEGF expression in RPE through ROS-dependent beta-catenin activation. *Mol Vis*. 2016;22(November 2015):116-128.
147. Augustin M, Fialov?? S, Himmel T, et al. Multi-functional OCT enables longitudinal study of retinal changes in a VLDLR knockout mouse model. *PLoS One*. 2016;11(10):1-20. doi:10.1371/journal.pone.0164419.
148. Ang JIEW, Hang MIAOZ, Wang THSH, et al. Reflectance-based projection-resolved optical coherence tomography angiography [Invited]. 2017;8(3):1536-1548.
149. Rojas M, Zhang W, Lee DL, et al. Role of IL-6 in angiotensin II-induced retinal vascular inflammation. *Investig Ophthalmol Vis Sci*. 2010;51(3):1709-1718. doi:10.1167/iovs.09-3375.
150. Kozak I, Luttrull JK. Modern retinal laser therapy. *Saudi J Ophthalmol*. 2015;29(2):137-146. doi:10.1016/j.sjopt.2014.09.001.
151. Pennesi ME, Michaels K V., Magee SS, et al. Long-Term Characterization of Retinal Degeneration in rd1 and rd10 Mice Using Spectral Domain Optical Coherence Tomography. *Invest Ophthalmol Vis Sci*. 2012;53(8):4644-4656. doi:10.1167/iovs.12-9611.
152. Giani A, Thanos A, Roh MI, et al. In vivo evaluation of laser-induced choroidal neovascularization using spectral-domain optical coherence tomography. *Invest Ophthalmol Vis Sci*. 2011;52(6):3880-3887. doi:10.1167/iovs.10-6266.
153. Saint-Geniez M, D'Amore PA. Development and pathology of the hyaloid, choroidal and retinal vasculature. *Int J Dev Biol*. 2004;48(8-9):1045-1058. doi:10.1387/ijdb.041895ms.

154. Heneghan C, Flynn J, O'Keefe M, Cahill M. Characterization of changes in blood vessel width and tortuosity in retinopathy of prematurity using image analysis. *Med Image Anal.* 2002;6(4):407-429. <http://www.ncbi.nlm.nih.gov/pubmed/12426111>.
155. Grossniklaus HE, Kang SJ, Berglin L. Animal models of choroidal and retinal neovascularization. *Prog Retin Eye Res.* 2010;29(6):500-519. doi:10.1016/j.preteyeres.2010.05.003.
156. Maldonado RS, Toth C a. Optical coherence tomography in retinopathy of prematurity. *Clin Perinatol.* 2014;40(2):271-296. doi:10.1016/j.clp.2013.02.007.Optical.
157. Wilson CM, Wong K, Ng J, Cocker KD, Ells AL, Fielder AR. Digital image analysis in retinopathy of prematurity: a comparison of vessel selection methods. *J AAPOS.* 2012;16(3):223-228. doi:10.1016/j.jaapos.2011.11.015.
158. Seo MS, Kwak N, Ozaki H, et al. Dramatic inhibition of retinal and choroidal neovascularization by oral administration of a kinase inhibitor. *Am J Pathol.* 1999;154(6):1743-1753. doi:10.1016/S0002-9440(10)65430-2.
159. Luttrull JK, Dorin G. Subthreshold diode micropulse laser photocoagulation (SDM) as invisible retinal phototherapy for diabetic macular edema: a review. *Curr Diabetes Rev.* 2012;8(4):274-284. doi:10.2174/157339912800840523.
160. Chang B. Mouse models for studies of retinal degeneration and diseases. *Methods Mol Biol.* 2013;935:27-39. doi:10.1007/978-1-62703-080-9-2.
161. Ferguson LR, Balaiya S, Grover S, Chalam K V. Modified protocol for in vivo imaging of wild-type mouse retina with customized miniature spectral domain optical coherence tomography (SD-OCT) device. *Biol Proced Online.* 2012;14(1):9. doi:10.1186/1480-9222-14-9.
162. Rodolfo M, Lisa T, Luca DA, et al. Optical coherence tomography angiography microvascular findings in macular edema due to central and branch retinal vein occlusions. *Sci Rep.* 2017;7(September 2016):40763. doi:10.1038/srep40763.
163. Sulaiman RS, Quigley J, Qi X, et al. A Simple Optical Coherence Tomography Quantification Method for Choroidal Neovascularization. *J Ocul Pharmacol Ther.* 2015;00(00):150610093445000. doi:10.1089/jop.2015.0049.
164. Luisi J, Lin J, Motamedi M. *Speckle Variance in the En-Face View as a Contrast for Optical Coherence Tomography Angiography (OCTA)*. 301 University blvd. Galveston TX
165. Fraz MM, Remagnino P, Hoppe a, et al. Blood vessel segmentation methodologies in retinal images--a survey. *Comput Methods Programs Biomed.* 2012;108(1):407-433. doi:10.1016/j.cmpb.2012.03.009.
166. Jia Y, Bailey ST, Wilson DJ, et al. Quantitative optical coherence tomography angiography of choroidal neovascularization in age-related macular degeneration. *Ophthalmology.* 2014;121(7):1435-1444. doi:10.1016/j.ophtha.2014.01.034.
167. Yu D-Y, Cringle SJ, Su E, Yu PK, Humayun MS, Dorin G. Laser-induced changes

- in intraretinal oxygen distribution in pigmented rabbits. *Invest Ophthalmol Vis Sci*. 2005;46(3):988-999. doi:10.1167/iovs.04-0767.
168. Uddin MI, Evans SM, Craft JR, et al. In Vivo Imaging of Retinal Hypoxia in a Model of Oxygen-Induced Retinopathy. *Sci Rep*. 2016;6:31011. doi:10.1038/srep31011.
 169. Oberwahrenbrock T, Weinhold M, Mikolajczak J, et al. Reliability of intra-retinal layer thickness estimates. *PLoS One*. 2015;10(9):1-16. doi:10.1371/journal.pone.0137316.
 170. Ferguson LR, Dominguez JM, Balaiya S, Grover S, Chalam K V. Retinal Thickness Normative Data in Wild-Type Mice Using Customized Miniature SD-OCT. *PLoS One*. 2013;8(6):e67265. doi:10.1371/journal.pone.0067265.
 171. Klawitter D, Hillmann D. Speckle variance optical coherence tomography for imaging microcirculation. *Student Conf* 2013. https://gruenderklinik.de/uploads/tx_wapublications/Klawitter__2013_Speckle_variance_optical_coherence_tomography_for_imaging_microcirculation.pdf. Accessed February 24, 2014.
 172. Eter N, Engel D, Meyer L, Helb H. In vivo visualization of dendritic cells, macrophages, and microglial cells responding to laser-induced damage in the fundus of the eye. ... *Ophthalmol Vis* 2008;49(228):1-33. <http://www.iovs.org/content/49/8/3649.short>. Accessed July 8, 2014.
 173. Kohno H, Koso H, Okano K, et al. Expression pattern of Ccr2 and Cx3cr1 in inherited retinal degeneration. *J Neuroinflammation*. 2015;12:188. doi:10.1186/s12974-015-0408-3.
 174. Bosco A, Romero CO, Breen KT, et al. Neurodegeneration severity is anticipated by early microglia alterations monitored in vivo in a mouse model of chronic glaucoma. *Dis Model Mech*. 2015:443-455. doi:10.1242/dmm.018788.
 175. Chen M, Hombrebueno JR, Luo C, et al. Age- and Light-Dependent Development of Localised Retinal Atrophy in CCL2-/-CX3CR1GFP/GFP Mice. *PLoS One*. 2013;8(4). doi:10.1371/journal.pone.0061381.
 176. Alt C, Runnels JM, Teo GSL, Lin CP. In vivo tracking of hematopoietic cells in the retina of chimeric mice with a scanning laser ophthalmoscope. *IntraVital*. 2014;1(2):132-140. doi:10.4161/intv.23561.
 177. Crespo-Garcia S, Reichhart N, Hernandez-Matas C, et al. In vivo analysis of the time and spatial activation pattern of microglia in the retina following laser-induced choroidal neovascularization. *Exp Eye Res*. 2015;139:13-21. doi:10.1016/j.exer.2015.07.012.
 178. Can a, Shen H, Turner JN, Tanenbaum HL, Roysam B. Rapid automated tracing and feature extraction from retinal fundus images using direct exploratory algorithms. *IEEE Trans Inf Technol Biomed*. 1999;3(2):125-138. <http://www.ncbi.nlm.nih.gov/pubmed/10719494>.
 179. Crain JM, Nikodemova M, Watters JJ. Microglia Express Distinct M1 and M2

- Phenotypic Markers in the Postnatal and Adult Central Nervous System in Male and Female Mice. *J Neurosci Res.* 2015;1151(2013):1143-1151. doi:10.1002/jnr.23242.
180. Orihuela R, McPherson CA, Harry GJ. Microglial M1/M2 polarization and metabolic states. *Br J Pharmacol.* 2016;173(4):649-665. doi:10.1111/bph.13139.
 181. Boche D, Perry VH, Nicoll JAR. Review: Activation patterns of microglia and their identification in the human brain. *Neuropathol Appl Neurobiol.* 2013;39(1):3-18. doi:10.1111/nan.12011.
 182. Chhor V, Le Charpentier T, Lebon S, et al. Characterization of phenotype markers and neuronotoxic potential of polarised primary microglia In vitro. *Brain Behav Immun.* 2013;32:70-85. doi:10.1016/j.bbi.2013.02.005.
 183. Zhou Y, Yoshida S, Nakao S, et al. M2 macrophages enhance pathological neovascularization in the mouse model of oxygen-induced retinopathy. *Investig Ophthalmol Vis Sci.* 2015;56(8):4767-4777. doi:10.1167/iovs.14-16012.
 184. Jetten N, Verbruggen S, Gijbels MJ, Post MJ, De Winther MPJ, Donners MMPC. Anti-inflammatory M2, but not pro-inflammatory M1 macrophages promote angiogenesis in vivo. *Angiogenesis.* 2014;17(1):109-118. doi:10.1007/s10456-013-9381-6.
 185. Yang Y, Liu F, Tang M, et al. Macrophage polarization in experimental and clinical choroidal neovascularization. *Sci Rep.* 2016;6(June):1-12. doi:10.1038/srep30933.
 186. Siani F, Greco R, Levandis G, et al. Influence of estrogen modulation on glia activation in a murine model of parkinson's disease. *Front Neurosci.* 2017;11(MAY):1-11. doi:10.3389/fnins.2017.00306.
 187. Poor SH, Qiu Y, Fassbender ES, et al. Reliability of the mouse model of choroidal neovascularization induced by laser photocoagulation. *Investig Ophthalmol Vis Sci.* 2014;55(10):6525-6534. doi:10.1167/iovs.14-15067.
 188. Sanders LH, Greenamyren JT. Oxidative damage to macromolecules in human Parkinson disease and the rotenone model. *Free Radic Biol Med.* 2013;62:111-120. doi:10.1016/j.freeradbiomed.2013.01.003.
 189. Cannon JR, Tapias VM, Na HM, Honick AS, Drolet RE, Greenamyre JT. A high reproducible rotenone model of Parkinson's disease. *Neurobiol Dis.* 2009;34(2):279-290. doi:10.1016/j.nbd.2009.01.016.A.
 190. Blesa J, Phani S, Jackson-Lewis V, Przedborski S. Classic and new animal models of Parkinson's disease. *J Biomed Biotechnol.* 2012;2012. doi:10.1155/2012/845618.
 191. Klintworth H, Garden G, Xia Z. Rotenone and paraquat do not directly activate microglia or induce inflammatory cytokine release. *Neurosci Lett.* 2009;462(1):1-5. doi:10.1016/j.neulet.2009.06.065.
 192. Yuan YH, Sun JD, Wu MM, Hu JF, Peng SY, Chen NH. Rotenone could activate microglia through NFkB associated pathway. *Neurochem Res.* 2013;38(8):1553-

1560. doi:10.1007/s11064-013-1055-7.
193. Emmrich J V., Hornik TC, Neher JJ, Brown GC. Rotenone induces neuronal death by microglial phagocytosis of neurons. *FEBS J.* 2013;280(20):5030-5038. doi:10.1111/febs.12401.
194. Gao H-M, Liu B, Hong J-S. Critical role for microglial NADPH oxidase in rotenone-induced degeneration of dopaminergic neurons. *J Neurosci Off J Soc Neurosci.* 2003;23(15):6181-6187. doi:23/15/6181 [pii].
195. Jha MK, Lee WH, Suk K. Functional polarization of neuroglia: Implications in neuroinflammation and neurological disorders. *Biochem Pharmacol.* 2016;103:1-16. doi:10.1016/j.bcp.2015.11.003.
196. Du C, Jin M, Hong Y, et al. Downregulation of cystathionine β -synthase/hydrogen sulfide contributes to rotenone-induced microglia polarization toward M1 type. *Biochem Biophys Res Commun.* 2014;451(2):239-245. doi:10.1016/j.bbrc.2014.07.107.
197. Sherer TB, Betarbet R, Kim JH, Greenamyre JT. Selective microglial activation in the rat rotenone model of Parkinson's disease. *Neurosci Lett.* 2003;341(2):87-90. doi:10.1016/S0304-3940(03)00172-1.
198. Gao HM, Jiang J, Wilson B, Zhang W, Hong JS, Liu B. Microglial activation-mediated delayed and progressive degeneration of rat nigral dopaminergic neurons: Relevance to Parkinson's disease. *J Neurochem.* 2002;81(6):1285-1297. doi:10.1046/j.1471-4159.2002.00928.x.
199. Wang Y, Liu D, Zhang H, et al. Ultrafine carbon particles promote rotenone-induced dopamine neuronal loss through activating microglial NADPH oxidase. *Toxicol Appl Pharmacol.* 2017;322:51-59. doi:10.1016/j.taap.2017.03.005.
200. Gao HM, Liu B, Zhang W, Hong JS. Synergistic dopaminergic neurotoxicity of MPTP and inflammogen lipopolysaccharide: relevance to the etiology of Parkinson's disease. *Faseb J.* 2003;17(13):1957-1959. doi:10.1096/fj.03-0203fje.
201. Zeng H, Ding M, Chen XX, Lu Q. Microglial NADPH oxidase activation mediates rod cell death in the retinal degeneration in rd mice. *Neuroscience.* 2014;275:54-61. doi:10.1016/j.neuroscience.2014.05.065.
202. Liang Y, Jing X, Zeng Z, et al. Rifampicin attenuates rotenone-induced inflammation via suppressing NLRP3 inflammasome activation in microglia. *Brain Res.* 2015;1622(107):43-50. doi:10.1016/j.brainres.2015.06.008.
203. Sarkar S, Malovic E, Harishchandra DS, et al. Mitochondrial impairment in microglia amplifies NLRP3 inflammasome proinflammatory signaling in cell culture and animal models of Parkinson's disease. *npj Park Dis.* 2017;3(1):30. doi:10.1038/s41531-017-0032-2.
204. Tanner CM, Kame F, Ross GW, et al. Rotenone, paraquat, and Parkinson's disease. *Environ Health Perspect.* 2011;119(6):866-872. doi:10.1289/ehp.1002839.
205. Zhang X, Jones D, Gonzalez-Lima F. Neurodegeneration produced by rotenone in

- the mouse retina: A potential model to investigate environmental pesticide contributions to neurodegenerative diseases. *J Toxicol Environ Heal - Part A Curr Issues*. 2006;69(18):1681-1697. doi:10.1080/15287390600630203.
206. Galvao J, Davis B, Tilley M, Normando E, Duchon MR, Cordeiro MF. Unexpected low-dose toxicity of the universal solvent DMSO. *FASEB J*. 2014;28(3):1317-1330. doi:10.1096/fj.13-235440.
 207. Fischer F, Martin G, Agostini HT, et al. Activation of retinal microglia rather than microglial cell density correlates with retinal neovascularization in the mouse model of oxygen-induced retinopathy. *J Neuroinflammation*. 2011;8(1):120. doi:10.1186/1742-2094-8-120.
 208. Zhang X, Jones D, Gonzalez-Lima F. Mouse model of optic neuropathy caused by mitochondrial complex I dysfunction. *Neurosci Lett*. 2002;326(2):97-100. doi:10.1016/S0304-3940(02)00327-0.
 209. Yuan C, Gao J, Guo J, et al. Dimethyl sulfoxide damages mitochondrial integrity and membrane potential in cultured astrocytes. *PLoS One*. 2014;9(9). doi:10.1371/journal.pone.0107447.
 210. Rood IM, Deegens JKJ, Merchant ML, et al. Comparison of three methods for isolation of urinary microvesicles to identify biomarkers of nephrotic syndrome. *Kidney Int*. 2010;78(8):810-816. doi:10.1038/ki.2010.262.
 211. Li P, Kaslan M, Lee SH, Yao J, Gao Z. Progress in exosome isolation techniques. *Theranostics*. 2017;7(3):789-804. doi:10.7150/thno.18133.
 212. Théry C, Amigorena S, Clayton A, Amigorena S, Raposo and G. Isolation and characterization of exosomes from cell culture supernatants and biological fluids. *Curr Protoc* 2006:1-29. <http://onlinelibrary.wiley.com/doi/10.1002/0471143030.cb0322s30/full>. Accessed December 7, 2014.
 213. Rekker K, Saare M, Roost AM, et al. Comparison of serum exosome isolation methods for microRNA profiling. *Clin Biochem*. 2014;47(1-2):135-138. doi:10.1016/j.clinbiochem.2013.10.020.
 214. Van Deun J, Mestdagh P, Sormunen R, et al. The impact of disparate isolation methods for extracellular vesicles on downstream RNA profiling. *J Extracell vesicles*. 2014;1:1-14. doi:10.3402/jev.v3.24858.
 215. Shah N, Ishii M, Brandon C, et al. Extracellular vesicle-mediated long-range communication in stressed retinal pigment epithelial cell monolayers. *Biochim Biophys Acta - Mol Basis Dis*. 2018;1864(8):2610-2622. doi:10.1016/j.bbadis.2018.04.016.
 216. Zhang W, Ma Y, Zhang Y, Yang J, He G, Chen S. Photo-Oxidative Blue-Light Stimulation in Retinal Pigment Epithelium Cells Promotes Exosome Secretion and Increases the Activity of the NLRP3 Inflammasome. *Curr Eye Res*. 2018;44(1):67-75. doi:10.1080/02713683.2018.1518458.
 217. Maroto R, Zhao Y, Jamaluddin M, et al. Effects of storage conditions on airway

- exosome integrity for diagnostic and functional analyses. *J Extracell vesicles*. 2017;6(1). doi:10.1080/20013078.2017.1359478.
218. Menck K, Sönmezer C, Worst TS, et al. Neutral sphingomyelinases control extracellular vesicles budding from the plasma membrane. *J Extracell Vesicles*. 2017;6(1). doi:10.1080/20013078.2017.1378056.
219. Lallemand T, Rouahi M, Swiader A, et al. nSMase2 (Type 2-Neutral Sphingomyelinase) Deficiency or Inhibition by GW4869 Reduces Inflammation and Atherosclerosis in Apoe^{-/-} Mice Highlights. *Arterioscler Thromb Vasc Biol*. 2018;38(7):1479-1492. doi:10.1161/ATVBAHA.118.311208.
220. Xie B, Shen J, Dong A, Rashid A, Stoller G, Campochiaro PA. Blockade of sphingosine-1-phosphate reduces macrophage influx and retinal and choroidal neovascularization. *J Cell Physiol*. 2009;218(1):192-198. doi:10.1002/jcp.21588.
221. Tabatadze N, Savonenko A, Song H, Bandaru VVR, Chu M, Haughey NJ. Inhibition of neutral sphingomyelinase-2 perturbs brain sphingolipid balance and spatial memory in mice. *J Neurosci Res*. 2010;88(13):2940-2951. doi:10.1002/jnr.22438.
222. Dinkins, M. B., Dasgupta, S., Wang, G., Zhu, G., Bieberich E. Plaque Load in the 5XFAD Mouse Model of Alzheimer's Disease. 2015;35(8):1792-1800. doi:10.1016/j.neurobiolaging.2014.02.012.Exosome.
223. Vuckovic S, Vandyke K, Rickards DA, et al. The cationic small molecule GW4869 is cytotoxic to high phosphatidylserine-expressing myeloma cells. *Br J Haematol*. 2017;177(3):423-440. doi:10.1111/bjh.14561.

Vita

<The vita is a brief biographical sketch of the writer. It should include the writer's date and place of birth; name of parents; schools and colleges attended; degrees awarded; publications and experience in teaching, business, and industry; military service, if any; and a permanent address.> Jonathan Luisi was born in San Antonio on March 16, 1987. Raised by parents William and Cathy in New Jersey, where he attended Kinnelon High School. Jonathan went to RPI (Rensselaer Polytechnic Institute) for a Bachelor in Science, majoring in Biomedical Engineering: imaging and minored in Electrical Engineering: instrumentation. Jonathan worked for Dr. Patrick Page-McCaw and Dr. Badrinath Roysam at RPI, before becoming lab manager at the Bio-Image Analytics Lab at the University of Houston. Jonathan also worked as a research associate for Dr. Laezza Fernanda at University of Texas Medical Branch.

Pier Reviewed Publications

1. Liu, Wei, **Jonathan Luisi**, Hua Liu, Massoud Motamedi, and Wenbo Zhang. 2017. "OCT-Angiography for Noninvasive Monitoring of Neuronal and Vascular Structure in Mouse Retina: Implication for Characterization of Retina Neurovascular Coupling." *EC Ophthalmology* 3 (2017): 89–98.
2. Maroto, Rosario, Yingxin Zhao, Mohammad Jamaluddin, Vsevolod L Popov, Hongwang Wan, Madumali Kalubowilage, Yueqing Zhang, et al. 2017. "Effects of Storage Conditions on Airway Exosome Integrity for Diagnostic and Functional Analyses." *Journal of Extracellular Vesicles* 6 (1). Taylor & Francis. doi:10.1080/20013078.2017.1359478.
3. James, Thomas F, Miroslav N Nenov, Norelle C Wildburger, Cheryl Lichti, **Jonathan Luisi**, Fernanda Vergara, Neli I Panova-Electronova, et al. 2015. "The Nav1.2 Channel Is Regulated by GSK3." *Biochimica et Biophysica Acta*, January. doi:10.1016/j.bbagen.2015.01.011.
4. **Luisi, Jonathan**, David Briley, Adam Boretsky, and Massoud Motamedi. 2014. "Automated Retinal Layer Segmentation and Characterization." In *SPIE Proceedings*, edited by Tomasz S. Tkaczyk, 3:91551N. doi:10.1117/12.2057814.
5. Adhikari, Ananta, Irene Rusakova, Ardebili Haleh, **Jonathan Luisi**, Neli Panova, Fernanda Laezza, and Wei-Kan Chu. 2014. "Thermal Property and Assessment of Biocompatibility of Poly (Lactic-Co-Glycolic) Acid/graphene Nanocomposites." *Journal of Applied Physics* 54701: 2–7. doi:10.1063/1.4864263.
6. **Luisi, Jonathan**, Arunachalam Narayanaswamy, Zachary Galbreath, and Badrinath Roysam. 2011. "The FARSIGHT Trace Editor: An Open Source Tool for 3-D Inspection and Efficient

Pattern Analysis Aided Editing of Automated Neuronal Reconstructions.” *Neuroinformatics* 9 (2–3): 305–15. doi:10.1007/s12021-011-9115-0.

Submitted Papers

- **Jonathan Luisi**, Jonathan Lin, Massoud Motamedi, “Spatial-Temporal Speckle Variance in the En-Face view as a contrast for Optical Coherence Tomography Angiography (OCTA)” to IEE TBME
- **Jonathan Luisi**, Wenbo Zhang, Gracie Vargas, Massoud Motamedi, “Imaging Microglia dynamics in laser-induced acute inflammation and Choroidal Neovascularization (L-CNV)”, to BOE

Permanent address: 103 Whiting Ave, Galveston TX, 77550

This dissertation was typed by Jonathan Luisi.